Semiconductors, Vol. 39, No. 3, 2005, pp. 273–276. Translated from Fizika i Tekhnika Poluprovodnikov, Vol. 39, No. 3, 2005, pp. 291–295.
Original Russian Text Copyright © 2005 by Lobanovskiĭ, Trukhanov, Bushinskiĭ, Troyanchuk.

Cationic Disorder in an Sr_2FeMoO_6 Binary Oxide with a Perovskite Structure

L. S. Lobanovskiĭ^, S. V. Trukhanov, M. V. Bushinskiĭ, and I. O. Troyanchuk

Institute of Solid-State and Semiconductor Physics, Belarussian Academy of Sciences, ul. Brovki 17, Minsk, 220072 Belarus

^e-mail: Lobanov@ifttp.bas-net.by

Submitted April 21, 2004; accepted for publication April 28, 2004

Abstract—To determine the influence that the degree of crystallographic ordering of the magnetoactive ions in Sr_2FeMoO_6 oxide has on the properties of this compound, samples produced by various methods are studied. A sample synthesized in an argon flow using conventional ceramic technology exhibits a high degree of cationic ordering involving iron and molybdenum ions. A sample grown under high pressure and quenched to room temperature exhibits a rather lower degree of ordering in relation to magnetoactive ions. It is ascertained that the crystallographic disorder of iron and molybdenum ions affects the compound's magnetic and magnetoresistive properties. In particular, this disorder results in a decrease in the specific magnetization due to the antiferromagnetic interactions between similar ions and a reduction of the magnetoresistance-effect magnitude due to a decrease in the degree to which the charge carriers experience spin polarization. *© 2005 Pleiades Publishing, Inc.*

1. INTRODUCTION

The detection of an anomalously high magnetoresistance (magnetoresistance effect) under moderate magnetic fields in ferromagnetic substituted lanthanum manganites $La_{1-x}(Ca,Sr,Ba)_xMnO_3$ stimulated a search for new magnetic systems exhibiting a similar effect, as there are a considerable number of potential applications for the ambiguous phenomenon of this mechanism [1, 2]. Studies of the magnetoresistance of various manganese-containing solid solutions showed that the magnetoresistance effect manifests itself in polycrystalline magnetic systems that possess carriers with a high degree of spin polarization at temperatures much lower than the magnetic ordering temperature [3]. The magnetoresistance arises due to a decrease in the carrier scattering at the interfaces of adjacent grains that have various orientations of the magnetization vector under an external magnetic field. This effect is referred to as giant magnetoresistance (GMR) [2].

Recently, it was found that A_2FeMoO_6 compounds (A = Ca, Sr, and Ba) with a doubled perovskite structure, as they are ferrimagnets, exhibit a pronounced magnetoresistance effect of an intergrain nature [4, 5]. Further publications showed that the conductivity of a Sr_2FeReO_6 compound is semimetallic [6]. Thus, it was verified that the conductivity in Sr_2FeMoO_6-type compounds is caused by charge carriers that have the same spin orientation at the Fermi level. When compared to other magnetic systems exhibiting GMR, the Sr_2FeMoO_6 magnetoresistance is closest to the behavior expected within existing theoretical models [7]. Therefore, Sr_2FeMoO_6-type compounds can be used as model objects when studying the correlation of the magnetic and transport properties in perovskite-like oxides.

At an earlier date, we studied the effect of oxygen nonstoichiometry on the magnetic and electrical properties of Sr_2FeMoO_6, Ba_2FeMoO_6, and Ca_2FeMoO_6 oxides [8, 9]. It was ascertained that a change in the oxygen nonstoichiometry of these compounds results, first of all, in a change of the intergrain layer state as well as the valence states consisting of iron and molybdenum ions. A metal–semiconductor transition was detected and many important features of the magnetoresistance dynamics were determined in relation to the oxygen content. Therefore, it is also of no small importance to study the effect of cationic disorder on the magnetoresistive properties of these compounds. It is expected that these magnetoresistive properties can be more pronounced in compounds with a crystallographically disordered arrangement of Fe and Mo ions, since disordering inside the grains causes magnetic inhomogeneities with various types of exchange interactions. In this case, an external magnetic field can have a significant effect on the magnetic order and, hence, on the conductance of these compounds. From a practical standpoint, it is of interest to study the correlation between the magnetic and magnetoresistive properties in binary oxides that have this Sr_2FeMoO_6-type perovskite structure, as the high magnetic-ordering temperature in these compounds and their possible room-temperature application means they lend themselves to being used as magnetic-field sensors or other devices for magnetic-to-electric signal conversion. Thus, the purpose of this study is to gain insight into the effect of the cationic disorder of the magnetoactive ions in an Sr_2FeMoO_6 oxide with a perovskite structure on the properties of this compound.

1063-7826/05/3903-0273$26.00 © 2005 Pleiades Publishing, Inc.

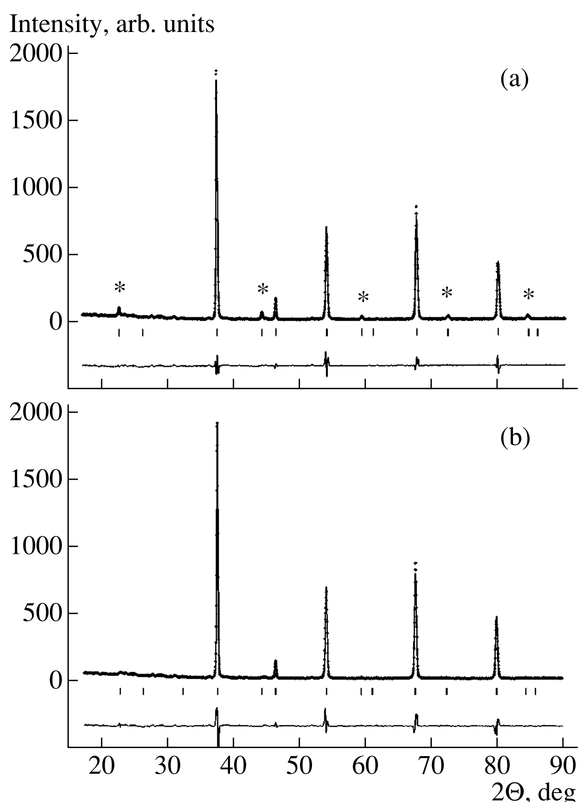

Fig. 1. X-ray patterns processed using the FULLPROF code [10] for (a) sample *1* and (b) sample *2*. Symbol * indicates superstructural reflections.

2. EXPERIMENTAL

In order to clarify the influence of the cationic order of iron and molybdenum ions on the $Sr_2(FeMo)O_6$ properties, we synthesized samples in which these ions exhibited various degrees of crystallographic ordering. The Sr_2FeMoO_6 samples were prepared from oxides of the corresponding elements taken in stoichiometric proportions. The first sample (designated as *1*) with a crystallographically ordered arrangement of iron and molybdenum ions was grown, using solid-phase reactions, by synthesis in an argon flow at a temperature of 1423 K and followed by annealing in an evacuated quartz cell. The second sample with a disordered arrangement of Fe and Mo ions (designated as *2*) was synthesized by using solid-phase reactions under high pressure. The disorder was attained by abrupt cooling of the sample from the synthesis temperature of 1423 K.

A chemical analysis showed that the chemical composition of these samples is close (within an allowable error) to the nominal chemical formula. An X-ray diffraction analysis, as well as refinement of the unit-cell parameters, was carried out using a DRON-3M X-ray diffractometer in conjunction with the software package FULLPROF, which performs full-profile analyses of X-ray patterns [10]. The magnetic properties were evaluated using a Foner magnetometer. The electrical properties and magnetoresistance were measured using the conventional four-probe method. The magnetoresistance was determined as $MR = (\rho_0 - \rho_H)/\rho_0$, where ρ_0 and ρ_H are the resistivities in the fields $H = 0$ and 0.71 MA/m, respectively.

3. RESULTS AND DISCUSSION

The X-ray diffraction analysis showed that the samples under study crystallize into a perovskite structure with cubic symmetry of its unit cells (Figs. 1a, 1b). The different intensities of the superstructural reflections of samples *1* and *2* indicate the ordering of iron and molybdenum ions at different degrees. The unit cell parameter of sample *1* (a = 7.86761 ± 0.00054 Å) is smaller than that of sample *2* (a = 7.88473 ± 0.00011 Å). This difference is somewhat unexpected considering the similar cationic radii of Fe^{3+} and Mo^{5+} and the similar synthesis techniques used. As a rule, compositions obtained under high pressure exhibit a denser packing of unit cells [11]. However, the result obtained can be interpreted by taking into account the valence and crystallographic state of the iron and molybdenum ions. As these ions are ordered, the Coulomb interaction energy over the entire lattice reaches its lowest point. The unit cell volume also tends to a minimum. Due to the disordering, the Coulomb repulsion energy increases and tends to increase the unit-cell parameter. This assumption is justified by the measured X-ray patterns processed using the Rietveld method [10]. For example, it was established that the degree to which iron and molybdenum ions are ordered in sample *1* is 97%, but this value is much lower in sample *2* (76%). The visually different order of iron and molybdenum ions can be estimated from the intensity of the superstructural reflections in the samples under study (Figs. 1a and 1b).

The magnetization measurements showed (Fig. 2) that the total magnetic moment of the sample produced under high pressure is M = 2.0 Bohr magnetons per molecule (μ_B/mol). This value is somewhat lower than the total magnetic moment of the sample synthesized in an argon flow ($M = 2.9\ \mu_B$/mol). The different magnetizations in the samples under consideration can also be interpreted from the assumption that Fe^{3+} and Mo^{5+} magnetoactive ions are disordered. Taking into account the specific magnetization of sample *1*, we may conclude that the magnetic moments of iron and molybdenum ions are ferrimagnetically ordered. Such ordering was previously observed in other A_2FeMoO_6-type compounds (A = Ca and Ba) with the doubled perovskite structure [8, 9]. The disordering of Fe^{3+} and Mo^{5+} ions results in the formation of additional Fe^{3+}–O^{2-}–Fe^{3+} and Mo^{5+}–O^{2-}–Mo^{5+} bonds. In this case, it is assumed that the indirect exchange interactions are negative, and it is this which gives rise to the antiferromagnetic ordering of the magnetic moments of these ions [3]. As a result, the specific magnetization decreases.

The Neel temperatures of the ordered and disordered samples differ and are 418 and 412 K, respec-

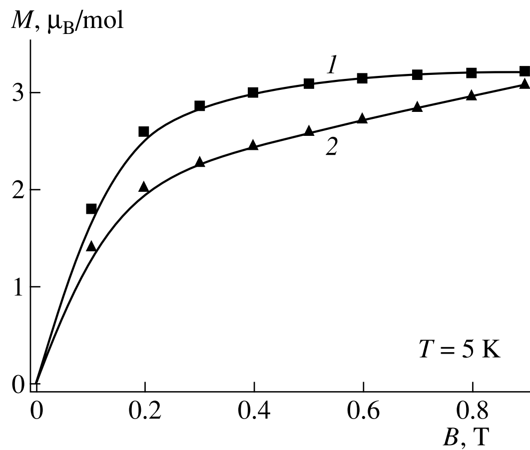

Fig. 2. The field dependence of the magnetization of samples *1* and *2* (curves *1* and *2*, respectively), measured at a temperature of 5 K.

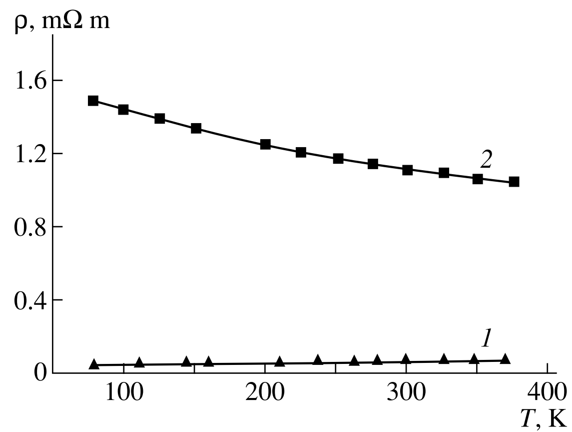

Fig. 3. The temperature dependence of the resistivity of Sr_2FeMoO_6 for samples *1* and *2* (curves *1* and *2*, respectively).

tively. This difference can also be attributed to the ion disorder in quenched sample *2*, since the formation of additional antiferromagnetic bonds results in a magnetic dilution of the ground ferrimagnetic state, which decreases the magnetic ordering temperature.

The resistivities of the samples under study is different both in magnitude and temperature dependence (Fig. 3). Sample *1* has a lower resistivity and metallic conductivity in the temperature dependence. A similar behavior was observed in [12] for single-crystal samples of double Sr_2FeMoO_6 perovskite, which were grown by the float-zone method. This fact indicates the high quality of the produced ceramics and the weak influence of the grain boundaries on the electrical properties in sample *1*. Quenched sample *2*, produced under high pressure, had a higher resistivity and exhibited a semiconductor-type resistivity in relation to temperature in the entire temperature range (Fig. 3).

It is difficult to interpret the electrical properties of the samples only within the cationic-disorder model, since the electrical properties of polycrystals depend heavily on the grain boundaries, whose structure, in turn, depends heavily on the synthesis conditions [13]. Two other models, describing the electrical properties of these compounds with a greater degree of accuracy, can be suggested. The electrical properties of polycrystals are controlled by the conductivity of the grains and intergrain layers. One of the models, which can be used to interpret the electrical properties of intergrain layers, was developed by Seto in relation to doped polycrystalline silicon samples [14]. Later, this theory was modified and applied to other polycrystalline semiconductor materials [15, 16]. According to this theory, the electrical properties of polycrystals are mainly controlled by the carrier trapping attributed to dangling bonds of atoms localized on the grain boundaries: first, this carrier trapping results in a decrease in the number of free carriers involved in conduction and, second, in a significant decrease in their mobility due to the scattering by potential barriers arising at the interfaces.

The second model, describing the behavior of the intergrain layer (i.e., individual crystallites), is often used to interpret the electrical properties of substituted lanthanum manganites [17]. This model implies that these electrical properties are controlled by a charge transfer between manganese ions of different valence. At a high content of manganese ions with identical valence, an antiferromagnetic state is formed and the conductivity type changes from a metallic to semiconductor type [17].

We believe that the properties of the samples under study can be interpreted by taking into account both models. For example, the sample produced under high pressure and quenched to room temperature immediately after annealing exhibits a higher defect density in both the intergrain and intragrain structures. This behavior can be qualitatively estimated by an insignificant broadening of the spectral lines shown in the X-ray patterns of the samples. In turn, the electrical transport in the defect structure features a lower mobility. According to the first model, such a state causes additional electron trapping by dangling bonds, depletion of the sample of conduction electrons, and a decrease in their mobility. According to the second model, the formation of additional antiferromagnetic bonds inside the grainsin sample *2* also causes a decrease in the sample's conductivity. In our opinion, the effect of all the above-listed factors resulted not only in an increase in the resistivity but also in a change in the conductivity type of the quenched sample. To study the effect of the cationic disorder on the electrical properties of Sr_2FeMoO_6 oxide in more detail, it is expedient to carry out measurements with single-crystal samples.

The magnetoresistance effect was detected in all the samples under study (Fig. 4). The magnetoresistance in sample *1* amounted to 18% at a temperature of 78 K. In sample *2*, a decrease in the magnetoresistance was observed. The significant slope of the field dependence of the magnetoresistance for quenched sample *2* in the region of strong magnetic fields indicates that there is a

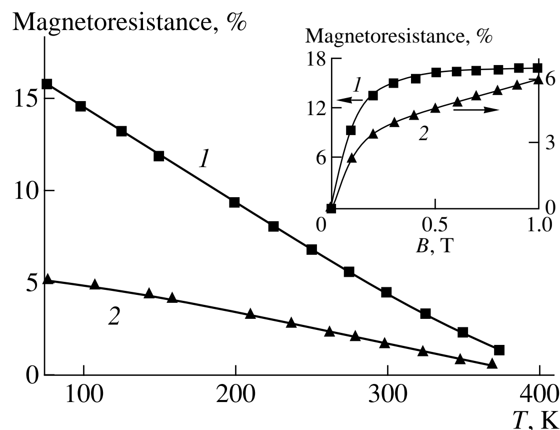

Fig. 4. The temperature dependence of the magnetoresistance of samples *1* and *2* (curves *1* and *2*, respectively). The inset shows the field dependence of the magnetoresistance of the samples under study, measured at a temperature of 78 K.

correlation between the magnetic properties and the magnetoresistance (cf Fig. 2 and the inset in Fig. 4). It is noteworthy that the fields, at which the magnetoresistance is saturated, are ~0.2 T in both samples. This fact suggests that the magnetoresistance effect's nature does not change due to the cation disordering; therefore, it is associated with the carrier scattering by the interfaces of adjacent grains.

Zhang *et al.* [13] showed, using experimental methods, that a higher defect density in the intergrain layer promotes a magnetoresistance effect of an intergrain nature. However, in the case under consideration, the reverse effect was observed. The magnetoresistive properties of sample *2*, produced under high pressure, became less pronounced, which indicated an alternate cause of the magnetoresistance change. It is difficult to describe a more than twofold decrease in the magnetoresistance by taking into account only a change in the specific magnetization, i.e., according to the theory in [7]. Therefore, we believe that the decrease in the magnetoresistance in quenched sample *2* is caused by, in addition to a change in the magnetization, a change in the degree of the spin polarization of the charge carriers, which is associated with the cationic disorder of iron and molybdenum ions. As was noted above, the cationic disorder results in the competition of the ferrimagnetic and antiferromagnetic interactions in the sample. Under these conditions, the crystal field becomes highly inhomogeneous, which weakens the splitting of two subbands with different spin orientations [3]. Moreover, the degree of carrier polarization decreases.

4. CONCLUSIONS

It was found that the crystallographic disorder of the iron and molybdenum ions in the Sr_2FeMoO_6 binary oxide with a perovskite structure results in a decrease in its specific magnetization and magnetoresistance due to the formation of additional antiferromagnetic bonds. The cationic disorder of the ions also causes a decrease in the degree to which spin polarization of the carriers occurs. These decreases in the specific magnetization and the degree of the carrier spin polarization results in a weakening of the magnetoresistance effect in the Sr_2FeMoO_6 compound.

ACKNOWLEDGMENTS

This study was supported by the Belarussian Republican Foundation for Basic Research, project no. F02M-098, and the state program for specific basic research "Nanomaterials and Nanotechnologies," task no. 3.3.

REFERENCES

1. V. M. Loktev and Yu. G. Pogorelov, Fiz. Nizk. Temp. **26**, 231 (2000) [Low Temp. Phys. **26**, 171 (2000)].
2. J. M. D. Coey, M. Viret, and S. von Molnár, Adv. Phys. **48**, 167 (1999).
3. J. B. Goodenough, *Magnetism and the Chemical Bond* (Interscience, New York, 1963; Metallurgiya, Moscow, 1968).
4. K.-I. Kobayashi, T. Kimura, H. Sawada, *et al.*, Nature **395**, 677 (1998).
5. A. Maignan, B. Raveau, C. Martin, and M. Hervieu, J. Solid State Chem. **144**, 224 (1999).
6. K.-I. Kobayashi, T. Kimura, Y. Tomioka, *et al.*, Phys. Rev. B **59**, 11 159 (1999).
7. H. Y. Hwang, S.-W. Cheong, N. P. Ong, and B. Batlogg, Phys. Rev. Lett. **77**, 2041 (1996).
8. L. S. Lobanovskiĭ, I. O. Troyanchuk, and G. Shimchak, Zh. Éksp. Teor. Fiz. **118**, 617 (2000) [JETP **91**, 537 (2000)].
9. L. S. Lobanovskiĭ, I. O. Troyanchuk, N. V. Pushkarev, and G. Shimchak, Fiz. Tverd. Tela (St. Petersburg) **43**, 651 (2001) [Phys. Solid State **43**, 677 (2001)].
10. J. Rodriguez-Carvajal, in *Abstracts of the Satellite Meeting on Powder Diffraction of the XV Congress of the IUCr* (Toulouse, France, 1990), p. 127.
11. P. Hagenmuller, in *Preparative Methods in Solid State Chemistry*, Ed. by P. Hagenmuller (Academic, New York, 1972; Mir, Moscow, 1976), Chap. 1.
12. Y. Tomioka, T. Okuda, Y. Okimoto, *et al.*, Phys. Rev. B **61**, 422 (2000).
13. N. Zhang, W. P. Ding, W. Zhong, and Y. W. Du, Phys. Rev. B **56**, 8138 (1997).
14. J. Y. W. Seto, J. Appl. Phys. **46**, 5247 (1975).
15. G. Baccarani, B. Riccò, and G. Spadini, J. Appl. Phys. **49**, 5565 (1978).
16. S. A. Kolosov, Yu. V. Klevkov, and A. F. Plotnikov, Fiz. Tekh. Poluprovodn. (St. Petersburg) **38**, 305 (2004) [Semiconductors **38**, 293 (2004)].
17. G. H. Jonker and J. H. van Santen, Physica (Amsterdam) **16**, 337 (1950).

Translated by A. Kazantsev

Semiconductors, Vol. 39, No. 3, 2005, pp. 277–280. Translated from Fizika i Tekhnika Poluprovodnikov, Vol. 39, No. 3, 2005, pp. 296–299.
Original Russian Text Copyright © 2005 by Lebedev, Davydov.

A Vacancy Model of the Heteropolytype Epitaxy of SiC

A. A. Lebedev^ and S. Yu. Davydov

Ioffe Physicotechnical Institute, Russian Academy of Sciences, St. Petersburg, 194021 Russia

^e-mail: shura.lebe@mail.ioffe.ru

Submitted June 29, 2004; accepted for publication July 7, 2004

Abstract—A model for the transformation of SiC polytypes occurring during the growth of an epitaxial layer is suggested that is based on the variation over time of the concentration of carbon vacancies in a transition layer. Experimental data are analyzed in terms of this model. It is shown that the parameter $\eta = G\tau/L_T$ (L_T is the thickness of the transition layer, G is the film growth rate, and τ is the lifetime of a vacancy in the transition layer) is invariant with respect to the method and temperature of the growth of the epitaxial layer. This parameter is determined only by the concentration of carbon vacancies in the substrate and in the film. © *2005 Pleiades Publishing, Inc.*

1. It is known that, despite having the same chemical composition, SiC polytypes may differ significantly in their electrical properties, which makes silicon carbide an exceedingly promising material for the fabrication of various types of heterostructures. At the same time, there still exists no commonly accepted theory that can explain the known experiments on the heteropolytype epitaxy of silicon carbide. One of the most important tasks to be carried out is to find the conditions under which the polytype of a growing layer changes. The aim of this study was to construct a simple model that could describe the process of the heteropolytype epitaxy of SiC in terms of a concentration of vacancies changing in the course of time.

It is known that only in two SiC polytypes are the positions of all the atoms equivalent; moreover, they belong either to cubic (3*C*-SiC) or to hexagonal (2*H*-SiC) lattice sites (see, e.g., [1]). In all other polytypes, atoms may occupy the sites of both types and the polytypes themselves differ in the number of atoms in the hexagonal (N_H) and cubic (N_K) positions. Therefore, it is convenient to characterize the polytypes of silicon carbide with the parameter "degree of hexagonality" γ [2], which is defined as the ratio of the number of atoms in hexagonal positions to the total number of atoms in a unit cell:

$$\gamma = N_H/(N_H + N_K). \qquad (1)$$

The degree of hexagonality for a polytype may vary from unity (2*H*-SiC) to zero (3*C*-SiC) (Table 1). It is noteworthy that the ability to crystallize in different types of crystal lattice is characteristic not only of SiC but also of quite a number of other compounds: GaN, ZnSe, ZnO, diamond, etc. Presently, there is no commonly accepted theory that can explain both the existence of different polytypes of silicon carbide and their mutual transformations in the course of growth. Therefore, one has to use a set of empirical technological conditions under which the formation of some SiC modification is highly probable. For example, it is known that the introduction of N, P, and H impurities, as well as making the [Si]/[C] ratio in the growth zone larger, results in epitaxial films of 3*C*-SiC or films of other polytypes with a degree of hexagonality smaller than that of 6*H*-SiC being formed on a 6*H*-SiC substrate. In contrast, the introduction of Sc, Tb, Al, and B impurities, in conjunction with making the [Si]/[C] ratio in the growth zone smaller, favors the formation of epitaxial films of 4*H*-SiC or of other polytypes with a degree of hexagonality exceeding that of 6*H*-SiC on a 6*H*-SiC substrate. According to [3], the technological conditions listed above affect the concentration of carbon vacancies, N_V^C, in a growing layer, and these vacancies favor the fixing of atoms at cubic lattice sites. In [3], it was believed that an introduction of carbon vacancies V_C, caused by an excess of silicon, leads to compression of a crystal lattice. In this case, a cubic structure of the layer is more favorable from the standpoint of energy than a hexagonal one. The averaged, between different reports, values of N_V^C for different polytypes (see [4]) and [Si]/[C] ratios [5] are listed in Table 1.

Table 1. The degree of hexagonality γ of silicon carbide polytypes, the [Si]/[C] ratio [5], and the averaged concentration N_V^C of carbon vacancies [4]

Polytypes	3*C*	6*H*	15*R*	4*H*	2*H*
γ	0	0.33	0.40	0.50	1
[Si]/[C]	1.046	1.022	1.012	1.001	–
N_V^C, 10^{20} cm^{-2}	33.6	16.3	15.1	7.3	–

Note: The 2*H* polytype is unstable, and no sizable wafers or epitaxial layers were obtained for it.

1063-7826/05/3903-0277$26.00 © 2005 Pleiades Publishing, Inc.

Table 2. Experimental characteristics of the growth process of a 3*C*-SiC film and the calculated parameter η, time constant τ, and motion velocity *g* of a vacancy, and its diffusion length l_V

Reference	Polytype of a substrate	Deposition method	*T*, K	*G*, μm/h	L_T, μm	η	τ, h	*g*, μm/h	l_V, μm
[6]	6*H*-SiC	SEV	2200	20	3.75	1.38	0.26	2.7	0.70
[7]	6*H*-SiC	SEV	2200	20	1.50	1.38	0.10	4.3	0.43
[8]	6*H*-SiC	CVD	1800	1.5	0.17	1.38	0.16	8.3×10^{-2}	1.3×10^{-2}
[8]	15*R*-SiC	CVD	1800	1.5	0.50	1.25	0.42	5.1×10^{-2}	2.1×10^{-2}
[9, 10]	6*H*-SiC	MBE	1500	7.5×10^{-3}	1.51×10^{-3}	1.38	0.28	1.1×10^{-3}	0.29×10^{-3}

Note: SEV denotes sublimation epitaxy in vacuum; CVD, vapor-phase epitaxy (chemical-vapor deposition); and MBE, molecular-beam epitaxy.

In the course of heteropolytype epitaxy, the technological conditions for the growth of an epitaxial layer with a polytype differing from that of the substrate are created (mainly because of a change in the [Si]/[C] ratio, or, which has the same effect, in N_V^C). Let us consider, for clarity, an epitaxial process in which the degree of hexagonality of the grown layer is larger than that of the substrate, which, according to the conditions discussed above, should be accompanied by a decrease in N_V^C.

2. Apparently, the hexagonality will change over a certain period of time, rather than instantaneously. Let us assume, for simplicity, that a transition layer of the same polytype as that of the substrate used for the growth will be formed during this time. Under such circumstances, the concentration of carbon vacancies in this transition layer will be lower than the concentration in the polytype of the substrate $(N_V^C)_S$. As soon as N_V^C decreases to a certain level of concentration $(N_V^C)_L$, the polytype of the growing layer will change.

Let us assume that N_V^C varies with time *t* in accordance with the equation

$$dN_V^C/dt = -N_V^C/\tau, \quad (2)$$

which gives

$$N_V^C = (N_V^C)_S \exp(-t/\tau), \quad (3)$$

Table 3. Experimental characteristics of the growth process of a 4*H*-SiC film on a 6*H*-SiC substrate [11] and the calculated parameter η, time constant τ, and motion velocity *g* of a vacancy, and its diffusion length l_V

T, K	Carbon content, %*	*G*, μm/h	L_T, μm/h	η	τ, h	*g*, μm/h	l_V, μm
1900	5	50	10	1.24	0.25	0.2	0.05
2100	20	400	6	1.24	0.02	4.4	0.09
2500	30	700	5	1.24	0.01	102	1.00

* Mass fraction of carbon.

where τ is the lifetime of the carbon vacancies in the transition layer. The time t_T, in which the transformation of the growing layer from the initial polytype to that being grown is completed, is given by

$$t_T = \tau \ln[(N_V^C)_S/(N_V^C)_L]. \quad (4)$$

Let us assume that $t_T = L_T/G$, where L_T is the thickness of the transition layer (i.e., the thickness of the buffer epitaxial layer, which, presumably, retains the polytype of the substrate), and *G* is the layer growth rate. Then we obtain

$$\tau = (L_T/G)\{\ln[(N_V^C)_S/(N_V^C)_L]\}^{-1}. \quad (5)$$

If the degree of hexagonality of the layer increases in the course of growth (with respect to that of the substrate), then a plus sign should be written in the right-hand part of Eq. (2) and the sign of τ in expressions (4) and (5) should be changed.

The parameters of the problem (τ, L_T, and *G*) are characteristics of a particular technological process. However, the parameter

$$\eta = G\tau/L_T = \left|\ln[(N_V^C)_S/(N_V^C)_L]\right|^{-1} \quad (6)$$

should be the same for all the technological processes leading, e.g., to a structural transformation from polytype 1 to polytype 2. For example, η ≈ 13.08 for the transition 6*H* ⟶ 15*R* and η ≈ 0.66 for the transition 3*C* ⟶ 4*H*, which corresponds to the smallest and largest values of the parameter η for the polytypes listed in Table 1. Here, it is assumed that the carbon vacancies are not thermodynamically equilibrium vacancies but, instead, are due to a deviation from stoichiometry, i.e., to the ratio [Si]/[C] ≠ 1, which is predetermined by the conditions of the film deposition. It is also noteworthy that, in accordance with expression (6), the value of the parameter η is independent of whether a film of polytype 1 is grown on a substrate of polytype 2 or, the opposite, a film of polytype 2 is obtained on a substrate of polytype 1.

If the values of L_T and *G* are known for various cases of heteropolytype epitaxy, we can determine, using the data of Table 1, the time constant τ (see Tables 2 and 3). It was noted in [3, 6–10] that the polytype transforma-

tion $6H \longrightarrow 3C$ occurs when there is an excess of Si; however, no precise data on the [Si]/[C] ratio in the growth zone were reported, nor was the value of L_T specified in [9, 10]. In our calculation, we assume that L_T is of the same order of magnitude as the lattice constant of 6*H*-SiC along the **c** axis, i.e., equal to 15.1 Å [12].

3. Let us consider the motion velocity of a vacancy. During its lifetime τ in the transition layer, a vacancy travels a distance equal to the diffusion length $l_V = \sqrt{D\tau}$, where $D = D_0\exp(-E_d/kT)$ is the diffusion coefficient of the carbon vacancies in SiC, E_d is the activation energy of the diffusion, D_0 is a preexponential factor, k is the Boltzmann constant, and T is the temperature. Consequently, the motion velocity of a vacancy is given by

$$g = \sqrt{D/\tau}. \tag{7}$$

Now, we can write the expression of the parameter η in the form

$$\eta = \frac{G}{g}\frac{l_V}{L_T}. \tag{8}$$

If, for simplicity, it is assumed that the diffusion flow is directed perpendicularly to the surface of the transition layer (or into the layer), then, according to the definition of the time constant τ, l_V should not exceed L_T. As $\eta > 1$ for the cases considered in Tables 2 and 3, the G/g ratio should also exceed unity.

Unfortunately, we have no data on the diffusion of the carbon vacancies in silicon carbide at our disposal, and, therefore, we can only make indirect estimates. The following data for the diffusion of nitrogen in 6*H*-SiC were reported in [13]: D_0 = (4.6–8.7) × 10^4 cm^2/s and E_d = 7.6–9.3 eV in the temperature range 2000–2550°C, which gives the maximum value $D \approx 1.7 \times 10^{-5}$ μm^2/h for T = 1800 K. For the case of boron diffusion in 6*H*-SiC at 1600–2250°C, we have [14]: D_0 = 3.2 cm^2/s and E_d = 5.1 eV, which gives $D \approx 6.1 \times 10^{-3}$ μm^2/h at T = 1800 K. It only remains to assume that $D \sim 10^{-4}$ μm^2/h for the diffusion coefficient of carbon in 6*H*-SiC at T = 1800 K. For calculations involving temperatures other than 1800 K, it is necessary to find D_0 and E_d. If E_d is taken to be the arithmetic mean of the values of 5.1 and 7.6 eV, we have E_d = 6.35 eV. Taking $D = 10^{-4}$ μm^2/h, we find D_0 = 1.89 cm^2/s. Both the vacancy velocities g calculated using formula (7) and the corresponding diffusion lengths l_V are listed in Tables 2 and 3. Indeed, $(G/g) > 1$ and $(l_V/L_T) < 1$. (It should be noted that, because of the lack of relevant experimental data, we used the same values of D_0 and E_d as in the case of the 6*H* polytype.)

Proceeding from definition (6), and assuming that the concentrations $(N_V^{\mathrm{C}})_S$ and $(N_V^{\mathrm{C}})_L$ of the nonequilibrium vacancies are strictly governed by the [Si]/[C] ratio, we come to the conclusion that the parameter η should not depend on temperature to any significant extent. Let us analyze this circumstance by assuming that

$$\tau = \bar{\tau}\exp(E_d/kT), \tag{9}$$

where $\bar{\tau}$ is a preexponential factor. Proceeding from simplified models for the growth of epitaxial films [15–19], we assume that

$$G = \bar{G}\exp(-Q_g/kT). \tag{10}$$

Here, Q_g is the energy governing the growth process. It is equal either to the heat Q during the sublimation of silicon carbide or, if the sticking coefficient is temperature dependent [16, 19], $Q_g = Q + E_a$, where E_a is the height of the potential barrier to be overcome by a particle in order to settle on the substrate surface and $\bar{G}$ is a preexponential factor. It is noteworthy that $\bar{G} \propto T^{-1/2}$ in terms of the Hertz–Knudsen theory [16–19]. However, because the other parameters of the problem (G and τ) can only be determined with an exponential accuracy, we assume, in what follows, that the factor $\bar{G}$ is temperature-independent.

Let us refine the parameter E_d. Since we are considering the emergence of a vacancy from the transition layer, we should take into account that, generally speaking, the value of E_d depends on the position of a vacancy with respect to the layer surface. As regards the process in question, the position of a vacancy within the layer is of no importance. We are only interested in whether or not a vacancy is present in the layer. Therefore, by E_d, we should understand the height of the diffusion barrier on the surface of the transition layer, which is negotiated when the vacancy leaves the crystal. Then, we can assume that $Q_g \approx E_d$. Taking the above into account, this relation looks quite natural. Indeed, both the sublimation and filling of a surface vacancy by a carbon atom occur as a result of the transition of an atom from the vapor phase to the surface of the layer.

The heat required for the sublimation of silicon carbide is Q = 5.88 eV according to [20] and 6.34 eV as reported in [21, 22], which is in good agreement with the average value obtained above: E_d = 6.35 eV. As was shown in [19], the height E_a of the activation barrier can vary from zero to several electronvolts, which presumably depends on the particular experimental installation employed and on the state of the substrate. If we take Q = 5.88 and 6.34 eV, we obtain $E_a = E_d - Q$ = 0.47 and 0.01 eV, respectively. This means that the assumption of the approximate equality $Q_g \approx E_d$ can be considered as sufficiently justified. Thus, we obtain

$$\eta \approx \bar{G}\bar{\tau}/L_T. \tag{11}$$

The thickness of the transition layer primarily depends on the film growth technology and on the chemical composition of the growth zone ([Si]/[C] ratio) rather than on the process temperature, as is indicated, e.g., by the data in Table 2. Indeed, when comparing the results

obtained from samples grown by sublimation epitaxy [6, 7] and by molecular-beam epitaxy [9, 10], we can see that lowering the growth temperature T by a factor of 1.5 leads to a decrease in the thickness L_T of the transition layer by three orders of magnitude. Comparison of the data for 3*C*-SiC films grown on 6*H*-SiC substrates by the sublimation technique [6, 7] and by vapor-phase epitaxy [8] also shows that lowering T by 20% leads to a decrease in L_T by an order of magnitude. At the same time, a more than twofold scatter of the values of L_T was observed at a constant growth temperature (sublimation technique [6, 7]). Thus, the value of L_T can be, at its first approximation, considered temperature-independent. Consequently, the parameter η weakly depends on temperature.

In conclusion, it should be noted that heteropolytype epitaxy is a complex phenomenon associated with a change in the crystal lattice of a substance in the course of its growth. As was mentioned in Section 1, no commonly accepted theory that can explain all the known details of the given mechanism has been developed as yet. The scheme for the heteropolytype epitaxy of SiC presented in this communication is strongly simplified and disregards numerous factors influencing the film growth. At the same time, the approach suggested may serve, in our opinion, as a basis for analyzing the already available published data and for finding ways to carry out further experimental research.

The study was supported by the Russian Foundation for Basic Research, project nos. 03-02-16054 and 04-02-16632.

REFERENCES

1. *Silicon Carbide-1968*, Ed. by H. K. Henisch and R. Roy (Pergamon, Oxford, 1968; Mir, Moscow, 1972).
2. H. Jagodzinskii, Acta Crystallogr., No. 2, 201 (1949).
3. Yu. A. Vodakov, G. A. Lomakina, and E. N. Mokhov, Fiz. Tverd. Tela (Leningrad) **24**, 1377 (1982) [Sov. Phys. Solid State **24**, 780 (1982)].
4. A. A. Lebedev, Fiz. Tekh. Poluprovodn. (St. Petersburg) **33**, 769 (1999) [Semiconductors **33**, 707 (1999)].
5. N. D. Sorokin, Yu. M. Tairov, V. F. Tsvetkov, and M. A. Chernov, Kristallografiya **28**, 910 (1983) [Sov. Phys. Crystallogr. **28**, 539 (1983)].
6. N. Savkina, A. Tregubova, M. Scheglov, *et al.*, Mater. Sci. Eng. B **91**, 317 (2002).
7. A. A. Lebedev, A. M. Strel'chuk, D. V. Davydov, *et al.*, Appl. Surf. Sci. **184**, 419 (2001).
8. F. R. Chien, S. R. Nutt, W. S. Yoo, *et al.*, J. Mater. Res. **9**, 940 (1994).
9. A. Fissel, B. Schroter, U. Kaiser, and W. Richter, Appl. Phys. Lett. **77**, 2418 (2000).
10. A. Fissel, B. Schroter, U. Kaiser, *et al.*, Appl. Surf. Sci. **184**, 37 (2001).
11. M. M. Anikin, Yu. A. Vodakov, E. N. Mokhov, and A. D. Roenkov, USSR Inventor's Certificate No. 816207 (4 June 1979).
12. V. I. Gavrilenko, A. M. Grekhov, D. V. Korbutyak, and V. G. Litovchenko, *Optical Properties of Semiconductors* (Naukova Dumka, Kiev, 1987) [in Russian].
13. L. G. Kroko and A. G. Milnes, Solid-State Electron. **9**, 1125 (1966).
14. Yu. A. Vodakov and E. N. Mokhov, in *Silicon Carbide*, Ed. by R. C. Marshall *et al.* (Univ. of South Carolina Press, Columbia, 1974), p. 508.
15. K. F. Jensen, *Handbook of Crystal Growth* (Elsevier, Amsterdam, 1994), Vol. 3.
16. T. Kaneko, J. Cryst. Growth **69**, 1 (1984).
17. D. D. Avrov, A. S. Baskin, S. I. Dorozhkin, *et al.*, J. Cryst. Growth **198–199**, 1011 (1999).
18. Q.-S. Chen, H. Zhang, V. Prasad, *et al.*, J. Cryst. Growth **224**, 101 (2001).
19. S. Yu. Davydov, A. A. Lebedev, N. S. Savkina, *et al.*, Fiz. Tekh. Poluprovodn. (St. Petersburg) **38**, 153 (2004) [Semiconductors **38**, 150 (2004)].
20. S. K. Lilov and I. Y. Yanchev, Cryst. Res. Technol. **28**, 495 (1993).
21. W. A. Harrison and E. A. Kraut, Phys. Rev. B **37**, 8244 (1988).
22. F. Bechstedt and W. A. Harrison, Phys. Rev. B **39**, 5041 (1989).

Translated by M. Tagirdzhanov

Semiconductors, Vol. 39, No. 3, 2005, pp. 281–284. Translated from Fizika i Tekhnika Poluprovodnikov, Vol. 39, No. 3, 2005, pp. 300–304.
Original Russian Text Copyright © 2005 by Il'in, Maksimov, Moshnikov, Yaroslavtsev.

Internal Friction in Semiconductor Thin Films Grown Using Sol–Gel Technology

A. S. Il'in*, A. I. Maksimov, V. A. Moshnikov**^, and N. P. Yaroslavtsev***

**Voronezh State Technical University, Moskovskiĭ pr. 14, Voronezh, 394711 Russia*

***St. Petersburg State Electrotechnical University, ul. Popova 5, St. Petersburg, 197376 Russia*

^e-mail: vamoshnikov@mail.eltech.ru

Submitted July 7, 2004; accepted for publication July 19, 2004

Abstract—A method for the efficient monitoring of the existence and composition of encapsulated nanophases in nanostructured thin films grown using sol–gel technology is suggested. The method is used to study the semiconductor film structures intended for gas-sensitive adsorption sensors. The potential for, and prospects of, studying materials and diagnosing sol–gel processes using this method are considered. © *2005 Pleiades Publishing, Inc.*

Methods based on internal friction (IF) measurements have various applications in science and engineering [1]. In this paper, we report the main results (obtained with the participation of the authors over twenty years) regarding the development of methods, based on IF techniques, for determining and monitoring the parameters of semiconductor materials. The new results are as follows:

(i) The development of methods for determining the foreign volumes of the foreign inclusions in III–V, II–VI, IV–VI, and II–V semiconductors and structures based on these semiconductors. The possibility of determining the excess metal components in GaP, GaAs, and other substrates was considered in [2]. This problem is especially urgent for the development of microelectronics, due to the need to pass to fast-response integrated microcircuits and GaAs-based circuits. The methods' sensitivity to an excess component when analyzing the temperature dependence of IF is ~0.01 vol %.

(ii) The study of singularities within the homogeneity regions of variable-composition phases. To date, the IF method has significantly complemented the classical physicochemical analysis. The theory shows that any compound is homogeneous in a certain domain of the chemical composition variability. For semiconductors, these domains are often rather narrow ($\sim10^{-3}$ at. %); however, a variation in the composition of these demands can cause a variation of several orders of magnitude in charge-carrier concentration [3]. Under such circumstances, homogeneity regions can contain specific compositions that are unchanged when their aggregate state changes (congruent melting, sublimation, and evaporation). Previously, it was thought that the experimental determination of such compositions was impossible. However, special methods developed for the concentration of microinclusions allowed an electron-probe determination of the compositions $V_{s\max}$ corresponding to the condition of congruent melting methods. For example, $V_{s\max}$ = 0.500135 [Te] (in atomic fractions) in $Pb_{1-y}Te_y$ [4]. In this case, the analytical sensitivity of an X-ray spectral microanalysis carried out for microprecipitates is higher than that of an immediate analysis of the surrounding host composition by a factor of 10^3–10^4. This fact made it possible to measure, for the first time, the dependences $V_{s\max} = f(x)$ for the semiconductor alloys $(Pb_{1-x}Sn_x)_{1-y}Te_y$ [5]. The IF method appeared to be more sensitive when applied to an analysis of microprecipitates formed under specific conditions, e.g., for $(Pb_{1-x}Sn_x)_{1-y}Te_y$ [6]. The IF method's advantage is an opportunity to obtain information about an entire sample without facing conductivity limitations. Since data on congruent-melting compositions are currently unavailable for almost all the compounds that have narrow homogeneity regions, the IF method seems a promising way to fill this gap.

(iii) Studies on the production of semiconductor materials using low-temperature halogen methods are actively being carried out in many countries (USA, Israel, Bulgaria, and others) [7]. The reaction takes place in a solvent medium, and a necessary condition for producing a high-quality material is the reaction's completeness at the synthesis stage. In [8], it was suggested that the IF method be applied to the technological control of this initial operation, which predetermines the entire process.

(iv) In [9], the IF method was successfully used when analyzing the submicroprecipitates in the doped polycrystalline layers of tin dioxide used in gas-sensitive semiconductor sensors. A technique that monitored the impurity segregation in adsorbed sensors by employing a temperature shift of the IF peak was suggested in [10].

Recently, in materials science, a special emphasis has been placed on the production and study of nanostructured materials. In semiconductor nanostructured

1063-7826/05/3903-0281$26.00 © 2005 Pleiades Publishing, Inc.

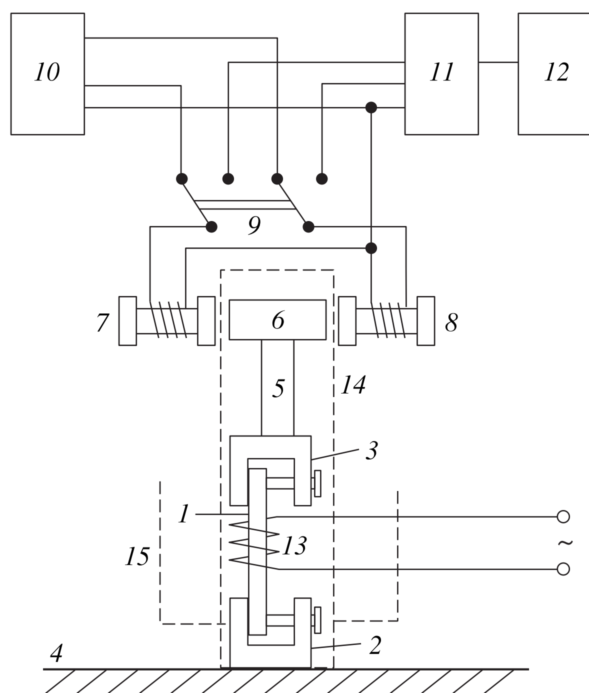

Fig. 1. The setup for internal friction measurements: (*1*) sample, (*2*, *3*) collets, (*4*) base, (*5*) pendulum, (*6*) ferromagnetic ring, (*7*, *8*) coils, (*9*) switch, (*10*) oscillator, (*11*) amplitude discriminator, (*12*) electronic counter, (*13*) heater, (*14*) vacuum-tight container, and (*15*) beaker.

materials, a variety of new effects, caused by the critical sizes of physical phenomena, begin to manifest themselves as crystallite sizes decrease. For gas-sensitive adsorption sensors, the critical size is the comparability of grain sizes with the Debye screening length. Moreover, the role of the natural microstructure, i.e., the agglomerate shape, degree of aggregation, and so on, increases in nanostructured materials.

One promising method for the production of materials is sol–gel technology [11]. This method allows nanocomposite material synthesis to be attained with relative ease [12] as well as modification of the surface of sensitive layers [13]. Put in perspective, the potential of sol–gel technology is that it enables the development of a multisensor system, i.e., a system of sensors that have an unmatched response and are formed on a single substrate using a unified technological process. The requirement that there be an unmatched response to an exposure to a single gas sample and the requirement of unified implementation are mutually contradictory. This contradiction can be removed using the nonuniform spatiotemporal distribution of the gas sensitivity of thin-film structures. This nonuniformity is due to the nonuniformity in the film parameters caused by the film growth conditions (thickness, doping, and material) or in the parameters related to the film modification.

The development of this line of technology is restrained by the absence of reliable techniques for analyzing the compositions of the nanophases that arise in formed open pores and isolated voids during the structure growth.

The aim of this study is to develop a new approach to the diagnostics of the nanophases that represent a byproduct of sol–gel processes and are located in the interior microvolumes and nanovolumes of grown samples.

The entire process of film growth using the sol–gel method can be separated into three main stages: sol synthesis, film deposition, and film annealing.

To deposit nanometer films onto a semiconductor surface, specially prepared sols are used [14, 15]. We generally used sols based on tetraethoxysilane (TEOS). Film formation from TEOS-based sols is based on the hydrolysis reaction and polycondensation of TEOS hydrolysis products,

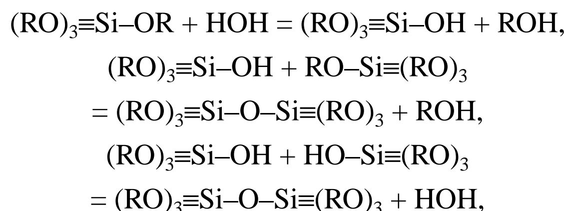

$$(RO)_3{\equiv}Si{-}OR + HOH = (RO)_3{\equiv}Si{-}OH + ROH,$$

$$(RO)_3{\equiv}Si{-}OH + RO{-}Si{\equiv}(RO)_3$$
$$= (RO)_3{\equiv}Si{-}O{-}Si{\equiv}(RO)_3 + ROH,$$

$$(RO)_3{\equiv}Si{-}OH + HO{-}Si{\equiv}(RO)_3$$
$$= (RO)_3{\equiv}Si{-}O{-}Si{\equiv}(RO)_3 + HOH,$$

where R is the hydrocarbonic radical $-C_2H_5$.

The hydrolysis and polycondensation take place simultaneously, and their degree of completion depends on many chemical and technology factors: the TEOS and water concentrations, solvent type and concentration, medium acidity (concentration of acid or other catalyst), synthesis temperature and duration, and homogenization method.

The basic objects that need to be studied are the films and modified coatings in an SnO_2–SiO_2 system, which are promising for the development of gas-sensitive adsorption sensors, including those that have an integrated design [16]. The results from an analysis of the topological features of the grown porous structures of these layers using optical, electron, and atomic-force microscopy are given in [17, 18].

However, none of the above-listed methods are efficient enough to analyze the nanophase precipitates encapsulated inside a material layer. To obtain such information, we developed techniques based on the IF method.

The method is based on a measurement of the temperature dependence of the IF using an inverted pendulum technique. A schematic diagram of the setup is shown in Fig. 1.

Sample *1* (a substrate with a formed layer), the first sample under study, is attached by one end to base *4* using collet *2*. Collet *3*, which is attached pendulum *5*, is connected to the other sample end. Ferromagnetic ring *6* is mounted on top of the pendulum. Electromagnetic coils *7* and *8* are symmetrically positioned near ring *6* and can be connected via switch *9* to low-frequency oscillator *10* or amplitude discriminator *11*, whose output is connected to electronic counter *12*. In

the former case, coils *7* and *8* are used as an activator for the mechanical vibrations of pendulum *5*, which are caused by the interaction of the magnetic field of the coils with the ferromagnetic ring. In the latter case, they are used as a sensor of ring *6* displacements. Heater *13* is arranged around sample *1*. The basic elements of the circuit are placed into vacuum-tight container *14*, which is made of fused-quartz glass. Air is evacuated from quartz container *14* in order to decrease the damping of the oscillations of pendulum *5*.

The internal friction is determined as the inverse Q factor of the oscillatory system $Q^{-1} = (1/\pi N)\ln(A_1/A_N)$, where N is the number of oscillations according to the counter, and A_1 and A_N are the amplitudes of the first and Nth oscillations.

To carry out the planned experiments, the setup was modernized so that it could measure the temperature dependences of the internal friction not only during the heating but also during the cooling of the sample. To this end, beaker *15*, which was welded to the quartz container, was filled with liquid nitrogen. In this case, cooling is due to the difference between the heat radiation fluxes from the liquid nitrogen to the sample and from the sample to the container with the liquid nitrogen.

In this study, semiconductor films consisting of nanocomposition systems based on tin dioxide were grown by a chemical method from sol solutions using sol–gel technology. The sols were ethanol solutions of TEOS, with additives of bivalent tin chloride ($SnCl_2 \cdot H_2O$) acting as a source of tin dioxide. The SiO_2 source was TEOS. In some experiments, several drops of concentrated hydrochloric acid were added to make the dispersion more complete. The film structures were grown by pouring the solution onto various substrates (silicon, glass, and glass ceramics) followed by centrifuging. The transition to gel or xerogel (dry gel) was attained by a natural evaporation of the solvent followed by an additional isothermal treatment at 600°C. Annealing of the film structures at temperatures above 500°C yields a material containing only the oxide semiconductor phases of silicon and tin. The technology of sol–gel systems and the films based on them was considered in more detail in [17].

The samples in which the solvent removal and crystallization were completed (according to the data of the differential thermal analysis and X-ray phase analysis), were analyzed using the IF method. At the same time, judging from the dynamics of the physicochemical processes in sol–gel systems, the gel network may contain nanophase inclusions consisting of water and organic solvent during its formation. However, we do not know of any techniques allowing an analysis of these structural defects, which can have a significant effect on the electrical and mechanical properties of the grown coatings. Thus, the suggested technique based on the IF method is promising for the development of operating conditions for the growth and analysis of the properties of the objects under study.

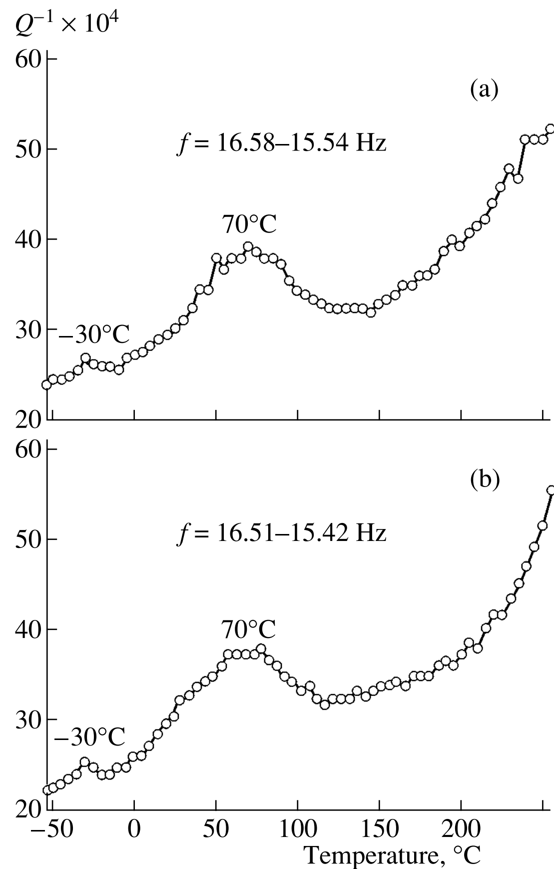

Fig. 2. Temperature dependences of the internal friction in SnO_2–SiO_2 nanocomposite films grown on glass substrates for the first (a) and second (b) sequential measurements.

The rectangular-shaped samples with a characteristic area of 12 × 4 mm^2 were cut and then placed into the vacuum chamber (Fig. 1). The samples in the setup were cooled to a temperatures of about –100°C followed by step-by-step heating and IF measurement. The results for the SiO_2–SnO_2 composite samples are shown in Figs. 2 and 3. These two figures show the temperature dependences of the IF for the samples formed on glass and glass-ceramic substrates, respectively, for two sequential measurements.

Figures 2 and 3 exhibit a low-temperature IF peak, which is also observed in the general case. The phase transition temperature of the inclusions in the film material is significantly lower than that of water; hence, the nanophase is a hydroalcoholic solution. The experimental data show that the peak's position is unchanged in sequential measurements of the dependences of the IF. This means that the measurement technique allows analysis of the encapsulated nanophases. A comparison of the dependences for the film structures grown on the various substrates used shows that mechanical energy

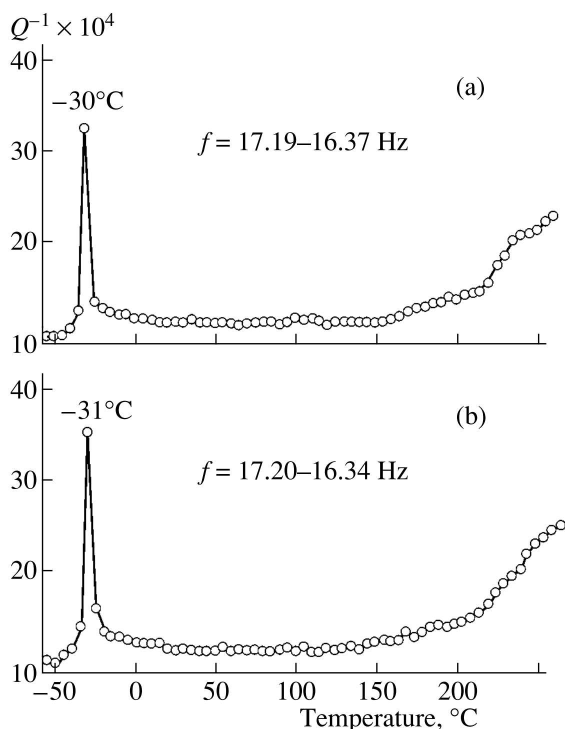

Fig. 3. The same as in Fig. 2; however, in this case, glass-ceramic substrates were used.

losses are observed in a temperature range of 40–100°C (broadened IF peak) in the samples grown on glass substrates but not in the ones grown on glass-ceramic substrates. We attribute this effect to a relaxation of the substrate–sample bonds. The absence of such losses during the glass-ceramics–film interaction can be indicative of both localized bonds (the absence of bond migration under exposure to temperature) and a short chain of atoms bonding the substrate to the film.

Thus, we have developed a method that allows efficient monitoring of the existence and composition of the encapsulated nanophases in nanostructured thin films grown using sol–gel technology. This method can serve as the basis for a new approach to the diagnostics of sol–gel processes that controls the trapping of matrix hydroalcoholic solutions, and the formation of clathrate (inclusion) compounds and phase transitions in nanoprecipitates.

This study was supported by the Russian Foundation for Basic Research, project no. 04-03-32509-a.

REFERENCES

1. V. S. Postnikov, *Internal Friction in Metals* (Metallurgiya, Moscow, 1974) [in Russian].
2. N. P. Yaroslavtsev, Doctoral Dissertation (Voronezh Polytechnical Inst., Voronezh, 1992).
3. F. A. Kröger, *The Chemistry of Imperfect Crystals* (Wiley, New York, 1964; Mir, Moscow, 1969).
4. T. T. Dedegkaev, N. E. Mokrousov, V. A. Moshnikov, and D. A. Yas'kov, Zh. Fiz. Khim. **57**, 1556 (1983).
5. T. T. Dedegkaev, N. E. Mokrousov, V. A. Moshnikov, and D. A. Yaskov, Cryst. Res. Technol. **8** (11), 119 (1983).
6. N. P. Izmaĭlov, Yu. L. Il'in, V. A. Moshnikov, *et al.*, Zh. Fiz. Khim. **62**, 1370 (1988).
7. W. Kwestroo, in *Preparative Methods in the Solid State Chemistry*, Ed. by P. Hagenmuller (Academic, New York, 1972; Mir, Moscow, 1976).
8. R. Assenov, N. P. Izmailov, V. A. Moshnikov, and N. P. Yaroslavtsev, Cryst. Res. Technol. **22**, 1189 (1987).
9. Yu. N. Andreev, M. V. Bestaev, D. Ts. Dimitrov, *et al.*, Fiz. Tekh. Poluprovodn. (St. Petersburg) **31**, 841 (1997) [Semiconductors **31**, 714 (1997)].
10. Yu. N. Andreev, B. M. Darinskiĭ, V. A. Moshnikov, *et al.*, Fiz. Tekh. Poluprovodn. (St. Petersburg) **34**, 644 (2000) [Semiconductors **34**, 618 (2000)].
11. C. J. Brinker and G. W. Scherer, *Sol–Gel Science. The Physics and Chemistry of Sol–Gel Processing* (Academic, San Diego, 1990).
12. A. Martucci, N. Bassiri, M. Guglielmi, *et al.*, J. Sol–Gel Sci. Technol. **26**, 1 (2003).
13. Yu. Z. Bubnov, V. A. Zhabrev, O. A. Shilova, *et al.*, in *Proceedings of VIII International Scientific and Technical Conference on High Technologies in Russian Industry* (OAO TsNITI TEKhNOMASh, Moscow, 2002), p. 298.
14. A. I. Borisenko, V. V. Novikov, N. E. Prikhid'ko, I. M. Mitnikova, and L. F. Chepik, *Thin Inorganic Films in Microelectronics* (Nauka, Leningrad, 1972) [in Russian].
15. O. A. Shilova, L. F. Chepik, and Yu. Z. Bubnov, Zh. Prikl. Khim. (St. Petersburg) **68**, 1608 (1995).
16. Yu. Z. Bubnov, V. A. Zhabrev, S. V. Koshcheev, *et al.*, in *Abstracts of IV International Scientific and Technical Conference on Electronics and Information Science* (MIÉT, Moscow, 2002), Chap. 2, p. 16.
17. L. F. Chepik, E. P. Troshina, T. S. Mashchenko, *et al.*, Zh. Prikl. Khim. (St. Petersburg) **74**, 1569 (2001).
18. D. Dimitrov, O. F. Loutskaya, and V. A. Moshnikov, Electron Technol. **33** (1/2), 61 (2000).

Translated by A. Kazantsev

Semiconductors, Vol. 39, No. 3, 2005, pp. 285–288. Translated from Fizika i Tekhnika Poluprovodnikov, Vol. 39, No. 3, 2005, pp. 305–308.
Original Russian Text Copyright © 2005 by Kozlov, Sobolev, Knjazev.

ELECTRONIC AND OPTICAL PROPERTIES OF SEMICONDUCTORS

Reflection Spectra of Two Polymorphic Modifications of Cadmium Arsenide

A. I. Kozlov*^, V. V. Sobolev^^, and A. F. Knjazev***^^^**

**International Laboratory for Superconductivity and Solid-State Electronics, Academy of Sciences of Moldova, Chisinau, MD2028 Moldova*

^e-mail: kozlov@lises.asm.md

***Udmurt State University, Izhevsk, 426034 Russia*

^^e-mail: sobolev@uni.udm.ru

****Kursk State University, Kursk, 305000 Russia*

^^^e-mail: sasha@kentavr.com.ru

Submitted October 14, 2003; accepted for publication May 19, 2004

Abstract—The optical properties of cadmium arsenide are studied. Reliable new data on the reflection spectra are obtained owing to the use of perfect crystals and high-precision spectral equipment. The reflection spectra of the polymorphic modifications α''-Cd_3As_2 (space group D_{4h}^{15}) and α'-Cd_3As_2 (space group D_{4h}^{11}) are recorded at room and liquid-nitrogen temperatures in polarized light ($\mathbf{E} \perp \mathbf{c}$, $\mathbf{E} \parallel \mathbf{c}$) at incident-light photon energies of 1–5 eV. For the α' modification, anisotropy is observed in the reflection spectra for the first time. The obtained results are compared with the known experimental and theoretical data. *© 2005 Pleiades Publishing, Inc.*

Compounds of II_3–V_2 are formed, in conformity with formal valence rules, as tetrahedral phases. The specific physical properties of these compounds are related to the presence of structural vacancies for metal atoms and the displacement of the atoms toward neighboring vacancies. Cd_3As_2 is a very interesting compound that has a very narrow band gap E_g and high mobility [1, 2].

Cadmium arsenide has five polymorphic modifications with a large number of atoms in their unit cells [3]. The lattice constants are listed in [4–6]. A simple mechanism for the structural transformations relating to this polymorphism is presented in [7]. It is noteworthy that, quite often, no precise indications of the crystal structure are given in publications devoted to Cd_3As_2 optical properties. This may be one of the reasons for the discrepancies found in the data presented by different authors.

Group-theory calculations of the band structure of Cd_3As_2 crystals (α modification) were made in [8]. In [9], the Cd_3As_2 band structure was calculated using the pseudopotential method, using the lattice of a hypothetical crystal with a fluorite structure instead of a real lattice. In [10], the calculations were performed for the real symmetry. The potentials for Cd and As were taken from the data for CdTe and GaAs. The matrix elements were constructed in the same way as in [8]. In [11], the band structure in the vicinity of the point Γ was calculated by the **k**–**p** method. It was assumed that E_g = –0.095 eV. The results of magnetooptical studies of a Cd–As–Zn system [12] were also interpreted under the assumption that cadmium arsenide has an inverted band structure, similar to that of HgTe. An empirical model of the Cd_3As_2 band structure with E_g = –0.19 eV was offered in [13]; however, the arguments in favor of this model were considered to be unconvincing in [3].

To date, the IR reflection spectra have only been measured for solid solutions of the Cd–As–Zn system [14]. In [15], the reflection spectra of polycrystalline Cd_3As_2 were recorded at room temperature, and two or three broad peaks were observed. In [16], the reflection spectra of single-crystal Cd_3As_2 were studied at 77 and 293 K, and five to seven spectral structures were observed in the range 1–5 eV. In [17], the reflection spectra of Cd_3As_2 crystals possessing a higher perfection were recorded in polarized light at 293 K, and the optical functions n, k, ε_1, and ε_2 were calculated. A characteristic feature of the results of [15–17] is a strong decrease in the reflectivity R in the energy range $h\nu > 3$ eV. Thermoreflection spectra were studied at 293 K in [18, 19]. Several of the peaks out of those obtained agree well with the reflection data, but the three longest-wavelength structures are not observed in the reflection. In [20], reflection spectra in the extreme UV range were studied, and the optical functions in the range 0–20 eV at room temperature were calculated. The reflection spectra and some optical functions of $Cd_{2.1}Zn_{0.9}As_2$ are presented in [21].

We have previously studied the reflection spectra of Cd_3As_2 in the range 1–5 eV in polarized light ($\mathbf{E} \perp \mathbf{c}$, $\mathbf{E} \parallel \mathbf{c}$) in a setup using a DFS-12 monochromator [22]. An electrical-compensation method was used in the

1063-7826/05/3903-0285$26.00 © 2005 Pleiades Publishing, Inc.

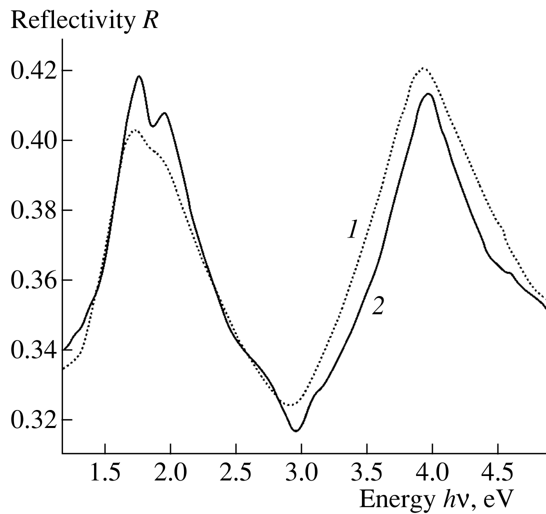

Fig. 1. Reflectivity spectra of α''-Cd_3As_2 at (*1*) 293 and (*2*) 80 K.

setup. This method consists in the electrical and optical separation of the signals corresponding to two light beams, i.e., incident light and that reflected from the sample; their processing; and finally, a comparison to obtain the absolute value of the mirror reflectivity. A light filter was placed before the entrance slit of the monochromator, and a Glan–Thomson prism was used to polarize the light. The light beam was divided by a beam-splitter into two beams of equal intensity and then directed into two channels. The sample under study, contained in a cryostat, was placed in the measuring channel. The intensity of the light incident on the sample was measured in the reference channel. A quartz plate was used to compensate for the absorption by the optical medium (cryostat window). The angle of incidence of the light beam was 6° from the normal. To prevent the penetration of light fractions of oil into the cryostat, three liquid-nitrogen traps were used. In addition, the cryostat was cut off from the vacuum system before charging the liquid nitrogen in order to prevent the formation of an oil film. The sample was fixed on the face of a copper vessel with a special alloy (T_m = 30–40°C). The surface temperature of the sample under study was 80 K. All the samples were obtained from a vapor phase in the form of long plates with the **c**-axis lying in the sample plane [23].

Two high-intensity reflection bands and several weak features are observed in the spectrum of the α'' cadmium arsenide (Fig. 1). The first band is doublet-split, with the splitting particularly clearly pronounced at low temperatures. This doublet is similar to the structure E_1, $E_1 + \Delta_1$ in InAs, which is attributed to transitions at the *L* point or in the Λ direction. The doubling is related to a spin–orbit splitting of the upper valence band constituted by *p* levels of As atoms, with the value of $\Delta_{s\text{-}o}$ in the Λ direction being equal to two thirds of $\Delta_{s\text{-}o}$ at the point Γ. The peak positions for the components of the doublet are listed in the table for the case shown in Fig. 1. In the other samples, the peak positions can be shifted by 0.01 eV to higher or lower energy. In several of the samples, different relative intensities of the doublet components are observed (approximately equal). The second high-intensity band, similar to the E_2 structure in III–V crystals, lies near 4 eV. The reflectivity at the peaks of both bands reaches 40–43%. Between the high-intensity bands, two weak shoulders are observed at 80 K (Fig. 1). In the other samples they are more clearly pronounced, and their positions can be shifted by 0.1–0.2 eV. In several of the samples, very weak structures (inflections) are observed at energies of about 1.6 and 4.3 eV, and a broad band is observed at 1.3–1.4 eV. A temperature rise from 80 to 293 K only slightly modifies the spectra: weak structures are not seen and the doublet splitting is less pronounced. The average temperature coefficient of the peak shift is

The energy positions (in electronvolts) of the spectral peaks of reflectivity and thermoreflectance for Cd_3As_2 crystals taken from the data of various authors

Our data (reflectivity)				Other publications (reflectivity)					Thermoreflectance		Theoretical calculations [8]
α'' crystals		α' crystals, 80 K		[16]		[17]		[20]	[18]	[19]	
293 K	80 K	**E** ∥ **c**	**E** ⊥ **c**	293 K	77 K	Single	Poly	293 K	293 K	293 K	
–	1.4	–	–	–	–	1.43	1.41	–	1.43	1.41	1.2
–	1.6	–	1.60	–	–	–	–	–	–	–	–
1.76	1.79	1.75	1.76	1.7	1.74	1.71	1.71	1.70	1.74	–	1.8
1.91	1.98	1.90	1.90	1.88	1.90	1.91	1.89	–	1.95	–	–
–	2.5	–	–	2.86	2.86	–	–	–	–	2.30	2.8
–	3.1	3.08	3.20	3.33	3.26	–	–	–	3.24	–	–
3.93	3.98	4.01	3.93	3.7	3.7	3.80	3.63	3.60	–	3.70	3.8
–	4.3	–	–	–	–	4.50	–	–	–	4.60	4.7
–	–	–	–	5.15	–	5.15	–	–	–	5.16	5.2

$-(1.5–3.0) \times 10^{-4}$ eV/K. It is necessary to note that no anisotropy is observed in the reflection spectra of α''-Cd_3As_2, even at 80 K.

The principal features in the α'-Cd_3As_2 reflection spectra (Fig. 2) are the same as those for the α'' polymorphic modification. However, the doublet structure of E_1 is less clearly pronounced, which may be due to the poorer structural perfection of samples under study. The splitting of the doublet peaks is the same as for the α'' modification, but the red shift is observed in both polarizations (see table). The anisotropy in the reflection spectra is clearly pronounced. The doublet components have different intensities (the short-wavelength component is more clearly pronounced in the $\mathbf{E} \perp \mathbf{c}$ polarization), and the position of the E_2 peak depends on the polarization. No structure was found in the range 2.5–2.7 eV, but polarized peaks of a noticeably high intensity are observed at 3.08 eV ($\mathbf{E} \parallel \mathbf{c}$) and 3.20 eV ($\mathbf{E} \perp \mathbf{c}$). A well-defined additional peak is observed at 1.60 eV (only at ($\mathbf{E} \perp \mathbf{c}$).

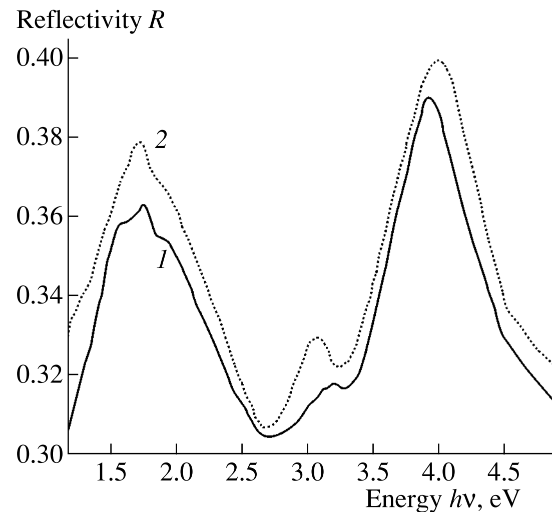

Fig. 2. Reflectivity spectra of α'-Cd_3As_2 at 80 K. Polarization of light: (*1*) $\mathbf{E} \perp \mathbf{c}$; (*2*) $\mathbf{E} \parallel \mathbf{c}$.

When comparing the obtained results with earlier data, it is necessary to note, first of all, a strong decrease in the reflectivity in the short-wavelength range, which was reported earlier. In this case, the peak E_2 may be red-shifted by 0.1 eV. In the energy range $h\nu > 3$ eV, a false peak may appear due to the superposition of a steep decrease of reflectivity onto the actually observed increase. It is quite possible that the peak at 3.33 eV [16] is related to the presence of a thin film on the surface, which is formed when there is a deviation from the optimal technology. We have shown that the lapping of such samples results in a 10–20% increase of R in the near-UV range. A film can also appear during the etching of the sample surface (in several studies, lapped samples with subsequent etching were used). It seems unlikely that the observed reduction of R can be accounted for only by the surface roughness [24], though it may make some contribution. It is significant that, as the temperature is lowered from 293 to 77 K [16], the peak at 3.33 eV is red-shifted while the peak at 3.7 eV remains at the same place, presumably, because of the formation of an additional oil film entering from the vacuum system. Thus, the difference in the spectral distributions of the Cd_3As_2 reflectivity observed by different authors can be attributed to the degree of perfection of sample surface. The same factor may be responsible for a large scatter at the position of the shortest-wavelength band E_2 (see table). In general, the worse the quality of the sample surface, the stronger the red shift of this structure. This pattern is well illustrated by the data from [17], where the E_2 peak lies at 3.80 eV for single crystals, and at 3.63 eV for polycrystals. As can be seen from the table, the positions of the E_1 and $E_1 + \Delta_1$ peaks reported by five of the represented authors satisfactorily coincide (after taking into account the natural scatter between the samples and the possible investigation of different modifications of Cd_3As_2). At the same time, the peaks lying between E_1 and E_2 strongly differ in their position, intensity, and anisotropy. It is not inconceivable that, in this case, certain "floating" specific features, which are related to the degree of long-range ordering in the positions of the vacancies in cationic sublattices, are being observed [25].

According to our data, the spin splitting is 0.15–0.19 eV, which is in good agreement with the theoretical calculations [26]. Based on our high-precision reflectivity spectra and using the Kramers–Kronig relations, a complete set of Cd_3As_2 optical functions can be obtained [27, 28], including the imaginary part of the dielectric constant ε_2. A comparison of this constant's value with the theoretical data can be used to verify calculations of the Cd_3As_2 band structure in a real structure.

REFERENCES

1. E. K. Arushanov, Prog. Cryst. Growth Charact. **3**, 211 (1981).
2. V. B. Lazarev, V. Ya. Shevchenko, Ya. Kh. Grinberg, and V. V. Sobolev, *The II–V Semiconductor Compounds* (Moscow, 1976) [in Russian].
3. V. V. Sobolev, *Energy Structure of Narrow-Gap Semiconductors* (Shtiintsa, Chisinau, 1983) [in Russian].
4. M. Stakelberg and P. Paulus, Z. Phys. Chem. (Leipzig) **28**, 5427 (1935).
5. G. A. Steigman and J. Gooder, Acta Crystallogr. B **24**, 1062 (1968).
6. A. Pietraszko and M. Lucaszevicz, Phys. Status Solidi A **18**, 723 (1973).
7. A. D. Izotov, V. P. Sanygin, and V. F. Ponomarev, Kristallografiya **23**, 764 (1978) [Sov. Phys. Crystallogr. **23**, 429 (1978)].
8. N. V. Kudryavtseva, Izv. Vyssh. Uchebn. Zaved., Fiz., No. 11, 93 (1971).
9. P. J. Ling-Chung, Phys. Rev. **188**, 1272 (1969).
10. B. Dowgiallo-Plenkievicz and P. Plenkievicz, Phys. Status Solidi B **94** (1), K57 (1979).

11. J. Bodnar, in *Proceedings of 3rd International Conference on Physics of Narrow-Gap Semiconductors* (Warsaw, 1978), p. 311.
12. I. Wagner, E. D. Palik, and E. M. Swiggard, J. Phys. Chem. Solids Suppl., No. 1, 471 (1971).
13. M. J. Aubin, L. G. Caron, and J. P. Jay-Gerin, Phys. Rev. B **15**, 3872 (1977).
14. A. I. Belogorokhov, I. S. Zakharov, A. V. Kochura, and A. F. Knjazev, Appl. Phys. Lett. **77** (14), 2121 (2000).
15. V. V. Sobolev and N. N. Syrbu, Izv. Akad. Nauk SSSR, Neorg. Mater. **2**, 1011 (1966).
16. V. V. Sobolev, N. N. Syrbu, T. A. Zyubina, and Ya. A. Ugaĭ, Fiz. Tekh. Poluprovodn. (Leningrad) **5**, 327 (1971) [Sov. Phys. Semicond. **5**, 279 (1971)].
17. K. Karnicka-Moscicka, A. Kisiel, and L. Zdanowicz, Solid State Commun. **44** (3), 373 (1982).
18. M. J. Aubin and J. P. Cloutier, Can. J. Phys. **53** (17), K42 (1975).
19. V. P. Bhola, Phys. Status Solidi A **34** (2), K179 (1976).
20. M. Zivitz and J. R. Stevenson, Phys. Rev. B **10**, 2457 (1974).
21. A. I. Kozlov, S. G. Kozlova, and A. F. Knjazev, Moldavian J. Phys. Sci. **2**, 2 (2003).
22. V. V. Sobolev and V. V. Nemoshkalenko, *The Methods of Computational Physics in the Theory of Solid State. Electronic Structure of Semiconductors* (Naukova Dumka, Kiev, 1988) [in Russian].
23. É. K. Arushanov, A. F. Knyazev, and L. S. Koval', in *Abstracts of Conference on Ternary Semiconductors and Their Application* (Chisinau, 1983), p. 165.
24. K. Karnicka-Moscicka and A. Kisiel, Surf. Sci. **121**, L545 (1982).
25. G. P. Chuĭko and N. M. Chuĭko, Fiz. Tekh. Poluprovodn. (Leningrad) **17**, 1145 (1983) [Sov. Phys. Semicond. **17**, 721 (1983)].
26. B. Dowgiallo-Plenkievicz and P. Plenkievicz, Phys. Status Solidi B **87**, 309 (1978).
27. A. I. Kozlov, in *Proceedings of International Conference on Material Science and Condensed Matter Physics* (Chisinau, 2001), p. 42.
28. A. I. Kozlov, V. E. Grachev, and V. V. Sobolev, in *Abstracts of 5th General Conference of Balkan Physical Union* (Vrnjaeka Banja, 2003).

Translated by D. Mashovets

Semiconductors, Vol. 39, No. 3, 2005, pp. 289–292. Translated from Fizika i Tekhnika Poluprovodnikov, Vol. 39, No. 3, 2005, pp. 309–312.
Original Russian Text Copyright © 2005 by Nemov, Nasredinov, P. Seregin, N. Seregin, Khuzhakulov.

ELECTRONIC AND OPTICAL PROPERTIES OF SEMICONDUCTORS

Statistics of Electrons in PbS with *U* Centers

S. A. Nemov*, F. S. Nasredinov*, P. P. Seregin*, N. P. Seregin*, and E. S. Khuzhakulov**

**St. Petersburg State Polytechnic University, St. Petersburg, 195251 Russia*

***Tashkent Oblast State Pedagogical Institute, Angren, 702500 Uzbekistan*

Submitted May 14, 2004; accepted for publication May 24, 2004

Abstract—The dependence of the concentration of two-electron tin centers in the intermediate charge state Sn^{3+} in PbS on the correlation energy is obtained using the Gibbs distribution. It is shown that this state cannot be observed by Mössbauer spectroscopy on an ^{119}Sn isotope (due to insufficient sensitivity), but it can manifest itself in the temperature dependence of the hole density in $Pb_{1-x-y}Sn_xNa_yS$ solid solutions. © *2005 Pleiades Publishing, Inc.*

1. INTRODUCTION

The tin in lead sulfide PbS is an isoelectronic substitution impurity; nevertheless, according to the available data on transport phenomena [1] and Mössbauer spectroscopy on an ^{119}Sn isotope, it behaves similarly to a donor at low concentrations [2]. Indeed, only bivalent tin (Sn^{2+}) was observed in the Mössbauer spectra of *n*-type $Pb_{1-x}Sn_xS$ samples containing superstoichiometric Pb and only tetravalent tin (Sn^{4+}) was observed for *p*-type $Pb_{1-x-y}Sn_xA_yS$ samples (here, A is a single-electron acceptor, e.g., Na or Tl, $y \geq 2x$). The Mössbauer spectra were interpreted under the assumption that Sn atoms replace bivalent Pb in a PbS cubic lattice to form donor states in the band gap. The line of the bivalent Sn^{2+} state corresponds to the states $[Sn]^0$, which are neutral in respect to a cationic sublattice, and the line of the tetravalent Sn^{4+} state corresponds to the doubly ionized $[Sn]^{2+}$ states of the tin donor center in PbS. If the relative concentrations of Sn and the acceptor impurity in PbS are varied, any controlled ratio between the intensities of the Sn^{2+} and Sn^{4+} lines can be obtained [1]. The absence of a Sn^{3+} line (singly ionized Sn donor center) in the Mössbauer spectra recorded at the temperature $T = 80$ K on partially compensated $Pb_{1-x-y}Sn_xA_yS$ samples indicates that Sn forms in PbS double-electron donor centers that have a negative correlation energy; i.e., the energy of the single ionization of these centers is higher than half the energy of their double ionization. Finally, the *p*-type conduction and the absence of degeneration in the partially compensated $Pb_{1-x-y}Sn_xA_yS$ samples indicates that the chemical potential level lies in the lower half of the band gap of the semiconductor (and, therefore, Sn donor states in PbS also lie in the lower half of the band gap).

Thus, two bands of localized Sn states are formed in the band gap of the semiconductor, and the energy spacing between them equals the correlation energy

$$U = E_1 - E_2, \qquad (1)$$

where E_1 is the energy of a level in which an electron is captured and the Sn^{3+} center changes to a Sn^{2+} center, and E_2 is the energy of a level in which an electron is captured and the Sn^{4+} center changes to a Sn^{3+} center. It was suggested that the density of states were a function of the energy in the band gap of $Pb_{1-x-y}Sn_xA_yS$ in [2]. The goal of this study is to determine the temperature dependences of the chemical potential and carrier density.

2. TEMPERATURE DEPENDENCES OF THE CHEMICAL POTENTIAL AND CARRIER DENSITY

According to the Gibbs distribution, the concentration of impurity centers with different numbers of electrons is determined by the relation

$$\frac{N_s}{N_{s-1}} = \frac{g_s}{g_{s-1}}\exp\frac{F-E_s}{kT}. \qquad (2)$$

Here, N_s and N_{s-1} are the concentrations of centers that have s and $s-1$ electrons, g_s and g_{s-1} are the spin degeneracy factors for the corresponding levels, F is the chemical potential level, E_s is the energy of the level that captures the sth electron, and k is the Boltzmann constant.

Thus, for the $Pb_{1-x-y}Sn_xA_yS$ solid solutions we obtain

$$\frac{N_{Sn^{2+}}}{N_{Sn^{3+}}} = \frac{g_{Sn^{2+}}}{g_{Sn^{3+}}}\exp\frac{F-E_1}{kT} \qquad (3)$$

and

$$\frac{N_{Sn^{3+}}}{N_{Sn^{4+}}} = \frac{g_{Sn^{3+}}}{g_{Sn^{4+}}}\exp\frac{F-E_2}{kT}, \qquad (4)$$

where $N_{Sn^{2+}}$, $N_{Sn^{3+}}$, and $N_{Sn^{4+}}$ are the concentrations of the Sn^{2+}, Sn^{3+}, and Sn^{4+} centers, respectively; and $g_{Sn^{2+}}$,

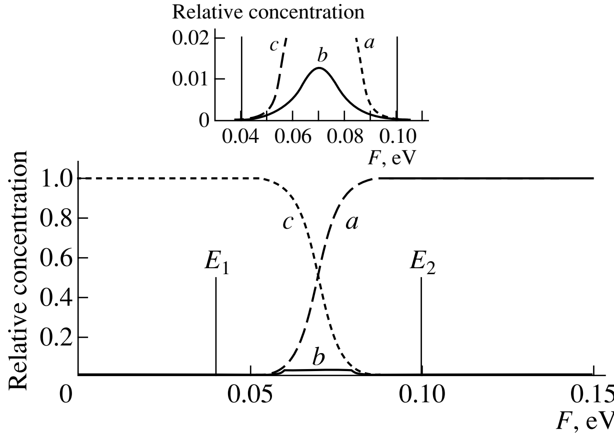

Fig. 1. The relative concentrations of (*a*) Sn^{2+}, (*b*) Sn^{3+}, and (*c*) Sn^{4+} vs. the chemical potential in $Pb_{1-x-y}Sn_xA_yS$ solid solutions, for $U < 0$. Inset: the range of low concentrations for Sn^{3+}.

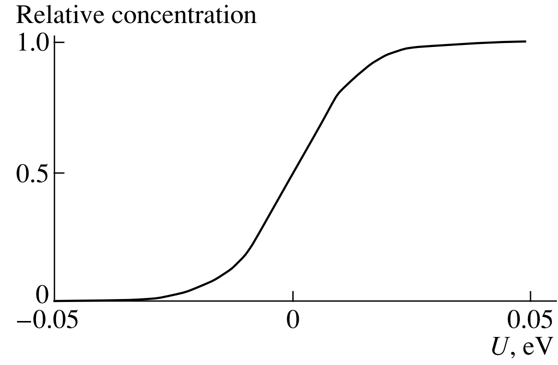

Fig. 2. The maximum relative concentration of Sn^{3+} in $Pb_{1-x-y}Sn_xA_yS$ solid solutions at 80 K vs. the correlation energy.

$g_{Sn^{3+}}$, and $g_{Sn^{4+}}$, the degeneracy factors for these centers. Assuming that 5*s* electrons are responsible for the donor properties of Sn, we obtain $g_{Sn^{2+}} = 1$, $g_{Sn^{3+}} = 2$, and $g_{Sn^{4+}} = 1$.

Since

$$N_{Sn^{2+}} + N_{Sn^{3+}} + N_{Sn^{4+}} = N_{Sn}, \quad (5)$$

where N_{Sn} is the total concentration of Sn, we obtain

$$N_{Sn^{2+}} = N_{Sn}\left[1 + \frac{g_{Sn^{3+}}}{g_{Sn^{2+}}}\exp\frac{E_1 - F}{kT} + \frac{g_{Sn^{4+}}}{g_{Sn^{2+}}}\exp\frac{E_1 + E_2 - 2F}{kT}\right]^{-1},$$

$$N_{Sn^{3+}} = N_{Sn}\left[1 + \frac{g_{Sn^{2+}}}{g_{Sn^{3+}}}\exp\frac{F - E_1}{kT} + \frac{g_{Sn^{4+}}}{g_{Sn^{3+}}}\exp\frac{E_2 - F}{kT}\right]^{-1},$$

$$N_{Sn^{4+}} = N_{Sn}\left[1 + \frac{g_{Sn^{3+}}}{g_{Sn^{4+}}}\exp\frac{F - E_1}{kT} + \frac{g_{Sn^{2+}}}{g_{Sn^{4+}}}\exp\frac{2F - E_1 - E_2}{kT}\right]^{-1}. \quad (6)$$

Figure 1 shows the dependences of $N_{Sn^{2+}}$, $N_{Sn^{3+}}$, and $N_{Sn^{4+}}$ on F for $U < 0$. In the calculation, the values $|U| = 0.06$ eV, $E_1 = 0.04$ eV, and $E_2 = 0.10$ eV [3] were used and the energy was calculated from the top of the valence band. The maximum concentration of Sn^{3+} (accurate to $kT\ln(g_{Sn^{3+}}/g_{Sn^{4+}})$) is reached at $F = (E_1 + E_2)/2$ and is given by

$$[N_{Sn^{3+}}]_{max} = N_{Sn}\left[1 + 2\frac{\sqrt{g_{Sn^{2+}}g_{Sn^{4+}}}}{g_{Sn^{3+}}}\exp\left(-\frac{U}{kT}\right)\right]^{-1}. \quad (7)$$

Figure 2 shows the dependence of $[N_{Sn^{3+}}]_{max}$ on the correlation energy for the temperature 80 K. It can be seen that, if the condition $|U| > 0.06$ eV is satisfied (the experimental data from [3]), $[N_{Sn^{3+}}]_{max} \ll N_{Sn}$ when there is negative correlation energy. This is the reason why it is difficult to observe Sn^{3+} centers in the Mössbauer spectra of ^{119}Sn.

The density of the positive charge on Sn centers (in units of elementary charge) is

$$\rho = 2N_{Sn^{4+}} + N_{Sn^{3+}} = N_{Sn}\frac{2 + (g_{Sn^{3+}}/g_{Sn^{4+}})\exp[(F - E_2)/kT]}{1 + \frac{g_{Sn^{3+}}}{g_{Sn^{4+}}}\exp\frac{F - E_2}{kT} + \frac{g_{Sn^{2+}}}{g_{Sn^{4+}}}\exp\frac{2F - E_1 - E_2}{kT}}; \quad (8)$$

hence, it follows that, for the case of $U < 0$, the charge on the Sn^{3+} centers must be taken into account only for $F \geq E_2$. At $F = E_2$

$$\rho = N_{Sn}\frac{4}{3 + \exp(-U/kT)},$$

and at $F = (E_1 + E_2)/2$ we obtain $\rho = N_{Sn}$.

In the general case, the electroneutrality equation for $Pb_{1-x-y}Sn_xA_yS$ solid solutions has the form

$$2N_{Sn^{4+}} + N_{Sn^{3+}} + p = N_A, \quad (9)$$

where p is the density of holes, and N_A is the density of the single-electron acceptors. In the range of extrinsic

conduction, we have $p \ll N_{Sn}$ and $p \ll N_A$; therefore, the electroneutrality equation can be written in an expanded form as

$$N_{Sn}\frac{2+(g_{Sn^{3+}}/g_{Sn^{4+}})\exp[(F-E_2)/kT]}{1+\frac{g_{Sn^{3+}}}{g_{Sn^{4+}}}\exp\frac{F-E_2}{kT}+\frac{g_{Sn^{2+}}}{g_{Sn^{4+}}}\exp\frac{2F-E_1-E_2}{kT}} = N_A. \quad (10)$$

If the designations

$$x = F-\frac{E_1+E_2}{2} \text{ and}$$

$$z^2 = \exp\frac{2F-E_1-E_2}{kT} = \exp\frac{2x}{kT}$$

are introduced, Eq. (10) is reduced to an equation that is quadratic in z:

$$\frac{g_{Sn^{2+}}}{g_{Sn^{4+}}}z^2+\frac{g_{Sn^{3+}}}{g_{Sn^{4+}}}\exp\frac{U}{kT}\left(1-\frac{N_{Sn}}{N_A}\right)z+\left(1-\frac{2N_{Sn}}{N_A}\right) = 0. \quad (11)$$

The solution to this equation is then used to determine the temperature dependence of the chemical potential F. We restrict the analysis to a consideration of the case $U < 0$ for two ranges in the $F(T)$ dependence that differ fundamentally in their relative values of $N_{Sn^{3+}}$ and $N_{Sn^{4+}}$.

Range I: $N_{Sn^{3+}} \gg N_{Sn^{4+}}$, or $p \approx N_{Sn^{3+}} = N_A$.

This is the case at $F - E_2 \gg kT$ (i.e., $\exp(F - E_2)/kT \gg 1$) when the compensation of Sn by the acceptor impurity is low (i.e., $N_{Sn} \gg N_A$), so that the condition $F - (E_1 + E_2)/2 \gg kT$ (i.e., $\exp[(2F - E_1 - E_2)/kT] \gg \exp[(F - E_2)/kT] \gg 1$) is further satisfied.

Then, Eq. (11) is reduced to

$$z = \frac{N_{Sn}g_{Sn^{3+}}}{N_A g_{Sn^{2+}}}\exp\frac{U}{kT}, \quad (12)$$

and the temperature dependence of the chemical potential is given by

$$F = E_1 + kT\ln\left[\frac{N_{Sn}}{N_A}\frac{g_{Sn^{3+}}}{g_{Sn^{2+}}}\right]. \quad (13)$$

If $\rho \ll N_{Sn}$ and $F > (E_1 + E_2)/2$, we obtain $[dF/dT]_{\rho = \text{const}} > 0$. Therefore, if $F > E_2$, the chemical-potential level rises as temperature increases at ρ = const.

When condition (13) is satisfied, the temperature dependence of the hole density is given by

$$p = N_V\exp\left[\frac{E_V-F}{kT}\right] = N_V\frac{N_A}{N_{Sn}}\frac{g_{Sn^{2+}}}{g_{Sn^{3+}}}\exp\left[\frac{E_V-E_1}{kT}\right], \quad (14)$$

where N_V is the effective density of the states near the top of the valence band (when calculating this value, the Kane correction for the nonparabolicity of a PbS valence band must be taken into account), and E_V is the energy of the valence band top.

Range II: $N_{Sn^{3+}} \ll N_{Sn^{4+}}$, or $\rho = 2N_{Sn^{4+}} = N_A$.

This is the case at $F < E_2$ when the compensation of Sn by the acceptor impurity is strong, with either the condition $2N_{Sn} - N_A \ll N_A$ (but $2N_{Sn} - N_A > 0$, i.e., $0 < 2N_{Sn} - N_A \ll N_A$) or the condition $\exp(U/kT) \ll 1$ (i.e., $|U| \gg kT$) being satisfied, i.e, at low temperatures.

In this case, Eq. (11) is reduced to

$$N_{Sn}\frac{2}{(g_{Sn^{2+}}/g_{Sn^{4+}})\exp[(2F-E_1-E_2)/kT]+1} = N_A; \quad (15)$$

therefore, the temperature dependence of the chemical potential is given by

$$F = \frac{E_1+E_2}{2}+kT\ln\left(\frac{g_{Sn^{4+}}}{g_{Sn^{2+}}}\frac{2N_{Sn}-N_A}{N_A}\right), \quad (16)$$

and, since $2N_{Sn} - N_A \ll N_A$,

$$\ln\left(\frac{g_{Sn^{4+}}}{g_{Sn^{2+}}}\frac{2N_{Sn}-N_A}{N_A}\right) < 0,$$

which corresponds to $[dF/dT]_{\rho = \text{const}} < 0$, when $F < (E_1 + E_2)/2$.

When condition (16) is satisfied, the temperature dependence of the hole density is given by

$$p = N_V\exp\frac{E_V-F}{kT} = N_V\sqrt{\frac{g_{Sn^{4+}}}{g_{Sn^{2+}}}\frac{2N_{Sn}-N_A}{N_A}}\exp\frac{E_V-(E_1+E_2)/2}{kT}. \quad (17)$$

3. EXPERIMENTAL RESULTS

By comparing Eqs. (14) and (17), we can conclude that the activation energy determined from the temperature dependence of the hole density in $Pb_{1-x-y}Sn_xA_yS$ samples must depend on the relative concentrations of Sn and the acceptor impurity. As an example, Fig. 3 shows the temperature dependences of the hole density in $Pb_{0.94}Sn_{0.05}Na_{0.01}S$ and $Pb_{0.985}Sn_{0.005}Na_{0.01}S$ solid solutions. For $Pb_{0.94}Sn_{0.05}Na_{0.01}S$, the obtained values of the activation energy are $E_{01} = (0.080 \pm 0.002)$ eV for extrinsic conduction ($T < 450$ K) and $E_{02} = (0.217 \pm 0.002)$ eV for intrinsic conduction ($T > 450$ K). For $Pb_{0.985}Sn_{0.005}Na_{0.01}S$, the activation energy for extrinsic conduction ($T < 500$ K) is $E_{01} = (0.099 \pm 0.002)$ eV, and for intrinsic conduction ($T > 500$ K) $E_{02} = (0.211 \pm 0.002)$ eV.

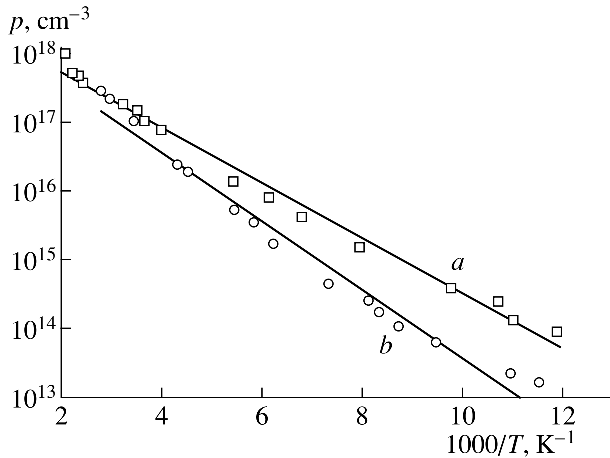

Fig. 3. Temperature dependences of the hole density in the (*a*) $Pb_{0.94}Sn_{0.05}Na_{0.01}S$ and (*b*) $Pb_{0.985}Sn_{0.005}Na_{0.01}S$ samples.

Thus, the difference between the activation energy for the extrinsic conduction in the $Pb_{0.94}Sn_{0.05}Na_{0.01}S$ and $Pb_{0.985}Sn_{0.005}Na_{0.01}S$ samples is ~0.02 eV, which corresponds to $U = 0.04$ eV. This result agrees with the data obtained in determining U from the frequency of the electron exchange between the neutral and ionized Sn centers in $Pb_{1-x-y}Sn_xA_yS$ solid solutions, measured by means of Mössbauer spectroscopy [3].

4. CONCLUSION

The dependence of the concentration of the two-electron tin centers in PbS in the intermediate charge state Sn^{3+} on the correlation energy is obtained. It is shown that this state cannot be observed by Mössbauer spectroscopy on an ^{119}Sn isotope, due to its insufficient sensitivity. However, the Sn^{3+} state is presumably manifested in the temperature dependence of the hole density in the $Pb_{1-x-y}Sn_xA_yS$ solid solutions.

ACKNOWLEDGMENTS

The study was supported by the Russian Foundation for Basic Research (project no. 02-02-17306).

REFERENCES

1. L. V. Prokof'eva, M. N. Vinogradova, and S. V. Zarubo, Fiz. Tekh. Poluprovodn. (Leningrad) **14**, 2201 (1980) [Sov. Phys. Semicond. **14**, 1304 (1980)].
2. F. S. Nasredinov, S. A. Nemov, V. F. Masterov, and P. P. Seregin, Fiz. Tverd. Tela (St. Petersburg) **41**, 1897 (1999) [Phys. Solid State **41**, 1741 (1999)].
3. V. F. Masterov, F. S. Nasredinov, S. A. Nemov, and P. P. Seregin, Fiz. Tekh. Poluprovodn. (St. Petersburg) **31**, 291 (1997) [Semiconductors **31**, 181 (1997)].

Translated by D. Mashovets

Semiconductors, Vol. 39, No. 3, 2005, pp. 293–295. Translated from Fizika i Tekhnika Poluprovodnikov, Vol. 39, No. 3, 2005, pp. 313–315.
Original Russian Text Copyright © 2005 by M. Ardyshev, V. Ardyshev, Kryuchkov.

ELECTRONIC AND OPTICAL PROPERTIES OF SEMICONDUCTORS

The Accumulation of Radiation Defects in Gallium Arsenide That Has Been Subjected to Pulsed and Continuous Ion Implantation

M. V. Ardyshev*^, V. M. Ardyshev*, and Yu. Yu. Kryuchkov**

**Kuznetsov Siberian Physicotechnical Institute, Tomsk State University, Tomsk, 634050 Russia*

^e-mail: ard.rff@elefot.tsu.ru

***Tomsk Polytechnical University, Tomsk, 634050 Russia*

Submitted June 8, 2004; accepted for publication July 5, 2004

Abstract—Measurements of electrical conductivity and Rutherford backscattering are used to study the accumulation of defects in GaAs that has been subjected to pulsed ($\tau_p = 1.3 \times 10^{-2}$ s and an off-duty factor of 100) and continuous irradiation with ^{32}S, ^{12}C, and ^{4}He ions at room temperature at the ion energies $E = 100$–150 keV, doses $\Phi = 1 \times 10^{9}$–6×10^{16} cm^{-2}, and current densities $j = 1 \times 10^{-9}$–3×10^{-6} A cm^{-2}. It is shown that the defect-accumulation rate during the pulsed implantation is much lower than it is during the continuous implantation.
© 2005 Pleiades Publishing, Inc.

1. INTRODUCTION

A continuous mode of irradiation has been used in the majority of the studies concerned with radiation damage in semiconductors and other materials subjected to irradiation with heavy and light ions. At the same time, it was noted, even in early studies [1–3], that the behavior of the defects produced by pulsed irradiation [3] differs greatly from the behaviour produced by continuous irradiation. In particular, it was experimentally ascertained that the buildup of a dose in small portions makes it possible (with all other factors being the same) to appreciably improve the electrical properties of ion-implanted n-GaAs layers [1]. In addition, the pulsed irradiation can affect the kinetics of the radiation-defect production, growth, and interaction, and can also lead to the annealing of these defects during the interval between the pulses [3]. In this context, the purpose of this study was to gain insight into the buildup of radiation damage in GaAs that has been subjected to continuous and pulsed ion implantation.

2. EXPERIMENTAL

We studied GaAs structures of an n–n_i type. We used chloride technology to grow an epitaxial film (n-type layer) on a semi-insulating substrate with a (100) orientation. The electron concentration in the n-type layer was approximately 3×10^{17} cm^{-3}, the layer thickness was 0.13–0.14 μm, and the electrical conductivity was 160–200 Ω^{-1} cm^{-1}. The wafers were first treated in an $H_2SO_4 : H_2O_2 : H_2O = 1 : 1 : 100$ etchant. Experimental parallelepiped-shaped samples were then cut from these wafers, and Au + Ge + Ni contacts were formed on the end faces of the parallelepipeds with the n-type layer. Finally, the samples were mounted on a massive brass sample holder, and the continuous or pulsed implantation of the ^{32}S, ^{12}C, and ^{4}He ions was performed at room temperature in vacuum with a residual pressure of 10^{-5} Pa. The duration of the pulses was 1.3×10^{-2} s, and the off-duty factor was equal to 100. The ions were implanted at a right angle into the surface of the samples. The implantation dose was varied from 1×10^{9}–6×10^{16} cm^{-2}, and the ion-current density was varied from 1×10^{-9}–3×10^{-6} A cm^{-2}. The energy of the implanted ions was chosen so that the radiation defects were produced over the entire thickness of the epitaxial layer: 100–150 keV for the film with the thickness of 0.13–0.14 μm. In the course of the implantation, we measured the resistance of the samples at an electric-field strength of no higher than 10 V cm^{-1}. This resistance was then recalculated to provide the electrical conductivity, taking into account the sample configuration. The sample's temperature was measured either by a temperature sensor with a thermoelectric transducer formed on the implanted surface of the control sample using photolithography or by a Chromel–Alumel thermocouple. At the highest absorbed-power density, 0.6 W cm^{-2}, the samples' temperature was no higher than 310 K.

The implantation-induced damage after the irradiation with ^{32}S ions at a dose of 1×10^{15} cm^{-2} was studied using a Rutherford backscattering of aligned-beam 1.8-MeV helium ions. The energy spectra were measured using a silicon surface-barrier detector mounted at an angle of 165° with respect to the angle of incidence of the helium beam. The energy resolution of the spectrometric channel was 25 keV, which corresponded to the depth resolution of 40 nm.

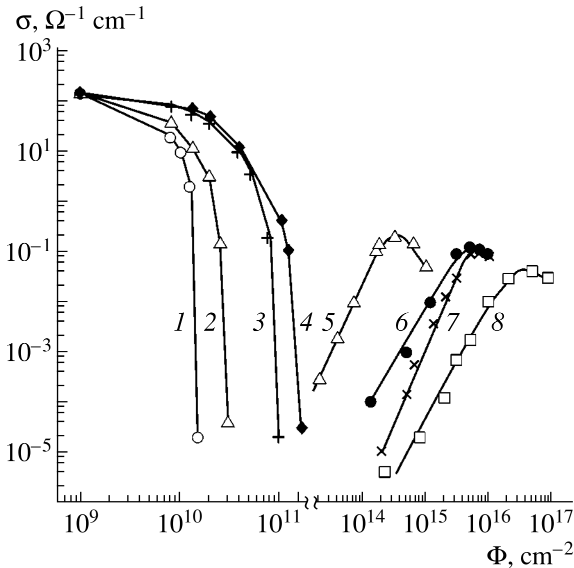

Fig. 1. Dependences of the electrical conductivity of the epitaxial *n*-GaAs layers on the implantation dose. The pulsed mode: irradiation with (*1*) ^{32}S, 150 keV, and 1×10^{-9} A cm^{-2}; (*2*) ^{12}C, 125 keV, and 1×10^{-9} A cm^{-2}; (*3*) ^{4}He, 100 keV, and 1×10^{-9} A cm^{-2}; (*4*) ^{4}He, 100 keV, and 5×10^{-9} A cm^{-2}; and (*6*) ^{32}S, 150 keV, and 3×10^{-6} A cm^{-2}. The continuous mode: irradiation with (*5*) ^{32}S, 150 keV, and 3×10^{-6} A cm^{-2}; (*7*) ^{12}C, 125 keV, and 8×10^{-8} A cm^{-2}; and (*8*) ^{4}He, 100 keV, and 8×10^{-8} A cm^{-2}.

3. RESULTS

In Fig. 1, we show the dependences of the electrical conductivity σ of the epitaxial films on the implantation dose Φ. It can be seen that, in the case of pulsed implantation (curves *1–4*), the values of σ decrease as Φ increases in the region of low doses ($\Phi < 2 \times 10^{11}$ cm^{-2}). It is worth noting that the lower the ion mass, the higher the dose required for reducing the electrical conductivity of the film to a level of ~10^{-5} Ω^{-1} cm^{-1}. This dose is equal to 1.5×10^{10} cm^{-2} for ^{32}S (curve *1*), 3×10^{10} cm^{-2} for ^{12}C (curve *2*), and 9×10^{10} and 1.5×10^{11} cm^{-2} for ^{4}He (curves *3*, *4*) at the ion-current densities of 1×10^{-9} and 5×10^{-9} A cm^{-2}, respectively. Assuming that the Fermi level is located in the vicinity of the midgap in GaAs with the conductivity $\sigma \approx 10^{-5}$ Ω^{-1} cm^{-1}, we can attribute the decrease in the free-carrier concentration to the compensation of shallow-level donors by radiation defects formed along the ion tracks. Assuming, also, that these local track-related defect-rich regions span the entire volume of the *n*-type layer at $\sigma \approx 10^{-5}$ Ω^{-1} cm^{-1}, we can use the so-called effective-medium model [4] to show that the average inner radius of these regions is equal to 8.1 nm for ^{32}S, 1.86 nm for ^{12}C, and 0.96 and 0.58 nm for ^{4}He (at 1×10^{-9} and 5×10^{-9} A cm^{-2}, respectively). The above-listed data are consistent with an increase in the size of the damaged regions as the mass of the implanted ions increases (see [5]). However, the reason why an increase in the current density of a specified ion leads to a decrease in the radius of the defect-production region (^{4}He, curves *3*, *4*) is not quite clear at present.

After the irradiation with a dose that resulted in the decrease in σ to the level of 10^{-5} Ω^{-1} cm^{-1} and after the shutoff of the ion gun, we observed a relaxation (an increase) of the electrical conductivity. The relaxation curve was exponential and included two portions: the first portion exhibited a fast relaxation (with a characteristic relaxation time of several seconds) and the second portion exhibited a slow relaxation (with a characteristic time of several hundreds of seconds).

In the case of the continuous implantation in the region of high doses ($\Phi > 2 \times 10^{13}$ cm^{-2} (see Fig. 1, curves *5*, *7*, *8*)), the electrical conductivity of GaAs increases with the dose and attains a maximum of 0.04–0.20 Ω^{-1} cm^{-1} at doses of 3×10^{14} cm^{-2} for ^{32}S (curve *5*), 6×10^{15} cm^{-2} for ^{12}C (curve *7*), and 5×10^{16} cm^{-2} for ^{4}He (curve *8*). A similar dependence was observed by Cato *et al.* [6], where an increase in σ was related [6] to the hopping mechanism of the electrical conductivity via localized states of defects in the vicinity of the Fermi level. It is noteworthy that the largest value of σ [6] corresponded to the highest defect concentration attained for the crystalline materials just before their amorphization. Indeed, in the region of low doses, the radiation-defect concentration increases as the implantation dose increases. The smallest value of σ(Φ) corresponds to the complete compensation of the shallow-level donors by the radiation defects. As the dose is increased further and the defect concentration becomes higher than the concentration of localized electrons, the latter can redistribute between the unoccupied and occupied defects (the electrical conductivity via defects).

In Fig. 1 (curves *5*, *6*), we show the dependences σ(Φ) for the continuous and pulsed modes of the implantation of ^{32}S at the ion-current density 3×10^{-6} A cm^{-2}. It can be seen that, in the case of the pulsed irradiation (curve *6*), the maximum of σ(Φ) corresponds to a dose of 4×10^{15} cm^{-2}, which exceeds the dose that corresponds to the maximum in the dependence σ(Φ) for the continuous irradiation (curve *5*) by more than an order of magnitude. Assuming that the increase in the electrical conductivity is caused by an increase in the concentration of the radiation defects, we may generally conclude that, when continuous irradiation at a certain dose Φ* is applied, the concentration of radiation defects, $N_{def}(\Phi^*)$, exceeds that of the case of pulsed implantation, $N_{def}(\sum_i \Phi_i^* = \Phi^*)$, in which the same dose is attained by small portions; i.e., $N_{def}(\Phi^*) > N_{def}(\sum_i \Phi_i^* = \Phi^*)$. In other words, the concentration of the generated radiation defects ceases to be additive in the case of the pulsed irradiation of gallium arsenide. At present, it is difficult to interpret this effect correctly; however, we believe that a certain fraction of the radiation defects

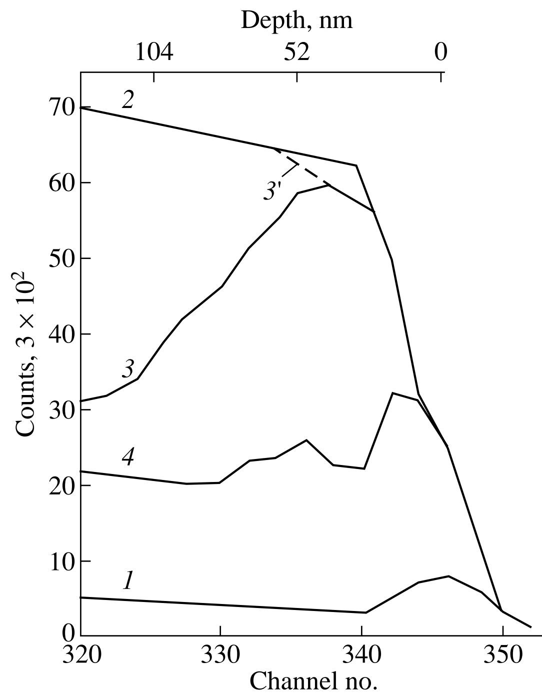

Fig. 2. Energy spectra of backscattered helium particles with E_0 = 1.8 MeV for GaAs [100]: curves (*1*, *2*) represent the aligned (axial) and random spectra measured before irradiation, respectively; curves (*3*) and (*4*) represent the aligned spectra after irradiation with ^{12}S ions ($\Phi = 1 \times 10^{15}$ cm^{-2}) in the (*3*) continuous and (*4*) pulsed modes of irradiation.

can be annealed out during the interval between the radiation pulses.

The Rutherford backscattering spectra for the GaAs samples implanted with the ^{32}S ions at a dose of 1×10^{15} cm^{-2} (Fig. 2) clearly indicate that a lower concentration of radiation defects is formed when the pulsed irradiation is applied and that the amorphization occurs at higher doses than it does for the continuous irradiation. It can be seen that a peak related to the damaged structure near the surface is observed in the spectra for the sample implanted in the continuous mode with the current density $j = 3 \times 10^{-6}$ A cm^{-2}. This peak is caused by helium ions scattered by the displaced Ga and As atoms (curve *3*). It is noteworthy that, in this case, the yield of the backscattering nearly coincides with that corresponding to an unoriented crystal (the random spectrum, curve *2*). This observation indicates that the surface region is heavily damaged before the onset of the amorphization. When the pulsed implantation is chosen, the damage peak is lower than that in the case of the backscattering from the nonaligned crystal (curve *4*). It is worth noting that, a "pitting" effect (in the portion *3*') is not observed in the backscattering spectrum for the continuous irradiation. Using the previous data [7], we may assume that the structure of the irradiated layer does not attain the amorphous state (although this layer is highly damaged) resulting from the pulsed ion irradiation with a dose of 1×10^{15} cm^{-2} at a current density of 3 μA cm^{-2}. In general, this conclusion is consistent with the results of measuring the electrical conductivity $\sigma(\Phi)$ (Fig. 1) in the cases of the continuous and pulsed implantation (curves *5*, *6*). The value of σ at $\Phi = 1 \times 10^{15}$ cm^{-2} (curve *5*) is found at the leveling-off portion of the electrical conductivity for the pulsed irradiation (curve *6*), whereas we have $\sigma \approx 0.01\ \Omega^{-1}$ cm^{-1} at the ascending portion of the dependence $\sigma(\Phi)$, which indicates that the amorphization state is not attained.

4. CONCLUSIONS

(i) It is found that, when the pulsed irradiation of epitaxial *n*-GaAs layers with ^{4}He, ^{12}C, and ^{32}S ions occurs, the dependence of the electrical conductivity σ of the layers on the radiation dose Φ in the region of low doses ($\Phi < 2 \times 10^{11}$ cm^{-2}) at the same ion-current density j shifts to lower doses as the ion mass increases and shifts to higher doses as j increases (^{4}He ions, 100 keV).

(ii) In the region of high doses ($\Phi > 2 \times 10^{13}$ cm^{-2}) of continuous irradiation, the radiation-defect concentration $N_{\text{def}}(\Phi)$ is higher than when the same dose is attained by portions in the case of pulsed implantation, $N_{\text{def}}(\sum_i \Phi_i = \Phi)$; i.e., $N_{\text{def}}(\Phi) > N_{\text{def}}(\sum_i \Phi_i = \Phi)$.

(iii) The rate of buildup for radiation defects in GaAs in the case of pulsed irradiation with ions is lower than it is for continuous irradiation.

ACKNOWLEDGMENTS

This study was supported by the Russian Foundation for Basic Research, project no. 02-02-16280.

REFERENCES

1. V. M. Ardyshev, A. P. Mamontov, and V. V. Peshev, USSR Inventor's Certificate, No. 1148516 (1 December 1984).
2. Yu. A. Biryutin and S. V. Gaponov, Fiz. Tekh. Poluprovodn. (Leningrad) **18**, 1729 (1984) [Sov. Phys. Semicond. **18**, 1083 (1984)].
3. E. P. Simonen, J. Nucl. Mater., Nos. 1–3, 122 (1984).
4. B. R. Gossik, J. Appl. Phys. **30**, 1214 (1959).
5. I. A. Abroyan, A. N. Andronov, and A. I. Titov, *Physical Foundations of Electron- and Ion-Beam Technology* (Vysshaya Shkola, Moscow, 1984) [in Russian].
6. Y. Cato, T. Shimada, and K. F. Komatsubare, J. Appl. Phys. **45**, 1044 (1974).
7. M. A. Kumakhov and I. S. Tashlykov, Poverkhnost, No. 2, 5 (1983).

Translated by A. Spitsyn

Semiconductors, Vol. 39, No. 3, 2005, pp. 296–299. Translated from Fizika i Tekhnika Poluprovodnikov, Vol. 39, No. 3, 2005, pp. 316–319.
Original Russian Text Copyright © 2005 by Bacherikov, Kitsyuk, Optasyuk, Stadnik.

The Effect of Pressing on the Luminescent Properties of ZnS:Ga Powders

Yu. Yu. Bacherikov^, N. V. Kitsyuk, S. V. Optasyuk, and A. A. Stadnik

Institute of Semiconductor Physics, National Academy of Sciences of Ukraine, Kiev, 03028 Ukraine

^e-mail: Yuyu@isp.kiev.ua

Submitted June 23, 2004; accepted for publication August 9, 2004

Abstract—Zinc sulfide powders that have been doped thermally with gallium are studied. The mechanisms of Ga diffusion in the ZnS powders are considered in relation to the packing density of the powders' particles. To this end, some of the ZnS powders under study have been pressed into pellets. It is established that the doping of ZnS powders with Ga proceeds more efficiently if the powders have been compressed. The electroluminescence of ZnS doped with Ga is observed. © *2005 Pleiades Publishing, Inc.*

1. INTRODUCTION

The high emissivity and wide band gap of zinc sulfide (ZnS) make this material promising for the fabrication of optical devices that emit in a wide range of wavelengths [1]. The introduction of various impurities into ZnS makes it possible to obtain luminophors with specified properties [2]. However, in spite of numerous studies, the issues concerning effective methods of introducing these impurities into the ZnS matrix remain open [3]. The development of new technological methods of doping ZnS can, to a great extent, be conducive to a realization of the promising properties of this material. The introduction of impurities that act as coactivators (for example, gallium [4]) into ZnS is of special interest. This circumstance is all the more important since, at present, it is still not clear what the origin of the emitting centers significantly affected by Ga is or which structure involves Ga.

The purpose of this study was to gain insight into the diffusion mechanisms that are active during the doping of ZnS powders with Ga and to study the effect of Ga on the luminescent properties of ZnS in relation to the method used to introduce Ga into ZnS. The final objective of this study was a minimization of the concentration of extraneous impurities in powderlike ZnS after the thermal introduction of Ga.

2. EXPERIMENTAL

We studied powderlike ZnS (ETO.035.295 TY) in which the sizes of the particles were on the order of 15 μm (80% of the composition), and the sizes of the largest particles of the powder did not exceed 20 μm. The ZnS powder was pressed into pellets and annealed in the presence of metallic Ga for 1 h at a temperature of 800°C with a limited access to air. This limited access to air was attained using a gas seal made of activated carbon. After the annealing, the pellets were crushed. The obtained powder was then separated into two portions: the first portion contained the powder in which the sizes of the particles were no larger than 40 μm, and the second portion contained the powder in which the sizes of the particles exceeded 40 μm.

The photoluminescence (PL) and electroluminescence (EL) spectra were measured using a KSVU-23 system. The PL was excited by radiation from an LGI-23 nitrogen laser (λ = 337.1 nm). We used an alternating-voltage generator that operated at U = 250 V and f = 5 kHz. All the measurements were performed at room temperature.

The samples used for studying the EL were, in fact, electroluminescent indicators. They were fabricated using the conventional technology for powder luminophors: the structure included a transparent In_2O_3:Sn electrode deposited onto glass, a second electrode formed of metallic Al, and a light-emitting layer that was formed between the electrodes and consisted of a mixture of a powderlike ZnS:Ga luminophor and an insulating binder (an epoxy varnish). The thickness of the light-emitting layer was ~50 μm.

3. RESULTS

Studies of the fractional composition of the powder with respect to the sizes of the particles showed that the annealing of ZnS powder pressed into pellets at 800°C led to an increase in the sizes d of separate particles to values that exceeded 40 μm, irrespective of the presence of the Ga doping impurity. The volume fraction of the powder with $d \geq 40$ μm amounted to ~40% after annealing.

Since the PL studies showed that pressing did not affect the luminescent properties of the as-prepared (unannealed) ZnS powder, Fig. 1 shows the PL spectrum of only the pressed ZnS powder (curve *1*). As can be seen from Fig. 1, the PL spectrum of this powder is

represented by a complex broad band with an emission peak at 500 nm and a half-width of 84 nm. The separation of the ZnS powder pressed and annealed at 800°C into two fractions (in which the size of the particles was larger and smaller than 40 μm) also showed that there were no differences (exceeding the measurement error) between the PL spectra of these two fractions. The annealing of the ZnS powder at 800°C (Fig. 1, curve *2*) led to a decrease in the band half-width to 67 nm and to a shift of the PL peak to a longer wavelength (λ_{max} = 515 nm) than the PL spectrum of the initial (unannealed) ZnS powder.

Interpretation of the luminescence band with its peak in the vicinity of 515 nm is ambiguous. For example, in [2, 5], this band was related to the O and Cu impurities in ZnS, while it was related to the emission of self-activated ZnS and also to the formation of anionic vacancies in [6, 7]. It is worth noting that the annealing-induced change in the spectral shape of the PL band occurs owing to a redistribution of the PL lines that form the band under consideration (Fig. 1). Bacherikov *et al.* [4] related this change in the spectral characteristics of ZnS powders to an increase in the concentration of sulfur vacancies (V_S) at the surface and also to the surface being relieved of radicals; as a result, the intensity of the band with λ_{max} = 520 μm increases and the nonradiative losses at the surface are reduced.

The presence of metallic Ga in the course of annealing does not lead to any changes in the PL spectrum for the powder in which the sizes *d* the particles are smaller than 40 μm (Fig. 1, curve *3*). The PL spectra of the annealed samples are nearly identical. It has previously been shown [4] that, if there are no extraneous atoms that can affect the diffusion rate and the rate of replacement of Zn by Ga in ZnS, the introduction of Ga atoms into the ZnS bulk is almost absent.

The behavior of the ZnS-powder fraction in which the sizes of the particles are larger than 40 μm is radically different. For the powder particles agglomerated into clusters in which the sizes exceed 40 μm, the presence of metallic Ga in the course of annealing leads to significant changes in the PL spectrum (Fig. 2, curve *3*). This spectrum consists of a complex band in the blue-green spectral region whose peak is located at λ_{max} = 505 nm. In addition, the shape of the short-wavelength wing of the PL spectrum indicates that there is at least one other single band in the region of ~470 nm. It was previously shown in [1, 8–10] that the band with λ_{max} = 470 nm could be attributed to the presence of Ga in ZnS.

In addition, efficient electroluminescence is a characteristic of ZnS powder, annealed in the presence of metallic Ga, in which the sizes of the particles are ≥40 μm. The EL spectrum of this powder (Fig. 2, curve *3*) consists of a band with a peak at λ_{max} = 500 nm and a half-width of 75 nm.

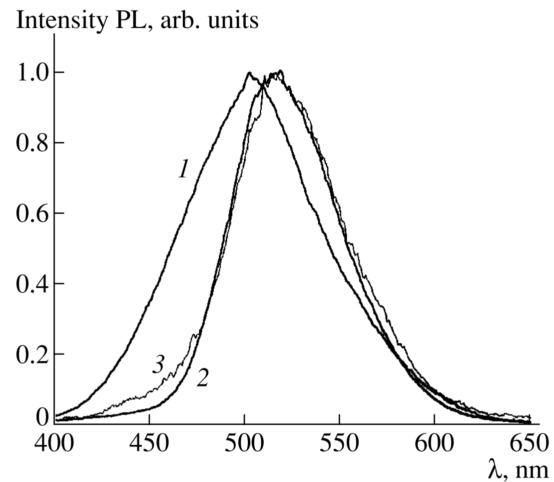

Fig. 1. Photoluminescence spectra of (*1*) the initial (unannealed) ZnS powder, (*2*) the annealed ZnS powder, and (*3*) the ZnS powder annealed in the presence of Ga (the powder in which the sizes of the particles were no larger than 40 μm). The curves are normalized to the maximum.

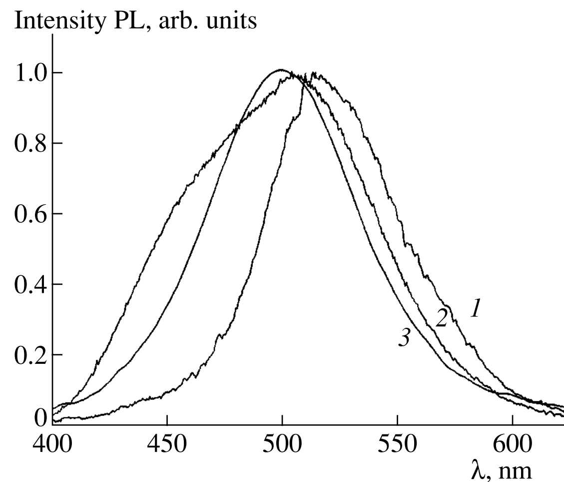

Fig. 2. Luminescence spectra of the ZnS powder annealed in the presence of Ga for the powders in which the sizes of the particles were (*1*) no larger and (*2*, *3*) larger than 40 μm. Curves *1* and *2* represent the photoluminescence spectrum and curve *3* represents the electroluminescence spectrum. The curves are normalized to the maximum.

4. DISCUSSION

Analysis of the obtained results showed that the fractions of the ZnS powder doped thermally with Ga in which $d \geq 40$ μm and $d < 40$ μm exhibited considerably different luminescent properties. For example, the PL spectrum of the ZnS powder with $d \geq 40$ μm included a band peaked at λ_{max} = 470 μm, caused by the presence of Ga in ZnS; the peak of this spectrum shifted by 10 nm to shorter wavelengths with respect to the PL spectrum of the powder with $d < 40$ μm. In addition, electroluminescence emission was not observed for the

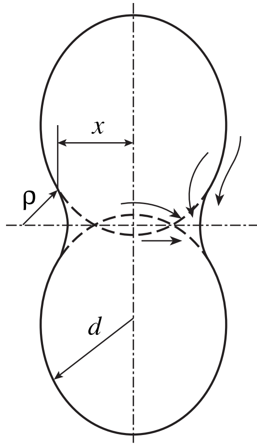

Fig. 3. A model of two agglomerating spheres (the possible diffusion directions are indicated).

ZnS powder that was doped thermally with Ga and had $d < 40$ μm, whereas the fraction of this powder that had $d \geq 40$ μm exhibited electroluminescence with an intensity sufficient for reliable detection (Fig. 2, curve *3*). We were unable to find any data in previous publications on the EL of zinc sulfide where Ga acted as a coactivator. In this case, Ga probably acts as a coactivator for the uncontrolled impurities (Cu, Mn, Al) or intrinsic ZnS defects that are responsible for self-activated emission.

Thus, the above reasoning makes it possible to conclude that the agglomeration of separate particles of the ZnS powder in the course of the annealing of this powder at 800°C in the presence of Ga gives rise to conditions under which Ga atoms penetrate into the ZnS bulk, where some of these atoms then occupy the Zn sites (Ga_{Zn}).

As was mentioned above, the pressing of the ZnS powder into pellets and their subsequent annealing at a temperature of 800°C leads to the agglomeration of ~40% of the ZnS volume into particles with $d \geq 40$ μm. The fact that some of the powder's particles agglomerate into larger clusters at a temperature that is several times lower than the melting point is well known and has been described in a number of publications [11, 12]. In the case under consideration, agglomeration occurs at a temperature that is lower than the ZnS melting point ($T_m = 1850$°C) [13] by a factor of 2.3.

The main driving force for the process of agglomeration (agglomeration in the solid phase is also referred to as densification) consists in a decrease in the free energy of the system, mainly of the system's surface energy. The surface tension (capillary forces) gives rise to stresses in a solid. These stresses depend on the surface curvature according to the Laplace equation; i.e.,

$$\sigma = \gamma(-1/\rho + 1/x), \quad (1)$$

where σ is the stress in the contact neck, γ is the surface tension, ρ is the curvature radius in the vicinity of the neck, and x is the neck radius. Equation (1) can be used to describe the process of agglomeration in a two-sphere model (Fig. 3). The material shifts to the neck region via the volume, grain-boundary, and surface diffusion that corresponds to either the Herring–Nabarro or Coble creep. This mechanism becomes the most important in the agglomeration of the powder's particles in the absence of an external pressure [12]. The initial stage of agglomeration, which is due to the volume diffusion, can be described by the equation

$$x^2/a^2 = (40\gamma\Omega D_v/RT)t, \quad (x^5/d) = Kt, \quad (2)$$

where d is the radius of the sphere, D_v is the volume-diffusion coefficient, Ω is the atomic volume, T is temperature, and t is time. Equation (2) makes it possible to draw an important conclusion: the agglomeration rate increases as temperature increases and the particle size decreases. In the first approximation, we may assume that, in the case of zinc sulfide, the particles with a diameter smaller than 20 μm are actively agglomerated in the solid phase at $T \geq 850$°C if the effect of pressing is disregarded.

In addition, the annealing gives rise to a thermal deformation of the surface of the powder's particles, which leads to surface destruction and is accompanied by the generation of an excess concentration of vacancies and interstitial atoms and to appearance of their clusters; as a result, a thin surface layer becomes preferentially thermally disordered [14].

All the aforementioned phenomena stimulate the agglomeration of separate particles, although these phenomena do not lead to the agglomeration of the entire mass of the material into a combined "porous" conglomerate. In our opinion, this behavior is caused by the fact that the crystallographic axes of the contacting faces of the crystallites in the powder are misoriented with respect to each other. Therefore, a good match between the lattices of the crystallites is not attained. Consequently, the agglomeration of crystallites over the entire volume of the powder subjected to annealing proceeds differently, and most of the powder's crystallites are not agglomerated. It is worth noting that this circumstance leads to a defect-rich agglomeration boundary.

Thus, taking into account both the data [4] that are indicative of the physical adsorption of Ga at the surface of powder's particles, but without any subsequent active penetration of Ga into the particle's volume during ZnS annealing in the presence of Ga, and the processes accompanying the agglomeration of the particles, we can suggest the main factors that allow the Ga atoms to penetrate easily into the ZnS bulk when the powder is pressed into pellets.

The first factor is related to the fact that Ga atoms, after being trapped at the surface, are found within newly formed (larger) 40-μm particles in the course of the agglomeration of the powder's particles. This behavior is caused by the surface diffusion of the main material into the neck region; as a result, Ga is found to

be under the corresponding layer (see Fig. 3). The second factor is related to the fact that the diffusion coefficient of the impurity increases as the size of the crystallites increases, as was shown in [15]. The third factor is related to the fact that the diffusion over the grain boundaries occurs at a higher rate than that in the crystals' bulk since the proper crystal structure is disrupted in the regions that include structural defects in the vicinity of the grain boundaries (dislocations and stacking faults).

Thus, the results reported in this paper indicate that annealing at temperatures corresponding to the agglomeration of ZnS particles in the solid phase, after ZnS has been pressed into pellets in the presence of Ga, is conducive to the active penetration of Ga into the ZnS bulk. We would like to emphasize that, in the case under consideration, we used a minimal number of materials in the course of introducing Ga into the ZnS matrix; as a result, we minimized the amount of extraneous impurities (such as S, Ga, and Zn; uncontrolled impurities; and impurities coming from the residual atmosphere) that accompanied the technological process of doping. In other thermal methods for doping ZnS with Ga, either Ga salts or Ga in combination with materials that increase the diffusion rate of Ga from the surface into the ZnS matrix were used; i.e., these materials acted as catalysts [1, 4, 8–10].

REFERENCES

1. *Physics and Chemistry of II–VI Compounds*, Ed. by M. Aven and J. S. Prener (North-Holland, Amsterdam, 1967; Mir, Moscow, 1970).
2. N. K. Morozova and V. A. Kuznetsov, *Zinc Sulfide. Production and Optical Properties*, Ed. by M. V. Fok (Nauka, Moscow, 1987) [in Russian].
3. I. K. Vereshchagin, B. A. Kovalev, L. A. Kosyachenko, and S. M. Kokin, *Electroluminescence Light Sources*, Ed. by I. K. Vereshchagin (Énergoatomizdat, Moscow, 1990) [in Russian].
4. Yu. Yu. Bacherikov, I. P. Vorona, S. V. Optasyuk, *et al.*, Fiz. Tekh. Poluprovodn. (St. Petersburg) **38**, 1025 (2004) [Semiconductors **38**, 987 (2004)].
5. W. van Gool and A. P. Cleiren, Philips Res. Rep. **15** (3), 253 (1960).
6. A. N. Georgobiani, M. B. Kotlyarevskiĭ, and V. N. Mikhalenko, Tr. Fiz. Inst. im. P.N. Lebedeva, Akad. Nauk SSSR **138**, 79 (1983).
7. N. P. Golubeva and M. V. Fok, Zh. Prikl. Spektrosk. **43**, 940 (1985).
8. J. S. Prener and D. J. Weil, J. Electrochem. Soc. **103**, 342 (1956).
9. J. E. Nicholls, J. J. Davis, and B. C. Cavenott, J. Phys. C: Solid State Phys. **12**, 370 (1979).
10. J. S. Prener and F. E. Williams, J. Chem. Phys. **25**, 361 (1956).
11. Ya. E. Geguzin, *Physics of Sintering* (Nauka, Moscow, 1984) [in Russian].
12. G. H. Gessinger, *Powder Metallurgy of Superalloys* (Butterworths, Baden, Switzerland, 1984; Metallurgiya, Chelyabinsk, 1988).
13. N. Kh. Abrikosov, V. F. Bankina, L. V. Poretskaya, E. V. Skudnova, and S. N. Chizhevskaya, *Semiconductor Chalcogenides and Chalcogenide-Base Alloys* (Nauka, Moscow, 1975) [in Russian].
14. G. B. Abdullaev and T. O. Dzhafarov, *Diffusion of Atoms in Semiconductor Structures* (Atomizdat, Moscow, 1980) [in Russian].
15. *Atomic Diffusion in Semiconductors*, Ed. by D. Shaw (Plenum, London, 1973; Mir, Moscow, 1975).

Translated by A. Spitsyn

Semiconductors, Vol. 39, No. 3, 2005, pp. 300–307. From Fizika i Tekhnika Poluprovodnikov, Vol. 39, No. 3, 2005, pp. 320–326.
Original English Text Copyright © 2005 by Sennikov, Kotereva, Kurganov, Andreev, Niemann, Schiel, Emtsev, Pohl.

ELECTRONIC AND OPTICAL PROPERTIES OF SEMICONDUCTORS

Spectroscopic Parameters of the Absorption Bands Related to the Local Vibrational Modes of Carbon and Oxygen Impurities in Silicon Enriched with ^{28}Si, ^{29}Si, and ^{30}Si Isotopes*

P. G. Sennikov[1], T. V. Kotereva[1], A. G. Kurganov[1], B. A. Andreev[2], H. Niemann[3], D. Schiel[3], V. V. Emtsev[4], and H.-J. Pohl[5]

[1]*Institute of Chemistry of High-Purity Substances, Russian Academy of Sciences, Nizhni Novgorod, Russia*
[2]*Institute for Physics of Microstructures, Russian Academy of Sciences, Nizhni Novgorod, 603950 Russia*
[3]*Physikalisch-Technische Bundesanstalt, Braunschweig, Germany*
[4]*Ioffe Physicotechnical Institute, Russian Academy of Sciences, St. Petersburg, 194021 Russia*
[5]*VITCON Projectconsult GmbH, Jena, Germany*
Submitted August 4, 2004; accepted for publication August 10, 2004

Abstract—The IR spectra of all three Si isotopes in the form of bulk single crystals (^{28}Si with an enrichment of more than 99.9%, and ^{29}Si and ^{30}Si with an enrichment of more than 90%) have been studied at $T = 300$, 17, and 5 K in the spectral range 550–1200 cm^{-1}. The IR active local vibrational modes (LVM) of Si–^{12}C centered at 605 cm^{-1} and Si–^{16}O–Si quasi-molecules in the region of 1136 cm^{-1} for all the Si isotopes, in comparison with Si possessing a natural isotopic composition, as well as their isotopic shift at 300 and 17 K, have been determined. The dependence of the shape of the antisymmetric stretching vibration band for ^{28}Si–^{16}O–^{28}Si in the spectrum of ^{28}Si on spectral resolution has been studied. The possibility of generalizing the IR spectroscopy method for the determination of carbon and oxygen impurities in Si possessing a natural isotopic composition to monoisotopic Si have been discussed. *© 2005 Pleiades Publishing, Inc.*

1. INTRODUCTION

Carbon and oxygen impurities are invariably present in silicon single crystals manufactured both by the Czochralski (Cz) (the manufacturing process itself is the main source of the impurities) and float-zone (FZ) methods as well as by deposition from a vapor phase. Oxygen atoms are located at interstitial sites of the silicon crystal lattice at a concentration lower than that corresponding to solubility (2×10^{18} cm^{-3} at the melting temperature) and dissolved carbon atoms (solubility at the melting temperature is 3.5×10^{17} cm^{-3}) are located at the lattice sites. Despite the fact that neither impurity is electrically active, the structure of an impurity in a lattice, as well as its concentration, are of importance both to provide controllable growth of silicon crystals and to apply Si in the manufacturing of semiconductor structures. It is known, for example, that heat treatment of Cz-Si leads to the formation of oxygen-containing thermal donors, i.e., electrically active centers affecting the main electrical parameters of the material [1] and playing the role, in the initial stage of formation, of second-phase inclusions (precipitates) [2]. The precipitates themselves are the source of a large number of structural defects (e.g., dislocations). These defects can also be the "intrinsic getters" of undesirable impurities in the process of manufacturing semiconductor devices. It is also known [3] that carbon noticeably affects the precipitation processes of oxygen and its gettering functions. In addition, if impurities of oxygen and carbon are present at a level of 3×10^{15} cm^{-3}, even in high-purity silicon crystals, they lead to a certain distortion in the crystal site that can be significant during precision measurements of its parameters [4].

Located at interstitial sites, the oxygen atoms form a Si–O–Si quasi-molecule that provides the environment in which, at room temperature, an IR active local vibrational mode (LVM) with the maximum of the most intensive antisymmetric stretching band ν_3 at 1106 cm^{-1} originates. The most intensive LVM absorption band of Si–C at 605 cm^{-1}, for the same temperature, is characteristic of carbon that has been substitutionally incorporated into the silicon lattice. Both these bands overlap, to different extents, with bands of the intrinsic phonon absorption of Si. The special features of these and other less intensive absorption bands of oxygen and carbon at various temperatures and impurity concentrations have been discussed in detail in the literature for many years (e.g., the reviews [5, 6]). On the basis of these data, standard measurement procedures have been developed for an IR spectroscopic determination of oxygen and carbon impurities [7, 8].

The above-mentioned statements refer to silicon samples possessing a natural isotopic composition con-

*This article was submitted by the authors in English.

1063-7826/05/3903-0300$26.00 © 2005 Pleiades Publishing, Inc.

Table 1. The concentration (cm^{-3}) of oxygen and carbon impurities in reference silicon samples with a natural isotopic composition according to an IR interlaboratory determination

Number of samples (thickness, mm)	Oxygen			Carbon		
	IChHPS (17 K)	PTB* (5.2 K)	Passport data	IChHPS (17 K)	PTB* (5.2 K)	Passport data
1 (2.21)	$\leq 3 \times 10^{14}$	$\leq 3 \times 10^{14}$	$(3.0 \pm 0.1) \times 10^{14}$	$\leq 3 \times 10^{15}$	$(1.8 \pm 0.9) \times 10^{15}$	$\leq 3 \times 10^{15}$
2 (4.02)	$(4.4 \pm 0.3) \times 10^{15}$	$(4.3 \pm 0.2) \times 10^{15}$	–	$\leq 3 \times 10^{15}$	$(2.0 \pm 0.3) \times 10^{15}$	–
3 (2.96)	$(2 \pm 01) \times 10^{15}$	$(1.9 \pm 0.2) \times 10^{15}$	$(1.8 \pm 0.1) \times 10^{15}$	$\leq 3 \times 10^{15}$	$(3.0 \pm 0.2) \times 10^{15}$	3×10^{15}
4 (1.95)	$(3.1 \pm 0.1) \times 10^{15}$	–	3.1×10^{15}	$(1.5 \pm 0.2) \times 10^{16}$	–	$(1.0 \pm 0.1) \times 10^{16}$
5 (0.37)	$(7.0 \pm 0.1) \times 10^{17}$	–	$(6.9 \pm 0.1) \times 10^{17}$	$< 1 \times 10^{16}$ (300 K)	–	–

* PTB denotes Physicalish-Technische Bundesanstalt.

taining ^{28}Si (92.21%), ^{29}Si (4.70%), and ^{30}Si (3.09%). It might be expected that, in employing samples of isotopically pure Si, any noticeable changes in the spectral parameters of the absorption bands of oxygen and carbon will be observed due to changes in the lattice parameters and phonon spectrum. Indeed, in [9], such an interpretation was evidently demonstrated for the oxygen band at 862 cm^{-1} in isotopically enriched germanium (98% enrichment). Similar studies for monoisotopic samples of Si are evidently of scientific and applied interest, primarily from the point of view of quantitatively determining these important impurities. However, to date, it has been impossible to carry out such studies due to a lack of bulk samples of ^{28}Si, ^{29}Si, and ^{30}Si with a sufficient degree of purity, crystalline perfection, and high enrichment. Experiments, including the investigation of IR spectra, with different silicon isotopes can now be realized due to the development of a technique [10, 11] for the production of high-purity monoisotopic ^{28}Si as well as ^{29}Si and ^{30}Si [12].

The goal of the present study is to investigate the IR absorption spectra of carbon and oxygen impurities in single crystal samples of ^{28}Si, ^{29}Si, and ^{30}Si that have a record-high isotopic enrichment (see below) at room temperature and at $T = 17$ and 5 K. One of the aims of this study was to discover if it is possible to apply the above-mentioned standard techniques [7, 8], developed for materials with natural isotopic composition, to a quantitative determination of the carbon and oxygen impurities in monoisotopic Si. It should be noted that, while this study was in progress, a paper by Kato *et al.* [13] was published in which a high-resolution IR absorption study, together with theoretical calculations of the LVM's of oxygen in isotopically enriched ^{28}Si (99.86%), ^{29}Si (97.10%), and ^{30}Si (98.74%), was reported.

2. EXPERIMENTAL

Bulk single-crystal samples of monoisotopic ^{28}Si, ^{29}Si, and ^{30}Si were investigated. The starting polycrystals were obtained, by the technique described in [10], at the Institute of Chemistry of High-Purity Substances (IChHPS) (Nizhni Novgorod) from silicon tetrafluoride enriched at the Science-Technical Centre Elechtrochemical Plant (CENTROTEKH, St. Petersburg). The single crystals were grown at the Institute of Crystal Growth (Berlin) either by a combination of the Cz method and crucibleless FZ method (^{28}Si) or only by the Cz method (^{29}Si and ^{30}Si). According to data from laser-ionization mass spectrometry, the enrichment of the studied ^{28}Si samples was, on average, equal to 99.91%. The enrichment was 99.86% for ^{29}Si and 99.74% for ^{30}Si. The samples were of *n*-(^{29}Si, ^{30}Si) and *p*-(^{28}Si) type conductivity and contained (according to the IR-spectroscopy data) electrically active impurities (B, P) at a level of ~10^{14}–10^{15} cm^{-3}.

Commercial samples of Si possessing a natural isotopic composition and an impurity content and structural perfection close to the samples of monoisotopic Si (Table 1) were used as reference samples.

The samples investigated were in the form of plane-parallel discs with a diameter of 8–12 mm and thickness of 0.37–2.2 mm. During the preparation of the samples for the IR measurements, they were ground and mechanically polished with diamond powder that had a 1 μm dispersion.

The absorption spectra were recorded using IFS-113v (IChHPS) and IFS-66 (PTB) IR spectrometers with spectral resolutions of 1 cm^{-1} (T = 300 K); 0.5 cm^{-1} (5 K); and 0.5, 0.3, and 0.1 cm^{-1} (T = 17 K) in the spectral range 500–1400 cm^{-1} and Happ Genzel apodization function.

The samples were cooled down to a temperature of 16 K using an RGD 210 (IChHPS) refrigerator-cryostat and down to 5 K using an Optistat CF helium flow-through cryostat (PTB).

3. RESULTS AND DISCUSSION

3.1. *IR Absorption Spectra of* C *and* O *in* Si *Possessing a Natural Isotopic Composition* (^{nat}Si)

Due to the fact that the measurement of the spectra was carried out in two different groups and on various equipment, with the goal being to determine the reproducibility of the results, an interlaboratory experiment

Table 2. The spectral positions (ν_{max}, cm^{-1}) of the phonon modes in the IR spectrum of the silicon with a natural isotopic composition (^{nat}Si) and monoisotopic Si at T = 300 K

Phonons	ν_{max} (^{nat}Si) [4]	ν_{max} (^{nat}Si)	ν_{max} (^{28}Si)	ν_{max} (^{29}Si)	ν_{max} (^{30}Si)
LO + TA	566	566.4	569.1	559	548.1
TO + TA	610	610.8	612	601.6	591.5
LO + LA	739	739.1	741	728.3	715.6
TO + LA	819	819	817.8	804.3	791
TO + LO	886	~888	~890	873.5	859
TO + TO	960	~959	~962	944	930
2TO + TA	1118	1119	1122.4	(*)	(*)
2TO + LO	1299	1299.5	~1302	1278.3	1253.5
3TO	1448	1448.8	~1450	1425.1	1398.6

Note: (*) Not determined because of the high concentration of oxygen in the sample. The error in the determination of the phonon peak does not exceed 0.3 cm^{-1}.

was carried out to investigate the impurity spectra of carbon and oxygen in five samples of single crystal silicon with a natural isotopic composition. In four samples containing oxygen and three samples containing carbon, the content of the impurities was determined independently (Table 1). The necessity of these measurements was also due to the fact that the known calibration coefficients, used in standard analytical techniques for the determination of C and O impurities in silicon [7, 8], refer to room-temperature conditions. At the same time a sufficiently low level of the mentioned impurities in the monoisotopic samples necessitated measurement at low (below 20 K) temperatures. The published data on the calibration coefficients in these conditions are rather contradictory, at least with respect to the oxygen impurity [5, 14].

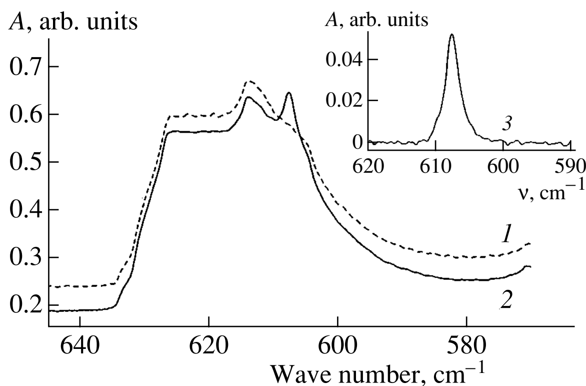

Fig. 1. The absorption spectra of ^{nat}Si at 607 cm^{-1} (T = 17 K): (*1*) sample 1, (*2*) sample 4, and (*3*) absorption band of the Si–^{12}C complex in sample 4. The numeration of the samples corresponds to Table 1.

3.1.1. The IR spectrum of carbon. The band of optical absorption at 605 cm^{-1} (300 K) and 607 cm^{-1} (16 K) is due to the LVM of the ^{nat}Si–C$_s$ group in combination with the participation of the atoms of the Si possessing a natural isotopic composition, which have the full width at half maximum (FWHM) ~6 cm^{-1} at 300 K and ~3 cm^{-1} below 80 K [6, 8]. Thus, in order to measure this width, a spectral resolution of 0.5 cm^{-1} is sufficient. However, real problems can occur due to the fact that the Si–C band is situated against the background of the strongest intrinsic absorption of Si, which is a combined absorption band of transverse optical (TO) and acoustic (TA) phonons at 610 cm^{-1} (Table 2).

Figure 1 gives the absorption spectrum of the carbon impurities in sample 4 (Table 1), which were obtained after a subtraction of the spectrum of a sample with an ultimately low content of carbon. The carbon content N_C (cm^{-3}) is found from the known relation

$$N_C = \alpha_C K_C, \quad (1)$$

where α_C is the experimentally determinable absorption coefficient and K_C is the calibration coefficient. According to the calculations given in [8], the values for the calibration coefficients in the case of carbon are equal to 8.2 × 10^{16} and 3.7 × 10^{16} at/cm^2 at T = 300 K and at T < 80 K, respectively.

The results of the determination of the carbon impurities in the investigated samples of polyisotopic Si are given in Table 1. The correlation between the data, including the passport data (“certified values”), of both laboratories is also given in Table 1.

3.1.2. The IR spectra of oxygen. As has already been pointed out, the most intensive band, corresponding to the oxygen impurity in the Si with a natural isotopic composition, is close to 1107 cm^{-1} at room temperature and has an FWHM of about 32 cm^{-1}. These values refer to an asymmetrical stretching vibration of the ^{nat}Si–^{16}O–^{nat}Si quasi-molecule and overlaps with the intrinsic absorption band of a silicon lattice consisting of a combination of a transverse optical phonon and a transverse acoustic phonon with a center at 1118 cm^{-1} and an FWHM of about 50 cm^{-1} at room temperature (Table 2). The content of oxygen in ^{nat}Si is determined by a relation similar to (1) but including the calibration coefficient K_O for oxygen, which amounts 3.14 × 10^{17} at/cm^2 according to [7] (in [14], a similar value of 3.07 × 10^{17} at/cm^2 is given). The oxygen band shows a complex temperature behavior. At low temperatures, near 5 K, a broad room-temperature band at 1107 cm^{-1} is removed by a relatively narrow band at 1136 cm^{-1} and two smaller band components at 1134 and 1132 cm^{-1} (Fig. 2). These three band components correspond to the isotopic LVM of the Si–O groups ^{28}Si–^{16}O–^{28}Si, ^{28}Si–^{16}O–^{29}Si, and ^{28}Si–^{16}O–^{30}Si.

For measurements at low temperatures, the influence of the lattice (phonon) absorption in this region is not significant, since, as can be seen from Fig. 2, a narrow band of the asymmetric stretching vibrations of the

quasi-molecule Si–O–Si is located in the range of the maximum of the much less intensive combination 2TO + TA band (the absorption coefficient is equal to ~0.345 cm^{-1} $T = 7$ K [15]).

In general, the calibration coefficient K_O of the band centered at 1136.4 cm^{-1} in a temperature range of 17 K < T < 50 K depends on the temperature, spectral resolution, and selected apodization function. However, as was shown in [16, 17], at $T < 17$ K, the value of K_O depends on only the resolution and apodization function, not the temperature [4]. Thus, at 8 K and at a resolution of 0.3 cm^{-1}, it is equal to 1.05×10^{16} at/cm^2 [4]. While determining the oxygen impurity in the natural and monoisotopic (see below) Si we used the value of $K_O = 1.23 \times 10^{16}$ at/cm^2, which was estimated for a series of silicon samples with various oxygen contents and registered with a spectral resolution of 0.5 cm^{-1} at $T = 17$ K (IChHPS) and $T = 5$ K (PTB). The coefficient $K_O = 1.23 \times 10^{16}$ at/cm^2 was derived by means of measurements of the same material at low and room temperature as well as the use of the generally accepted value of $K_O = 3.14 \times 10^{16}$ at/cm^2 for the calculation of the oxygen content from the room temperature spectrum. The used sample thickness was 3 cm for the 393 K and 0.3 cm for the 5 K measurement.

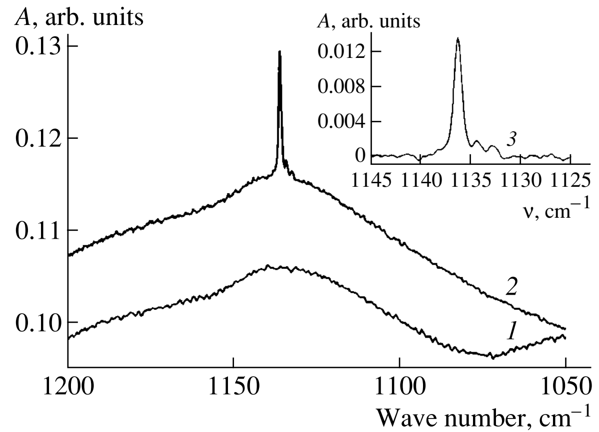

Fig. 2. The absorption spectra of ^{nat}Si at 1136 cm^{-1} ($T = 17$ K): (*1*) sample 1, (*2*) sample 4, and (*3*) absorption band of the Si–^{16}O–Si quasi-molecule in sample 4. The numeration of the samples corresponds to Table 1.

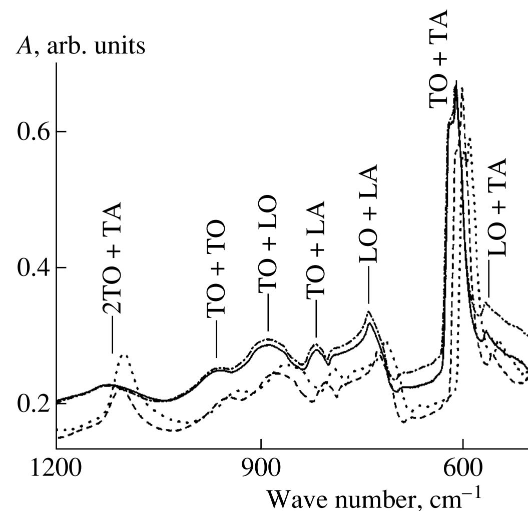

Fig. 3. The phonon spectra of the monoisotopic ^{28}Si, ^{29}Si, ^{30}Si, and ^{nat}Si compositions in the range 1200—500 cm^{-1} at $T = 300$ K.

3.2. The IR Absorption Spectra of C *and* O *in Samples of Monoisotopic Silicon*

3.2.1. Phonon spectra of the samples ^{28}Si, ^{29}Si, and ^{30}Si. It follows from the previous section that, in order to provide an adequate description of the absorption bands of the carbon and oxygen impurities in the silicon possessing a natural composition, data on lattice vibrations are required, i.e. on the spectral position and intensity of the different phonon modes observed in the absorption range of the stated impurities. The transition to isotopically enriched samples, alongside the averaged lattice mass, changes the phonon spectrum of the matrix. The positions of the Si–^{16}O–Si and Si–^{12}C quasi-molecule bands corresponding to the silicon atoms of the given isotopes should also change.

Figure 3 gives the experimental phonon spectra for monoisotopic ^{28}Si, ^{29}Si, and ^{30}Si, and for ^{nat}Si at room temperature in the range from 600 to 1200 cm^{-1}. It can be seen that the absorption bands of the ^{28}Si lattice are shifted to higher frequencies with respect to the phonon spectrum of ^{nat}Si, and the corresponding bands of isotopic ^{30}Si and ^{29}Si are shifted in the opposite frequency direction according to the well-known relation between the frequency of a phonon $\omega(k)$ and the atomic mass m [18, 19]:

$$\omega(k) \propto m^{-1/2}. \quad (2)$$

Table 2 gives the maxima of the phonon absorption for Si with different isotopic contents in the stated spectral range at room temperature. The dependence of the phonon frequency $\omega(k)$ (with an LO + LA phonon as an example) on the average isotopic atomic mass of Si for the samples with different isotopic compositions is given in Fig. 4.

3.2.2. The IR spectra of carbon in monoisotopic silicon. As was stated above, the absorption band of the Si–C groups in the spectrum of ^{nat}Si is situated against the background of the strongest phonon absorption of Si. As can be seen from Fig. 5, the same situation is also observed in case of enriched Si. In this figure, the composite band near 610 cm^{-1} shifts with respect to the same band in ^{nat}Si in accordance with (2). Due to the fact that samples with a different isotopic composition and a carbon content lower than the detection limit of

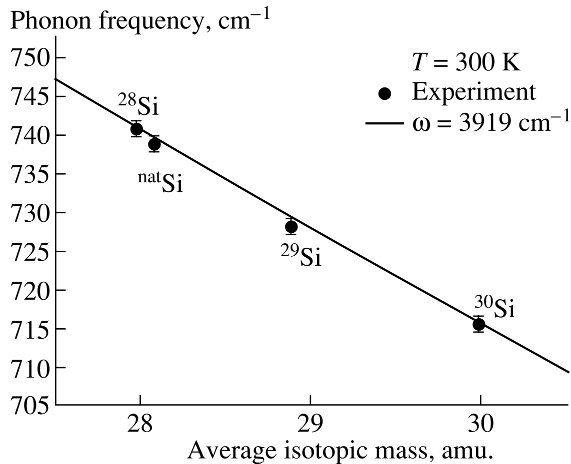

Fig. 4. The LO + LA phonon frequencies as a function of the average nuclear mass in samples of various isotopic Si composition, including ^{nat}Si ($T = 300$ K).

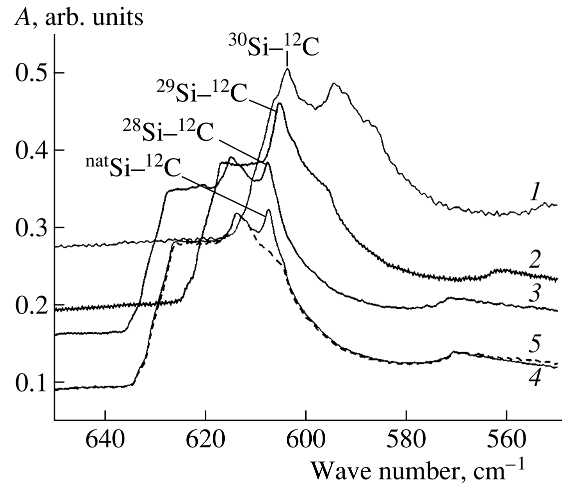

Fig. 5. The absorption spectrum of TO + TA phonons and the Si–C complex in silicon samples of various isotopic composition (T = 17 K): (*1*) sample Si30-2-Pr8-part2, (*2*) sample Si29-2-Pr8-part2, (*3*) sample Si28-4-Pr10, (*4*) sample 4, and (*5*) sample 1. The numeration of the samples corresponds to Table 4 and Table 1.

the IR spectroscopic method were not available (~5×10^{14} cm^{-3}) [8], it was, strictly speaking, impossible to isolate the absorption band of carbon from the composite bands shown in Fig. 5. Assuming that the band shape of the TO + TA phonon band does not change significantly due to the isotope exchange (though this assumption needs additional experimental testing), the phonon band of the sample possessing a natural isotopic composition with a carbon content of less than 3×10^{15} cm^{-3} in Fig. 1 can used for the baseline subtraction. The obtained absorption bands of the quasi-molecules ^{28}Si–C, ^{29}Si–C, and ^{30}Si–C are shown in Fig. 6 and their spectral parameters at 17 K are listed in Table 3. For the determination of the carbon in the investigated monoisotopic samples, we used the above-given values taken from [8] for the calibration coefficients at room temperature and below 80 K for the band centered at 607 cm^{-1}. The data obtained are listed in Table 4.

3.2.3. The IR spectrum of oxygen in monoisotopic silicon. Table 6 lists the spectral positions and FWHMs of the absorption bands of the quasi-molecules ^{28}Si–^{16}O–^{28}Si, ^{29}Si–^{16}O–^{29}Si, and ^{30}Si–^{16}O–^{30}Si at room temperature for the corresponding samples of monoisotopic silicon. A small low-frequency shift at the practically unchanged half-width is observed.

The oxygen spectra for the samples of monoisotopic silicon at low temperatures, i.e., below 20 K, are of the greatest interest since, as can be seen from Fig. 2, for the ^{nat}Si, an isotopic splitting of the band centered at 1136 cm^{-1} takes place.

Determination of the principal spectral parameters (position and FWHM) of the Si–^{16}O–Si band at low temperatures in the spectra of the monoisotopic silicon calls for their registration at the spectral resolution $\lesssim 0.3$ cm^{-1} [5]. Figure 7 demonstrates the ^{28}Si–^{16}O–^{28}Si band at 1136.4 cm^{-1} for the sample Si28-4-Pr10 taken from Table 4 and recorded with four different values of

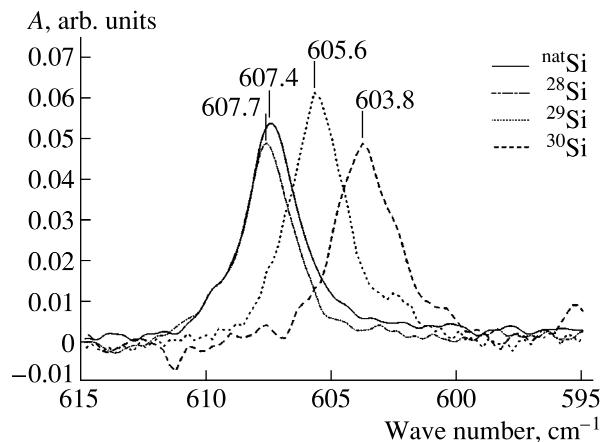

Fig. 6. The absorption spectra of the Si–^{12}C complex at 600 cm^{-1} (T = 17 K) in the samples of monoisotopic Si and the silicon with a natural isotopic composition: ^{30}Si, sample Si30-2-Pr8-part2; ^{29}Si, sample Si29-2-Pr8-part2; ^{28}Si, sample Si28-4-Pr10; and ^{nat}Si, sample 4. The numeration of the samples corresponds to Table 4 and Table 1.

spectral resolution. The obtained values of the FWHM of this band are given in Table 6. It can be seen that a change in the resolution from 0.5 cm^{-1} to 0.1 cm^{-1} results in a slight decrease of the FWHM, while a further increase of the resolution leads to the FWHM becoming constant and equal to (0.59 ± 0.01) cm^{-1}. These results provide evidence for the registration of the true shape of this band. Moreover, this value agrees with the FWHM of the same band in the spectrum of the ^{nat}Si [5, 16, 17].

Table 3. The spectral position ν_{max} (cm^{-1}) and full width at half-maximum (FWHM) $\Delta\nu_{1/2}$ (cm^{-1}) of the absorption bands of the Si–^{12}C quasi-molecule in the IR spectra of the silicon with a natural isotopic composition (^{nat}Si) and monoisotopic Si

T, K	^{nat}Si–^{12}C		^{28}Si–^{12}C		^{29}Si–^{12}C		^{30}Si–^{12}C	
	ν_{max}	$\Delta\nu_{1/2}$	ν_{max}	$\Delta\nu_{1/2}$	ν_{max}	$\Delta\nu_{1/2}$	ν_{max}	$\Delta\nu_{1/2}$
300	605*	5.3 ± 0.1	605	**	603.1	**	600.2	**
17	607.4*	2.57 ± 0.03	607.7	2.44 ± 0.04	605.6	2.67 ± 0.06	603.8	2.89 ± 0.11

* 605.0 cm^{-1}, $\Delta\nu_{1/2}$ = 6 cm^{-1} at T = 300 K [5] and 607.5 cm^{-1}, $\Delta\nu_{1/2}$ = 3 cm^{-1} at T < 80 K [5].

** Not determined because of the large error in the separation of the bands.

Table 4. The concentration (cm^{-3}) of oxygen and carbon impurities in monoisotopic silicon according to an IR interlaboratory determination

Designation of sample according to SIC (thickness, mm)*	Oxygen		Carbon	
	IChHPS, T = 300 K	PTB, T = 5 K	IChHPS, T = 300 K	PTB, T = 5 K
Si28-4-Pr10 (1.66)	$(3.2 \pm 0.5) \times 10^{16}$	$(4 \pm 0.4) \times 10^{16}$	$(2.8 \pm 1.4) \times 10^{16}$	$(1.4 \pm 0.1) \times 10^{16}$
Si28-3-Pr10 (2.18)	$\leq 8 \times 10^{15}$	$(3.3 \pm 0.1) \times 10^{14}$	$\leq 5 \times 10^{15}$	$(1.6 \pm 1.0) \times 10^{15}$
Si28-6.1-Pr10-part4 (2.18)	$(2.3 \pm 0.4) \times 10^{17}$	$(2.0 \pm 0.2) \times 10^{17}$	$(3.7 \pm 0.2) \times 10^{16}$	$(3.3 \pm 0.4) \times 10^{16}$
Si29-2-Pr8-part2 (2.33)	$(3.1 \pm 0.8) \times 10^{17}$	**	$(5 \pm 1) \times 10^{16}$	**
Si30-2-Pr8-part2 (1.78)	$(5.6 \pm 0.6) \times 10^{17}$	**	$(4 \pm 1.5) \times 10^{16}$	$(4.6 \pm 0.1) \times 10^{16}$

* Sample Identification Code (SIC): isotope–number of charge–number of product (10 denotes an FZ single crystal and 8, a Cz single crystal)–number of the studied part of the crystal according to the cutting scheme. For samples in the first and second rows of Table 4, the number of the studied part of the crystal is not determined.

** Not determined because of the high concentration of oxygen and carbon in the sample (full absorption).

Unfortunately, the registration of the true band shapes of the ^{29}Si–^{16}O–^{29}Si and ^{30}Si–^{16}O–^{30}Si quasi-molecules in the spectra of ^{29}Si and ^{30}Si was impossible due to the high concentration of oxygen in the sample. Even at the sample's minimal thickness (0.9 mm), a total absorption of the corresponding bands was observed. Therefore, Table 6 summarizes only the spectral positions of the absorption bands of the quasi-molecules Si–^{16}O–Si. It should be noted that, as was expected, the position of the ^{28}Si–^{16}O–^{28}Si band for ^{28}Si coincides with the position of the same band in the spectrum of natural silicon; however, it does not have the low-frequency components corresponding to the vibrations of ^{28}Si–^{16}O–^{29}Si and ^{28}Si–^{16}O–^{30}Si. The early theoretically obtained [20, 21] and later experimentally determined [13] spectral position of the ^{29}Si–^{16}O–^{29}Si band agrees satisfactorily with the experimental value for ^{29}Si obtained in this study (Table 6). The spectral position of the ^{30}Si–^{16}O–^{30}Si band was previously determined in [22] from the spectrum of ^{nat}Si that contained ~3×10^{17} cm^{-3} of oxygen, as well as in isotopically enriched ^{30}Si [13]. It can be seen from Table 6 that this value are very close to the experimental one obtained here for ^{30}Si and is 3.6 cm^{-1} higher than the predicted value [20]. The isotopic shift of the oxygen bands of ^{28}Si and of ^{29}Si amounts to 3.8 cm^{-1}, which is the same as the shift of the oxygen bands of ^{29}Si and ^{30}Si. The isotopic shift theoretically predicted in [20, 21] was slightly greater than the experimentally found value and equal to 5.3 cm^{-1}, which can probably be explained by the fact that the theoretical model does not consider the influence of the nearest and extended silicon atoms. It should be noted that the vibrational frequencies of the Si–O–Si molecule (for all isotopic species) recently predicted according to the improved multiatom model in [13] are very close to the experimental values.

Figure 8 presents the spectra of the quasi-molecules Si–^{16}O–Si at 1130 cm^{-1} (T = 17 K) for the samples Si30-2-Pr8-part2, Si28-6.1-Pr10-part4, Si29-2-Pr8-part2, and natural silicon sample 5 from Table 1 (with the

Table 5. The dependence of the position ν_{max}, full width at the half maximum (FWHM) $\Delta\nu_{1/2}$, and the intensity of the absorption band of the ^{28}Si–^{16}O–^{28}Si quasi-molecule in the IR spectrum of the monoisotopic silicon ^{28}Si (sample Si28-4-Pr10) on the spectral resolution at T = 17 K (Happ–Genzel apodization function)

Resolution, cm^{-1}	ν_{max}, cm^{-1}	$\Delta\nu_{1/2}$, cm^{-1}	Intensity, r.u.
0.5	1136.3	0.81 ± 0.02*	0.32
0.3	″	0.68 ± 0.01*	0.38
0.2	″	0.63 ± 0.01*	0.39
0.1	″	0.59 ± 0.01*	0.40

* The FWHM was determined by an approximation of the band shape with the Lorenz function.

Table 6. The position (ν_{max}, cm^{-1}) and full width at half maximum (FWHM) $\Delta\nu_{1/2}$ (cm^{-1}) of the absorption bands of the Si–^{16}O–Si quasi-molecules in the IR spectra of the silicon with a natural isotopic composition (^{nat}Si) and monoisotopic silicon at two temperatures

T, K	^{28}Si–^{16}O–^{28}Si		^{29}Si–^{16}O–^{29}Si		^{30}Si–^{16}O–^{30}Si	
	ν_{max}	$\Delta\nu_{1/2}$	ν_{max}	$\Delta\nu_{1/2}$	ν_{max}	$\Delta\nu_{1/2}$
300	1107	32 ± 1	1103.1	36 ± 1	1099.3	33 ± 0.5
17	1136.3$^{1)}$	0.60 ± 0.01	1132.5$^{2)}$	(*)	1128.9$^{3)}$	(*)

Notes: 1. ν_{max} = 1136.4 cm^{-1} [5].
2. ν_{max} = 1131.0 cm^{-1} according to theoretical data [20], and ν_{max} = 1132.5 cm^{-1} according to experimental data [13].
3. ν_{max} = 1125.3 cm^{-1} according to theoretical data [20], ν_{max} = 1129.2 cm^{-1} [22] and ν_{max} = 1129.1 cm^{-1} according to experimental data [13].

* Not determined because of the high concentration of oxygen in the sample.

thickness taken into account). This figure clearly demonstrates the isotopic shift of the antisymmetric stretching vibration band of the quasi-molecule Si–^{16}O–Si as a result of the change from the silicon with a natural isotopic composition to the monoisotopic samples.

In fact, there is no difference between the quantitative determination of the oxygen content in ^{28}Si and in natural silicon.

As regards the ^{29}Si and ^{30}Si isotopes, due to the absence, for known reasons, of calibration coefficients for the ^{29}Si–^{16}O–^{29}Si and ^{30}Si–^{16}O–^{30}Si bands, and assuming that their band shape does not differ strongly from the shape of the ^{28}Si–^{16}O–^{28}Si band in natural silicon, we also used the calibration coefficient of the ^{28}Si–^{16}O–^{28}Si band in natural silicon equal to 1.23 × 10^{16} cm^{-2} for the determination of the oxygen in ^{29}Si and ^{30}Si (for the resolution 0.5 cm^{-1} at T = 17 K and 5.2 K). The results for the oxygen concentration in all the studied samples are given in Table 4.

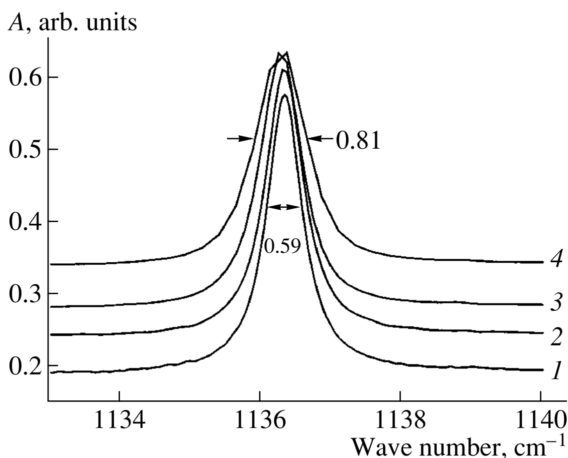

Fig. 7. The dependences of the full width at half maximum (FWHM) of the absorbtion band of the ^{28}Si–^{16}O–^{28}Si quasi-molecule in monoisotopic ^{28}Si (sample Si28-4-Pr10 from Table 4) on the spectral resolution (T = 17 K): (*1*) 0.1 cm^{-1}, (*2*) 0.2 cm^{-1}, (*3*) 0.3 cm^{-1}, and (*4*) 0.5 cm^{-1}.

As can be seen from the above-presented results, generalization of IR spectroscopy methods for the determination of the carbon and oxygen in monoisotopic silicon, and elaborated for natural silicon, can, at the moment, only be done by taking into account certain limitations and assumptions. The possible errors that can occur in this determination are apparently minimal for ^{28}Si but may be considerable for ^{29}Si and ^{30}Si. For the development of a completely satisfactory IR method for the determination of the carbon and oxygen impurities in monoisotopic silicon, a study of the IR spectra of high-purity samples (in relation to carbon and oxygen, a content of about 10^{14} cm^{-3}) of monoiso-

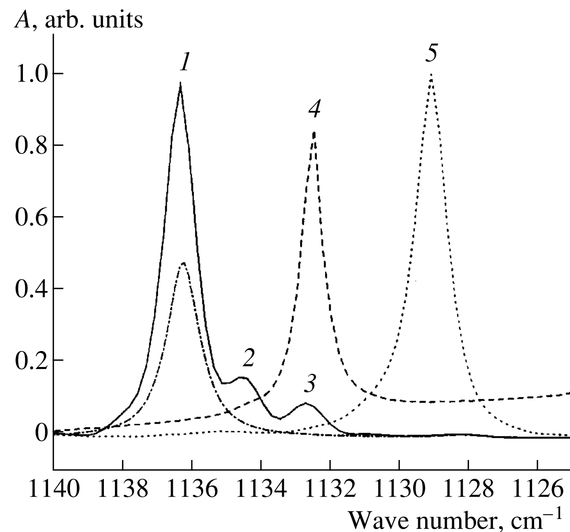

Fig. 8. The spectra of the Si–^{16}O–Si quasi-molecule at 1130 cm^{-1} (T = 17 K), with the thickness taken into account, in the monoisotopic samples Si30-2-Pr8-part2, Si28-6.1-Pr10-part4, and Si29-2-Pr8-part2 (Table 4), and, in ^{nat}Si, sample 5 (Table 1): (*1*) ^{28}Si–^{16}O–^{28}Si (1136.4 cm^{-1}), (*2*) ^{28}Si–^{16}O–^{29}Si (1134.5 cm^{-1}), (*3*) ^{28}Si–^{16}O–^{30}Si (1132.2 cm^{-1}), (*4*) ^{29}Si–^{16}O–^{29}Si (1132.5 cm^{-1}), and (*5*) ^{30}Si–^{16}O–^{30}Si (1129.2 cm^{-1}). The last spectrum is reduced twice along the ordinate axis.

topic silicon are first required. These samples could then be used as reference samples. For each isotope, a series of samples with a known content of C and O that is estimated by an independent method for the determination of the calibration coefficient in relationship (1) is also strongly needed.

4. CONCLUSIONS

(1) The IR spectra of all three silicon isotopes in the form of bulk single crystals (^{28}Si with an enrichment of more than 99.9%, and ^{29}Si and ^{30}Si with an enrichment of more than 90%) were studied at $T = 300$, 17, and 5 K in the spectral range 550–1200 cm^{-1}, which refers to the absorption of the Si–^{16}O–Si and Si–^{12}C group. The spectral position of the phonon maximum at 300 K was determined.

(2) The spectral features of the Si–^{12}C band centered at 605 cm^{-1} for all the silicon isotopes in comparison to those of the silicon possessing a natural isotopic composition were determined. Moreover, the band's isotopic shift at 300 and 17 K was identified.

(3) The spectral position of the Si–^{16}O–Si band in the vicinity of 1136 cm^{-1} for all the silicon isotopes in comparison to that of the silicon possessing a natural isotopic composition was determined in addition to its isotopic shift at 300 and 17 K. The dependence of the shape of the asymmetric stretching vibration band for the quasi-molecule ^{28}Si–^{16}O–^{28}Si in the spectrum of ^{28}Si on the spectral resolution was studied. Its full width at half-maximum height, 0.6 cm^{-1}, agrees with the value for the natural silicon.

(4) The possibility of generalizing the IR spectroscopy method for the determination of the carbon and oxygen impurities in silicon possessing a natural isotopic composition to monoisotopic silicon was discussed. The content of the C and O impurities in the ^{28}Si, ^{29}Si and ^{30}Si single crystals was estimated. It was shown that the content of carbon and oxygen in the studied samples of ^{28}Si and the content of carbon in ^{29}Si and ^{30}Si is ~10^{16} cm^{-3} on average. The content of oxygen in ^{30}Si is an order of magnitude greater.

ACKNOWLEDGMENTS

This work was supported in part by ISTC (grant no. 1354) and INTAS (01-0468).

REFERENCES

1. P. Wagner and J. Hage, Appl. Phys. A **49**, 123 (1989).
2. S. Kashino, Y. Matsushita, M. Kanamori, and T. Iisaka, Jpn. J. Appl. Phys. **21** (1) (1982).
3. H. Foll and B. O. Kolbesen, *The Electrochemical Society Softbond Proceedings Series* (Princeton, N.J., 1977), p. 565.
4. P. Becker, H. Bettin, L. Kolnders, *et al.*, PTB Mitt. **106**, 321 (1996).
5. B. Pajot, Analusis **5** (7), 293 (1977).
6. B. O. Kolbesen and T. Kladenović, Krist. Tech. **15** (1), K1 (1980).
7. DIN 50 438 (Testing of Materials for Semiconductor Technology Determination of Impurity Content in Semiconductors by Infrared Absorption Oxygen in Silicon) (1993), Part 1, p. 809.
8. ASTM F 1391-92 (Standard Test Method for Substitutional Atomic Carbon Content of Silicon by Infrared Absorption), p. 646.
9. L. I. Khirunenko, V. I. Shakhovtsov, V. I. Shinkarenko, and F. M. Vorobkalo, Fiz. Tekh. Poluprovodn. (Leningrad) **24**, 1051 (1990) [Sov. Phys. Semicond. **24**, 663 (1990)].
10. G. G. Devyatykh, A. D. Bulanov, A. V. Gusev, *et al.*, Dokl. Akad. Nauk **376**, 492 (2001).
11. A. D. Bulanov, G. G. Devyatych, A. V. Gusev, *et al.*, Cryst. Res. Technol. **35**, 1023 (2000).
12. K. M. Itoh, J. Kato, M. Uemura, *et al.*, Jpn. J. Appl. Phys., Part 1 **42**, 6248 (2003).
13. K. M. Itoh, J. Kato, H. Yamada-Kaneta, and H.-J. Pohl, Phys. Rev. B **68**, 035205 (2003).
14. B. Pajot, in *Properties of Crystalline Silicon*, Ed. by B. L. Weiss, EMIS Datarev. Ser., No. 20, 492 (1998).
15. A. Sassella, Appl. Phys. Lett. **79**, 4339 (2001).
16. P. Wagner, Appl. Phys. A: Solids Surf. **53**, 20 (1991).
17. O. DeGryse and P. Clauws, J. Appl. Phys. **87**, 3294 (2000).
18. T. Ruf, H. D. Fushs, and M. Cardona, Phys. Bl. **52**, 1115 (1996).
19. M. Cardona, in *Festkörperprobleme (Advances in Solid State Physics)*, Ed. by R. Helbig (Vieweg, Braunschweig, 1994), Vol. 34, p. 35.
20. R. C. Newman, in *Infrared Studies of Crystal Defects* (Taylor and Francis, London, 1973), p. 88.
21. D. R. Bosomworth, W. Hayes, A. R. L. Spray, and G. D. Watkins, Proc. R. Soc. London, Ser. A **317**, 133 (1970).
22. B. Pajot, E. Artacho, C. A. J. Ammerlaan, and J.-M. Spaeth, J. Phys.: Condens. Matter **7**, 7077 (1995).

Semiconductors, Vol. 39, No. 3, 2005, pp. 308–312. Translated from Fizika i Tekhnika Poluprovodnikov, Vol. 39, No. 3, 2005, pp. 327–331.
Original Russian Text Copyright © 2005 by Voronina, Lagunova, Lipaev, Kunitsyna, Parkhomenko, Sipovskaya, Yakovlev.

The Effect of Tellurium Diffusion from an *n*-GaSb:Te Substrate on the Properties of GaInAsSb Solid Solutions Grown from Lead-Containing Melt

T. I. Voronina, T. S. Lagunova, A. F. Lipaev, E. V. Kunitsyna, Ya. A. Parkhomenko^, M. A. Sipovskaya, and Yu. P. Yakovlev

Ioffe Physicotechnical Institute, Russian Academy of Sciences, St. Petersburg, 194021 Russia

^e-mail: parkhomen@mail.ioffe.ru

Submitted August 3, 2004; accepted for publication August 19, 2004

Abstract—The effect of tellurium diffusion from an *n*-GaSb:Te substrate on the transport and photoelectric properties of GaInAsSb solid solutions grown from lead-containing melt is investigated. The strongest influence observed for tellurium diffusion from the substrate is in 1- to 2-μm-thick epitaxial layers of solid solutions with low hole density and hole mobility. Under the illumination of these samples, a large photovoltage is observed in the spectral range of band-gap absorption. © *2005 Pleiades Publishing, Inc.*

1. INTRODUCTION

As was shown in [1, 2], the growth of undoped $Ga_{1-x}In_xAs_ySb_{1-y}$ ($0 < x < 0.22$, $0 < y < 0.18$) epitaxial layers (of up to 5 μm in thickness) on *n*-GaSb:Te substrates is accompanied by the diffusion of the tellurium from this substrate. Two kinds of Te activity can occur: One possibility is that shallow donor levels are formed. The other is that, in addition to the intrinsic acceptor levels in a GaInAsSb solid solution, which have the activation energies $E_{A1} = 0.035$ eV and $E_{A2} = 0.07$ eV and are related to natural defects, a new acceptor level, with the activation energy $E_{A3} = 0.1$ eV, is formed. This level is related to the formation of the structural defect V_{Ga}Te. It was also found that the Te impurity, diffusing from the substrate, strongly reduces the mobility of the holes in the solid solution; raises the transverse ($\mathbf{H} \perp \mathbf{j}$, where $\mathbf{j}$ is the vector of the current density in the sample) magnetoresistance $\left(\frac{\Delta\rho}{\rho}\right)^{\perp}$ (in this case, the magnetoresistance factor $B_r = \left(\frac{\Delta\rho}{\rho}\right)^{\perp} / \left(\frac{\mu H}{c}\right)^2 > 1$); and gives rise to the longitudinal ($\mathbf{H} \parallel \mathbf{j}$) magnetoresistance $\left(\frac{\Delta\rho}{\rho}\right)^{\parallel}$, negative photoconductivity, and long-term relaxation of photoconductivity. These effects can be attributed to the existence of nonuniformly distributed charged centers in the material, which are associated with Te diffusion and lead to the formation of clusters. Therefore, this Te diffusion process changes the properties of GaInAsSb solid solutions.

2. RESULTS

The study of the properties of $Ga_{1-x}In_xAs_ySb_{1-y}$ solid solutions grown without the use of lead has shown [1, 2] that the hole density passes a minimum at the In content $x = 0.15$ (Fig. 1, curve *1*). This minimum can be attributed to an increase in the degree of compensation related to the decreasing concentration of a $V_{Ga}Ga_{Sb}$ defect complex with the activation energies E_{A1} and E_{A2}. The effect of the Te diffusion from the substrate is most pronounced in solid solutions with $x = 0.15$.

Under illumination, such samples demonstrate, along with photoconductivity, a strong photovoltage. In order

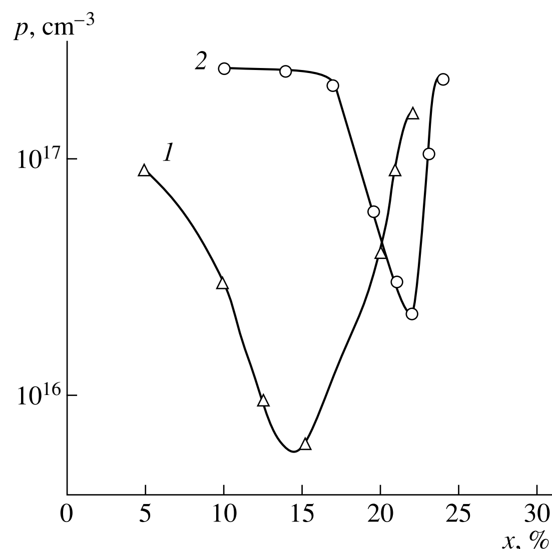

Fig. 1. The density of holes vs. the In content *x* in $Ga_{1-x}In_xAs_ySb_{1-y}$ solid solutions (*1*) without a neutral Pb solvent and (*2*) in presence of Pb.

1063-7826/05/3903-0308$26.00 © 2005 Pleiades Publishing, Inc.

to raise the sensitivity, spectral studies were performed with a modulated illumination of the samples. The resulting ac signal was detected and amplified in the lock-in mode. The photovoltage in the p-$Ga_{1-x}In_xAs_ySb_{1-y}$ ($x = 0.15$) solid solution was studied in two types of samples grown on n-GaSb:Te substrates: one type had an additional p-GaSb insulating sublayer and the other was without it. Figure 2 shows photovoltage spectra recorded at $T = 80$ and 300 K. The long-wavelength threshold of the curves corresponds to the intrinsic absorption edge. The band gap of the material is $E_g = 0.606$ eV at $T = 80$ K. The appearance of a low photovoltage at $T = 80$ K in the sample with the insulating sublayer ($p_{77} = 6 \times 10^{15}$ cm^{-3} and $\mu_{77} = 1950$ cm^2/(V s) (Fig. 2, curve *2*)) is related to a nonuniform distribution of compensating impurities and structural defects in the solid solution with $x = 0.15$. The growth of the solid solutions without the insulating sublayer leads to the formation of the structural defect $V_{Ga}Te$, due to the diffusion of Te from the substrate into the layer. These defects are nonuniformly distributed charged centers that form into clusters, which give rise to significant potential barriers in the bulk of the semiconductor. In the sample without the additional insulating sublayer ($p_{77} = 3.3 \times 10^{16}$ cm^{-3} and $\mu_{77} = 377$ cm^2/(V s) (Fig. 2, curve *1*)), in which Te diffusion was possible, the photovoltage was higher by more than an order of magnitude. This effect can be related to the considerable energy barriers in the material, which separate excess carriers by their field. It is necessary to note that the photovoltage decreases by an order of magnitude as the temperature increases (Fig. 2, curves *1* and *3*) due to the decreasing volume and height of the potential barriers and to an enhancement of the thermal ionization of the centers.

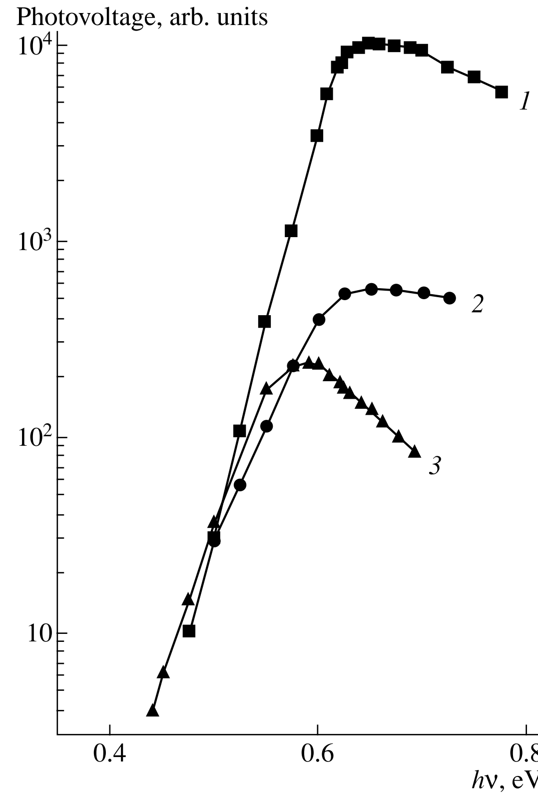

Fig. 2. Photovoltage spectra for $Ga_{1-x}In_xAs_ySb_{1-y}$ solid solutions ($x = 0.15$) grown without lead and (*1*, *3*) with no insulating sublayer and (*2*) with an insulating sublayer. (*1*, *2*) $T = 80$ K; (*3*) $T = 300$ K.

Furthermore, we discuss the results from studying the effect of the Te diffusion from the n-GaSb:Te substrate on the transport and photoelectric properties of the epitaxial layers of GaInAsSb solid solutions grown

Table

Sample no.	Sublayer	x	Thickness, μm	300 K				77 K					E_{A1}, eV	$K = \frac{N_D}{N_A}$	Photovoltage, arb. units	
				Conductivity type	σ, Ω^{-1} cm^{-1}	R, cm^3 C^{-1}	μ_{300}, cm^2 V^{-1} s^{-1}	Conductivity type	σ, Ω^{-1} cm^{-1}	R, cm^3 C^{-1}	μ_{77}, cm^2 V^{-1} s^{-1}	B_r			300 K	77 K
1	Yes	0.18	1.7	p	120	4.68	562	p	115	20.8	2400	1.0	0.023 0.07	0.1	3	5
2	No	0.18	5.0	p	46	5.6	233	p	14	26	366	5.2	0.02 0.06 0.11	0.61	11	25
3	No	0.18	2.0	n	–	–	2940	p	11	14.4	157	11.8	0.023 0.067	0.65	14	307
4	Yes	0.215	1.7	p	51	1.08	55	p	2.8	137.5	385	–	0.03 0.07	0.84	8	26
5	No	0.215	1.7	n	–	–	3330	n	–	–	450	–	–	–	11	360

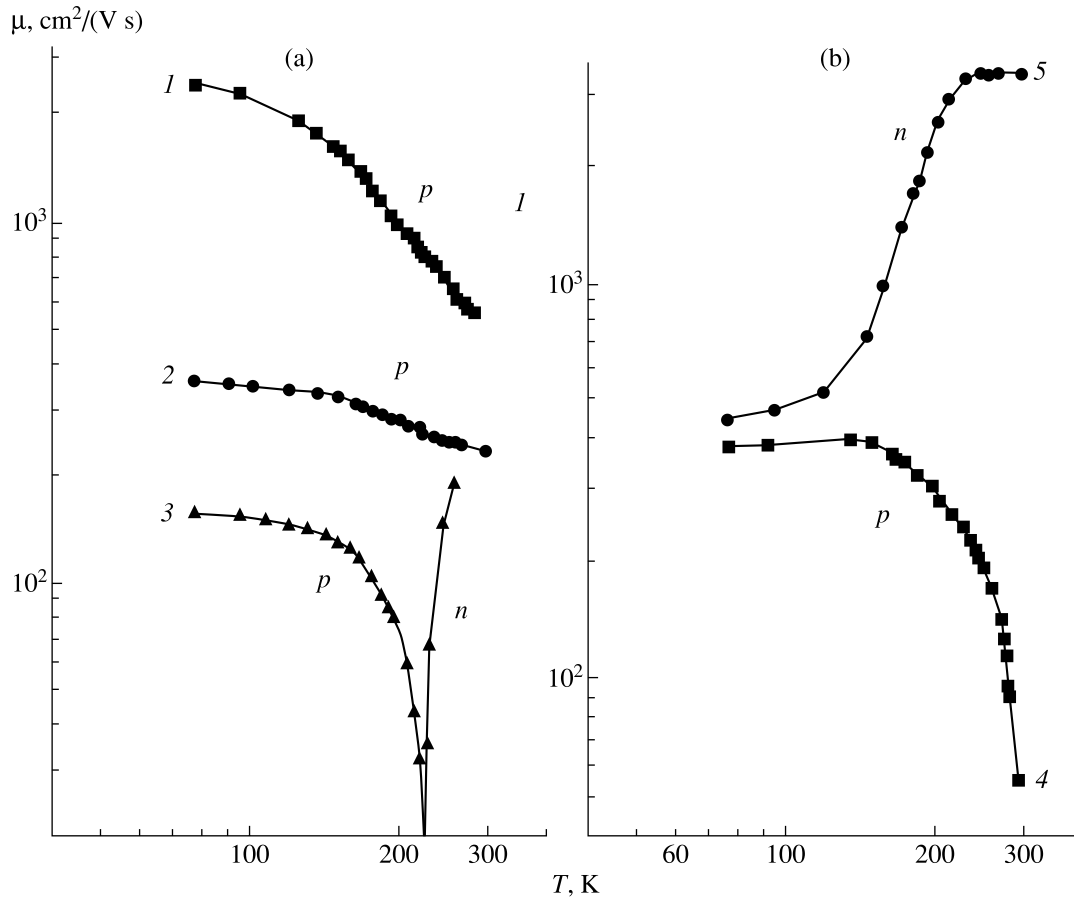

Fig. 3. Temperature dependences of the carrier mobility in $Ga_{1-x}In_xAs_ySb_{1-y}$ solid solutions grown in the presence of lead: (a) $x = 0.18$ and (b) $x = 0.215$. The curve numbers correspond to the sample numbers in the table.

from lead-containing melts, and compare the data with the properties of the solid solutions grown on the *n*-GaSb:Te substrate without the use of lead.

Lead plays an important role in obtaining $Ga_{1-x}In_xAs_ySb_{1-y}$ solid solutions with $x > 0.22$, because it makes it possible to produce solid solutions with the high In content $x = 0.22$–0.27 in a solid phase [3]. The band gap of these solid solutions is $E_g = 0.49$–0.52 eV ($T = 300$ K); therefore, they can be used in the fabrication of optoelectronic devices for the wavelength range $\lambda = 2.3$–2.7 μm.

As we have already shown in [3], $Ga_{1-x}In_xAs_ySb_{1-y}$ solid solutions grown from lead-containing melts on *n*-GaSb:Te substrates with an additional *p*-GaSb insulating sublayer (the sublayer was produced from a lead-containing melt, and its parameters were $p = 6 \times 10^{14}$ cm^{-3} at $T = 77$ k, $\rho \gtrsim 400$ Ω cm) demonstrate a minimum in their hole density at the In content $x = 0.22$ (Fig. 1, curve *2*). Taking into account the similarity of dependences *1* and *2* in Fig. 1, we can expect that the properties of $Ga_{1-x}In_xAs_ySb_{1-y}$ solid solutions grown from lead-containing melts will be more strongly affected by the Te diffusing from the substrate in the range of compositions $x \approx 0.22$.

Now we discuss the effect of the Te diffusion from the substrate on the properties of $Ga_{1-x}In_xAs_ySb_{1-y}$ solid solutions with $x = 0.18$ and 0.215 grown with the use of lead. Two series of samples were studied: epitaxial layers of solid solutions grown on the above-mentioned additional insulating sublayer (sample nos. 1 and 4 (see table)), and layers grown directly on the *n*-GaSb:Te substrate (sample nos. 2, 3, and 5). Under study were conductivity σ, the Hall factor *R*, mobility μ, transverse magnetoresistance $\left(\frac{\Delta\rho}{\rho}\right)^{\perp}$, and photovoltage at temperatures in the range $T = 77$–300 K. The results are listed in the table and shown in Figs. 3 and 4.

As can be seen from the table, a high hole mobility, $\mu_{77} = 2400$ cm²/(V s), governed by the scattering on impurity ions and lattice vibrations, is observed in the solid solution with $x = 0.18$ (sample 1). The temperature dependence of the Hall factor is revealed in the material levels with the activation energies $E_{A1} = 0.023$ eV and

$E_{A2} = 0.07$ eV. The magnetoresistance $\left(\frac{\Delta\rho}{\rho}\right)^{\perp}$ in sample no. 1 is not large: $B_r = \left(\frac{\Delta\rho}{\rho}\right)^{\perp} / \left(\frac{\mu H}{c}\right)^2 = 1$, longitudinal magnetoresistance is absent, and photovoltage is virtually absent.

Quite different behavior is observed for the same solid solution with $x = 0.18$ when it is grown without the additional sublayer, leading to the Te diffusion from the substrate into the solid solution. If the sample thickness is 5 μm (sample no. 2), Te does not penetrate across the entire layer thickness. In this case, p-type conduction is retained, but the mobility is lower than in sample no. 1, both at 77 and 300 K (Fig. 3a, cf. curves *2* and *1*). The transverse magnetoresistance $\left(\frac{\Delta\rho}{\rho}\right)^{\perp}$ increases, with $B_r = \left(\frac{\Delta\rho}{\rho}\right)^{\perp} / \left(\frac{\mu H}{c}\right)^2$ reaching a value of 5 and photovoltage appearing. All these effects indicate the presence of large inhomogeneities, which arise due to the penetration of Te from the substrate into the epitaxial layer. The strongest modification of the properties of the $Ga_{1-x}In_xAs_ySb_{1-y}$ solid solution (with $x = 0.18$ and no additional sublayer) is observed for a layer that is ~2 μm in thickness (sample no. 3). In this case, Te penetrates across the entire thickness, forming into large clusters. Due to the strong compensation, there is a change from p- to n-type conduction at $T > 200$ K. A very high photovoltage, reaching 307 arb. units, is observed at $T = 77$ K (see table). This value is much higher than in similar samples grown with the additional sublayer.

Now we consider $Ga_{1-x}In_xAs_ySb_{1-y}$ solid solutions with $x = 0.215$ (the layer thickness ~1.7 μm) grown from lead-containing melts either on the additional insulating sublayer (sample no. 4), or directly on the n-GaSb:Te substrate (sample no. 5). Sample no. 4 (Fig. 3b, curve *4*) demonstrates p-type conduction, but the mobility is much lower than in sample no. 1, which was grown on the additional sublayer (Fig. 3a, curve *1*). This is related to the fact that maximum compensation occurs at $x \approx 0.22$, which results in the strong inhomogeneity of the material (Fig. 1, curve *2*). The activation energies $E_{A1} = 0.03$ eV and $E_{A2} = 0.07$ eV can be determined from the temperature dependence of the Hall factor. The photovoltage in sample no. 4 was 26 arb. units at $T = 77$ K and 8 arb. units at $T = 300$ K.

In the GaInAsSb solid solutions with $x = 0.215$ grown directly on the n-GaSb:Te substrate (sample no. 5), n-type conduction is observed at $77 \text{ K} < T < 300$ K. The mobility at $T = 77$ K is $\mu_{77} = 450$ cm^2/(V s), and, at temperatures above 150 K, the Hall mobility sharply increases due to a transition to intrinsic conduction (Fig. 3b, curve *5*). The photovoltage at $T < 150$ K is 360 arb. units (Fig. 4, curve *5*). As the temperature increases, the photovoltage slowly decreases; it then falls sharply until, at $T = 300$ K, it reaches 11 arb. units. This temperature dependence is accounted for by the presence of potential barriers in the sample, which become lower as the temperature increases, and by an enhanced thermal ionization of the centers.

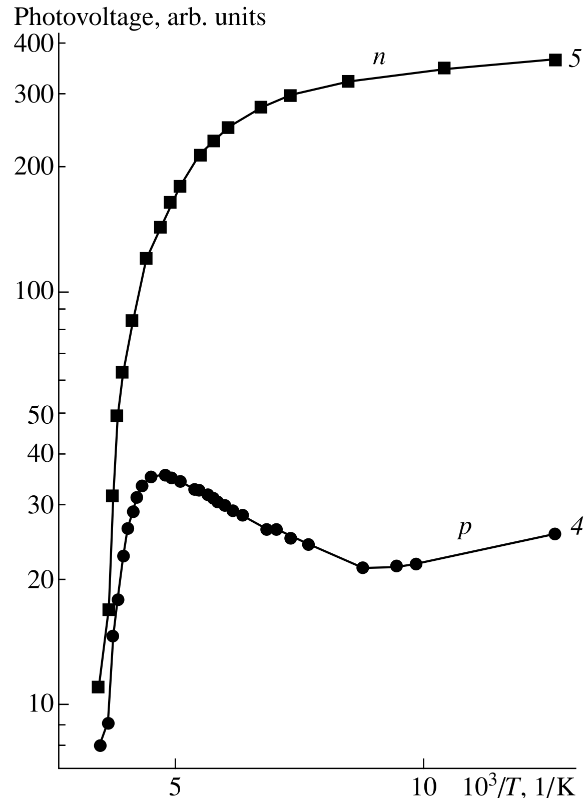

Fig. 4. Temperature dependences of the photovoltage for $Ga_{1-x}In_xAs_ySb_{1-y}$ solid solutions ($x = 0.215$) (*4*) with the insulating sublayer and (*5*) without it. The curve numbers correspond to the sample numbers in the table.

It is important to note that such a high photovoltage was observed only in the samples grown without the additional sublayer (Fig. 4, curve *5*). In the samples grown with the additional sublayer, the photovoltage was an order of magnitude lower (Fig. 4, curve *4*).

3. CONCLUSION

The effect of tellurium diffusion from an n-GaSb:Te substrate on the transport and photoelectric properties of $Ga_{1-x}In_xAs_ySb_{1-y}$ solid solutions grown without lead ($x = 0.15$), and from lead-containing melts ($x = 0.18$ and 0.215) was investigated.

The main results are as follows.

(1) The strongest effect of the Te diffusion from the substrate is observed in $Ga_{1-x}In_xAs_ySb_{1-y}$ solid solutions with the In content $x = 0.15$, produced without lead, and those with $x = 0.215$ obtained in the presence of lead, which have a low hole density and hole mobility.

(2) Tellurium diffusion from the *n*-GaSb:Te substrate into $Ga_{1-x}In_xAs_ySb_{1-y}$ solid solutions grown without the additional sublayer results in the generation of a high photovoltage under illumination in the spectral range of the intrinsic absorption. The highest photovoltage was observed at $T = 77$ K in thin samples with $x = 0.15$, grown without lead, and those with $x = 0.215$, fabricated in the presence of lead.

The observed effect of the appearance of photovoltage is in need of further detailed investigation, due to its possible relevance to the fabrication of high-sensitivity photocells.

REFERENCES

1. A. N. Baranov, A. N. Dakhno, B. E. Dzhurtanov, *et al.*, Fiz. Tekh. Poluprovodn. (Leningrad) **24**, 98 (1990) [Sov. Phys. Semicond. **24**, 59 (1990)].
2. A. N. Baranov, T. I. Voronina, A. N. Dakhno, *et al.*, Fiz. Tekh. Poluprovodn. (Leningrad) **24**, 1072 (1990) [Sov. Phys. Semicond. **24**, 676 (1990)].
3. T. I. Voronina, T. S. Lagunova, E. V. Kunitsyna, *et al.*, Fiz. Tekh. Poluprovodn. (St. Petersburg) **35**, 941 (2001) [Semiconductors **35**, 904 (2001)].

Translated by D. Mashovets

Semiconductors, Vol. 39, No. 3, 2005, pp. 313–316. Translated from Fizika i Tekhnika Poluprovodnikov, Vol. 39, No. 3, 2005, pp. 332–335.
Original Russian Text Copyright © 2005 by Berman.

SEMICONDUCTOR STRUCTURES, INTERFACES, AND SURFACES

Depolarization in a Metal–*p*-Ferroelectric–*n*-Semiconductor Structure

L. S. Berman

Ioffe Physicotechnical Institute, Russian Academy of Sciences, St. Petersburg, 194021 Russia

Submitted July 5, 2004; accepted for publication July 13, 2004

Abstract—The depolarization in a metal–*p*-ferroelectric–*n*-semiconductor structure is calculated based on an analysis of the experimental parameters of a ferroelectric hysteresis loop in a metal–ferroelectric–metal structure. For a semiconductor, the Poisson equation is solved using a standard method, while, for a ferroelectric, a numerical integration is applied. Two variants of semiconductor parameters are considered: (i) a thick *n*-type region (there is a region of electrical neutrality beyond a space-charge region), and (ii) a thin *n*-type region (an electric field penetrates all the way through this region). It is shown that depolarization significantly reduces ferroelectric polarization, and this reduction is stronger in the case of a semiconductor with lower doping. If the electric field penetrates all the way through the *n*-type region, depolarization decreases as the *n*-type region becomes thinner. © *2005 Pleiades Publishing, Inc.*

1. INTRODUCTION

At present, memory elements based on field-effect transistors (FETs) with a ferroelectric gate insulator are being intensively developed (see, e.g., [1–5]). One of the major difficulties encountered when developing FETs is depolarization, i.e., decreasing polarization P in the ferroelectric due to the formation of an opposite charge in a thin semiconductor layer and a voltage drop across this layer. Therefore, analysis of the depolarization in a metal–ferroelectric–semiconductor (MFS) structure and the search for ways to reduce it are currently topical areas of research. Several studies have been devoted to this problem [6–9]. In our own earlier study [10], the hysteresis in a metal–*p*-ferroelectic–*p*-semiconductor was simulated.

In this study, a theoretical analysis of the depolarization and hysteresis in a metal–*p*-ferroelectic–*n*-semiconductor is performed. One example of this kind of structure is the $PbZr_xTi_{1-x}O_3/SnO_2$:Sb structure used in FETs [11–13]. The advantages of these structures are the presence of a *p*–*n* junction, which limits reverse current, and a higher carrier mobility than in perovskite semiconductors.

2. FORMULATION OF THE PROBLEM

A gold layer, forming the Schottky barrier, is deposited onto the ferroelectric, and the contact of the semiconductor to the gold layer is ohmic. In a $PbZrTiO_3$ (PZT) ferroelectric, a passive (blocking) layer, whose thickness d_p is much less than the thickness of PZT [14, 15], can be formed under the gold layer.

Let the voltage drop in the passive layer be negligible; then, the relation

$$V + V_{bi} = \Psi_s + V_f \tag{1}$$

is valid. Here, V is the external bias, V_{bi} is the potential-contact difference between the contact to the ferroelectric and the contact to the semiconductor, Ψ_s is the potential of the semiconductor surface, and V_f is the voltage drop across the ferroelectric.

The inhomogeneity of the ferroelectric was taken into account using the parameters of an experimental hysteresis loop. The inhomogeneity of the semiconductor was considered using the average values of the donor concentration N_d and dielectric constant ε_s. We have assumed that only shallow acceptors are present in the ferroelectric and only donors in the semiconductor, and that defects are located at the interface between the ferroelectric and semiconductor (surface states).

On the interface, the relation

$$-(Q_{sc} + Q_{ss}) = \varepsilon_0 E_f + P(E_f) \tag{2}$$

is valid. Here, Q_{sc} is the charge in the space-charge region of the semiconductor, Q_{ss} is the charge of the surface states, $\varepsilon_0 = 8.85 \times 10^{-12}$ F/m is the permittivity of free space, E_f is the electric field in the ferroelectric, and $P(E_f)$ is the polarization in the ferroelectric at E_f.

We now consider the general case for research using an unsaturated hysteresis loop (Fig. 1). For this situation, we have approximated the $P(E_f)$ dependence with the following expressions [16]:

For an ascending branch,

$$P(E_f) = P_s \tanh\left(\frac{E_f - E_c}{2d}\right) + P_r(1 - a). \tag{3}$$

For a descending branch,

$$P(E_f) = -P_s \tanh\left(\frac{-E_f - E_c}{2d}\right) - P_r(1 - a), \tag{4}$$

1063-7826/05/3903-0313$26.00 © 2005 Pleiades Publishing, Inc.

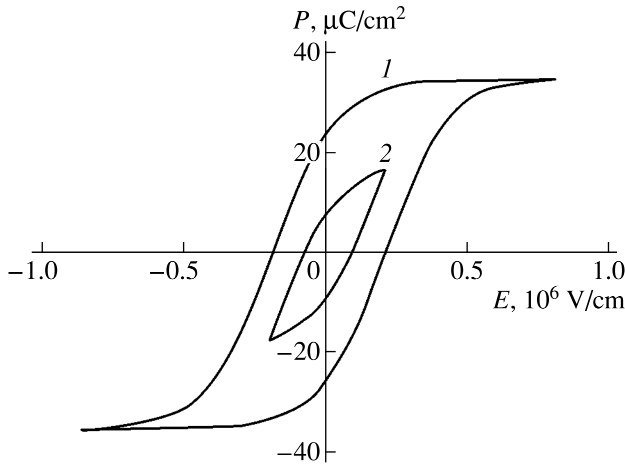

Fig. 1. Hysteresis loops for an MFM structure: (*1*) saturated, $P_s = 35\ \mu C/cm^2$, $P_r = 25\ \mu C/cm^2$, $E_c = 2 \times 10^5$ V/cm; and (*2*) unsaturated, $a = 0.5$.

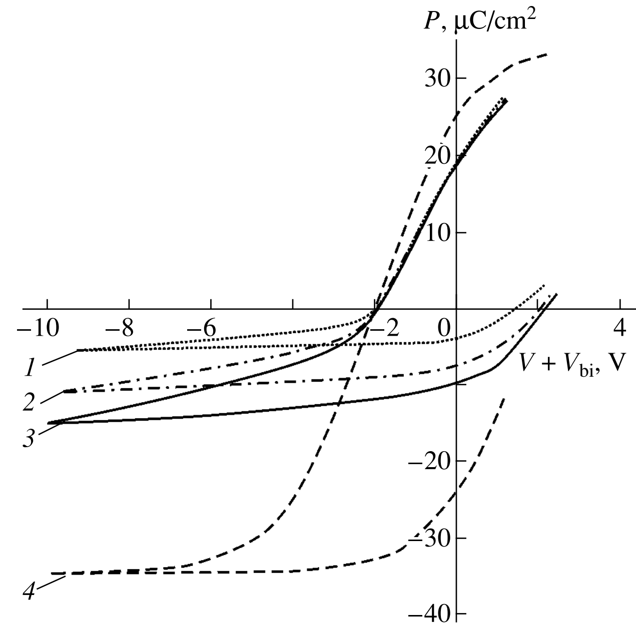

Fig. 2. Saturated hysteresis loops for the metal–*p*-ferroelectric–*n*-semiconductor structure at different donor concentrations ($N_{ss} = 0$). N_d: (*1*) 10^{19}; (*2*) 5×10^{19}; (*3*) 10^{20} cm^{-3}; (*4*) a ferroelectric with the same parameters but without impurities; an MFM structure with $w_f = 1000$ Å.

where P_s is the saturated polarization, P_r is the remanent polarization, E_c is the coercive field, and the coefficient $a \le 1$. At $a = 1$, Eqs. (3) and (4) change into equations for a saturated hysteresis loop [17]. In the calculation of the ascending branch, we use, along with Eq. (3), Eqs. (1)–(3) from [18].

The solution to the Poisson equation for a semiconductor is well known (see, e.g., [19]). For a ferroelectric, the Poisson equation is integrated numerically.

In the calculation, we used the following parameters of the ferroelectric: $P_s = 35\ \mu C/cm^2$, $P_r = 25\ \mu C/cm^2$, $E_c = 2 \times 10^5$ V/cm, the acceptor concentration $N_a = 10^{18}$ cm^{-3}, and the thickness of the ferroelectric $w_f = 1000$ Å. For the semiconductor, we set $\varepsilon_s = 10$, and the concentration of donors N_d is varied in the limits 10^{17}–10^{20} cm^{-3}.

To estimate the effect of the surface states on the shape of the hysteresis loop, we assume that the density of the surface states is constant across the entire width of the band gap. The characteristic time for a thermal emission of electrons from the surface states strongly (exponentially) depends on the ionization energy (see, e.g., [19]). Therefore, we assume that the charge of the surface states has enough time to follow the variation of the external bias for states with the ionization energy E below some critical value E_{cr} and fails to do so for states with energy above E_{cr}. We set $E_{cr} = 0.7$–0.8 eV.

3. CALCULATION RESULTS

We will discuss two possible variants of the semiconductor parameters.

1. The thickness of the space-charge region h is less than the n-type region thickness W. This situation is typical of the PZT/SnO_2 structure.

2. The space charge region extends across the n-type region as far as the base contact. In the general case, the field on the contact is not equal to zero. This situation can arise in the metal–p-PZT–metal structure when an n-type region is formed on p-PZT during the deposition of the contacts [20, 21].

We now take each case in succession and examine it.

3.1. $h < W$

Figure 2 shows the calculated dependences $P = f(V + V_{bi})$ for $N_{ss} = 0$ and three values of N_d (curves *1*–*3*). For comparison, curve *4* shows a hysteresis loop for a metal–ferroelectric–metal (MFM) structure with the same parameters of the ferroelectric but without impurities (curve *4*).

When the semiconductor surface is enriched ($\Psi_s > 0$), its properties are close to the properties of metal; therefore, at $\Psi_s > 0$, the portions of the descending branches of the MFM and metal–p-ferroelectric–n-semiconductor–metal structures are close to each other.

When the semiconductor surface is depleted ($\Psi_s < 0$), an increase in the bias leads to an increase in the magnitude of the semiconductor surface potential. Under such circumstances, the voltage across the ferroelectric and its polarization are only slightly changed. Therefore, the polarization of the metal–p-ferroelectric–n-semiconductor–metal structure is significantly less than the polarization of the MFM structure. This behavior is more clearly pronounced for semiconductors with

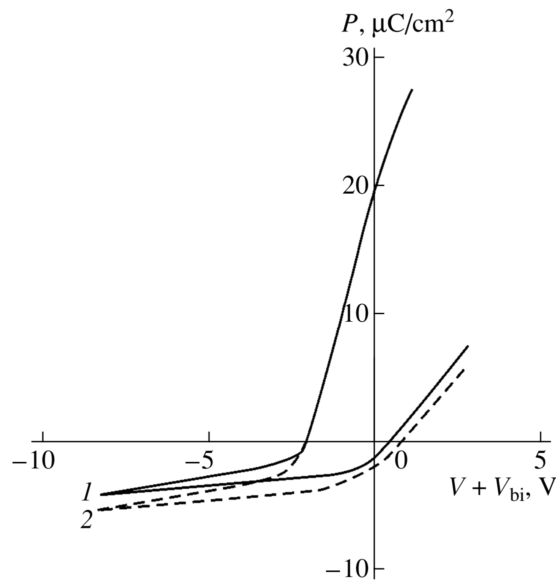

Fig. 3. Saturated hysteresis loops for the metal–p-ferroelectric–n-semiconductor structure at different densities of the surface states. N_{ss}: (*1*) 0 and (*2*) 10^{13} cm^{-2} eV^{-1}. N_d = 10^{19} cm^{-3}, w_f = 1000 Å.

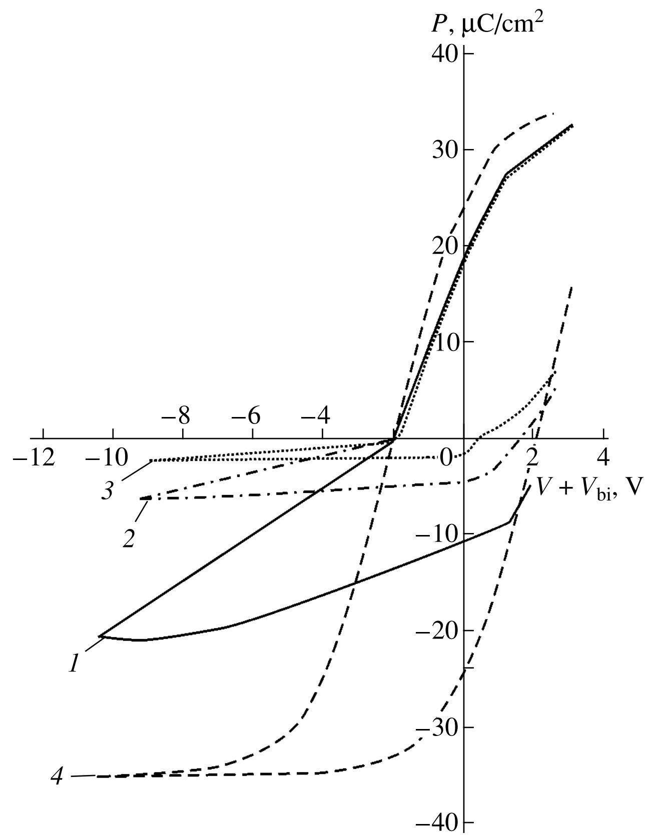

Fig. 4. Saturated hysteresis loops for N_{ss} = 0, w_f = 1000 Å, and N_d = 10^{17} cm^{-3}. W: (*1*) 30 and (*2*) 100 Å, (*3*) the space-charge region does not extend all the way through the n-type region (for curve *3*, the negative polarization is multiplied by 5), and (*4*) a ferroelectric with the same parameters but without impurities and an n-layer.

lower donor concentrations (cf curves *1*–*3* at a negative polarization). The dependences $P = f(V + V_{bi})$ for metal–p-ferroelectric–n-semiconductor–metal and metal–p-ferroelectric–p-semiconductor–metal structures are symmetric; moreover, in both structures, the remanent polarization (all the other factors being equal) has the same order of magnitude (cf the data from [10]). The hysteresis loops for the metal–p-ferroelectric–n-semiconductor–metal structure are qualitatively similar to the experimental hysteresis loop for the metal–p-(triglycine sulfate)–n-Si–metal structure [9], which confirms the validity of our method.

The hysteresis loops were calculated for two surface-state densities: $N_{ss} = 0$ and $N_{ss} = 10^{13}$ cm^{-2} eV^{-1} (at $N_d = 10^{19}$ cm^{-3}) (see Fig. 3). At h = 100 Å, the density of the surface states $N_{ss} = 10^{13}$ cm^{-2} eV^{-1} corresponds to the concentration of traps in the space-charge region $N_t = N_{ss}E_{cr}/h = 0.8 \times 10^{19}$ cm^{-3}. As can be seen from the results of the calculation, at $N_t < N_d$, the surface states exert only a slight effect on the parameters of the hysteresis loop.

3.2. h = W

The space-charge region extends across the n-type region. In this case, w_f is the thickness of the ferroelectric without an n-layer. Figure 4 shows the calculated dependences $P = f(V + V_{bi})$ for $N_{ss} = 0$ and $N_d = 10^{17}$ cm^{-3} at W = 30 and 100 Å. For comparison, the dependence $P = f(V + V_{bi})$ for a case in which the space charge region does not extend across the entire n-type region is also shown (see Section 3.1, Fig. 4, curve *3*).

When the semiconductor surface is enriched, the dependences $P = f(V + V_{bi})$ are close for three values of W due to the electron density on the interface approaching the electron density in the metal.

When the semiconductor surface is depleted, the parameters of the structure approach the parameters of the MFM structure without an n-layer as the thickness of its n-layer decreases. Therefore, as the n-layer thickness decreases, the depolarization also decreases (cf Fig. 4, curves *1*–*3*).

4. CONCLUSION

The depolarization of a metal–p-ferroelectric–n-semiconductor structure, in which the semiconductor parameters are varied, is analyzed based on the experimental data on a hysteresis loop for an MFM structure.

The Poisson equation for the semiconductor is solved using a standard method, while, for the ferroelectric, a numerical integration is applied.

Two variants of semiconductor parameters were considered:

(i) The thick n-type region with a region of electrical neutrality beyond a space-charge region. In this case, the depolarizing effect of the semiconductor leads to a significant decrease in the polarization of the ferroelectric, with this reduction being stronger for a high-resistivity semiconductor. The concentration of the donors in the semiconductor can be estimated from the hysteresis loop in the case of depletion.

(ii) A thin n-type region with an electric field penetrating all the way through it as far as the contact. In this case, the depolarization is reduced as the n-type region thickness decreases. The n-type region thickness can be estimated from the parameters of the hysteresis loop in the case of depletion.

ACKNOWLEDGMENTS

The study was supported by the Russian Foundation for Basic Research (project no. 00-15-96770).

The author is grateful to I.V. Grekhov for the formulation of the problem and discussion of the results.

REFERENCES

1. J. F. Scott and D. A. Araujo, Science **246**, 1400 (1989).
2. Y. Watanabe, Y. Matsumoto, and M. Tanamura, Jpn. J. Appl. Phys., Part 1 **34**, 5254 (1995).
3. Y. Watanabe, Phys. Rev. B **59**, 11257 (1999).
4. W. Wu, K. H. Wong, C. L. Mak, *et al.*, J. Appl. Phys. **88**, 2068 (2000).
5. Y. T. Kim and D. S. Shin, Appl. Phys. Lett. **71**, 3507 (1997).
6. B. M. Vul, G. M. Guro, and I. I. Ivanchik, Fiz. Tekh. Poluprovodn. (Leningrad) **4**, 162 (1970) [Sov. Phys. Semicond. **4**, 128 (1970)].
7. R. R. Mehta, B. D. Silverman, and J. T. Jacobs, J. Appl. Phys. **44**, 3379 (1973).
8. I. P. Batra and P. Wurfel, Phys. Rev. B **8**, 3257 (1973).
9. P. Wurfel and I. P. Batra, Phys. Rev. B **8**, 5126 (1973).
10. L. S. Berman, Fiz. Tekh. Poluprovodn. (St. Petersburg) **35**, 200 (2001) [Semiconductors **35**, 193 (2001)].
11. M. W. Prins, K. O. Grosse-Holz, G. Muller, *et al.*, Appl. Phys. Lett. **68**, 3650 (1996).
12. M. W. Prins, S. E. Zinnemers, J. F. M. Cillessen, *et al.*, Appl. Phys. Lett. **70**, 458 (1997).
13. M. W. Prins, K. O. Grosse-Holz, J. F. M. Cillessen, *et al.*, J. Appl. Phys. **83**, 888 (1998).
14. J. M. Benedetto, R. A. Moore, and F. B. McLean, J. Appl. Phys. **75**, 460 (1994).
15. P. K. Larsen, G. J. M. Dormans, D. J. Taylor, and P. J. van Veldhoven, J. Appl. Phys. **76**, 2405 (1994).
16. L. S. Berman and I. E. Titkov, Fiz. Tekh. Poluprovodn. (St. Petersburg) **38**, 710 (2004) [Semiconductors **38**, 683 (2004)].
17. S. L. Miller, J. P. Schwank, R. D. Nasby, and M. S. Rodgers, J. Appl. Phys. **68**, 6463 (1990).
18. S. L. Miller, J. R. Schwank, R. D. Nasby, and M. S. Rodgers, J. Appl. Phys. **70**, 2849 (1991).
19. S. M. Sze, *Physics of Semiconductor Devices*, 2nd ed. (Wiley, New York, 1981; Mir, Moscow, 1984), Vol. 1.
20. J. F. M. Cillessen, M. W. J. Prins, and R. M. Wolf, J. Appl. Phys. **81**, 2777 (1997).
21. V. P. Afanasjev, A. A. Petrov, I. P. Pronin, and E. A. Tarakanov, J. Phys.: Condens. Matter **39** (13), 138 (2001).

Translated by D. Mashovets

Semiconductors, Vol. 39, No. 3, 2005, pp. 317–324. Translated from Fizika i Tekhnika Poluprovodnikov, Vol. 39, No. 3, 2005, pp. 336–342.
Original Russian Text Copyright © 2005 by Karavaev, Chernyshov.

SEMICONDUCTOR STRUCTURES, INTERFACES, AND SURFACES

A Model for Describing Hole Scattering at GaAs/AlAs(001) Heterointerfaces

G. F. Karavaev and V. N. Chernyshov^

Siberian Physicotechnical Institute, Tomsk State University, Tomsk, 634050 Russia

^e-mail: vnchern@elefot.tsu.ru

Submitted May 31, 2004; accepted for publication July 14, 2004

Abstract—The wave functions of the states in a valence band are analyzed based on an 18-band **kp** model. It is found that the conventionally used approximation of energy-independent effective masses for bands of light and heavy holes is valid only near the valence-band top. The matching conditions for the envelope functions of holes at GaAs/AlAs(001) interfaces are considered both with and without an allowance being made for the spin–orbit interaction of energies in the vicinity of the valence-band top. These conditions are obtained based on a simplification of the description of electronic states provided by the pseudopotential method. It is shown that light and heavy holes are mixed at a heterointerface. The obtained matching conditions are completely consistent with the symmetry of the problem. In these conditions, envelope functions are mixed with their normal derivatives and the derivatives are mixed with the functions. The parameters describing the mixing of light and heavy holes at the heterointerface are rather small, which is consistent with recent calculations by other authors but contradicts earlier assumptions and estimates. *© 2005 Pleiades Publishing, Inc.*

At present, there is considerable interest in studying the hole states in nanostructures. This interest is supported both by the necessity of considering general problems in the behavior of elementary excitations in structures with heterointerfaces and by the great number of practical needs requiring a description of the electrical, optical, and other properties of nanostructures, in which electrons and holes interact with heterointerfaces.

There are substantial distinctions to be made when descripting electron and hole scattering in the most widely used GaAs/AlAs heterostructures. Electrons usually only occupy the conduction band. Therefore, when considering electron scattering at heterointerfaces, in a certain energy range below the conduction band bottom for AlAs, we can, in principle, restrict ourselves to a single-band method of the effective mass [1]; however, the matching conditions for envelope functions need to be determined more exactly. It is clear that, for higher energies, it is necessary to take into account the mixing of different states in the conduction bands of GaAs and AlAs. To describe this mixing, various models for the matching of envelope functions have been developed [2–5]. The splitting of the conduction band caused by spin–orbit interactions is insignificant; therefore, we can disregard it.

When describing the hole states, in contrast with the electrons, it is necessary to make an allowance for the spin–orbit interaction and, also, the fundamentally multiband character of the valence band. In terms of spin, there are six valence bands in a narrow energy range in the vicinity of the valence band top (E_v). These are the bands of heavy holes, bands of light holes, and spin–split-off bands. Therefore, a model describing the matching of the envelope functions of holes should initially be of a multiband type.

There have been a series of studies devoted to the development of theoretical models and their subsequent application to a description of hole scattering at heterointerfaces. These studies were carried out mainly in the context of a method employing envelope functions, since this method makes it possible to consider the complex phenomena occurring in heterostructures using relatively simple means [6–15]. Certain studies were carried out in the context of a tight-binding method [16] or using a pseudopotential method [17]. However, there are still no studies establishing the relation between these different approaches, although the necessity of such studies is considered important [6, 14, 15]. In all these studies [6–15], the use of the envelope-function method is accompanied by a postulation of one or another form of the matching conditions at the heterointerface. Most often, it is considered that the envelope functions are continuous at the heterointerface, while the matching conditions of their derivatives can be found by integrating the set of equations for the envelope functions over a short interval, which includes the heterointerface. Such an approach leads to the result that no mixing of the states of light and heavy holes with zero wave vectors parallel to the heterointerface occurs at the (001) heterointerface [6]. However, similar mixing is not forbidden by the symmetry of the structure, while the experimentally found giant anisotropy of the exchange splitting of excitonic levels can be attributed to the presence of such mixing. In order to interpret these experiments, the authors of studies [6, 18, 19] suggested introducing a term (into the

matching conditions of the derivatives of envelope functions) responsible for the mixing of light and heavy holes at the heterointerface and estimated its magnitude by comparison with the experiments and calculations of other authors.

As far as we know, no direct analysis of the matching conditions for the envelope functions of holes at the GaAs/AlAs interface was carried out. In this study, we tried to compensate for this lack by making an allowance for the great interest in this problem and the important conclusions obtainable based on the previously suggested models.

Let us briefly recall the main ideas of the method for finding the boundary conditions of envelope functions. We previously used this method for the states in the conduction band [3, 5]. The method was developed without an being allowance made for the spin–orbit interaction. We now consider a heterostructure that includes several layers. Let us number these layers with the number l in the order in which they are arranged from right to left. In a model with a discontinuous potential at the interface, the general solution to the Schrödinger equation Ψ^l in a medium with the number l at fixed values of energy E and the component of the wave vector $\mathbf{k}_{\parallel}$ parallel to the heterointerface can be written as

$$\Psi^l = \sum_{\nu} C_{\nu}^l \Psi_{\mathbf{k}_\nu}^l, \tag{1}$$

where $\mathbf{k}_\nu = \mathbf{k}_{\parallel} + \mathbf{k}_{\perp\nu}$ are the wave vectors for the subsystem with the number l; $\mathbf{k}_{\perp\nu}(E, \mathbf{k}_{\parallel})$ are the vectors normal to the interface, which can be found from a consideration of the so-called complex band structure; and $\Psi_{\mathbf{k}_\nu}^l$ are the partial solutions to the Schrödinger equation for the lth medium, which are numbered by the vector $\mathbf{k}_\nu$. The number of various partial solutions in expansion (1) depends on the basis used for the representation of the wave functions. This number equals $2\nu_{\max}$, where $\nu_{\max}$ is the number of various independent projections of basis functions on the heterointerface plane.

The requirement for the equality of wave functions and their normal derivatives is used to determine the $2\nu_{\max}$ relations at each heterointerface. This requirement is imposed on the coefficients, for example, C_ν^1 and C_ν^2:

$$\mathbf{C}^1 = \mathbf{I}(z_0)\mathbf{C}^2, \tag{2}$$

where $\mathbf{C}$ is a column vector with the components C_ν; and $\mathbf{I}(z_0)$ is the so-called matching matrix at the interface $z = z_0$, which separates media 1 and 2. In principle, relations of type (2), along with the conditions at infinity, are sufficient to solve a quantum problem for structures of any complexity. However, the large rank of the matrix $\mathbf{I}(z_0)$ and its strong energy dependence hamper the use of this approach.

Let us turn to a description of our method for constructing simplified models. These models are based on the envelope-function method for the heterostructures. This approximation is substantiated by the fact that the difference in the potential energy of the electrons located in various crystals is often significantly lower than the variations in the potential energy of the electrons within the unit cell of a bulk crystal.

Let us write general solution (1) as a sum by using the bands m and reference points $\mathbf{k}_{\nu_0}$ of the Brillouin zone for the heterointerfaces parallel to the (001) plane:

$$\Psi^l = \exp[i(q_x x + q_y y)] \sum_{m\nu_0} F_{\nu_0 m}^l(z) |\mathbf{K}_{\nu_0 m}^l\rangle, \tag{3}$$

where $\mathbf{q}_\nu = \mathbf{k}_\nu - \mathbf{k}_{\nu_0}$ and $|\mathbf{K}_{\nu_0 m}^l\rangle$ are the Bloch wave functions at the points $\mathbf{k}_{\nu_0}$. These reference points ($\mathbf{k}_{\nu_0}$) can be arbitrary; however, it is more convenient to select them so that they are equal to the magnitudes of the wave vectors at the bottom of different valleys. Thus, the totality of the points $\mathbf{k}_{\perp\nu}$ can be divided into several groups, each of which has an eigenvalue of $\mathbf{k}_{\nu_0}$. It is clear that the functions $F_{\nu_0 m}^l(z)$ have the meaning of envelope functions. From relations (1) and (3), it is also clear that the functions $F_m^l(z)$, where the subscript ν_0 is hereinafter omitted, can take the form

$$F_m^l(z) = \sum_{\nu} C_\nu^l D_m^l(\mathbf{k}_\nu) \exp(i q_{z\nu} z), \tag{4}$$

where the coefficients of expansion, $D_m^l(\mathbf{k}_\nu)$, can be found from the set of algebraic equations belonging to the $\mathbf{kp}$ method. Assuming, in relation (3), that $z = z_0$, the relation of the envelope functions and their derivatives to the coefficients C^l can be represented in a matrix form as

$$\mathbf{F}^l(z_0) = \Phi^l(z_0)\mathbf{C}^l, \tag{5}$$

where $\mathbf{F}$ is a column vector of the rank $2m_{\max}$ with the components $F_m(z_0)$ and $F_m'(z_0)$; and Φ^l is a matrix of the rank $2m_{\max} \times 2\nu_{\max}$, whose matrix elements are easily determinable using relations (3) and (4). Here, $m_{\max}$ is the number of valleys taken into account in expansion (3). When carrying out numerical calculations, for example, by the pseudopotential method, $\nu_{\max} < m_{\max}$. Therefore, the number of envelope functions and their derivatives in relation (5) exceeds the number of different arbitrary coefficients C_ν^l.

It is clear that unambiguous matching conditions for the envelope functions can be obtained from matching conditions (2) only for wave functions in square matrices Φ, i.e., it is necessary to select different variables F_m^l in the quantity $\nu_{\max}$ in general solution (3). In this case, we use relation (2) to obtain

$$\mathbf{F}^1(z_0) = \mathbf{T}(z_0)\mathbf{F}^2(z_0), \tag{6}$$

where the matching matrix **T** for envelope functions takes the form

$$\mathbf{T}(z_0) = \mathbf{\Phi}^1(z_0)\mathbf{I}(z_0)[\mathbf{\Phi}^2(z_0)]^{-1}. \quad (7)$$

The adequacy of the matching conditions for envelope functions (6) in the problem to be solved can be determined from an analysis of relations (4)–(7) for each particular case.

The problem of determining the matching conditions for the envelope functions is significantly simplified by the fact that quantum states are only of interest in a narrow energy range, where the number $2\nu_m$ of different significant coefficients C_ν^n is rather small compared with $2\nu_{\max}$. This circumstance follows from the fact that the matrix $\mathbf{I}(z_0)$ is almost quasi-diagonal, and the block of the rank $(2\nu_m \times 2\nu_m)$ $(\nu_m \ll \nu_{\max})$, which links these C_ν^n, can be separated in this matrix in a highly accurate manner. Therefore, it is sufficient to introduce the ν_m envelope functions and to consider the quantity **F** in expression (6) to be a column vector with the components $F_m(z_0)$ and $F'_m(z_0)$ $(m = 1, \ldots, \nu_m)$. In this case, the matching matrix of the envelope functions $\mathbf{T}(z_0)$ of the rank $(2\nu_m \times 2\nu_m)$ depends only slightly on energy. As a result, the initial problem is substantially simplified and a corresponding model appears.

Thus, there are two main problems to be solved to obtain sufficiently accurate boundary conditions in a model of envelope functions:

(i) The number ν_m of envelope functions that appear in the boundary conditions should be determined. This quantity can be determined from an analysis of matching matrices (2), which are obtained using numerical calculations within the pseudopotential method, and depends on the orientation of the heterointerfaces, on the energy range, and on the magnitudes of the components of the wave vector $\mathbf{k}_\parallel$ parallel to the heterointerfaces.

(ii) The **kp** model for the calculation of the band structure should be rather simple. Nevertheless, this model should still accurately reproduce the data of the pseudopotential calculations for the above-mentioned most important branches of a complex band structure. However, it should be noted that, in this case, so-called fictitious solutions emerge. These solutions do not satisfy the conditions for the applicability of an approximate **kp** model, and they are absent in more exact models. Therefore, they should be rejected and disregarded when constructing general solutions. Note that, when constructing the **kp** model for the calculation of the band structure, the number of the valleys $m_{\max}$ taken into account in expansion (3) can be larger than ν_m. However, only the ν_m envelope functions appear in matching conditions (6).

The above-considered approach can be generalized to the case of the spin–orbit interaction. Then, the partial solutions $\Psi^l_{\mathbf{k}_\nu}$ and the basis functions $|\mathbf{K}^l_{\nu_0 m}\rangle$ become two-component spinors, while the ranks of the matrices $\mathbf{I}(z_0)$ and $\mathbf{T}(z_0)$ are doubled.

In this study, we restricted ourselves to a simpler algorithm to take into account the spin–orbit interaction. At the first stage of the calculations, we determined the matching matrices of the envelope functions $\mathbf{T}(z_0)$ and the basis functions $|\mathbf{K}^l_{\nu_0 m}\rangle$ and disregarded the spin–orbit splitting. We then constructed a corresponding **kp** model for the calculation of the band structure in the basis of the functions $|\mathbf{K}^l_{\nu_0 m}\rangle\alpha$ and $|\mathbf{K}^l_{\nu_0 m}\rangle\beta$, where α and β are the two-component spinors that have projections of the spin σ_z on the axis z equal to 1/2 and –1/2, respectively:

$$\alpha = \begin{pmatrix} 1 \\ 0 \end{pmatrix}, \quad \beta = \begin{pmatrix} 0 \\ 1 \end{pmatrix}.$$

In this approach, the **kp** Hamiltonian operator is a matrix of the rank $(2m_{\max} \times 2m_{\max})$:

$$H_{\mathbf{kp}} = H^0_{\mathbf{kp}} + H_{\mathrm{SO}}, \quad (8)$$

$$H^0_{\mathbf{kp}} = \begin{pmatrix} \bar{H}^0_{\mathbf{kp}} & 0 \\ 0 & \bar{H}^0_{\mathbf{kp}} \end{pmatrix}. \quad (9)$$

Here, $\bar{H}^0_{\mathbf{kp}}$ is the **kp** Hamiltonian operator in which the spin–orbit interaction is disregarded, and H_{SO} is the matrix of the operator of the spin–orbit interaction.

We carried out the pseudopotential calculations and constructed models of the envelope functions for the GaAs/AlAs(001) heterostructures at $\mathbf{k}_\parallel = 0$. We choose $\mathbf{k}_\parallel$ because the hole states for these materials are mainly located in the vicinity of the point Γ; Γ_{15} is the state in which the spin is disregarded. The other valleys (X and L) are located either considerably lower (with respect to the energy) in the valence band or considerably higher in the conduction band. Therefore, the states of these valleys are not considered in the **kp** model and the corresponding envelope functions are absent in the boundary conditions. Consequently, the subscript ν_0 in the functions $|\mathbf{K}^l_{\nu_0 m}\rangle\alpha$ and $|\mathbf{K}^l_{\nu_0 m}\rangle\beta$ corresponds only to different Γ states. Therefore, the subscript ν_0 will hereafter be omitted.

When constructing the **kp** model in which the spin is disregarded, we took into account the states Γ_{15v}, Γ_{1c}, Γ_{15c}, and Γ_{12c}. Here, indices v and c indicate that the states belong to the valence band and the conduction band. Thus, if an allowance is made for these states, the $\bar{H}^0_{\mathbf{kp}}$ matrices are of the rank (9×9), while the $H^0_{\mathbf{kp}}$ and $H_{\mathbf{kp}}$ matrices are of the rank (18×18). We took into

account the following matrix elements of the operator of the spin–orbit interaction:

$$\langle X_v|H_{SO}|Y_v\rangle = -i\Delta_0/3; \quad \langle X_c|H_{SO}|Y_c\rangle = -i\Delta_1/3; \quad \langle X_v|H_{SO}|Y_c\rangle = -i\bar{\Delta}/3. \tag{10}$$

Here, $|X_v\rangle$, $|Y_v\rangle$, $|X_c\rangle$, and $|Y_c\rangle$ are the states of the symmetry Γ_{15} belonging to types X and Y. Using the symmetry properties, we can easily obtain other matrix elements (H_{SO}) from relations (10). Our studies show that the role of the states Γ_{12c} in the case of the heterointerface under consideration is insignificant, and the matrix elements $\langle X_v|H_{SO}|\Gamma_{12c}\rangle$ and $\langle X_c|H_{SO}|\Gamma_{12c}\rangle$ can be disregarded.

The values of the parameters Δ_0, Δ_1, and $\bar{\Delta}$ are well known from various publications [20, 21]. We used the following values in our calculations: Δ_0 = 0.341 eV, Δ_1 = 0.171 eV, and $\bar{\Delta}$ = –0.061 eV for GaAs; Δ_0 = 0.30 eV, Δ_1 = 0.15 eV, and $\bar{\Delta}$ = –0.05 eV for AlAs.

The matching conditions for the envelope functions take form (6), in which **F** is a column vector with the components $F_m(z_0)\alpha$, $F_m(z_0)\beta$ and $F'_m(z_0)\alpha$, $F'_m(z_0)\beta$ ($m = 1, \ldots, \nu_m$). We do not assume that there is an additional mixing of the states by the heterointerfaces as a result of the spin–orbit interaction. Consequently, the matching matrix for the envelope functions in which an allowance is made for the spin–orbit interaction $\mathbf{T}(z_0)$ takes the form

$$\mathbf{T} = \begin{pmatrix} \bar{T}_{11} & 0 & \bar{T}_{12} & 0 \\ 0 & \bar{T}_{11} & 0 & \bar{T}_{12} \\ \bar{T}_{21} & 0 & \bar{T}_{22} & 0 \\ 0 & \bar{T}_{21} & 0 & \bar{T}_{22} \end{pmatrix}, \tag{11}$$

where $\bar{T}_{ij}$ ($i, j = 1, \ldots, \nu_m$) are the blocks of the matrix $\bar{\mathbf{T}}(z_0)$, which are found when solving the problem in which the spin–orbit interaction is disregarded. The block $\bar{T}_{11}$ corresponds to the matching of the envelope functions for the states $|\mathbf{K}_m^l\rangle\,\alpha$ and $|\mathbf{K}_m^l\rangle\,\beta$ at $m = 1, \ldots, \nu_m$; the block $\bar{T}_{22}$ corresponds to the matching of their derivatives; and the blocks $\bar{T}_{12}$ and $\bar{T}_{21}$ correspond to the matching of the functions with the derivatives and vice versa.

When solving various problems in which the spin–orbit interaction is taken into account, eigenfunctions of the angular-momentum operator $|j, m_j\rangle$, (j = 3/2, 1/2; $m_j = \pm 1/2, \ldots, \pm j$) are often used instead of functions that have certain values for projections of the spin onto the axis z $|\mathbf{K}_m^l\rangle\,\alpha$ and $|\mathbf{K}_m^l\rangle\,\beta$. In particular, instead of the functions of the states Γ_{15v}:

$$|X_v\rangle\alpha, \quad |Y_v\rangle\alpha, \quad |Z_v\rangle\alpha, \quad |X_v\rangle\beta, \quad |Y_v\rangle\beta, \quad |Z_v\rangle\beta, \tag{12}$$

we can use their linear combinations:

$$\begin{aligned} |3/2, 3/2\rangle &= (1/\sqrt{2})(X_v + iY_v)\alpha, \\ |3/2, -3/2\rangle &= (1/\sqrt{2})(X_v - iY_v)\beta, \\ |3/2, 1/2\rangle &= (1/\sqrt{6})[(X_v + iY_v)\beta - 2Z_v\alpha], \\ |3/2, -1/2\rangle &= (1/\sqrt{6})[(X_v - iY_v)\alpha + 2Z_v\beta], \\ |1/2, 1/2\rangle &= (1/\sqrt{3})[(X_v + iY_v)\beta + Z_v\alpha], \\ |1/2, -1/2\rangle &= (1/\sqrt{3})[-(X_v - iY_v)\alpha + Z_v\beta]. \end{aligned} \tag{13}$$

It is known that the first four functions from set (13) form the basis of the representation Γ_8 of the double group T_d^2, and the last two last are the basis functions of the representation Γ_7. Corresponding linear combinations can also be constructed from the functions of the state Γ_{15c}. We will hereafter denote these functions with the subscript c for the functions $|j, m_j\rangle_c$.

Let us now consider the obtained results. The electron scattering by heterointerfaces was studied within an approximation of the discontinuous pseudopotential at the heterointerfaces using the scattering matrix method [3, 5, 22]. The complex band structure was determined by the empirical pseudopotential method. The calculation techniques were previously described in detail in [3, 5]. For the calculations, we used the pseudopotential values reported in [23]. The calculations were carried out in the energy range from 0 to –0.5 eV. The energy was measured from the valence-band top for GaAs. In the matching matrices for the envelope functions discussed below, the matrix elements are given in atomic units. It was assumed that GaAs is located on the left of AlAs, and, therefore, the heterointerface was chosen to pass over the common plane consisting of As atoms.

An analysis of the matching matrices $\mathbf{I}(z_0)$ showed that, with the spin–orbit interaction disregarded for energies in the vicinity of the valence-band top, the symmetry band Δ_1 and the doubly degenerate band $\Delta_3 + \Delta_4$ make the main contribution to the matching conditions for wave functions. It was shown that when we use the above-mentioned nine-band **kp** model, these branches, the most important branches of a complex band structure, accurately reproduce the data of the pseudopotential calculations. The matching conditions for the envelope functions include three Γ_{15}-type states:

$$|Z_v\rangle, \quad |(X_v + Y_v)\rangle/\sqrt{2}, \quad |(X_v - Y_v)\rangle/\sqrt{2}. \tag{14}$$

Let **F** be a column vector with the components $F_m(z_0)$ and $F'_m(z_0)$, $m = 1, 2, 3$, which are arranged in an order corresponding to set (14). According to the problem symmetry (group C_{2v}), the matching matrix for the envelopes $\bar{T}$ of the rank (6 × 6) is divided into three quasi-diagonal blocks of the rank (2 × 2), which correspond to the states Δ_1, Δ_3, and Δ_4. The numerical values of the matrix elements t_{ij} ($i, j = 1, \ldots, 6$) belonging to the matrix $\bar{\mathbf{T}}$ can be determined using relation (7) with subsequent averaging over the energy. We found that $t_{11} = 1.045$ and $t_{22} = t_{33} = 1.048$. The deviation of these numbers from unity is caused by differences in the wave functions of the states Γ_{15v} for GaAs and AlAs and indicates that the envelope functions at the heterointerface are discontinuous. The derivatives of the envelope functions for different materials are mutually related via the matrix elements $t_{44} = 0.618$ and $t_{55} = t_{66} = 1.099$. These numerical values reflect the difference in effective masses for GaAs and AlAs. The relation between the envelope functions with the symmetry $\Delta_3(\Delta_4)$ and their derivatives, and vice versa, is given via the matrix elements $t_{25} = -t_{36} = -0.297$ and $t_{52} = -t_{63} = -0.0059$, respectively. We will see that, in what follows (making an allowance for the spin–orbit interaction), it is precisely these matrix elements that determine the mixing of the states of light and heavy holes. According to the problem symmetry, the other elements of the matrix $\bar{\mathbf{T}}$ are equal to zero. Calculations of the hole transmittances for various structures with quantum wells and barriers showed the adequacy of the suggested model.

Let us now consider the results in terms of the spin–orbit interaction. There are three doubly degenerate symmetry bands Δ_5 of a double group in the energy region in the vicinity of E_v. These are the band of heavy holes (h); the band of light holes (l); and the band (s) split off due to spin–orbit interaction and located at $k = 0$ lower in energy by a value close to Δ_0. The matching matrix for the envelopes **T** of the rank (12 × 12) in the basis of the functions

$$|Z_v\rangle\alpha, \quad |Z_v\rangle\beta, \quad (1/\sqrt{2})|X_V + Y_V\rangle\alpha,$$
$$(1/\sqrt{2})|X_v + Y_v\rangle\beta, \quad (1/\sqrt{2})|X_v - Y_v\rangle\alpha, \qquad (15)$$
$$(1/\sqrt{2})|X_v - Y_v\rangle\beta$$

can be obtained from $\bar{\mathbf{T}}$ using matrix (11).

It is more convenient to carry out an analysis of the wave functions, the corresponding envelope functions, and their matching conditions in the basis of the functions $|j, m_j\rangle$ than in the basis $|K^l_m\rangle\,\alpha$ and $|K^l_m\rangle\,\beta$, since it is precisely the former functions that form the basis of the representation Δ_5 of the double group C_{2v}. This selection yields two sets of wave functions for the doubly degenerate states of the representation Δ_5. The first set is a linear combination of the functions $|3/2, -3/2\rangle$, $|3/2, 1/2\rangle$, and $|1/2, 1/2\rangle$ as well as the similar functions obtained from Γ_{15c}, Γ_{12c}, and Γ_{1c}. The second set involves the functions $|3/2, 3/2\rangle$, $|3/2, -1/2\rangle$, and $|1/2, -1/2\rangle$ as well as the corresponding functions obtained from Γ_{15c}, Γ_{12c}, and Γ_{1c}. These sets are transformed by different lines of the two-dimensional representation Δ_5; furthermore, they mix neither in the bulk nor at the heterointerfaces.

Let us now analyze the valence band states. The wave functions of the states of heavy holes can be written as

$$\begin{aligned} |h1\rangle &= \exp(ikz)D_{h1}|3/2, 3/2\rangle + |\chi_{h1}\rangle; \\ |h2\rangle &= \exp(ikz)D_{h2}|3/2, -3/2\rangle + |\chi_{h2}\rangle, \end{aligned} \qquad (16)$$

where the functions $|\chi\rangle$ represent the contribution of the other basis functions. Numerical calculations showed that the values of $|D_h\rangle$ varied from 1 to ~0.93 in the aforementioned energy range for GaAs. Thus, as should be expected, the functions $|3/2, -3/2\rangle$ and $|3/2, 3/2\rangle$ make the main contribution to the wave functions of heavy holes. The functions $|\chi\rangle$ are mainly related to $|3/2, -3/2\rangle_c$ and $|3/2, 3/2\rangle_c$, respectively. The contribution of all the other states is negligible. The bands of heavy holes are nonparabolic, and the energy-dependent effective mass $m_h^*(E)$ decreases as we recede from the valence band top. The average values of the spin (the spin Pauli matrices), $\bar{\sigma}_x$ and $\bar{\sigma}_y$, equal zero for the states of heavy holes. For all the energies in this range, the values of $\bar{\sigma}_z(h1)$ and $\bar{\sigma}_z(h2)$ for GaAs are very close to 1 and –1, respectively.

For light holes, let us express the wave functions in the form

$$\begin{aligned} |l1\rangle &= \exp(ikz)D_{l1}|3/2, -1/2\rangle + |\chi_{l1}\rangle; \\ |l2\rangle &= \exp(ikz)D_{l2}|3/2, 1/2\rangle + |\chi_{l2}\rangle, \end{aligned} \qquad (17)$$

where the functions $|\chi\rangle$ have the same meaning as above. It was found that the values of $|D_l\rangle$ in this energy range for GaAs varied from 1 to ~0.67. The main contribution to the functions $|\chi\rangle$ is associated with the functions $|1/2, -1/2\rangle$ and $|1/2, 1/2\rangle$, respectively. For energies in the region of the spin–split-off band, the contributions of the functions $|3/2, -1/2\rangle$ and $|1/2, -1/2\rangle$ to $|l1\rangle$ or the functions $|3/2, 1/2\rangle$ and $|1/2, 1/2\rangle$ to $|l2\rangle$ become almost identical. Thus, the often used approximate representation of the wave functions of light holes in form (17), which is without the summand $|\chi_{l1}\rangle$ ($|\chi_{l2}\rangle$), is valid only for energies close to E_v and becomes incorrect for energies in the region of the spin–split-off band. The bands of light holes are also nonparabolic, and $m_l^*(E)$ increases as we recede from the valence-band top. This dependence becomes especially noticeable in the region of the energies of the spin–split-off band. The average values for light holes, $\bar{\sigma}_x$ and $\bar{\sigma}_y$, are equal to zero.

For GaAs, $\bar{\sigma}_z(l1)$, in the specified energy range, varies monotonically from –1/3 to ~0.89 ($\bar{\sigma}_z(l2) = -\bar{\sigma}_z(l1)$).

Let us represent the functions of the states of the band split off due to the spin–orbit interaction in the form

$$\begin{aligned} |s1\rangle &= \exp(ikz)D_{s1}|1/2, -1/2\rangle + |\chi_{s1}\rangle; \\ |s2\rangle &= \exp(ikz)D_{s2}|1/2, 1/2\rangle + |\chi_{s2}\rangle. \end{aligned} \quad (18)$$

For GaAs, it was found that the values of $|D_s|$ vary from 1 to ~0.92 in the energy range from the spin–split-off band top ($-\Delta_0$) to –0.5 eV. The functions $|3/2, -1/2\rangle$ and $|3/2, 1/2\rangle$ make the main contribution to the functions $|\chi\rangle$ for $|s1\rangle$ and $|s2\rangle$, respectively. Similarly to the other bands, $\bar{\sigma}_x = \bar{\sigma}_y = 0$. In the energy range of the spin–split-off band, $\bar{\sigma}_z(s1)$ varies monotonically from –1/3 to ~0.30 ($\bar{\sigma}_z(s2) = -\bar{\sigma}_z(s1)$) for GaAs.

Thus, this analysis of the wave functions shows that, in order to describe all valence bands correctly, the **kp** interaction of the states Γ_8 and Γ_7 should be taken into account. Moreover, the often used approximation of energy-independent effective masses for the bands of light and heavy holes becomes incorrect as we recede insignificantly from E_v. Let us consider the matching conditions for the envelope functions in the basis of the functions $|j, m_j\rangle$, which are determined by relations (13):

$$\tilde{\mathbf{F}}^1(z_0) = \tilde{\mathbf{T}}(z_0)\tilde{\mathbf{F}}^2(z_0). \quad (19)$$

Here, $\tilde{\mathbf{F}}(z_0)$ is a column vector with the components $\tilde{\mathbf{F}}_m(z_0)$ and $\tilde{\mathbf{F}}'_m(z_0)$ ($m = 1, \ldots, 6$), which are defined in the same order as in relations (13). It is clear that the matching matrix for the envelope functions in the basis **T** can be obtained using the corresponding unitary transformation from the matrix **T** determined by formula (11). As a result, we obtain the matrix elements $\tilde{t}_{ij}$ of the matrix $\tilde{\mathbf{T}}$ in terms of the elements t_{ij} of the above-considered matrix $\tilde{\mathbf{T}}$.

The matching of the envelope functions $\tilde{\mathbf{F}}_m$ is described by the matrix elements $\tilde{t}_{ij}$ for ($i, j = 1, \ldots, 6$):

$$\begin{gathered} \tilde{t}_{11} = \tilde{t}_{22} = t_{22}, \quad \tilde{t}_{33} = \tilde{t}_{44} = \frac{2}{3}t_{11} + \frac{1}{3}t_{22}; \\ \tilde{t}_{55} = \tilde{t}_{66} = \frac{1}{3}t_{11} + \frac{2}{3}t_{22}; \\ \tilde{t}_{35} = -\tilde{t}_{46} = \tilde{t}_{53} = -\tilde{t}_{64} = \frac{2}{\sqrt{3}}(-t_{11} + t_{22}). \end{gathered} \quad (20)$$

It should be noted that there is an insignificant mixing of the envelope functions $\tilde{\mathbf{F}}_m$ of the states of light holes ($i, j = 3, 4$) and the spin–split-off band ($i, j = 5, 6$) due to the difference $t_{11} - t_{22}$ being small.

The matching of the derivatives of the envelope functions $\tilde{\mathbf{F}}'_m$ corresponds to the matrix elements $\tilde{t}_{ij}$, where ($i, j = 7, \ldots, 12$):

$$\begin{gathered} \tilde{t}_{77} = \tilde{t}_{88} = t_{55}, \quad \tilde{t}_{99} = \tilde{t}_{1010} = \frac{2}{3}t_{44} + \frac{1}{3}t_{55}; \\ \tilde{t}_{1111} = \tilde{t}_{1212} = \frac{1}{3}t_{44} + \frac{1}{3}t_{55}; \\ \tilde{t}_{911} = -\tilde{t}_{1012} = \tilde{t}_{119} = -\tilde{t}_{1210} = \frac{2}{\sqrt{3}}(-t_{44} + t_{55}). \end{gathered} \quad (21)$$

The functions $\tilde{\mathbf{F}}'_m$ are mixed by the heterointerface due to the fact that $t_{44} \neq t_{55}$. It is precisely these matrix elements that mainly determine the mixing of the states of light holes and the spin–split-off band by the heterointerfaces.

The matching of the envelope functions $\tilde{\mathbf{F}}_m$ with their derivatives $\tilde{\mathbf{F}}'_m$ is described by the matrix elements $\tilde{t}_{ij}$, where ($i = 1, \ldots, 6; j = 7, \ldots, 12$):

$$\begin{aligned} \tilde{t}_{110} &= -\tilde{t}_{29} = \tilde{t}_{38} = -\tilde{t}_{47} = -\frac{i}{\sqrt{3}}t_{25}; \\ \tilde{t}_{112} &= -\tilde{t}_{211} = -\tilde{t}_{58} = -\tilde{t}_{67} = -\frac{2i}{\sqrt{6}}t_{25}. \end{aligned} \quad (22)$$

The matching of the derivatives $\tilde{\mathbf{F}}'_m$ with the envelope functions $\tilde{\mathbf{F}}_m$ is described by the matrix elements $\tilde{t}_{ij}$, where ($i = 7, \ldots, 12; j = 1, \ldots, 6$):

$$\begin{aligned} \tilde{t}_{101} &= -\tilde{t}_{92} = \tilde{t}_{83} = -\tilde{t}_{74} = -\frac{i}{\sqrt{3}}t_{52}; \\ \tilde{t}_{121} &= -\tilde{t}_{112} = -\tilde{t}_{85} = -\tilde{t}_{76} = -\frac{2i}{\sqrt{6}}t_{52}. \end{aligned} \quad (23)$$

Matrix elements (22) and (23) are mainly responsible for the mixing of the states of heavy holes with the states of light holes and spin–split-off band by the heterointerfaces. The other elements of the matrix $\tilde{\mathbf{T}}$ are equal to zero.

Relations (20)–(23) show that, as was mentioned above, no mixing of the envelopes corresponding to the functions $|3/2, -3/2\rangle$, $|3/2, 1/2\rangle$, and $|1/2, 1/2\rangle$ with the envelopes of the functions $|3/2, 3/2\rangle$, $|3/2, -1/2\rangle$, and $|1/2, -1/2\rangle$ occurs at the heterointerfaces.

As an example, let us present the results of a calculation of the transmittances for a GaAs/AlAs(4)/GaAs(16)/AlAs(4)/GaAs(001) structure. The number of monolayers expressed in the lattice constant units is parenthesized. In the course of tunneling, a mixing of the $|h1\rangle$, $|l1\rangle$, and $|s1\rangle$ states, as well as the $|h2\rangle$, $|l2\rangle$, and $|s2\rangle$ states, is observed. We then have the following transmittances: P_{hh}, P_{ll}, P_{hl}, P_{lh}, P_{ss}, P_{sh}, P_{sl}, P_{hs}, and P_{ls}. The first and second indices indicate the

type of incident wave and passed wave, respectively. The first four coefficients are determined for all the energies in the aforementioned energy range, and the last five coefficients are determined only for energies of the spin–split-off band. According to the symmetry of the problem, all the states in this structure are doubly degenerate.

Figure 1 shows the transmittances P_{hh}, P_{ll}, and P_{lh} ($P_{hl} \approx P_{lh}$). There is a series of resonance peaks for the intraband coefficients P_{hh} and P_{ll}. The mixing of the states (P_{lh}) of heavy and light holes (*hl* mixing) is generally poorly pronounced and is only noticeable at resonance energies. This result of our study differs substantially from the results in [6, 18, 19], where pronounced *hl* mixing was observed. The authors of publications [6, 18, 19] estimated the magnitude of the mixing via a comparison with the experiments and calculations of other authors, who used the tight-binding and pseudopotential methods [24], or indirectly, via the nondiagonal reflectance. They also carried out their own calculations using the tight-binding method. In our calculation, the reflectance R_{hl} at the GaAs/AlAs interface for energies in the vicinity of the spin–split-off band top is approximately an order of magnitude smaller than that obtained in [6]. It should be noted that our conclusion on the small extent of *hl* mixing follows from calculations performed using the pseudopotential method in a model with a discontinuous potential at the interface. The direct comparison of our results with those reported in [6] is complicated, since we do not imply the continuity of the envelopes at the heterointerface (see relation (20)). Furthermore, our model includes the mixing of the envelopes that have the functions $\tilde{\mathbf{F}}_m$ with their derivatives $\tilde{\mathbf{F}}'_m$ (see relation (22)).

However, it should be noted that there are more recent calculations completed by other authors [17] that also lead to results differing from those reported in [6]. According to the pseudopotential calculation in [17], the parameter for the mixing of light and heavy holes is an order of magnitude smaller than that obtained in the phenomenological models in [6]. The authors of [17] identified the character of the mixing of light and heavy holes based on an analysis of the anticrossing of the levels of light and heavy holes in quantum-well structures and superlattices possessing a variable width of wells and barriers. Pronounced *hl* mixing was observed only if the levels of the states of heavy and light holes in the quantum well were close to each other in energy [17].

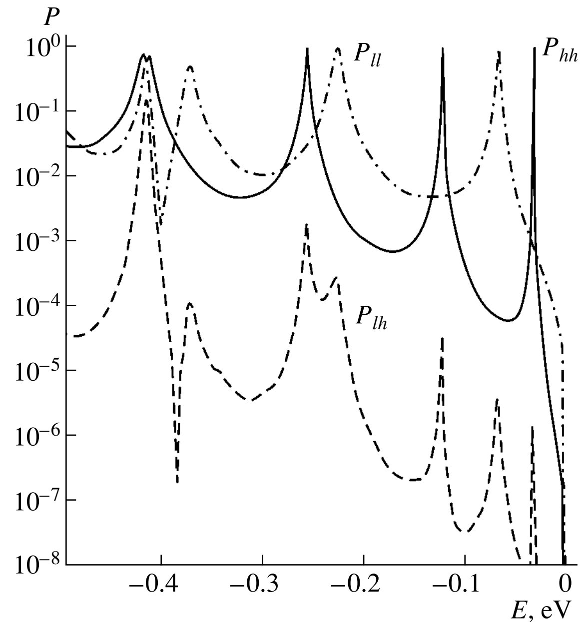

Fig. 1. Transmittances P_{hh}, P_{ll}, and P_{lh} for the GaAs/AlAs(4)/GaAs(16)/AlAs(4)/GaAs(001) structure at $\mathbf{k}_{\parallel} = 0$. The solid line represents the dependence $P_{hh}(E)$, the dashed-and-dotted line represents the dependence $P_{ll}(E)$, and the dashed line represents the dependence $P_{lh}(E)$.

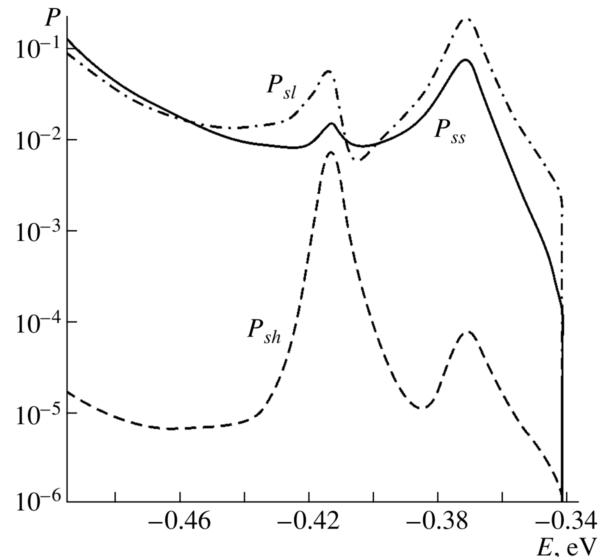

Fig. 2. Transmittances P_{ss}, P_{sl}, and P_{sh} for the GaAs/AlAs(4)/GaAs(16)/AlAs(4)/GaAs structure at $\mathbf{k}_{\parallel} = 0$ in the energy region of the spin–split-off band. The solid line represents the dependence $P_{ss}(E)$, the dashed-and-dotted line represents the dependence $P_{sl}(E)$, and the dashed line represents the dependence $P_{sh}(E)$.

Figure 2 shows the transmittances P_{ss}, P_{sl}, and P_{sh} ($P_{ls} \approx P_{sl}$ and $P_{hs} \approx P_{sh}$) in the energy region of the spin–split-off band. There is a pronounced mixing of the states from the band of light holes and the spin–split-off band. This is associated with the fact that the states $|s1\rangle$ and $|l1\rangle$ in the energy region of the spin–split-off band (see relations (17) and (18)) are similar.

In conclusion, let us formulate the main results and conclusions of this study. The analysis of the states of the valence band showed that the conventionally used approximation of energy-independent effective masses for the bands of light and heavy holes is valid only near the valence-band top. It was also shown that the **kp** interactions of the states Γ_8 and Γ_7 should be taken

into account in order to describe the valence bands correctly. We also determined the matching conditions for the envelope functions of the holes at GaAs/AlAs(001) heterointerfaces both with and without an allowance being made for the spin–orbit interaction for energies in the vicinity of the valence-band top. These conditions were obtained by simplifying the description of electronic states provided by the pseudopotential method and are completely consistent with the symmetry of the problem. In the matching condition, the envelope functions are mixed with their normal derivatives, and the derivatives are mixed with the functions. To our knowledge, this result has never been reported. The efficiency of our model for the envelope functions is confirmed by the good agreement obtained for the results of the model and the pseudopotential calculations (in which no allowance is made for the spin–orbit interaction) of the transmittances for various structures. Using the numerical values found for the elements of the matching matrix for envelope functions, we can estimate the parameters of the hole mixing at the heterointerface. It is especially noteworthy that the mixing of light and heavy holes turned out to be insignificant in our case. Indeed, it was approximately an order of magnitude weaker than that found in [6]. However, the order of mixing agrees with the conclusion made in [17]. The obtained results call for a further analysis aimed at an explanation of the experimentally found anisotropy.

ACKNOWLEDGMENTS

This study was supported by the Russian Foundation for Basic Research, project no. 04-02-17508.

REFERENCES

1. D. J. BenDaniel and C. D. Duke, Phys. Rev. **152**, 683 (1966); G. Bastard, Phys. Rev. B **24**, 5693 (1981).
2. T. Ando, S. Wakahara, and H. Akera, Phys. Rev. B **40**, 609 (1989); T. Ando and H. Akera, Phys. Rev. B **40**, 11619 (1989).
3. S. N. Grinyaev and V. N. Chernyshov, Fiz. Tekh. Poluprovodn. (St. Petersburg) **26**, 2057 (1992) [Sov. Phys. Semicond. **26**, 1157 (1992)]; G. F. Karavaev, S. N. Grinyaev, and V. N. Chernyshov, Izv. Vyssh. Uchebn. Zaved., Fiz., No. 9, 64 (1992).
4. Y. Fu, M. Willander, E. L. Ivchenko, and A. A. Kiselev, Phys. Rev. B **47**, 13498 (1993).
5. G. F. Karavaev and S. N. Grinyaev, Izv. Vyssh. Uchebn. Zaved., Fiz., No. 9, 89 (1998); G. F. Karavaev and V. N. Chernyshov, Fiz. Tekh. Poluprovodn. (St. Petersburg) **35**, 105 (2001) [Semiconductors **35**, 106 (2001)]; G. F. Karavaev and V. N. Chernyshov, Fiz. Tekh. Poluprovodn. (St. Petersburg) **35**, 841 (2001) [Semiconductors **35**, 807 (2001)]; G. F. Karavaev and V. N. Chernyshov, Izv. Vyssh. Uchebn. Zaved., Fiz., No. 6, 51 (2003).
6. E. L. Ivchenko, A. Yu. Kaminski, and U. Rossler, Phys. Rev. B **54**, 5852 (1996).
7. F. B. Pedersen and Yia-Chung Chang, Phys. Rev. B **53**, 1507 (1996).
8. G. Rau, P. C. Klipstein, V. Nikos Nicopoulos, and N. F. Johnson, Phys. Rev. B **54**, 5700 (1996).
9. N. J. Traynor, R. J. Warburton, M. J. Snelling, and R. T. Harley, Phys. Rev. B **55**, 15701 (1997).
10. T. Sogawa, H. Ando, S. Ando, and H. Kanbe, Phys. Rev. B **58**, 15652 (1998).
11. A. M. Malik, M. J. Godfrey, and P. Dawson, Phys. Rev. B **59**, 2861 (1999).
12. G. Bastard, *Wave Mechanics Applied to Semiconductor Heterostructures* (Physique, Paris, 1992).
13. G. Bastard, Phys. Rev. B **24**, 5693 (1981).
14. Xiao-Ling Ye, Y. H. Chen, J. Z. Wang, *et al.*, Phys. Rev. B **63**, 115317 (2001).
15. M. V. Kisin, B. L. Gelmont, and S. Luryi, Phys. Rev. B **58**, 4605 (1998).
16. M. Morifuji and C. Hamaguchi, Phys. Rev. B **52**, 14131 (1995).
17. R. Magri and A. Zunger, Phys. Rev. B **62**, 10364 (2000).
18. I. L. Aleĭner and E. L. Ivchenko, Pis'ma Zh. Éksp. Teor. Fiz. **55**, 662 (1992) [JETP Lett. **55**, 692 (1992)].
19. E. L. Ivchenko, A. Yu. Kaminskiĭ, and I. L. Aleĭner, Zh. Éksp. Teor. Fiz. **104**, 3401 (1993) [JETP **77**, 609 (1993)].
20. M. Cardona, N. E. Christensen, and G. Fasol, Phys. Rev. B **38**, 1806 (1988).
21. P. Pfeffer and W. Zawadzki, Phys. Rev. B **53**, 12813 (1996).
22. D. Y. Ko and J. S. Inkson, Phys. Rev. B **38**, 9945 (1988).
23. V. A. Chaldyshev and S. N. Grinyaev, Izv. Vyssh. Uchebn. Zaved., Fiz., No. 3, 38 (1983).
24. G. Edwards and J. C. Inkson, Solid State Commun. **89**, 595 (1994).

Translated by N. Korovin

Semiconductors, Vol. 39, No. 3, 2005, pp. 325–330. Translated from Fizika i Tekhnika Poluprovodnikov, Vol. 39, No. 3, 2005, pp. 343–348.
Original Russian Text Copyright © 2005 by Gorskiĭ.

SEMICONDUCTOR STRUCTURES, INTERFACES, AND SURFACES

A Quasi-Classical Description of the Conductivity Oscillations in Layered Crystals Under the Condition of Charge-Carrier Scattering by Acoustic Phonons

P. V. Gorskiĭ

Chernivtsi National University, Chernivtsi, 58012 Ukraine

Submitted March 22, 2004; accepted for publication May 17, 2004

Abstract—The oscillating part of the longitudinal conductivity of layered crystals is considered within the quasi-classical approximation, where both the electric field and quantizing magnetic field are perpendicular to the layers. Our approach differs from the conventional one by taking into account both the nonparabolicity of a narrow conduction miniband and the dependence of the Fermi surface size in the direction of the magnetic field on charge-carrier concentration. This approach makes it possible to consider not only the standard case, with open Fermi surfaces, but also the case of closed Fermi surfaces. It is shown that, for closed Fermi surfaces, the existence of frequencies that do not correspond to extreme cross sections of the Fermi surfaces cut by planes normal to the magnetic field can serve as a criterion for the narrowness of the conduction miniband, which determines the translational motion of charge carriers across the layers. *© 2005 Pleiades Publishing, Inc.*

1. INTRODUCTION

If it is assumed that there are many Landau levels in the allowed band of a crystal, the Lifshitz–Kosevich theory of magnetic susceptibility [1] and the Kosevich–Andreev theory of transport coefficients [2, 3] are valid in the quasi-classical approximation. Furthermore, interband transitions are not forbidden, and charge-carrier scattering probabilities are either the same as they would be in the absence of a magnetic field or oscillate with the variations in a magnetic field [4]. The Kosevich–Andreev theory was developed for a case in which electric and magnetic fields are mutually perpendicular. However, experimental studies of the oscillations of transport coefficients, in particular, of thermopower, are quite often performed for a situation in which an electric field (or temperature gradient) and a magnetic field are parallel. Moreover, neither the Lifshitz–Kosevich theory nor the Kosevich–Andreev theory take into account the explicit form of the nonparabolicity of a conduction band and the dependence of the size of the Fermi surface along the direction of a magnetic field on charge-carrier concentration. However, there exist numerous highly anisotropic crystals with layered structures where the motion of the charge carriers in the layer plane is described using the effective mass approximation and the motion in the perpendicular direction by the tight-binding approximation or by some nonparabolic dispersion relation [5]. Examples of such crystals include transition metal dichalcogenides [6], intercalated graphite compounds (synthetic metals) [7], multinary semiconductor compounds with superlattices (in particular, II–VI–VII compounds) [8], quasi-two-dimensional organic conductors [9], etc. The aim of this study is to describe, within the quasi-classical approximation, the oscillations of electrical conductivity and to establish the conditions for the applicability of this description to crystals in which the electric and magnetic fields are parallel to each other (longitudinal electrical conductivity) and are perpendicular to the layers.

It should be noted that layered conductors are usually considered as being quasi-two-dimensional, i.e., conductors for which the Fermi energy is much greater than the width of the narrow conduction miniband, which determines charge-carrier motion in a direction normal to the layers. The theory relating to the Shubnikov–de Haas effect (in a magnetic field perpendicular to the current) for such crystals has already undergone a sufficiently detailed development in the quasi-classical approximation [9]. However, there are also layered crystals that, though they are described by a model of the band-spectrum characteristic of quasi-two-dimensional crystals, are not quasi-two-dimensional in the above sense. The Fermi energy in these crystals is smaller than the width of the narrow miniband that determines the motion of electrons across the layers; however, these quantities are comparable, which means that the usual effective mass approximation is not valid [7, 8]. Nevertheless, these crystals can be transformed into a quasi-two-dimensional form by doping. In this study, we derive expressions that describe the oscillating part of the longitudinal electrical conductivity in crystals of both types.

2. RESULTS AND DISCUSSION

The most general expression for the energy levels of charge carriers in a layered crystal in a quantizing magnetic field perpendicular to the layers is

$$\varepsilon(n, k_z) = \mu^* H(2n+1) + W(x), \qquad (1)$$

1063-7826/05/3903-0325$26.00 © 2005 Pleiades Publishing, Inc.

where $\mu^* = \mu_B(m_0/m^*)$; μ_B is the Bohr magneton; n is the number of the Landau level; m^* is the effective mass of an electron in the layer plane, which is, for simplicity, assumed to be isotropic; k_z is the component of the quasi-momentum in the direction perpendicular to the layers; H is the quantizing magnetic field; $W(x)$ is the charge-carrier dispersion relation, which is not parabolic and describes the carrier motion in the direction normal to the layers; $x = ak_z$; and a is the distance between the translationally equivalent layers.

When describing the Shubnikov–de Haas effect in the quasi-crystal approximation for charge-carrier scattering by acoustic phonons, we assume, for simplicity, that the relaxation time of the longitudinal quasi-momentum does not depend on the carrier energy and that the temperature dependence of this time obeys the Bloch–Grüneisen law [10]. Then, the relaxation time is given by

$$\tau = \tau_0(\Theta_D/T^5), \tag{2}$$

where, for the crystal under consideration, τ_0 is a constant that has the dimensions of time and describes the scattering intensity, and Θ_D is the Debye temperature of the crystal.

The conductivity is obtained from the Kubo formula [11] by summation over the Landau levels, which can be precisely performed for spectrum (1) using the longitudinal quasi-momentum relaxation time given by (2) for any form of the function $W(x)$. In the approximation $\zeta/kT \gg 1$ and $\Delta/kT \gg 1$, we obtain the following expression for the magnetic-field-independent part of the conductivity:

$$\sigma_0 = \frac{32\pi\tau_0 e^2 m^* a\Theta_D^5}{h^4 T^5}\int\limits_{W(x)\le\zeta}(W'(x))^2 dx, \tag{3}$$

and the oscillating part of the conductivity assumes the form

$$\sigma_{osc} = \frac{32\pi\tau_0 e^2 m^* a\Theta_D^5}{h^4 T^5} \times\sum_{l=1}^{\infty}(-1)^{l-1} f_l^{\sigma}\int\limits_{W(x)\le\zeta}(W'(x))^2\cos\left[\pi l\frac{(\zeta - W(x))}{\mu^* H}\right]. \tag{4}$$

In (4), f_l^{σ} denotes the temperature-related damping factor of the oscillations,

$$f_l^{\sigma} = \frac{\pi^2 lkT/\mu^* H}{\sinh(\pi^2 lkT/\mu^* H)}. \tag{5}$$

In (3)–(5), ζ is the Fermi energy measured from the bottom of the narrow conduction miniband and $W'(x)$ is the derivative. The integration in (3) and (4) is performed only with respect to positive values of x.

Using formulas (3) and (4), we can now calculate the conductivity for the dispersion relations $W(x)$.

The simplest tight-binding dispersion relation, which is used to describe a warped Fermi surface of a layered crystal, is written as [5]

$$W(x) = \Delta(1 - \cos x), \tag{6}$$

where Δ is the half-width of the narrow miniband in the direction normal to the layers. For this dispersion law, as well as for nonquasi-two-dimensional crystals, i.e., for $\zeta \le 2\Delta$, the magnetic-field-independent part of the conductivity assumes the form

$$\sigma_0 = \frac{16\pi\tau_0 e^2 m^* a\Theta_D^5\Delta^2}{h^4 T^5}(C_0 - C_2), \tag{7}$$

and the oscillating part is

$$\begin{aligned}\sigma_{osc} = {} & \frac{16\pi\tau_0 e^2 m^* a\Theta_D^5\Delta^2}{h^4 T^5} \\ & \times\sum_{l=1}^{\infty}(-1)^{l-1} f_l^{\sigma}\left\{\cos\left[\frac{\pi l(\zeta-\Delta)}{\mu^* H}\right]\left[(C_0 - C_2)J_0\left(\frac{\pi l\Delta}{\mu^* H}\right)\right.\right. \\ & \left.\times\sum_{r=1}^{\infty}(-1)^r(2C_{2r} - C_{2r+2} - C_{2r-2})J_{2r}\left(\frac{\pi l\Delta}{\mu^* H}\right)\right] \\ & - \sin\left[\frac{\pi l(\zeta-\Delta)}{\mu^* H}\right]\sum_{r=1}^{\infty}(-1)^r(2C_{2r+1} - C_{2r+3} - C_{|2r-1|}) \\ & \left.\times J_{2r+1}\left(\frac{\pi l\Delta}{\mu^* H}\right)\right\},\end{aligned} \tag{8}$$

where $J_m(y)$ are the Bessel functions of the real argument y, and C_m are the modulating coefficients defined by the relations

$$C_0 = \kappa_\zeta = \arccos\left(1 - \frac{\zeta}{\Delta}\right), \tag{9}$$

$$C_m = \frac{\sin m\kappa_\zeta}{m}. \tag{10}$$

When deriving formula (8), we expanded the oscillating part of the integrand in (4) in the Bessel functions of integer index using dispersion relation (6) [12]. In expansion (8), there are many Bessel functions, since, for $\zeta \le 2\Delta$, the Fermi surface of a layered crystal is closed and occupies the region $[-\kappa_\zeta; \kappa_\zeta]$ within the one-dimensional Brillouin zone. For $\zeta > 2\Delta$, the Fermi surface is open, and the integration in (4) should be per-

formed over the entire Brillouin zone; therefore expression (4) can be written in the more compact form

$$\sigma_{\rm osc} = \frac{16\pi^2\tau_0 e^2 m^* a\Theta_{\rm D}^5\Delta^2}{h^4T^5} \times \sum_{l=1}^{\infty}(-1)^{l-1}f_l^{\sigma}\left[J_0\left(\frac{\pi l\Delta}{\mu^*H}\right)+J_2\left(\frac{\pi l\Delta}{\mu^*H}\right)\right] \times \cos\left[\pi l\left(\frac{\zeta-\Delta}{\mu^*H}\right)\right]. \quad (11)$$

Let us analyze these results in more detail. First, we should note that, initially, the magnetic-field-independent part of the longitudinal electrical conductivity increases monotonically with κ_ζ, i.e., with the charge-carrier concentration. It then attains a maximum, and finally becomes independent of the carrier concentration as the Fermi level crosses the top of the narrow miniband. This behavior occurs because any restriction imposed on the free motion of the charge carriers reduces the conductivity of the crystal.

We now consider the oscillating component of the electrical conductivity. General formula (4) for the conductivity differs from the conventional expression in the explicit allowance it makes for the dependence of the Fermi surface size along the direction of the magnetic field on the carrier concentration as a result of a restriction of the region of integration with respect to x [13, 14]. This restriction is quite justified, since the "disappearance" of the Fermi surface implies that the oscillating component of the conductivity vanishes. Therefore, it follows from (8) that not only the frequencies but also the amplitudes of the conductivity oscillations depend on the charge-carrier concentration via the concentration dependence of the Fermi energy. For the considered specific case of a layered crystal with a superlattice, this dependence is determined by the modulating coefficients of the Bessel functions defined by expressions (9) and (10). The series in r and l in expression (8) converge quite rapidly. However, for the specific case in which $\zeta = \Delta$, a more compact formula without trigonometric factors can be obtained from (8):

$$\sigma_{\rm osc} = \frac{8\pi^2\tau_0 e^2 m^* a\Theta_{\rm D}^5\Delta^2}{h^4T^5} \times \sum_{l=1}^{\infty}(-1)^{l-1}f_l^{\sigma}\left[J_0\left(\frac{\pi l\Delta}{\mu^*H}\right)+J_2\left(\frac{\pi l\Delta}{\mu^*H}\right)\right]. \quad (12)$$

This circumstance is a direct consequence of dispersion relation (6), which is representative of the small width of the conduction miniband and is characteristic of crystals with superlattices. However, when the magnetic field is so weak that there are a large number Landau levels in the narrow conduction miniband, we may use the traditional quasi-classical approximation in (4), which is not based on any model assumptions about the form of the function $W(x)$, i.e., about the character of the warping of a cylinder (which is actually the Fermi surface of the layered crystal). To apply this approximation to (4), we must retain the first nonvanishing terms in the expansions of $W(x)$ and $W'(x)$ in x near the extreme cross sections of the Fermi surface cut by the planes normal to the direction of the magnetic field. Furthermore, we must evaluate the integrals obtained using the method of steepest descent and the subsequent differentiation with respect to the parameter. The result for the oscillating component of the longitudinal conductivity is

$$\sigma_{\rm osc}^{cc} = \mp\frac{4\tau_0 e^2 m^* a\Theta_{\rm D}^5(\mu^*H)^{3/2}|W''_{\rm ex}|^{1/2}}{h^4T^5} \times \sum_{l=1}^{\infty}(-1)^{l-1}f_l^{\sigma}l^{-3/2}\sin\left(\pi l\frac{\zeta-W_{\rm ex}}{\mu^*H}\pm\frac{\pi}{4}\right). \quad (13)$$

In this formula, $W_{\rm ex}$ and $|W''_{\rm ex}|$ are values of the function $W(x)$ and the modulus of its second derivative at the extremum points (if there are several extrema, then the sum in (13) must be taken over all the extrema belonging to the Fermi surface). The plus sign at the initial phase and the minus sign at the amplitude correspond to the minimal cross section, and the opposite signs correspond to the maximal cross section of the Fermi surface. In contrast to the traditional formula [2, 3, 9], in expression (13), the magnetic-field dependence of the oscillation amplitude and the curvature of the Fermi surface near the extreme cross sections is different, and cosines are replaced by sines. These differences are exclusively due to the fact that, in this study, we consider the longitudinal electrical conductivity whereas, in the traditional approach, the transverse conductivity is considered.

If, in formulas (8) and (11), we use an asymptotic limit in the form $\Delta/\mu^*H \gg 1$, then, retaining only the leading terms in the asymptotic expansions of the Bessel function [12], we see that the oscillating component of the conductivity vanishes in an identical manner. By including the subsequent terms in these expansions, we obtain two quasi-classical formulas of type (13): the first for a Fermi surface with one extreme cross section (cut by the $k_z = 0$ plane) when $0 < \zeta < 2\Delta$ and the second for a Fermi surface with three extreme cross sections (cut by the $k_z = 0$ plane and the $k_z = \pm\pi/a$ planes) when $\zeta > 2\Delta$. We then combine these formulas into the single expression

$$\sigma_{\rm osc}^{cc} = \frac{16\sqrt{2}\tau_0 e^2 m^* a\Theta_{\rm D}^5\Delta^{1/2}(\mu^*H)^{3/2}}{h^4T^5} \times \sum_{l=1}^{\infty}(-1)^{l-1}l^{-3/2}f_l^{\sigma}\left\{\sin\left(\frac{\pi l\zeta}{\mu^*H}-\frac{\pi}{4}\right) - \theta(\zeta-2\Delta)\sin\left(\frac{\pi l(\zeta-2\Delta)}{\mu^*H}+\frac{\pi}{4}\right)\right\}. \quad (14)$$

In this expression, $\theta(y)$ is the θ-pulse step function. In this context, we should note that, in the traditional approach, we always obtain a formula for the Fermi surface with three extreme cross sections. At the same time, from an analysis of the geometry of the Fermi surface, it follows that, for $0 < \zeta \le 2\Delta$, this surface has only one extremal cross section; however, this case was not considered in [9]. It is also can be seen in (14) that, in the traditional quasi-classical approach, in which the dependence of the size of the Fermi surface along the direction of the magnetic field on the charge-carrier concentration is disregarded, the oscillating component of the conductivity changes abruptly with variations in ζ. At the same time, formulas (8) and (11) predict that the conductivity dependence on ζ is continuous. Such a contradiction can be explained by the fact that, in the model under consideration, the Fermi surfaces are closed for $0 < \zeta < 2\Delta$ and open for $\zeta > 2\Delta$. It can also be explained in a purely mathematical form: the formulas for the series summation over r, which appear after passing to the asymptotic representations of the Bessel function [11] in (8), are incorrect for $\kappa_\zeta = 0$ and $\kappa_\zeta = \pi$. Furthermore, it is clear from the expression itself that expression (14) is valid only if the Fermi level is not too close to the bottom or top of the narrow conduction miniband, whereas the general formulas (8) and (11) are valid for any relation between ζ and Δ. In addition, the quasi-classical condition, for which formula (2) is valid, must be satisfied; i.e., a large number Landau levels must lie below the Fermi level in the narrow conduction miniband.

This contradiction can be resolved if we note that, even for $\zeta < 2\Delta$, the oscillating component of the conductivity of a layered crystal contains two, rather than one, sets of oscillation frequencies. These frequencies can be defined by the formulas

$$h_l^H = \frac{l\zeta}{2\mu^*}, \tag{15}$$

$$h_l'^H = \frac{l|\zeta - 2\Delta|}{2\mu^*}. \tag{16}$$

The first of these sets is always associated with the maximal cross section of the Fermi surface cut by the $k_z = 0$ plane. The second set is not associated with any cross section of the Fermi surface cut by the plane perpendicular to the direction of the magnetic field if $0 < \zeta < \Delta$. However, it is associated with two nonextreme cross sections of the Fermi surface cut by the planes

$$k_z = \pm\frac{\arccos(3 - 2\zeta/\Delta)}{a}$$

if $\Delta < \zeta < 2\Delta$ and with two minimal cross sections of the Fermi surface cut by the $k_z = \pm\pi/a$ planes if $\zeta > 2\Delta$. The contribution of the harmonics with frequencies (16) increases if the ratio ζ/Δ increases and the ratio Δ/μ^*H decreases, i.e., if the Fermi level lies closer to the top of the miniband and the miniband is narrower, leading to larger anisotropy of the layered crystal. This behavior is caused by the fact that a decrease in the ratio Δ/μ^*H leads to a decrease in the dephasing of the oscillations related to the nonextremal cross sections of the Fermi surface. A similar decrease in dephasing can be also caused by an increase in the ratio ζ/Δ. Such behavior may be accounted for by a slower change, as the Fermi level approaches the top of the miniband, in the areas of the cross sections of the Fermi surface regarded as functions of the longitudinal quasi-momentum. In the quasi-classical approximation, at $\zeta < 2\Delta$, the contribution of frequencies (16) is only a small correction, on the order of μ^*H/Δ, to formula (14); i.e., this contribution gives rise to a fine structure when $\zeta < \Delta$ or beats when $\zeta < \Delta$. However, if $\zeta = \Delta$, frequencies (15) and (16) are indistinguishable.

We can illustrate the appearance of non-quasi-classical frequencies of the conductivity oscillations by expanding the integrand in (4) (taking into account (6)) in the Bessel functions of half-integer index [12], which are elementary functions expressed in terms of the products of sines and cosines by polynomials. A similar procedure was used in [14] for magnetic susceptibility. Then, the amplitudes of the oscillations with different frequencies depend continuously on the charge-carrier concentration, i.e., on ζ, thus ensuring the continuity of the change in the oscillating component of the conductivity dependence on ζ. However, the statement about the presence of non-quasi-classical oscillation frequencies is not true for all dispersion relations. For example, if we calculate the conductivity with formulas (3) and (4) using a purely quadratic function $W(x)$, we obtain the following formulas for the monotonic and oscillating components:

$$\sigma_0^{sq} = \frac{16\tau_0 e^2 m^* \Theta_D^5 \sqrt{8\zeta^3}}{3h^3 T^5 \sqrt{m_l^*}}, \tag{17}$$

$$\begin{aligned}\sigma_0^{sq} = {} & \frac{16\tau_0 e^2 m^* \Theta_D^5 \sqrt{(\mu^* H)^3}}{\pi h^3 T^5 \sqrt{m_l^*}} \\ & \times \sum_{l=1}^{\infty} (-1)^{l-1} f_l^\sigma l^{-3/2} \left[\sin\left(\frac{\pi l\zeta}{\mu^* H}\right) \mathrm{Ci}\left(\sqrt{\frac{2l\zeta}{\mu^* H}}\right)\right. \\ & \left. - \cos\left(\frac{\pi l\zeta}{\mu^* H}\right) \mathrm{Si}\left(\sqrt{\frac{2l\zeta}{\mu^* H}}\right)\right].\end{aligned} \tag{18}$$

Here, m_l^* is the longitudinal electron effective mass, and $\mathrm{Ci}(y)$ and $\mathrm{Si}(y)$ are the cosine and sine Fresnel integrals, respectively (the other notation is specified above). Formula (18), as well as formulas (8) and (11) for a crystal with superlattice, take into account the effect of the charge-carrier concentration dependence of the Fermi surface size along the direction of the magnetic field on the oscillations of the longitudinal conductivity. When passing to the asymptotic limit $\zeta/\mu^*H \gg 1$ in (18) and retaining only the leading terms in the expansions

of the Fresnel integrals, we obtain a formula of type (14) for the Fermi surface with a unique stationary cross section cut by the $k_z = 0$ plane. Thus, we find that, for $\zeta < 2\Delta$ in the traditional quasi-classical approximation, dispersion relation (6) is virtually parabolic. In the same way, without using the method of steepest descent, we can also obtain formula (13) for a general case. Using the expansions of the Fresnel integrals in the Bessel functions of half-integer index [12], we can show that, for a parabolic dispersion relation, having a finite size of the Fermi surface along the direction of the magnetic field does not result in the appearance of non-quasi-classical oscillation frequencies. Moreover, this conclusion is valid not only for a quadratic dispersion relation but also for a linear relation of the form

$$W(x) = \Delta_0|x|, \tag{19}$$

which is used, for example, to describe the band structure of graphite and synthetic metals based on graphite intercalation compounds (Δ_0 is a parameter of the model and has the dimensions of energy) [6]. For this dispersion relation, we obtain the following formulas for the components of the longitudinal conductivity of the crystal:

$$\sigma_0^{\text{lin}} = \frac{32\pi\tau_0 e^2 m^* a\Theta_{\text{D}}^5\Delta_0\zeta}{h^4T^5}, \tag{20}$$

$$\sigma_{\text{osc}}^{\text{lin}} = \frac{32\tau_0 e^2 m^* a\Theta_{\text{D}}^5\Delta_0\mu^* H}{h^4T^5} \times \sum_{l=1}^{\infty}(-1)^{l-1} f_l^{\sigma} l^{-1}\sin\left(\frac{\pi l\zeta}{\mu^* H}\right). \tag{21}$$

Formula (21) describes the oscillations of the longitudinal conductivity related to the only stationary (maximal) cross section of the Fermi surface cut by the $k_z = 0$ plane; this circumstance is quite understandable if we take into account that, for model (19), the Fermi surface of the crystal consists of two cones with contacting bases. If we try to apply formula (13) to model (19), we obtain an obviously incorrect result, $\sigma_{\text{osc}}^{\text{lin}} = 0$, since, in this model, $W''(x) \equiv 0$. Thus, we arrive at the conclusion that the presence of harmonics with non-quasi-classical frequencies in the oscillating component of the longitudinal conductivity and the deviation of the field dependence of the oscillation amplitudes from the "$H^{3/2}$ law" under the conditions of applicability for the quasi-classical approximation can serve as a measure of the nonparabolicity of the conduction band. Furthermore, it can be seen from (13), (14), and (21) that, due to the quasi-classical condition, in each of the cases considered, the oscillating component of the conductivity is small compared to the magnetic-field-independent component. Comparing these results with those of [1, 2], we see that, under the quasi-classical conditions, the longitudinal magnetooscillation effects are much less pronounced than the transverse effects. However, in layered crystals, the magnitude of the former effects may be larger because of the pronounced anisotropy of the electronic spectrum.

Using an elementary model of the band spectrum of a layered crystal as an example, we now analyze the limits of the applicability of the obtained results. For this purpose, we should take into account that the phonon energy is approximately kT at low temperatures and the scattering-induced change in the energy of the longitudinal motion of an electron cannot exceed the width of the narrow miniband 2Δ if we disregard the Umklapp processes. Therefore, the scattering-induced change in the number of the Landau subband is estimated to be

$$|\delta n| = \frac{kT}{2\mu^* H} + \frac{\Delta}{\mu^* H}. \tag{22}$$

The second term on the right-hand side is approximately equal to 100 for $m^* = m_0$, $\Delta = 0.01$ eV, and magnetic fields of approximately 1 T; therefore, the quasi-classical condition is satisfied, intersubband transitions are not suppressed, representation (2) for the relaxation time is valid, and the results obtained above are correct. However, under conditions in which the Shubnikov–de Haas effect is clearly pronounced, it is not always possible to disregard the suppression of intersubband transitions. Indeed, at low temperatures, where $q_z a \ll 1$ (q_z is the longitudinal component of the phonon wave vector), the absolute value of the scattering-induced change in the energy of the longitudinal motion of an electron does not exceed $q_z a\Delta$. Therefore, taking into account that $q_z = 2\pi kT/hs$, where s is the velocity of sound in the crystal, we use the condition $\delta n \le 1$ to estimate the freeze-out temperature for intersubband transitions:

$$T_f = \frac{2\mu^* Hhs}{k(2\pi a\Delta + hs)}. \tag{23}$$

This temperature is, of course, lower than $2\mu^* H/k$. For $m^* = m_0$, $\Delta = 0.01$ eV, $s = 5 \times 10^3$ m/s, and $a = 10$ nm, we obtain $T_f = 0.074$ K in magnetic fields of approximately 1 T. At first sight, this condition for the freeze-out of intersubband transitions seems to be quite restrictive, especially if we take into account that, generally, magnetoinsulating experiments are performed at much higher temperatures [13]. However, if, taking into account the magnitude of the factor of the thermal smearing of the oscillations determined by (5), we write the condition necessary for the Shubnikov–de Haas effect to be clearly pronounced in the form

$$\frac{\mu^* H}{kT} \ge \pi^2, \tag{24}$$

then, for the same parameters values, we obtain $T \le 0.068$ K; i.e., the temperature must be lower than T_f.

Expression (23) has a quite clear physical meaning. If we set $\Delta = 0$ in this expression, we will transform the

system of Landau subbands into a system of discrete levels for which $T_f = 2\mu^* H/k$. This formula allows us to understand why, in typical metals, e.g., alkali metals, even in a situation where the Shubnikov–de Haas effect is well pronounced, the intersubband transitions do not freeze out and the quasi-classical approximation of the above sense is valid. For the purpose of estimation, if we set $\Delta = 5$ eV, $a = 0.5$ nm, and $s = 5 \times 10^3$ m/s in (23), we find that $2\pi a\Delta/hs \approx 850$; this value has the same order of magnitude as the ratio $2\mu^* H/kT_f$. Thus we see that, even if the thermal smearing of the oscillations is negligible, intersubband transitions in typical metals are important and, therefore, the quasi-classical approximation is valid. A different situation is realized in semimetals, e.g., in bismuth. If a magnetic field of about 1.25 T is applied to a Bi crystal along the long bisector ellipsoid axis of the constant-energy surface for a conduction band with the effective mass $m^*/m_0 = 8.2 \times 10^{-3}$, the distance between the Landau levels is $2\mu^* H/k \approx 204$ K [13]. If we also take into account the data [13] on the value of the Fermi energy for electrons and, for the purposes of estimation, set $2\Delta = 0.03$ eV = 348 K, then the ratio $\Delta/\mu^* H = 1.71$; moreover, according to (22), we may assume that, in the observation of the Shubnikov–de Haas effect, the intersubband transitions are frozen out. The freeze-out temperature in this case can be determined from inequality (24), which gives a temperature value equal to 10.3 K, in satisfactory agreement with experiment [15]. A similar situation is encountered in highly anisotropic layered crystals. However, in this situation we must take into account the effect of the magnetic field on charge-carrier scattering and, since the quasi-classical approximation is no longer valid, use the formulas from [16] rather than the formulas of this study. In addition, we should note that the authors of [4] consider oscillations of the scattering probability of charge carriers as the main cause of the Shubnikov–de Haas effect. This is equivalent to the assumption that the relaxation time is inversely proportional to the density of states in the magnetic field, with an allowance made for the effect of all the lower lying Landau subbands on the density of states. However, the resulting correction to the oscillating component of the conductivity does not affect the oscillation frequencies.

3. CONCLUSIONS

Thus, we have shown that, under the conditions of the applicability of the quasi-classical approximation, the presence of frequencies in the spectrum of the oscillations of the longitudinal conductivity that are not associated with the stationary cross sections of the Fermi surface cut by planes normal to the field, as well as the deviation of the field dependence of the corresponding amplitudes from the linear law or "the 3/2 law," can serve as a measure of the deviation of the dispersion relation, which describes the charge carrier motion, from linear or parabolic, respectively. Furthermore, it is shown that, in crystals with narrow conduction minibands or with small values of the Fermi energy and small transverse charge-carrier effective masses, the intersubband transitions in the Shubnikov–de Haas effect can freeze out. This freeze out is, at least, in qualitative agreement with the experiment and with the theoretical results obtained by previous authors without using the assumption of the nonparabolicity of the conduction band. On the basis of the results obtained during the preparation of this publication, it should be noted that, in order to study fine details of the topology of the Fermi surface of conducting materials (especially unconventional ones), it is necessary to perform the experiments in strong quantizing magnetic fields, i.e., in the region of large deviations from the traditional quasi-classical approximation. However, for this purpose, the topology the Fermi surface must be first parametrized, e.g., on the basis of rough calculations of the band structure, and the optimum set of orientations of the magnetic field for which these deviations are pronounced most clearly must be determined.

REFERENCES

1. I. M. Lifshitz and A. M. Kosevich, Izv. Akad. Nauk SSSR, Ser. Fiz. **19**, 395 (1955).
2. V. V. Andreev and A. M. Kosevich, Zh. Éksp. Teor. Fiz. **39**, 741 (1960) [Sov. Phys. JETP **12**, 517 (1960)].
3. E. M. Lifshitz and L. P. Pitaevskiĭ, *Physical Kinetics* (Nauka, Moscow, 1979; Pergamon, Oxford, 1981).
4. A. A. Abrikosov, *Fundamentals of the Theory of Metals* (Nauka, Moscow, 1987; North-Holland, Amsterdam, 1988).
5. R. F. Fivaz, J. Phys. Chem. Solids **28**, 839 (1967).
6. J. M. Harper and T. H. Geballe, Phys. Lett. A **54A**, 27 (1975).
7. A. S. Bender and D. A. Young, J. Phys. C **5**, 2163 (1972).
8. M. P. Zayachkovskiĭ, D. M. Bercha, and N. F. Zayachkovskaya, Ukr. Fiz. Zh. **23**, 1119 (1978).
9. V. G. Peschanskiĭ, Zh. Éksp. Teor. Fiz. **121**, 1204 (2002) [JETP **94**, 1035 (2002)].
10. V. F. Gantmakher and I. B. Levinson, *Scattering of Carriers in Metals and Semiconductors* (Nauka, Moscow, 1984; North-Holland, Amsterdam, 1987).
11. A. Isihara, *Statistical Physics* (Academic, New York, 1971; Mir, Moscow, 1973).
12. I. S. Gradshteyn and I. M. Ryzhik, *Table of Integrals, Series, and Products*, 5th ed. (Nauka, Moscow, 1971; Academic, New York, 1980).
13. P. V. Gorskiĭ, Ukr. Fiz. Zh. **26**, 1528 (1981).
14. D. Shoenberg, *Magnetic Oscillations in Metals* (Cambridge Univ. Press, Cambridge, 1984; Mir, Moscow, 1986).
15. S. Tanuma and R. Inada, J. Phys.: Condens. Matter **19**, 95 (1975).
16. P. V. Gorskiĭ, Fiz. Nizk. Temp. **12**, 584 (1986) [Low Temp. Phys. **12**, 329 (1986)].

Translated by I. Zvyagin

Semiconductors, Vol. 39, No. 3, 2005, pp. 331–335. Translated from Fizika i Tekhnika Poluprovodnikov, Vol. 39, No. 3, 2005, pp. 349–353.
Original Russian Text Copyright © 2005 by Il'chuk, Nikitin, Nikolaev, V. Rud', Yu. Rud', Terukov.

The Charge-Transport Mechanisms and Photosensitivity of *n*-ZnO:Al/Cu*Pc*/*p*-Cu(In,Ga)Se_2 Structures

G. A. Il'chuk*, S. E. Nikitin*, Yu. A. Nikolaev*, V. Yu. Rud'^, Yu. V. Rud'*, and E. I. Terukov***

**Ioffe Physicotechnical Institute, Russian Academy of Sciences, St. Petersburg, 194021 Russia*

***St. Petersburg State Polytechnic University, St. Petersburg, 195251 Russia*

^e-mail: rudvas@spbstu.ru

Submitted May 11, 2004; accepted for publication May 17, 2004

Abstract—The first photosensitive *n*-ZnO:Al/Cu*Pc*/*p*-Cu(In,Ga)Se_2 structures are produced by a vacuum sublimation of copper phthalocyanine onto the surface of thin *p*-Cu(In,Ga)Se_2 films and a subsequent magnetron deposition of *n*-ZnO:Al films. The steady-state current–voltage characteristics of the resulting structures are studied. The charge-transport and photosensitivity mechanisms of the thin-film structures are discussed. The structures appear promising for the fabrication of wide-range (1.2–3.3 eV) thin-film photoelectric converters.
© 2005 Pleiades Publishing, Inc.

1. INTRODUCTION

Studies of I–III–V ternary diamond-like compounds have resulted in the fabrication of ZnO/CdS/Cu(In,Ga)Se_2 structures with a record-high quantum photoconversion efficiency of η = 19.2% and extraordinary radiation hardness [1–3]. The presence of toxic Cd in these structures has stimulated a search for candidates to replace the CdS barrier component [2]. Recently, we have found that it is possible to use films of synthetic copper phthalocyanine Cu*Pc*, whose semiconductor properties have long been known [4–6], in the production of photosensitive structures. In this paper, we report the results from the first study of the photoelectric characteristics of thin-film *n*-ZnO:Al/Cu*Pc*/Cu(In,Ga)Se_2 structures, in which the copper phthalocyanine films are used as the barrier component.

1. In the production of the photosensitive structures, we used thin ($d \approx 2$ μm) *p*-$CuIn_xGa_{1-x}Se_2$ polycrystalline films grown on glass substrates covered with a pure molybdenum ($d \approx 1$ μm) sublayer. Elemental analysis of the $CuIn_xGa_{1-x}Se_2$ films showed that, depending on the fabrication conditions, x varies between different films by 5–8%, whereas it remains constant, within the experimental error, over the surface of each film, which is indicative of the high homogeneity of the material.

The copper phthalocyanine Cu*Pc* films were deposited onto the surface of a Cu(In,Ga)Se_2 solid solution by thermal sublimation in vacuum at a substrate temperature of approximately 50°C. Phthalocyanine films are uniformly blue and their surfaces are mirror-smooth. Furthermore, they demonstrate a good adhesion to the surface of as-grown Cu(In,Ga)Se_2. The thickness of the Cu*Pc* films reached ~0.5 μm. In addition, a ZnO:Al film was deposited onto the as-grown Cu*Pc* film by the magnetron sputtering of a sintered (ZnO + 2.5 wt % Al) target in an Ar atmosphere. The deposited ZnO:Al film demonstrated high conductivity (50 Ω/cm^2) and was transparent in the spectral range 0.365–1.0 μm. The density of the free electrons in these films, which had a thickness of up to 1 μm, was ~10^{20} cm^{-3} at 300 K. The outer surface of the ZnO:Al films deposited onto Cu*Pc* was mirror-smooth, and their color was defined by the thickness.

2. Studies of the steady-state current–voltage [$I(U)$] characteristics of the first obtained *n*-ZnO:Al/Cu*Pc*/*p*-Cu(In,Ga)Se_2 structures demonstrated a distinct rectification (Fig. 1, curve *1*). The forward bias in these structures corresponds to the negative potential at the top *n*-ZnO:Al film, in much the same way as it does in the already known ZnO:Al/CdS/Cu(In,Ga)Se_2 solar cells [6]. Therefore, we may assume that the organic semiconductor Cu*Pc* plays the role of the energy barrier in contact with the Cu(In,Ga)Se_2 surface, as, indeed, we expected when we replaced CdS with Cu*Pc* in these structures (see the inset in Fig. 1).

As well as the $I(U)$ characteristics of the *n*-ZnO:Al/Cu*Pc*/Cu(In,Ga)Se_2 structures, we also studied the characteristics of the constituent heterostructures Cu*Pc*/Cu(In,Ga)Se_2 (Fig. 1, curve *2*) and *n*-ZnO:Al/Cu*Pc* (Fig. 1, curve *3*). The conducting direction in the *n*-ZnO:Al/Cu*Pc* structure corresponds to the negative potential at ZnO, and the conducting direction in the Cu*Pc*/Cu(In,Ga)Se_2 structure, to the negative potential at Cu*Pc*. As a result, the active regions in both components of the *n*-ZnO:Al/Cu*Pc*/Cu(In,Ga)Se_2 structure, i.e., *n*-ZnO:Al/Cu*Pc* and Cu*Pc*/Cu(In,Ga)Se_2, are connected in series in such a way that their rectification directions coincide.

When considering the charge-transport mechanism, we also took into account the properties of an *n*-ZnO:Al/*p*-Cu(In,Ga)Se_2 heterojunction. As can be seen in Fig 1 (curve *4*), the structures under consider-

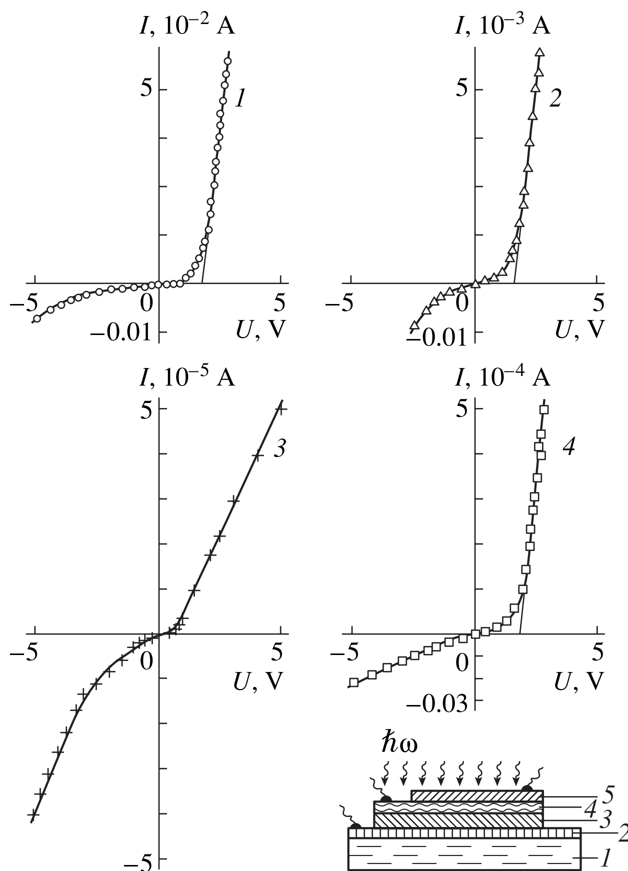

Fig. 1. Steady-state $I(U)$ characteristics at $T = 300$ K for the structures (*1*) *n*-ZnO:Al/Cu*Pc*/*p*-Cu(In,Ga)Se_2, (*2*) Cu*Pc*/*p*-Cu(In,Ga)Se_2, (*3*) *n*-ZnO:Al/Cu*Pc*, and (*4*) *n*-ZnO:Al/*p*-Cu(In,Ga)Se_2. Forward bias: the positive potential at (*1*, *2*, *4*) *p*-Cu(In,Ga)Se_2 and (*3*) Cu*Pc*. In the inset, the configuration of the *n*-ZnO:Al/Cu*Pc*/*p*-Cu(In,Ga)Se_2 structure—(*1*) glass plate, (*2*) Mo film, (*3*) *p*-Cu(In,Ga)Se_2, (*4*) Cu*Pc*, and (*5*) *n*-ZnO:Al—and its illumination is shown.

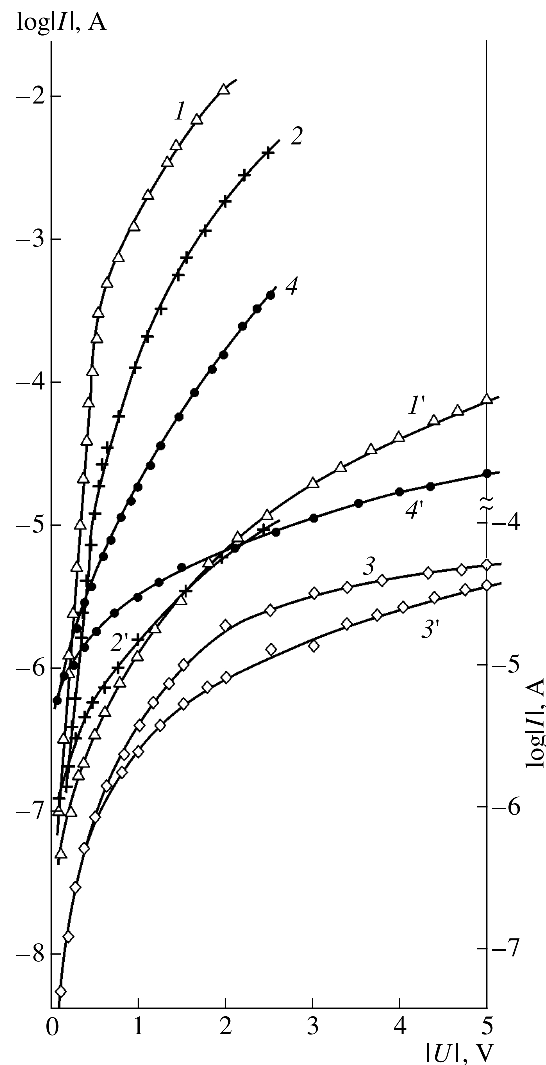

Fig. 2. Steady-state $I(U)$ characteristics at $T = 300$ K (semi-log scale) for the structures (*1*, *1*') *n*-ZnO:Al/Cu*Pc*/*p*-Cu(In,Ga)Se_2, (*2*, *2*') Cu*Pc*/*p*-Cu(In,Ga)Se_2, (*3*, *3*') *n*-ZnO:Al/Cu*Pc*, and (*4*, *4*') *n*-ZnO:Al/Cu*Pc*/*p*-Cu(In,Ga)Se_2. Curves *1*–*4* show the forward characteristics; curves *1*'–*4*', the reverse characteristics. For curves *1*, *1*', *2*, *2*', *4*, and *4*', refer to the left-hand scale; for curves *3* and *3*', the right-hand scale.

ation also demonstrate rectification, with the conducting direction corresponding to the negative potential at the *n*-ZnO:Al film. As can be seen, the insertion of the Cu*Pc* film into the ZnO:Al/Cu*Pc*/Cu(In,Ga)Se_2 structure does not affect the characteristic rectification direction of the ZnO:Al/*p*-Cu(In,Ga)Se_2 structure.

Figure 2 shows the steady-state $I(U)$ characteristics of the structures under study in a semilogarithmic scale. These data show that the initial portion of the $I(U)$ characteristic is described by the exponential diode equation [6]

$$I = I_s\left[\exp\left(\frac{eU}{nkT}\right) - 1\right]. \quad (1)$$

The saturation current I_s and the diode factor n for the structures being compared are listed in the table. As can be seen from Fig. 2 (curve *1*), the exponential dependence of the forward current is most clearly pronounced in the ZnO:Al/Cu*Pc*/Cu(In,Ga)Se_2 structure and is observed within a current variation of approximately four orders of magnitude. Namely, in these structures, the diode factor can be related to a recombination of the carriers in the active region [6]. In the constituent heterojunctions Cu*Pc*/Cu(In,Ga)Se_2 and ZnO:Al/Cu*Pc*, and also in the ZnO:Al/Cu(In,Ga)Se_2 heterojunction, the value of the factor n far exceeds $n = 2$ (see table), which allows us to assume that the forward current in the compared structures is of a tunnel-recombination nature. For the ZnO:Al/Cu(In,Ga)Se_2 heterojunction, an increase in the saturation current I_s with respect to that in the ZnO:Al/Cu*Pc*/Cu(In,Ga)Se_2 structure is observed (see table). The rectification factor K for the structures under study, which is defined as the ratio of forward to reverse current at the same mag-

Photoelectric properties of the structures at $T = 300$ K

Structure type	K^*	I_s, 10^{-8} A	n	R_0, Ω	U_0, V	$\hbar\omega^m$, eV	δ, eV	S_U^m, V W^{-1}
n-ZnO : Al/CuPc/p-Cu(In, Ga)Se_2	3200	1	1.6	70	1.75	1.5	0.76	50
	(2.5)					2.45	0.67	
CuPc/p-Cu(In, Ga)Se_2	300	2	3.3	630	1.6	1.5	0.44	0.02
	(2)							
n-ZnO : Al/CuPc	2	0.1	5.1	105	0.6	1.5	0.44	5
	(2)					2.45	0.4	
n-ZnO : Al/p-Cu(In, Ga)Se_2	40	4	15–20	6×10^3	~1.7	1.65	1.28	200
	(2.5)							

Note: The bias voltage (in volts) is given in parentheses.

nitude of bias (see the table and Fig. 2), is at its highest ($K \approx 3200$ at $U = 2.5$ V) for the thin-film ZnO:Al/CuPc/Cu(In,Ga)Se_2 structures. In combination with the lowest n in these structures, this fact leads to the conclusion that the introduction of organic semiconductors into thin-film structures does not impair the charge-transport process as it does in heterostructures based on inorganic materials, for which a precise matching of crystal lattice parameters and thermal expansion coefficients is necessary [7, 8]. In the case of organic semiconductors (e.g., CuPc), this condition is removed.

As can be seen from Fig. 1, when the forward bias exceeds a certain value, the dark current starts to follow the linear law

$$I = \frac{U - U_0}{R_0}. \quad (2)$$

The cutoff voltage U_0 and the residual resistance R_0 for the different structures under study are listed in the table. The similar values of U_0 in the ZnO:Al/CuPc/Cu(In,Ga)Se_2 and CuPc/Cu(In,Ga)Se_2 structures evidently indicate that the charge-transport properties are mainly defined by the height of the energy barrier on the CuPc/Cu(In,Ga)Se_2 interface. At the same time, the significant decrease in U_0 for the ZnO:Al/CuPc heterojunction may indicate a decrease in the barrier height on the heterointerface in respect to CuPc/Cu(In,Ga)Se_2. It is also very important to note that ZnO:Al/CuPc/Cu(In,Ga)Se_2 demonstrates the lowest resistance, $R_0 \approx 70$ Ω, among all the structures under study. This fact is a strong argument in favor of the application of organic semiconductors (for example, CuPc) for the production of thin-film photovoltaic structures.

Figure 3 shows the typical steady-state $I(U)$ characteristics of the structures under study on the log–log scale. The principal feature of these structures is the power-law dependence of the current on the voltage, $I \propto U^m$, which is typical of inorganic semiconductors. The values of m for the forward and reverse biases are shown in Fig. 3 (adjacent to the curves for the forward and reverse biases). In the ZnO:Al/CuPc/Cu(In,Ga)Se_2 structures (Fig. 3, curves *1* and *1*'), the reverse current at $U \leq 0.4$ V is described by the exponent $m \approx 1$; according to [9], this can be attributed to the tunneling of carriers or to a space-charge-limited current in the velocity-saturation mode. The exponent $m \approx 1$ was also observed for the reverse $I(U)$ characteristics in the other

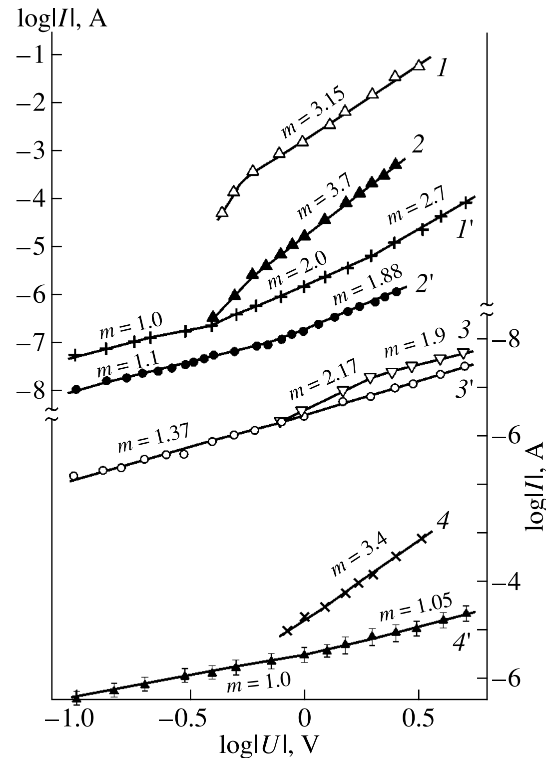

Fig. 3. Steady-state $I(U)$ characteristics at $T = 300$ K (log-log scale) for the structures (*1*, *1*') n-ZnO:Al/CuPc/p-Cu(In,Ga)Se_2, (*2*, *2*') CuPc/p-Cu(In,Ga)Se_2, (*3*, *3*') n-ZnO:Al/CuPc, and (*4*, *4*') n-ZnO:Al/p-Cu(In,Ga)Se_2. Curves *1*–*4* show the forward characteristics; curves *1*'–*4*', reverse characteristics. For curves *1*, *1*', *2*, and *2*', refer to the left-hand scale; for curves *3*, *3*', *4*, and *4*', the right-hand scale.

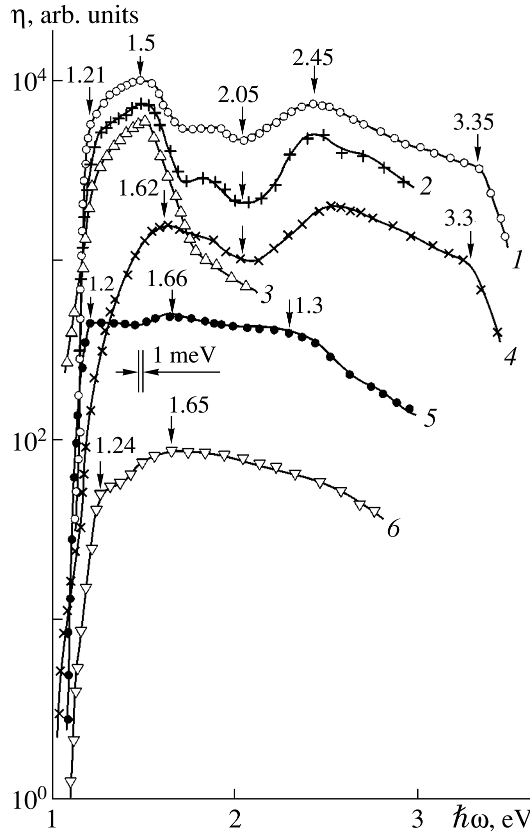

Fig. 4. Spectra of the relative quantum photoconversion efficiency of the structures (*1*) *n*-ZnO:Al/Cu*Pc*/*p*-Cu(In,Ga)Se_2, (*2*) *n*-ZnO:Al/Cu*Pc*, (*3*) Cu*Pc*/*p*-Cu(In,Ga)Se_2, (*4*) *n*-ZnO:Al/Cu*Pc*/*p*-Si, (*5*) *n*-ZnO:Al/*n*-CdS/*p*-Cu(In,Ga)Se_2, and (*6*) *n*-ZnO:Al/*p*-Cu(In,Ga)Se_2. Unpolarized illumination at $T = 300$ K. Illumination: (*1*, *2*, *4*–*6*) from the side of ZnO:Al and (*3*) from the side of Cu*Pc*.

structures (Fig. 3, curves *2*'–*4*'), in different ranges of bias; therefore, it can be interpreted in a similar way as in the case of the ZnO:Al/Cu*Pc*/Cu(In,Ga)Se_2 structure. As can be seen in Fig. 3, in the ZnO:Al/Cu*Pc*/Cu(In,Ga)Se_2 and Cu*Pc*/Cu(In,Ga)Se_2 structures, the exponent $m \approx 2$ at the reverse bias $U \geq 0.4$ V. This behavior is usually attributed to the space-charge-limited current in the mobility mode [9]. At the forward bias $U \geq 0.4$ V, the rise in current becomes steeper, with the exponent $m = 3$–3.7, which means that a continuous (exponential) energy distribution of traps must be taken into account [9]. For the ZnO:Al/Cu*Pc* heterojunction, the dependence $I \propto U^m$ is only weakly dependent on the direction of the current, and the values of m correspond to those discussed above (Fig. 3, curves *3*, *3*'). Finally, the $I(U)$ characteristics of the ZnO:Al/Cu(In,Ga)Se_2 heterojunction (Fig. 3, curves *4*, *4*') are quite similar to those of the ZnO:Al/Cu*Pc*/Cu(In,Ga)Se_2 structure, which indicates the similarity of the charge-transport mechanisms in structures produced from semiconductors of different types.

3. Illumination of the ZnO:Al/Cu*Pc*/Cu(In,Ga)Se_2 structures induces photovoltage with the ZnO:Al film negative, which correlates with the direction of the rectification and is not sensitive to illumination intensity, photon energy, or the position of the light probe (which is ~0.3 mm in diameter) on the structure surface. The maximum open-circuit photovoltage of the ZnO:Al/Cu*Pc*/Cu(In,Ga)Se_2 structures is $U_{oc} \approx 100$ mV, the short-circuit current is $I_{sc} \approx 1$ mA at a power density of light from an incandescent lamp equal to 10 mW/cm^2. The maximum voltage sensitivity S_u of the ZnO:Al/Cu*Pc*/Cu(In,Ga)Se_2 structures is ~50 V/W (see the table), and it is usually reached under illumination from the side of the ZnO:Al film. It is noteworthy that the sign of the photovoltage in the ZnO:Al/Cu*Pc*/Cu(In,Ga)Se_2 structures coincides with that typical of the widely studied and recognized ZnO:Al/CdS/Cu(In,Ga)Se_2 [1] and ZnO:Al/Cu(In,Ga)Se_2 structures, i.e., in these structures, the ZnO film is negatively charged. The fact that the Cu(In,Ga)Se_2 film in the Cu*Pc*/Cu(In,Ga)Se_2 structure is positively charged while the ZnO film in ZnO:Al/Cu*Pc* has a negative charge, indicates that the barriers in these structures are connected so that their photovoltages are summed up, which excludes the possibility of the conversion of the photovoltage sign.

Figure 4 (curve *1*) shows a typical spectrum for the relative photoconversion efficiency $\eta(\hbar\omega)$ of one of the ZnO:Al/Cu*Pc*/Cu(In,Ga)Se_2 structures at $T = 300$ K under illumination with nonpolarized light from the side of the *n*-ZnO:Al film. A wide-band spectrum of $\eta(\hbar\omega)$ is observed, with the red edge defined by direct band-to-band transitions in the solid solution. This dependence obeys a relation typical of the direct band-to-band transitions in the absorption spectrum of the Cu(In,Ga)Se_2 solid solution [7]:

$$\eta\hbar\omega = A(E_g - \hbar\omega)^{1/2}, \quad (3)$$

where A is a constant and E_g is the band gap of Cu(In,Ga)Se_2. An extrapolation of the type $(\eta\hbar\omega)^2 \longrightarrow 0$ yields the band gap $E_g \approx 1.2$ eV for the solid solution, which is in agreement with the optical-absorption data [6]. The onset of a short-wavelength cutoff at $\hbar\omega > 3.35$ eV agrees with the band gap of ZnO [10]; therefore, it can be related to the increase in the optical absorption of the front *n*-ZnO:Al film in the range $\hbar\omega > E_g^{ZnO}$. In the range between the band gaps of the wide- and narrow-gap components of the ZnO:Al/Cu*Pc*/Cu(In,Ga)Se_2 structure, a maximum photosensitivity, with two peaks at $\hbar\omega_1 = 1.5$ eV and $\hbar\omega_2 = 2.45$ eV, and a distinct dip in the range $\hbar\omega \cong 2.5$ eV is observed. As can be seen in Fig. 4, the specific features discussed in relation to the $\eta(\hbar\omega)$ spectrum of the ZnO:Al/Cu*Pc*/Cu(In,Ga)Se_2 structure (curve *1*) are also satisfactorily reproduced in the photosensitivity spectra of the constituents of this structure (curves *2* and *3*), with similar values of the FWHM (δ) of the photosensitivity peak (see the table).

It is necessary to note that, in the range of its peak, the $\eta(\hbar\omega)$ spectrum of the ZnO:Al/Cu*Pc*/Cu(In,Ga)Se_2 structure is similar to that observed earlier in the thin-film ZnO:Al/Cu*Pc*/Si structures [11]. This similarity is related to the discrete character of the optical absorption spectrum of Cu*Pc* and results in the photosensitivity spectrum also becoming discrete. In principle, this circumstance can ensure that a photoelectric converter will exhibit photosensitivity only in certain spectral ranges.

Figure 4 shows also the typical $\eta(\hbar\omega)$ spectra of thin-film photoelectric converters based on the *n*-ZnO:Al/*n*-CdS/*p*-Cu(In,Ga)Se_2 and *n*-ZnO:Al/*p*-Cu(In,Ga)Se_2 structures (curves *5* and *6*, respectively). These structures were fabricated on the same Cu(In,Ga)Se_2 films as in the case of the ZnO:Al/Cu*Pc*/Cu(In,Ga)Se_2 structure. It can be seen that the red edge $\eta(\hbar\omega)$ for these structures is the same as for the ZnO:Al/Cu*Pc*/Cu(In,Ga)Se_2 structure. A certain amount of scatter in the energy position of the step in the $\eta(\hbar\omega)$ spectrum at $\hbar\omega_0$ = 1.20–1.24 eV (Fig. 4, curves *1*, *5*, and *6*) is related to fluctuations of the atomic composition x in the Cu(In,Ga)Se_2 films; moreover, the decrease of $\eta(\hbar\omega)$ in these structures begins at $\hbar\omega > 1.7$ eV, which can be related to absorption by the CdS and ZnO films [10]. The principal distinctive feature of the $\eta(\hbar\omega)$ spectra in the photosensitivity range for the ZnO:Al/CdS/Cu(In,Ga)Se_2 and ZnO:Al/Cu*Pc*/Cu(In,Ga)Se_2 structures is that these spectra don't demonstrate the dip (Fig. 4, curves *5* and *6*) typical of the structures containing the Cu*Pc* film (Fig. 4, curve *1*). Therefore, the photosensitivity spectra of the structures without the Cu*Pc* film exhibit no dips and a higher $\delta \approx 1.3$ eV is observed (see table).

4. Thus, the first thin-film photosensitive ZnO:Al/Cu*Pc*/Cu(In,Ga)Se_2 structures have been produced. The wide-band character of the photosensitivity of structures containing copper phthalocyanine is demonstrated. The results obtained in the study of the charge-transport and photosensitivity processes indicate that these structures are promising for application in wide-band ecologically safe photoelectric converters.

The study was supported by the program "New Principles of Energy Conversion in Semiconductor Structures" of the Russian Academy of Sciences.

REFERENCES

1. U. Rau and H. W. Schock, Ser. Photoconvers. Sol. Energy **1**, 277 (2001).
2. A. Jasenek and U. Rau, J. Appl. Phys. **90**, 650 (2001).
3. K. Weinert, U. Rau, A. Jasenek, *et al.*, in *Proceedings of 17th European Photovoltaic Solar Energy Conference* (WIP-Munich, Germany, 2002), p. 2167.
4. A. T. Vartyanyan, Zh. Fiz. Khim. **22**, 769 (1948).
5. D. D. Eley, Nature **162**, 819 (1948).
6. T. J. Couts, L. L. Kazmerskii, and S. Wagner, *Copper Indium Diselenide for Photovoltaic Applications* (Pergamon, New York, 1986).
7. S. M. Sze, *Physics of Semiconductor Devices*, 2nd ed. (Wiley, New York, 1981; Mir, Moscow, 1984).
8. A. G. Milns and J. J. Feucht, *Heterojunctions and Metal–Semiconductor Junctions* (Academic, New York, 1972; Mir, Moscow, 1975).
9. M. A. Lampert and P. Mark, *Current Injection in Solids* (Academic, New York, 1970; Mir, Moscow, 1973).
10. *Physicochemical Properties of Semiconductor Materials: Handbook*, Ed. by A. V. Novoselova and V. B. Lazarev (Nauka, Moscow, 1979) [in Russian].
11. G. A. Il'chuk, N. V. Klimova, O. I. Kon'kov, *et al.*, Fiz. Tekh. Poluprovodn. (St. Petersburg) **38**, 1056 (2004) [Semiconductors **38**, 1018 (2004)].

Translated by D. Mashovets

Semiconductors, Vol. 39, No. 3, 2005, pp. 336–342. Translated from Fizika i Tekhnika Poluprovodnikov, Vol. 39, No. 3, 2005, pp. 354–360.
Original Russian Text Copyright © 2005 by Domashevskaya, Seredin, Dolgopolova, Zanin, Arsent'ev, Vinokurov, Stankevich, Tarasov.

SEMICONDUCTOR STRUCTURES, INTERFACES, AND SURFACES

Vegard's Law and Superstructural Phases in $Al_xGa_{1-x}As$/GaAs(100) Epitaxial Heterostructures

É. P. Domashevskaya*^, P. V. Seredin*, É. A. Dolgopolova*, I. E. Zanin*, I. N. Arsent'ev, D. A. Vinokurov**^^, A. L. Stankevich**, and I. S. Tarasov****

**Voronezh State University, Universitetskaya pl. 1, Voronezh, 394006 Russia*

^e-mail: root@ftt.vsu.ru

***Ioffe Physicotechnical Institute, Russian Academy of Sciences, Politekhnicheskaya ul. 26, St. Petersburg, 194021 Russia*

^^e-mail: dmitry.vinokurov@mail.ioffe.ru

Submitted May 25, 2004; accepted for publication June 7, 2004

Abstract—The lattice constants of $Al_xGa_{1-x}As$ epitaxial alloys with various AlAs (x) contents are determined for $Al_xGa_{1-x}As$/GaAs(100) heterostructures grown by MOC-hydride epitaxy using X-ray diffractometry and an X-ray back-reflection method. An ordered $AlGaAs_2$ (superstructural) phase is found in epitaxial heterostructures with $x \approx 0.50$. The lattice constant of this phase is smaller than the lattice constants of an $Al_{0.50}Ga_{0.50}As$ alloy and GaAs single-crystal substrate. © *2005 Pleiades Publishing, Inc.*

1. INTRODUCTION

The main tendency in the development of modern electronics is the use of submicron- and nanometer-sized functional objects (components). The unique properties of these objects (nanostructures) are determined by the atomic and electron processes both in the bulk and at the boundaries of heterostructures [1]. In this context, researchers are currently intensively developing both the theory of the phenomena in small objects, the so-called low-dimensional systems, and new precision methods for their study [2]. It is well known that isomorphic compounds, including AlAs and GaAs, form continuous solid solutions [3]. For epitaxial growth, the lattice matching of a film and a substrate possessing different chemical compositions is of great importance. The $Al_xGa_{1-x}As$/GaAs heterostructure possesses this property. This structure, whose lattice mismatch is $\lesssim 0.15\%$, is widely used in various structures and devices [4].

Gallium arsenide is the best-studied and most widely used III–V material. In contrast, AlAs is one of the least known compounds, which can be explained by its very high melting point (1700°C) and its instability, which is due to its decomposition in air. Gallium arsenide and AlAs both have sphalerite crystal lattices with almost equal values for the lattice constants and ionicity; as a result, the growth of $Al_xGa_{1-x}As$ layers on GaAs substrates is quite straightforward and the crystal quality of the obtained alloys is relatively high. A specific feature of this system is an increase in the crystal-lattice constants of the alloy in conjunction with an increase in the content of the Al atoms, which replace the Ga atoms in the metal sublattice, owing to the larger size of an Al atom.

When growing thin heteroepitaxial layers on a bulk substrate, the lattice mismatch, in some cases, does not cause the generation of misfit dislocations. However, the epitaxial layer is uniformly elastically strained in the plane parallel to the heterointerface [5]. Under these circumstances, in order to find the lattice constant of the alloy a^{ν}, taking into account the elastic strain in the heteroepitaxial layer, the normal and parallel components of the lattice constant, $a^{\perp}$ and $a^{\parallel}$, should be determined from the results of an X-ray diffraction analysis. According to the theory of elasticity, this constant can be calculated as [6]

$$a^{\nu} = a^{\perp}\frac{1-\nu}{1+\nu} + a^{\parallel}\frac{2\nu}{1+\nu}, \tag{1}$$

where ν are the Poisson ratios for the epitaxial layers.

The expressions for the lattice constants of the AlAs and AlGaAs epitaxial layers are written as [6]

$$a^{\nu}_{AlAs} = a^{\perp}_{AlAs}\frac{1-\nu_{AlAs}}{1+\nu_{AlAs}} + a^{\nu}_{GaAs}\frac{2\nu_{AlAs}}{1+\nu_{AlAs}}, \tag{2}$$

$$\begin{aligned} a^{\nu}_{Al_xGa_{1-x}As} = {} & a^{\perp}_{Al_xGa_{1-x}As}\frac{1-\nu_{Al_xGa_{1-x}As}}{1+\nu_{Al_xGa_{1-x}As}} \\ & + a^{\nu}_{GaAs}\frac{2\nu_{Al_xGa_{1-x}As}}{1+\nu_{Al_xGa_{1-x}As}}, \end{aligned} \tag{3}$$

where

$$\nu_{Al_xGa_{1-x}As} = x\nu_{AlAs} + (1-x)\nu_{GaAs},$$

1063-7826/05/3903-0336$26.00 © 2005 Pleiades Publishing, Inc.

and relation (3) can be rewritten as

$$a^{\nu}_{Al_xGa_{1-x}As} = a^{\perp}_{Al_xGa_{1-x}As}\frac{1-(x\nu_{AlAs}-(1-x)\nu_{GaAs})}{1+(x\nu_{AlAs}+(1-x)\nu_{GaAs})} + a^{\nu}_{GaAs}\frac{2(x\nu_{AlAs}+(1-x)\nu_{GaAs})}{1+(x\nu_{AlAs}+(1-x)\nu_{GaAs})}. \quad (4)$$

To calculate the lattice constants of the alloys, we used Poisson ratios taken from previously published data, namely $\nu_{AlAs} = 0.255$ [6, 7] and $\nu_{GaAs} = 0.312$ [8]. However, we experimentally determined only the $a^{\perp}$ components of the lattice constant for the heteroepitaxial structures, which correspond to measured values of the interplanar spacings $d^{\perp}$.

It is generally assumed that the dependence of the lattice constant on the Al content in the $Al_xGa_{1-x}As$ alloys follows Vegard's law [9]. However, the published data on the linearity or nonlinearity of the dependence of the lattice constants of alloys in the AlAs–GaAs system are contradictory [10, 11].

The purpose of this study is to determine the dependence of these lattice constants on the composition of $Al_xGa_{1-x}As$ epitaxial layers grown on a single-crystal GaAs (100) substrate by MOC-hydride epitaxy.

2. RESULTS AND DISCUSSION

2.1. Characteristics of the Epitaxial Structures under Study

The heterostructures under study were grown at the Ioffe Physicotechnical Institute. The epitaxial $Al_xGa_{1-x}As$ single-crystal films were grown on single-crystal GaAs (100) substrates by MOC-hydride epitaxy. The data on the Al content in the $Al_xGa_{1-x}As$ alloys and the film thicknesses are listed in Table 1.

Since the thickness of the $Al_xGa_{1-x}As$ films was rather large, it was possible to use an X-ray structure analysis to determine their lattice constants. The layer of half-absorptance for Cu$K\alpha_{1,2}$ radiation, which primarily diffracts the X-ray beam, was about 15 μm thick for the $Al_xGa_{1-x}As$/GaAs(100) system under study. Consequently, we could expect, at least for large angles, two independent reflections of different intensities, one from the film and the other from the substrate, which are caused by a lattice mismatch between the epitaxial film of the $Al_xGa_{1-x}As$ alloy and the GaAs (100) substrate. We determined the interplanar spacings and lattice constants of the $Al_xGa_{1-x}As$ epitaxial films and the GaAs (100) substrates for the samples under study using two methods of X-ray structure analysis, namely, X-ray diffractometry and, for the planar sample, the X-ray back-reflection method.

2.2. Results of Measurements of the Lattice Constants Using X-Ray Diffractometry

We carried out all the X-ray diffraction measurements using DRON-4-07 and DRON-3 diffractometers

Table 1. Characteristics of the studied samples

Samples	Heterostructures	Thicknesses of epitaxial layers, μm
EM28	$Al_{0.12}Ga_{0.88}As$/GaAs	1
EM29	$Al_{0.16}Ga_{0.84}As$/GaAs	1
EM135	$Al_{0.50}Ga_{0.50}As$/GaAs	1
EM49	$Al_{0.54}Ga_{0.49}As$/GaAs	1
EM77	$Al_{>0.80}Ga_{<0.20}As/Al_{0.30}Ga_{0.70}As/Al_{>0.80}Ga_{<0.20}As$/GaAs	~0.5/0.2/0.1
EM72	AlAs/GaInP/AlAs/GaAs	~0.5/0.2/1

(Cu$K\alpha_{1,2}$ radiation). A specific feature of an X-ray diffraction analysis of single-crystal samples of a certain orientation is the fact that we can record very few X-ray diffraction lines; indeed, only one or two, but rarely three, are possible. The set of diffraction lines depends on the orientation of the single crystal during its growth. For example, for the $Al_xGa_{1-x}As$/GaAs(100) samples under study, there are only two diffraction lines, namely, the (200) line in the range from 31.10° to 31.80° and the (400) line in the range from 65.40° to 66.40°. Figure 1 shows the so-called full-range X-ray diffraction pattern of sample EM135, which was recorded over the entire angle range 2θ using the DRON-4-07 diffractometer. To determine the lattice constants of the epitaxial films, we selected the (400) line. The interplanar spacings and lattice constants at this stage of study were determined with an accuracy of ~0.001 Å.

When investigating the profiles of diffraction lines for multicomponent samples, the X-ray diffraction lines of various phases can overlap, which, in fact, occurs for $Al_xGa_{1-x}As$ films grown on a GaAs (100)

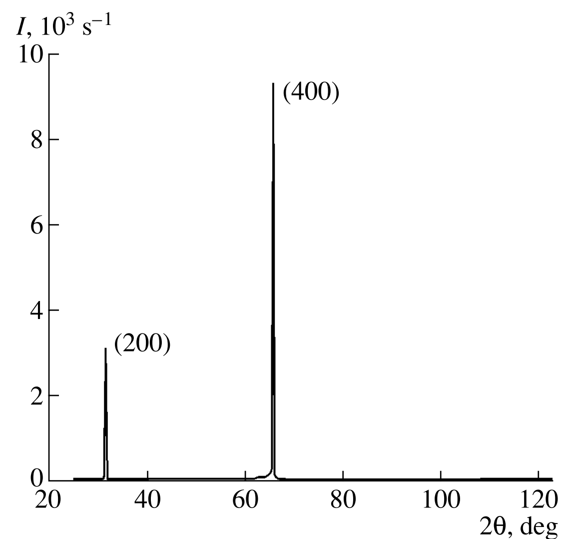

Fig. 1. The survey X-ray diffraction pattern of the $Al_{0.50}Ga_{0.50}As$/GaAs(100) epitaxial heterostructure.

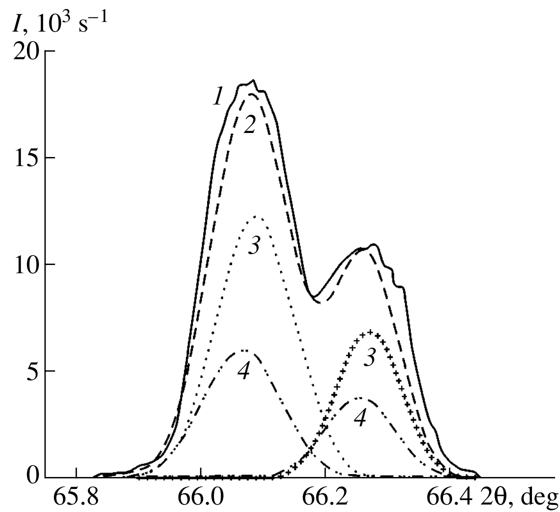

Fig. 2. Diffraction lines (400) from the $Al_{0.16}Ga_{0.84}As$/GaAs(100) heterostructure. Curve *1* corresponds to the experiment, and curves *2–4* correspond to the approximation. The diffraction lines correspond to (*1*, *2*) the heterostructure, (*3*) GaAs (substrate), and (*4*) the $Al_{0.16}Ga_{0.84}As$ alloy.

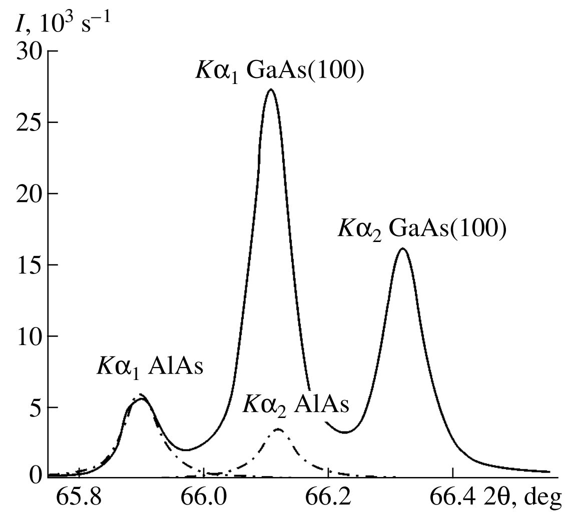

Fig. 3. Diffraction lines (400) for the AlAs/GaInP/AlAs/GaAs(100) heterostructure. The solid line corresponds to the experiment, and the dash-and-dot lines correspond to AlAs (approximation).

substrate. Since the atomic radii of Ga and Al do not significantly differ from each other, this overlap also occurs for the constants of the sphalerite lattices of GaAs and $Al_xGa_{1-x}As$ alloys.

Figure 2 shows the (400) diffraction line of the $Al_xGa_{1-x}As$/GaAs heterostructure with a relatively low Al content ($x = 0.16$). It can be seen from this figure that the diffraction line of the $Al_xGa_{1-x}As$ epitaxial layer with low x practically merges with the diffraction line of the GaAs (100) substrate and appears as a single $K\alpha_{1,2}$ doublet with distorted lines. The shape of this doublet differs from the dispersion lines of the $K\alpha_{1,2}$ doublet for the single-crystal substrate due to the fact that the former doublet is the result of a superposition of two $K\alpha_{1,2}$ doublets. This circumstance introduces additional difficulties when attempting an exact determination of the lattice constants of epitaxial films. The results of the splitting of the (400) line into two $K\alpha_{1,2}$ doublets show (Table 2) that the alloy and the substrate are almost completely lattice-matched at low x. At the highest values of x (samples EM72 and EM77), the angular distance between the $K\alpha_{1,2}$ doublets of the film and the substrate is at its largest. Since the thickness of the film of the $Al_xGa_{1-x}As$ alloy is considerably larger than the thicknesses of the intermediate layers (GaInP in sample EM72 and $Al_{0.30}Ga_{0.70}As$ in sample EM77), the diffraction lines of the intermediate layers do not make much contribution to the (400) diffraction pattern. This circumstance allows us to calculate the lattice constants for these samples without resolving the lines into components (Fig. 3).

Table 2. Lattice constants of the $A_xGa_{1-x}As$ epitaxial films in the $Al_xGa_{1-x}As$/GaAs(100) heterostructure

Sample no.	Value of x	Experiment		[11]
		$a^{\perp}$, Å	a^{ν}, Å	a^{ν}, Å
GaAs(100)	0	5.654	5.654	5.653
EM 28	0.12	5.655	5.655	5.654
EM 29	0.16	5.655	5.655	5.655
EM 135	0.50	5.661	5.658	5.657
EM 49	0.54	5.661	5.658	5.658
EM 77	>0.80	5.665	5.660	5.660
EM 72	1.00	5.667	5.661	5.661

Note: Values of $a^{\perp}$ are determined to within an accuracy of ±0.001 Å.

The solid line in Fig. 4 represents the (400) diffraction line of sample EM135, i.e., the $Al_{0.50}Ga_{0.50}As$/GaAs(100) heterostructure. The profile of the (400) line for this sample includes five features in the form of peaks or so-called shoulders. It can be seen from the line profile that the diffraction line of the epitaxial film is superimposed onto the doublet from the substrate. To single out the diffraction line of the film, it is necessary to subtract the doublet of the (400) line of the GaAs (100) substrate from the integrated profile of the experimental line of the heterostructure. The reason for this subtraction is that the epitaxial film insignificantly weakens the Bragg reflection from the substrate by virtue of its small thickness ~1 μm [12].

After the subtraction of the experimental line corresponding to the $K\alpha_{1,2}$ doublet for the GaAs (100) substrate, three lines, lines (*1*), (*2*), and (*3*) (Fig. 4, curve *4*), remained instead of the expected single doublet from

the $Al_{0.50}Ga_{0.50}As$ alloy. Judging from the ratio of the intensities of the three remaining diffraction components for the epitaxial film, these lines are, in turn, the result of a superposition of two $K\alpha_{1,2}$ doublets. The first is the doublet from the alloy with $x = 0.50$ (lines (*1*) and (*2*)), which has a larger lattice constant than the substrate ($a^{\perp}_{x=0.5} > a^{\perp}_{GaAs}$). The second doublet is assigned to an unknown phase (un. ph.) in the same film, which has a smaller lattice constant than the substrate ($a^{\perp}_{un.ph} < a^{\perp}_{GaAs}$) (lines (*2*) and (*3*)). Using the Sigma Plot-8 software package to perform a regression analysis, we find that line (*2*) is indeed a superposition of two components: $K\alpha_2$, from the $Al_xGa_{1-x}As$ alloy with a larger $a^{\perp}$, and $K\alpha_1$, from the unknown phase in which $a^{\perp}$ is smaller than $a^{\perp}_{GaAs}$. The difference between the experimental (curve *1*) and simulated (curve *2*) profiles is about 10%. Thus, the studied profile of the (400) diffraction line of sample EM135 is the superposition of three $K\alpha_{1,2}$ doublets from different phases with almost equal lattice constants, namely, $a^{\perp}_{GaAs} = 5.654$ Å (substrate), $a^{\perp}_{x=0.50} = 5.661$ Å (film), and $a^{\perp}_{un.ph} = 5.646$ Å (film). Table 3 lists the results from the decomposition of the (400) line of the $Al_{0.50}Ga_{0.50}As$/GaAs(100) heterostructure, specifically, the interplanar spacings $d^{\perp}$, lattice constant $a^{\perp}$, and lattice constant a^{v} calculated using formula (4). A similar result was obtained by resolving the (400) line into components for sample EM49, where $x = 0.54$.

From the results of the decomposition into components, we determined the lattice constants of the $Al_xGa_{1-x}As$ alloys, which are given in Table 2 along with the lattice constants expected according to the linear Vegard's law given on the site of the Ioffe Physicotechnical Institute, Russian Academy of Sciences [11]. The lattice constants $a^{\perp}$ for the single-crystal GaAs (100) substrates, which are given in the first row of Table 2, have the same value both for all the studied heterostructures and for the GaAs (100) single-crystal wafer of corresponding thickness. Therefore, we used this value in formulas (2)–(4), assuming that $a^{v}_{GaAs} = a^{\perp}_{GaAs}$, in order to calculate a^{v} for the AlAs and AlGaAs epitaxial films.

2.3. Results of Measurements of the Lattice Constants by the X-ray Back-Reflection Method

It has been shown in previous experiments with a KROS-1 camera that the X-ray photographic back-reflection method can be used at large diffraction angles to accurately measure the interplanar spacings and lattice constants of plane single-crystal samples. This measurement is achieved by rotating both the sample and the cassette with the X-ray film relative to the axis normal to the sample surface so that the planes with smallest interplanar spacings can occupy the reflecting position [12]. These planes cannot be recorded using a diffractometer because of the limitations of the goniometer.

In order to study samples EM28, EM29, EM49, and EM135, the camera was tuned to record the line (711) GaAs with the interplanar spacing $d = 0.7916$ Å [13]. The recording conditions were as follows: the anode voltage of the X-ray tube was 30 kV; the current, 15 mA; the distance between the sample and the cassette with film, 104 mm; the distance between the cassette and a diaphragm, 26.3 mm; and the exposure time, 1 h.

An analysis of the X-ray diffraction patterns obtained for samples EM28, EM29, and EM40 by the

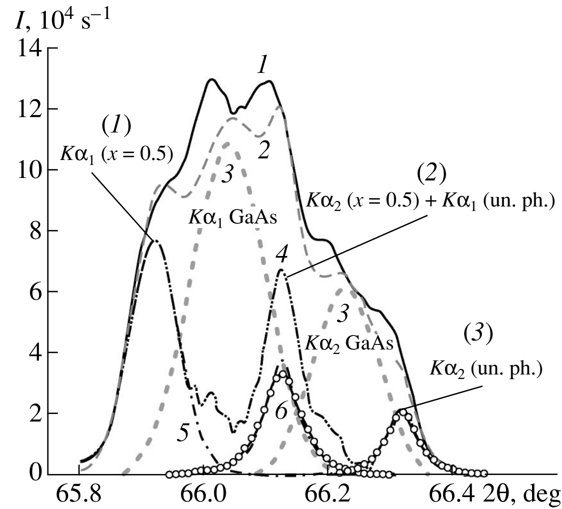

Fig. 4. Resolution of the (400) diffraction line of the $Al_{0.50}Ga_{0.50}As$/GaAs(100) heterostructure. Curve *1* corresponds to the experiment, and curves *2–6* correspond to the approximation. The diffraction lines of (curves *1* and *2*) the heterostructure, (curve *3*) GaAs, (curve *4*) the heterostructure diffraction minus the diffraction from the substrate, (curve *5*) $Al_{0.5}Ga_{0.5}As$, and (curve *6*) an unknown phase (un. ph.) are shown; (*1*), (*2*), and (*3*) are the components of curve *4*.

Table 3. Results of resolving the (400) diffraction line of the $Al_{0.50}Ga_{0.50}As$/GaAs(100) heterostructure (sample EM135)

Components of the heterostructure	$d^{\perp}$, Å	$I(K\alpha_2/K\alpha_1)$	$a^{\perp}_{expt}$, Å	a^{v}, Å
GaAs(100) (substrate)	1.414	0.57	5.654	5.654
$Al_{0.50}Ga_{0.50}As$ (film)	1.415	0.54	5.661	5.658
An unknown Al–Ga–As phase (in the film)	1.412	0.54	5.646	5.650

Note: Values of d', $a^{\perp}$, and a^{v} are determined to within an accuracy of ±0.001 Å; $a^{\perp}_{expt}$ are the experimental values.

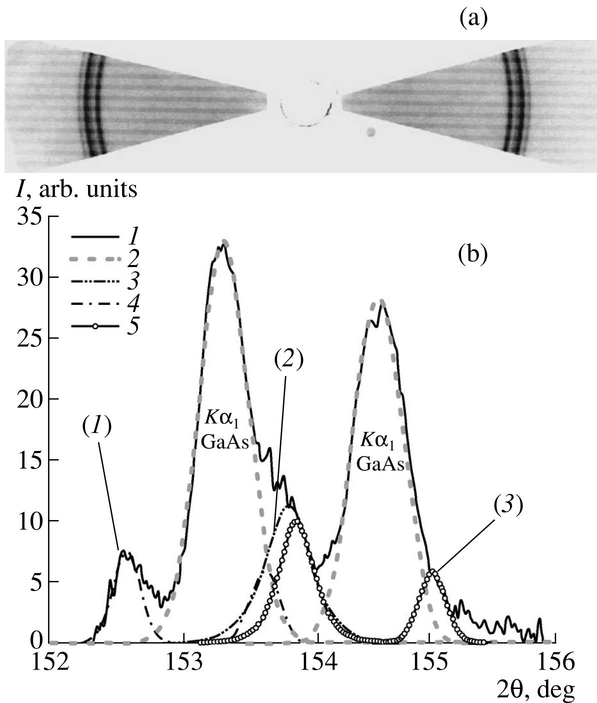

Fig. 5. (a) The Bragg reflection from the (711) planes of the $Al_{0.50}Ga_{0.50}As/GaAs(100)$ heterostructure recorded on X-ray film using the back-reflection method, and (b) the result of the digitization of this diffraction pattern. Curve *1* corresponds to the experiment, and the diffraction lines of (curve *2*) the GaAs substrate, (curve *4*) $Al_{0.5}Ga_{0.5}As$, and (curve *5*) an unknown phase (un. ph.) are shown. Curve *3* corresponds to the lines $K\alpha_2(x = 0.5) + K\alpha_1$(un. ph); (*1*), (*2*), and (*3*) represent the heterostructure diffraction minus the substrate diffraction.

back-reflection method using the KROS-1 camera without the rotation of the sample and the cassette with the X-ray film showed a slight deviation of the sample surface orientation from the (100) plane. Therefore, only the $K\alpha_2$ line of the GaAs (100) substrate in the X-ray diffraction patterns of these samples satisfied the conditions for the Bragg diffraction. As a result, it was impossible to obtain data on the crystal structure of the epitaxial films of these samples using the photographic method. However, we managed to obtain complete diffraction by the back-reflection method for sample EM135. Two doublets are present in the X-ray diffraction pattern obtained for this sample, namely, a more intense doublet from the GaAs (100) substrate and a doublet related to the $Al_{0.50}Ga_{0.50}As$ film (Fig. 5).

The results of the diffraction onto the X-ray film at the (711) plane of this sample were processed using a procedure involving a digital representation of the data [12]. The result of this digitization is shown in Fig. 5. After resolving the (711) diffraction line into components, we obtained a result similar to the splitting of the (400) X-ray diffraction line for the same sample. Figure 5b shows that the (711) diffraction line is a superposition of three doublets. The first doublet is the most intense $K\alpha_{1,2}$ doublet for the substrate, the second doublet is the $K\alpha_{1,2}$ doublet for the $Al_{0.5}Ga_{0.5}As$ alloy with the interplanar spacing $d^{\perp}_{x=0.5} > d^{\perp}_{\text{GaAs}}$, and the third doublet is the doublet from the unknown phase (un. ph.) with the smaller interplanar spacing $d^{\perp}_{\text{un. ph}} < d^{\perp}_{\text{GaAs}}$. Table 4 lists the results from calculations of the interplanar spacings for the (711) planes and lattice constants.

Table 4. Interplanar spacings and lattice constants determined from the (711) line for the $Al_{0.5}Ga_{0.5}As/GaAs(100)$ heterostructure

Sample no.	Components of the heterostructure	$a^{\perp}_{\text{expt}}$, Å	$a^{\perp}_{\text{expt}}$, Å	a^{v}, Å	a^{v}, Å [7]
EM 135	GaAs (substrate)	0.7916	5.6532	5.6532	5.6533
	$Al_{0.50}Ga_{0.50}As$ (film)	0.7927	5.6612	5.6582	5.6572
	An unknown phase (in the film)	0.7906	5.6465	5.6495	

Note: Values of $d^{\perp}$, $a^{\perp}$, and a^{v} are determined to within an accuracy of 0.0001 Å.

3. DISCUSSION

According to the data obtained by the diffractometric and photographic methods of X-ray structure analysis, the lattice constant of the GaAs (100) substrate, for all the samples, practically coincides with the value given on the site of the Ioffe Physicotechnical Institute [11] when the experimental error is taken into account. The exact determination of the lattice constant for GaAs is of great importance, since this parameter is a reference point for further calculations, and the fact that the measured parameter remains constant for all the samples indicates that the reproducibility of the experimental results is high. The most accurate measurements of the lattice constant for GaAs (100) were obtained using the X-ray back-reflection method for the (711) line, and gave the value 5.6532 ± 0.0001 Å. This value coincides with that given in [11].

For Vegard's law in relation to the $Al_xGa_{1-x}As$ epitaxial layers, the lattice constant a^{v} calculated taking into account the elastic stresses for alloys of various compositions depends linearly on the alloy composition in the AlAs–GaAs system given in [11] (see Fig. 6) for all the heterostructures (see Table 2). We also illustrated Vegard's law with line *1* in Fig. 6, which shows the quantities $a^{\perp}_{\text{expt}}$ determined from the experimentally measured $d^{\perp}_{\text{expt}}$.

In addition, the diffraction lines of an unknown phase with a lattice constant smaller than that of GaAs are found by resolving the (400) diffraction line for

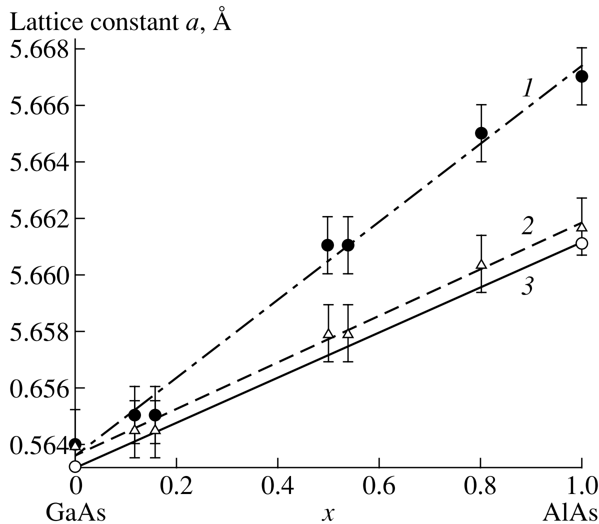

Fig. 6. Composition dependences of the lattice constants (Vegard's law) for the AlAs–GaAs system. Curve *1* corresponds to $a^{\perp}_{\text{expt}}$; curve *2*, to a^{v}; and curve *3*, to a^{v} [7].

samples EM49 and EM135. This is also the case for the (711) diffraction line for sample EM135.

The possible formation of superlattices in $Al_xGa_{1-x}As$ films at $x = 0.25$–0.75 has already been discussed in a number of publications [14–17]. Its formed ordered structure can have a tetragonal symmetry similar to the structure of an CuAu I alloy and consist of alternating AlAs and GaAs layers [14, 15]. However, an analysis of our results allows us to conclude that the unknown phase found during this investigation is an $AlGaAs_2$ chemical compound. This phase is a superstructure related to the sphalerite lattice, which is characteristic of GaAs, AlAs, and $Al_xGa_{1-x}As$ alloys. The lattice of the $AlGaAs_2$ phase that we identified can be described by a structure of the $InGaAs_2$ type (layered tetragonal) [18] with a [100] ordering direction. In this structure, the unit cell corresponds to the sphalerite-type cell doubled along the c axis. The ratio $c/2a$, observed in phases with this structure, can be both larger and smaller than unity [19].

The decrease in the lattice constant for the identified $AlGaAs_2$ superstructure is explained by the fact that the distribution of the Al and Ga atoms in the metal sublattice of an ideal $Al_xGa_{1-x}As$ alloy is statistical, and the lattice constant of the alloy is the average value of the lattice constants for the multitude of cells. In contrast, the $AlGaAs_2$ chemical compound is formed for a superstructure, and a so-called tetragonal compression of the layers filled with various Ga or Al atoms takes place. As a result, owing to the layered ordering of the sites of the Al and Ga atoms in the III sublattice, the lattice constant $c^{\perp} = 2a^{\perp}_{\text{AlGaAs}_2} = 11.292$ Å $< 2a^{\perp}_{x=0.5} = 11.322$ Å. In this case, the lattice constant $c^{\perp}$ is oriented along the normal to the (100) plane, i.e., the unit cell is tetragonally compressed in the growth direction of the epitaxial film, and the magnitude of this compression is $c^{\perp}_{\text{AlGaAs}_2}/2a^{\perp}_{x=0.5} = 0.997 < 1$ in the ordering region.

The ratio for the intensities of the $K\alpha_{1,2}$ doublets of the $AlGaAs_2$ superstructural phase and the alloy for the (400) and (711) reflections is indicative of the considerable volume (~15%) of regions in the $Al_{0.50}Ga_{0.50}As$ ordered alloy accompanied by the $AlGaAs_2$ superstructural phase in the epitaxial heterostructures in which $x \approx 0.50$.

4. CONCLUSIONS

Based on the studies carried out, we can put forward the following conclusions.

(i) Vegard's law is valid for $Al_xGa_{1-x}As$/GaAs(100) heterostructures grown by MOC-hydride epitaxy.

(ii) A superstructural phase is found in the $Al_xGa_{1-x}As$GaAs (100) heterostructures with $x \approx 0.5$. This phase is an $AlGaAs_2$ chemical compound with the lattice constant $c^{\perp} = 2a^{\perp}_{\text{AlGaAs}_2} = 11.292$ Å. The magnitude of tetragonal distortion in the direction of the epitaxial growth is $a^{\perp}_{\text{AlGaAs}_2}/2a^{\perp}_{x=0.5} = 0.997$.

ACKNOWLEDGMENTS

We thank D.N. Nikolaev for his help during the experiments and V.V. Shamakhov for his valuable comments during a discussion of the results.

REFERENCES

1. Zh. I. Alferov, Fiz. Tekh. Poluprovodn. (St. Petersburg) **32**, 3 (1998) [Semiconductors **32**, 1 (1998)].
2. É. P. Domashevskaya, V. A. Terekhov, V. M. Kashkarov, *et al.*, Fiz. Tekh. Poluprovodn. (St. Petersburg) **37**, 1017 (2003) [Semiconductors **37**, 992 (2003)].
3. Zh. I. Alferov, V. M. Andreev, S. G. Konnikov, *et al.*, Krist. Tech. **11**, 1013 (1976).
4. *Molecular Beam Epitaxy and Heterostructures*, Ed. by L. L. Chang and K. Ploog (Martimus Nishoff, Amsterdam, 1985; Mir, Moscow, 1989).
5. I. N. Arsent'ev, N. A. Bert, S. G. Konnikov, and V. E. Umanskiĭ, Fiz. Tekh. Poluprovodn. (Leningrad) **14**, 96 (1980) [Sov. Phys. Semicond. **14**, 53 (1980)].
6. D. Zhou and B. F. Usher, J. Phys. D: Appl. Phys. **34**, 1461 (2001).
7. Z. R. Wasilewski, M. M. Dion, D. Lockwood, *et al.*, J. Appl. Phys. **81**, 1683 (1997).
8. S. Adachi, J. Appl. Phys. **58**, R1 (1985).
9. M. Herman, *Semiconductor Superlattices* (Akademie, Berlin, 1986; Mir, Moscow, 1989).

10. *Solid Solutions in Semiconductor Systems: A Handbook*, Ed. by V. S. Zemskov *et al.* (Nauka, Moscow, 1978) [in Russian].
11. *Characteristics of Semiconductor Materials* (Fiz.–Tekh. Inst., St. Petersburg), www.ioffe.ru.
12. P. V. Seredin, Kondens. Sredy Mezhfaz. Granitsy **5** (1) (2001).
13. *Diffraction Data Cards* (ASTM, 1972).
14. T. S. Kuan, T. F. Kuech, and W. I. Wang, Phys. Rev. Lett. **54**, 201 (1985).
15. B. Koiller and A. M. Davidovich, Phys. Rev. B **41**, 3670 (1990).
16. E. Muller, B. Patterson, *et al.*, PSI Annual Report 2000, www.physik.unizh.ch/reports/report2000.html.
17. B. D. Patterson *et al.*, PSI Annual Report 1997, www.physik.unizh.ch/reports/report1999.html.
18. Alex Zunger, MRS-IRS Bulletin (1997), http://www.sst.nrel.gov/images/mrs97.
19. W. B. Pearson, *Crystal Chemistry and Physics of Metals and Alloys* (Wiley, New York, 1972; Mir, Moscow, 1977), Parts 1, 2.

Translated by N. Korovin

Semiconductors, Vol. 39, No. 3, 2005, pp. 343–346. From Fizika i Tekhnika Poluprovodnikov, Vol. 39, No. 3, 2005, pp. 361–364.
Original English Text Copyright © 2005 by Persheyev, Smirnov, O'Neill, Reynolds, Rose.

Atmospheric Adsorption Effects in Hot-Wire Chemical-Vapor-Deposition Microcrystalline Silicon Films with Different Electrode Configurations[1]

S. K. Persheyev*^, V. Smirnov, K. A. O'Neill*, S. Reynolds**, and M. J. Rose***

*Carnegie Laboratory of Physics, Electronic Engineering and Physics Division, University of Dundee, Dundee, DD1 4HN, Scotland, UK

^e-mail: s.persheyev@dundee.ac.uk

**EPICentre, School of Computing and Advanced Technologies, University of Abertay Dundee, Dundee, DD1 1HG, Scotland, UK

Submitted June 21, 2004; accepted for publication June 30, 2004

Abstract—Hot-wire chemical-vapor-disposition (CVD) thin silicon films are studied by means of dark conductivity, FTIR, hydrogen evolution, and SEM surface characterization. Three types of metastability are observed: (1) long term irreversible degradation due to oxidization processes on the film surface, (2) reversible degradation determined by uncontrolled water and/or oxygen adsorption, and (3) a fast field-switching effect in the film bulk. We propose that this effect is associated with the morphology changes during film growth and an electrical field induced by adsorbed atmospheric components on the film surface. It is found that metastable processes close to the film surface are stronger than in the bulk. © *2005 Pleiades Publishing, Inc.*

1. INTRODUCTION

The hot-wire chemical-vapor-deposition (HWCVD) technique [1–4] has been extensively studied in relation to the deposition of silicon-related materials at low temperatures without the use of plasma to decompose the source gas. The metastability in microcrystalline thin silicon films deposited using a high hydrogen dilution is probably one of the major issues limiting the technique's application for solar cells, thin-film transistors (TFT), and other devices. It is known that the properties of thin silicon films are affected by atmospheric adsorption processes (aging). Both reversible (short term) and irreversible (long term) effects on the conductivity in different kinds of thin-film materials exposed to atmospheric air have been reported [5–9]. The irreversible effect has been related to surface chemical reactions of the oxygen-incorporation processes [5] in amorphous silicon films. The reversible effects are related to physical adsorption of the atmospheric components on the film surface. However, it is still unclear to what extent the material bulk is involved in the aging process or even whether it is only a surface effect. In the present study we investigate the influence of an exposure to atmospheric gases on both the bulk and surface of hot-wire microcrystalline silicon films. Furthermore, we propose a model for the adsorption of the atmospheric components, based on the obtained results. The results of this study can be used to improve the stability of hot-wire microcrystalline silicon films in atmospheric processes.

[1] This article was submitted by the authors in English.

2. EXPERIMENTAL

As an improvement to the conventional hot-wire technique, a deposition system [1] incorporating independently controlled heated substrate holders on both sides of the filaments has been built. The aim of this improvement was to increase the technique's effectiveness by depositing two different substrate-temperature films in one process. Two straight tungsten filaments, both 0.5 mm in diameter and approximately 8 cm in length, were placed between the substrate holders. The filament-to-substrate distance was kept constant at 5 cm. Direct-current power was applied, and the filament temperature was varied between 1500 and 2300°C. The hydrogen gas inlets to the reactor were positioned to minimize silicide formation in the lower temperature regions at the clamped ends of the filaments. An optical pyrometer was used to monitor the filament temperature during the deposition process. Hydrogen-diluted silane gas ($R = \{[SiH_4]/[SiH_4 + H_2]\} \times 100\% = 60\%$) was introduced, and the total gas pressure varied between 30 and 50 mTorr. In our experiments we investigated silicon films with a thickness of about 1 μm.

To investigate the atmosphere-induced metastable processes in detail, two types of coplanar contacts were introduced: top aluminum contacts to control changes on the film surface and bottom chromium contacts to monitor bulk effects.

A series of microcrystalline silicon films were then deposited at substrate temperatures (varied between 200 and 500°C) for a postdeposition oxidization investigation using the HWCVD technique. The film are

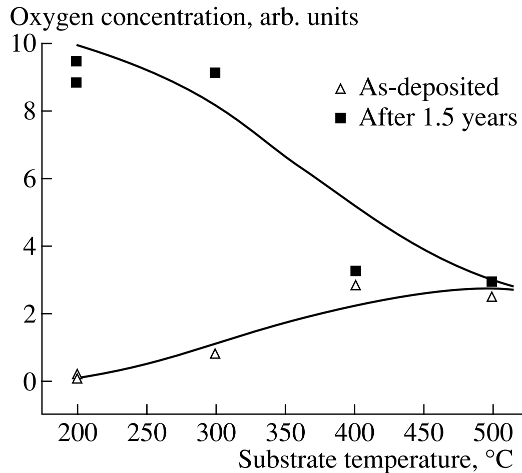

Fig. 1. Postdeposition oxidation effects in μ*c*-Si films. T_f = 1700°C.

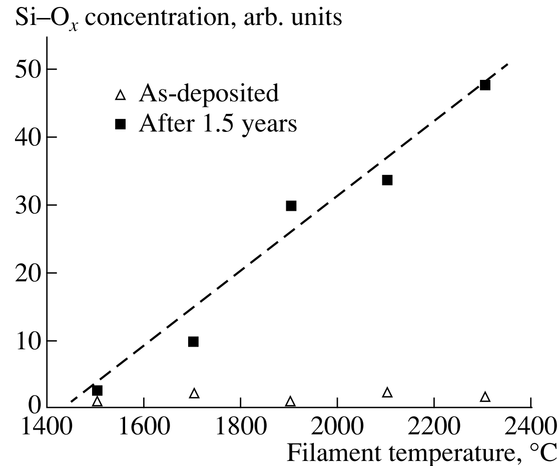

Fig. 2. Postdeposition oxidation effects in μ*c*-Si films. T_s = 300°C.

grown by the deposition of an amorphous phase and nucleation of crystallites followed by open structure growth. Fourier-transform infrared (FTIR) spectroscopy was used to investigate the content and bonding configuration of the oxygen and hydrogen in the microcrystalline films (after the deposition and 1.5 years later). The instrument used was a Mattson 7000 FTIR spectrometer. Scans were made in the 400–4000 cm^{-1} wavenumber range. The oxygen and hydrogen absorption peaks were integrated in order to calculate the concentration values.

3. RESULTS AND DISCUSSION

Microcrystalline silicon films are known to show an increase in dark conductivity, which is associated with postdeposition oxygen incorporation [7–9]. Over the given period of 1.5 years, the studied films show an irreversible (long-term aging) increase in their conductivity by up to 2 orders of magnitude. It was found that the largest conductivity increase corresponded to the films deposited at low substrate temperatures. To investigate the correlation between changes in conductivity and oxygen content, the above-mentioned FTIR measurements were performed. Changes in the oxygen concentration depending on the substrate temperature T_s and with the constant filament temperature T_f = 1700°C occurring over a period of 1.5 years are presented in Fig. 1. One can see that the material deposited at temperatures higher than T_s = 400°C is hardly able to adsorb any oxygen atoms over the time period, whereas the materials grown at low substrate temperatures are found to be more sensitive to the postdeposition oxidization process. Hydrogen-concentration measurements using the FTIR technique were carried out on the films obtained at different substrate temperatures. The results (not presented here) show that the hydrogen content decreases as the substrate temperature rises. Both these facts suggest that the compactness of the material increases with the substrate temperature while the material porosity decreases with a rise in temperature. The oxygen-concentration changes depending on the filament temperature for the time period in question are presented in Fig. 2. The films were deposited at a 300°C substrate temperature. It can clearly be seen that the silicon oxide concentration is initially very small; however, when the wire temperature is increased, the concentration rises so that, after 1.5 years, it is significantly higher. At a wire temperature of 1500°C there is no increase in oxidation.

Note that the conductivity values of the as-deposited films are in correlation with the substrate temperature: the dark conductivity of the films deposited at T_s = 400°C is about 1 order of magnitude higher than of the films deposited at T_s = 200°C. This fact could be due to the higher oxygen concentration (see Fig. 2), which causes the oxygen atoms to act as donors, and it could also be due to crystallinity variations, with maximum crystallinity being obtained at T_s = 400°C [10]. This behavior correlates with the conductivity changes observed, confirming the dominant role of oxygen in the postdeposition irreversible increase of dark conductivity.

To clarify the contribution of both the bulk and surface [11, 12], reversible changes in dark conductivity were investigated on microcrystalline films with different electrode configurations. The films were deposited at substrate temperatures of less than 300°C. The changes in the dark conductivity of these films, which was measured with coplanar electrodes exposed to air, are presented in Fig. 3. The general trend shows that, over a period of many hours, the dark conductivity decreases on the bottom and top electrodes exposed to atmosphere. However, during the first few seconds, the conductivity on the bottom electrodes rapidly rises, giving a sharply pronounced peak. This fast conductivity change is associated with atmospheric gas adsorption [7]. These changes can be reversed by heating the sample in vac-

uum at 180°C and, thus, removing the adsorbed water. The response to the exposure to air, obtained on the bottom electrode, suggests that the material bulk is involved in the atmospheric-gas adsorption. The sharply pronounced peak is associated with surface-adsorbed atmospheric components (a proposed model of this effect is discussed below).

We also investigated the effect of selected gases on coplanar dark-conductivity changes. The effect of nitrogen (Fig. 4) on dark conductivity provides a similar effect to that observed during the water and/or oxygen adsorption in relation to the direction of the changes. However, the sharp conductivity peak on the amorphous region (bottom electrodes) was not observed. Moreover, the influence of nitrogen on the surface conductivity is smaller than in the case of water adsorption (see Fig. 3). One of the possible explanations is that the penetrating nitrogen molecules are electro-neutral in comparison to the water molecules; however, a residual amount of atmospheric gases might participate in this process.

Our model of atmospheric gas adsorption in microcrystalline silicon was proposed to explain the difference in the results obtained for the bulk and surface of the material, taking into account the data of atomic-force microscopy (AFM) and FTIR measurements. The AFM studies [8] show a uniform distribution of grains over the film area. For the 1-μm film thickness, the typical grain sizes were ~50 nm, and the grains were mainly joined into "cauliflower-like" conglomerates. A slight increase in the grain size was observed for higher substrate temperatures. The rms surface roughness in the investigated structures was about 25–30 nm. Such morphology suggests the presence of a highly porous structure that may be sensitive to the incorporation of atmospheric components. The oxidized, "cauliflower-like," and highly developed microcrystalline silicon surface instantly attracts molecules of H_2O or O_2 (FTIR observations) after its exposure to atmospheric air. A schematic diagram of the hot-wire microcrystalline silicon-film morphology and water-moisture adsorption is presented in Fig. 5. It is known that the adsorption of atmospheric moisture can change conductivity in both directions [7–9] depending on a material's microstructure. Highly crystalline structures show a conductivity decrease, while more amorphous materials show an increase of conductivity. The different behavior observed at the bottom and top electrodes is associated with morphological changes during the material growth. On exposure to air, we observe a conductivity decrease on the top electrode, which is an expected behavior for a highly crystalline material. It is proposed that H_2O molecules are first chemisorbed at certain surface sites and the adsorbed components then collect electrons from the material. The adsorbed molecules give rise to a negative space-charge layer on the μ*c*-Si surface when it is oxidised, in the same way as in the crystalline silicon described by Jäntsch [13]. However, the bottom contact reflects the conductivity

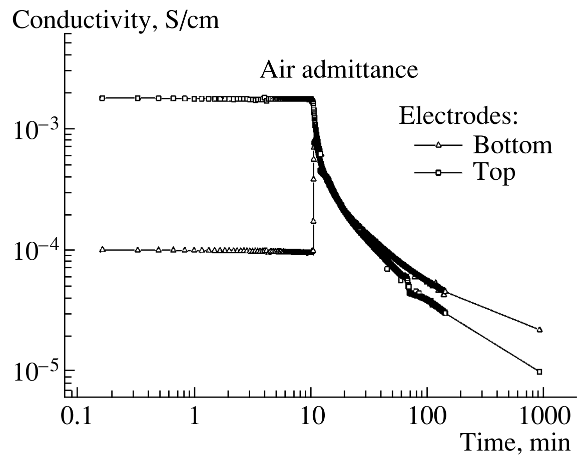

Fig. 3. The effect of air admittance (admittance starts at 10 minutes) on the dark conductivity in μ*c*-Si films. This effect is reversible by annealing.

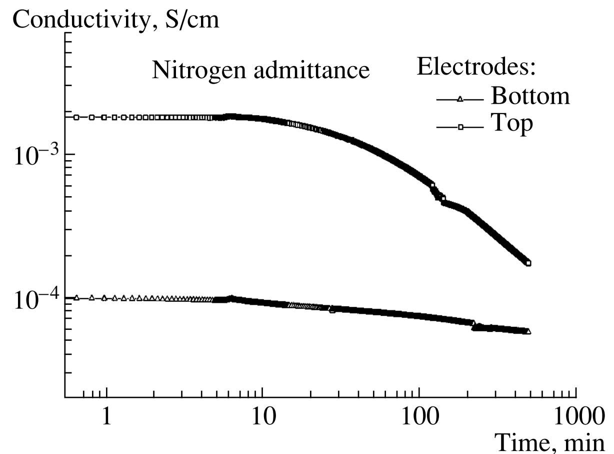

Fig. 4. The effect of nitrogen on the dark conductivity in μ*c*-Si films. This effect is reversible by annealing.

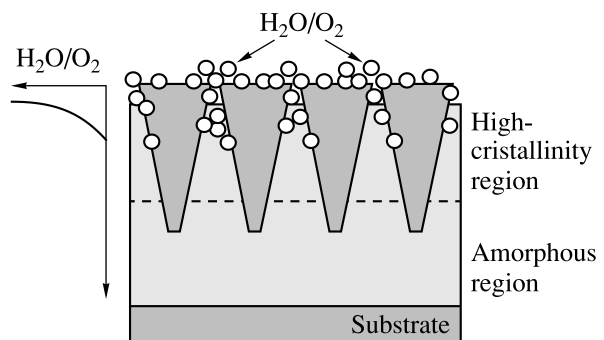

Fig. 5. Atmospheric moisture adsorption in a microcrystalline silicon film.

changes of the more amorphous region, where the adsorbed components give electrons to the material and, thus, raise the conductivity. Differently charged adsorbates create an electric field, perpendicular to the substrate, which is associated with the different behavior observed on the top and bottom electrodes. The field provides extra charge carriers for the amorphous region, shifting the Fermi level up to the conduction band and providing a rapid conductivity rise. Thus, water donates electrons to the amorphous region and collects electrons from the crystalline region, providing the different behavior observed on the bottom and top electrodes. Because the "working" area of the highly crystalline material is much larger, the effect of conductivity decrease becomes dominant with time. A much slower reaction occurs, which decreases the field, when chemisorbed water reacts with a bridging oxygen Si–O–Si at the interface and forms two neutral nonbridging silanol groups Si–O–H. This slow reaction decreases the electron concentration in the amorphous region, and, together with the contribution from the crystalline part, results in a slow conductivity decrease. Silanol is unstable and releases H_2O at temperatures above 100°C, which explains the vacuum annealing removal of the water-induced metastability. It provides the possibility of completely removing the adsorbed components. The reproducibility of the short-term aging cycles was obtained during ten experimental cycles, giving an error within 20%, which was mainly determined by variations in the air humidity.

4. CONCLUSIONS

Hot-wire microcrystalline silicon films are sensitive to atmospheric-gas exposure. The material microstructure depends significantly on the substrate and filament temperatures. More compact materials were obtained at low filament temperatures (below 1700°C) and at high substrate temperatures (over 400°C). At substrate temperatures below 300°C, microcrystalline films are likely to be porous. Such porous films are found to be strongly affected by the irreversible process of oxygen incorporation. Reversible processes on the film surface involve water vapor and/or oxygen adsorption and a field accumulated by moisture that induces band bending and a Fermi level shift. The different responses observed on exposure to air are associated with microstructure changes during the material growth. Absorbed moisture can be removed from the material by annealing at temperatures around 180°C. Investigations of the material properties resulting from thickness variations and corresponding conductivity changes were performed. Our future investigations include studies of the chemical processes on the surface and in the bulk involving X-ray photo-spectroscopy depth profiling.

REFERENCES

1. S. K. Persheyev, D. M. Goldie, R. A. G. Gibson, *et al.*, Thin Solid Films **395**, 130 (2001).
2. S. Klein, F. Finger, R. Carius, *et al.*, Thin Solid Films **430**, 202 (2003).
3. H. Matsumura, H. Umemoto, A. Izumi, and A. Masuda, Thin Solid Films **430**, 7 (2003).
4. A. H. Mahan, Sol. Energy Mater. Sol. Cells **78**, 299 (2003).
5. M. Tanielian, M. Chatani, H. Fritzche, *et al.*, J. Non-Cryst. Solids **35–36**, 575 (1980).
6. I. Solomon, in *Proceedings of Kyoto Sum. Inst.*, Ed. by F. Yonezawa (1981), p. 33.
7. F. Finger, R. Carius, T. Dylla, *et al.*, IEE Proc. G: Circuits Devices Syst. **150**, 300 (2003).
8. S. K. Persheyev, K. A. O'Neill, S. Anthony, *et al.*, Mater. Res. Soc. Symp. Proc. **808**, A9.10 (2004).
9. V. Smirnov, S. Reynolds, C. Main, *et al.*, J. Non-Cryst. Solids **338–340**, 421 (2004).
10. A. Matsuda, J. Non-Cryst. Solids **338–340**, 1 (2004).
11. H. R. Moutinho, C.-S. Jiang, J. Perkins, *et al.*, Thin Solid Films **430**, 135 (2003).
12. M. Kondo, H. Fujiwara, and A. Matsuda, Thin Solid Films **430**, 130 (2003).
13. O. Jäntsch, J. Phys. Chem. Solids **26**, 1233 (1965).

Semiconductors, Vol. 39, No. 3, 2005, pp. 347–350. Translated from Fizika i Tekhnika Poluprovodnikov, Vol. 39, No. 3, 2005, pp. 365–368.
Original Russian Text Copyright © 2005 by Osminkina, Konstantinova, Sharov, Kashkarov, Timoshenko.

AMORPHOUS, VITREOUS, AND POROUS SEMICONDUCTORS

The Role of Boron Impurity in the Activation of Free Charge Carriers in Layers of Porous Silicon during the Adsorption of Acceptor Molecules

L. A. Osminkina^, E. A. Konstantinova, K. S. Sharov, P. K. Kashkarov, and V. Yu. Timoshenko

Physics Department, Moscow State University, Vorob'evy gory, Moscow, 119992 Russia

^e-mail: osminkina@vega.phys.msu.ru

Submitted July 12, 2004; accepted for publication August 9, 2004

Abstract—Infrared-absorption spectroscopy and electron spin resonance are used to study the role of boron impurity in the activation of free charge carriers in layers of porous silicon that have been exposed to nitrogen dioxide acceptor molecules. It is found that the higher the level of doping is for the substrates used in the production of porous silicon, the higher the concentration of free holes that appear as a result of the adsorption of nitrogen dioxide. The experimental results are accounted for by the appearance of donor–acceptor pairs formed by anionic radicals $(NO_2)^-$ and positively charged defects (dangling silicon bonds) at the surface of the silicon nanocrystals that comprise porous silicon. © *2005 Pleiades Publishing, Inc.*

1. INTRODUCTION

Porous silicon (*por*-Si) formed by electrochemical etching of single-crystal silicon (*c*-Si) can consist of a set of Si nanocrystals with an extremely large specific surface area (~10^3 m^2/g [1]) under certain production conditions. This large specific surface area leads to the high sensitivity of the *por*-Si's physicochemical properties to the adsorption of molecules [2]. In particular, it was established that the adsorption of NO_2 molecules led to a substantial increase in both the electrical conductivity [3] and the concentration of free charge carriers (holes) [4] in mesoporous Si layers that had Si nanocrystals whose characteristic size was larger than 4–5 nm, i.e., under the conditions of a slightly pronounced quantum-confinement effect [5]. Later, certain hypotheses were advanced suggesting that the adsorption-induced appearance of free charge carriers was related to the destruction of the bound state of holes by the Coulomb fields of adsorbed complexes [6] or to the recharging of the surface states of defects, which affected the position of the Fermi level in the ensemble of Si nanocrystals [7]. According to [8], the interaction of the NO_2 molecules with the surface of the silicon nanocrystals is a complex physicochemical process that involves both adsorption with a charge transfer and chemisorption that leads to the oxidation of the surface of the Si nanocrystals and to the formation of P_b-type centers (the dangling silicon bonds at the boundary). These defects, both existing initially [7] and formed owing to adsorption [8], are effective centers for hole capture; at the same time, complexes of the $P_b^+–NO_2^-$ type, which appear owing to the adsorption, can give rise to a significant increase in the hole concentration in nanocrystalline Si [8].

In spite of the appreciable progress that has been made in understanding the mechanisms of interaction between NO_2 molecules and Si nanocrystals, the issue concerning the role of the initial impurity (boron) in the effect of the adsorption-related doping of *por*-Si remains unclarified. In particular, it is unclear whether it is possible to generate free holes as a result of the interaction of NO_2 with the *por*-Si that is obtained on Si substrates possessing a low boron concentration. In this study, in order to clarify this issue, we used infrared (IR) and electron-spin-resonance (ESR) spectroscopy to gain insight into the effect of the adsorption of NO_2 molecules on the concentrations of the free charge carriers and defects in the layers of porous Si grown on substrates with different levels of boron doping.

2. EXPERIMENTAL

The *por*-Si samples were prepared using the conventional method, i.e., the electrochemical etching of *c*-Si:B single crystals in a HF(48%) : C_2H_6OH = 1 : 1 solution at a current density of 50 mA/cm^2. We used wafers with a (100) surface orientation and a resistivity of 1–2 mΩ cm, 10–20 mΩ cm, or 10–15 Ω cm. In what follows, the corresponding *por*-Si layers are designated as samples of types I, II, and III, respectively (see table). After the completion of the pore-formation process, the *por*-Si layers were separated from the substrate by increasing the current density to 500 mA/cm^2 for a short period. The thickness of the obtained layers was 40–60 μm. The porosity of the *por*-Si layers was determined from gravimetric measurements and is listed in the table for various samples.

The transmission spectra of the *por*-Si films were measured using a PERKIN ELMER RX I spectrometer

1063-7826/05/3903-0347$26.00 © 2005 Pleiades Publishing, Inc.

Parameters of the samples

Sample	Substrate's resistivity	Hole concentration N_p, cm^{-3}		Defect concentration N_s, cm^{-3}	
		Initial	Highest with NO_2	Initial	Highest with NO_2
I	1–2 mΩ cm	4×10^{18}	2.2×10^{19}	5.2×10^{16}	1.1×10^{19}
II	10–20 mΩ cm	2×10^{17}	4×10^{18}	9.1×10^{16}	4.6×10^{18}
III	10–15 Ω cm	$<10^{16}$	$<10^{16}$	7.3×10^{17}	2.5×10^{19}

with a double Fourier transform (at a wave-number range of 400–6000 cm^{-1} and a resolution of 2 cm^{-1}). The absorption-coefficient spectra $\alpha(\nu)$ were obtained from the measured transmission spectra according to the relation $\alpha(\nu) \approx -d^{-1}\ln[T(\nu)]$, where ν is the wave number (sometimes referred to as the frequency) of the IR radiation, $T(\nu)$ is the transmission coefficient, and d is the layer thickness.

We measured the ESR spectra for the free *por*-Si films using a PS_100.X spectrometer (at an operation frequency of 9.5 GHz and a sensitivity of 5×10^{10} spin/G). In order to calculate the g factors and the concentrations of defects, we used both MgO reference samples with Mn^{++} ions and $CuCl_2 \cdot 2H_2O$, respectively.

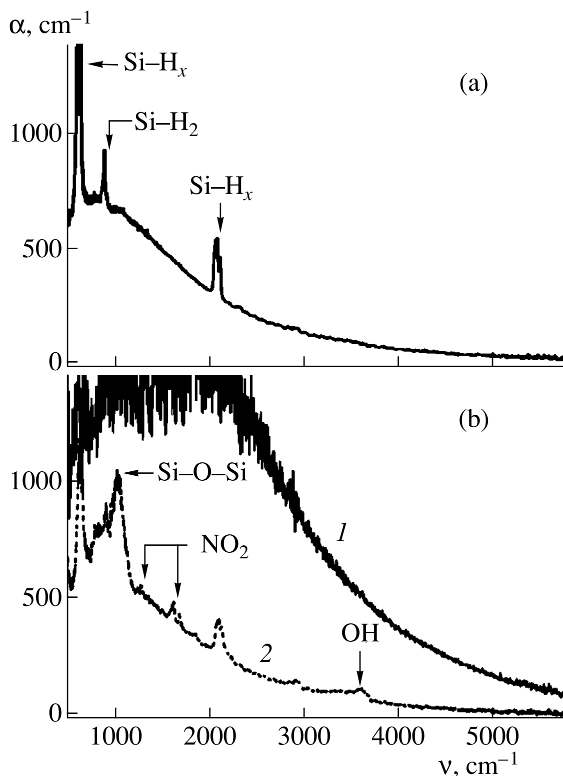

Fig. 1. The absorption-coefficient spectra for a sample of type I. Conditions of measurement: (a) in vacuum with a residual pressure of 10^{-6} Torr and (b) in an NO_2 atmosphere with pressures P_{NO_2} = (*1*) 0.1 and (*2*) 10 Torr. The arrows indicate the absorption peaks related to the corresponding molecular groups.

The nitrogen dioxide was obtained as a result of the chemical reaction Cu(chips) + $4HNO_3 = 2NO_2$(gas) + $Cu(NO_3)_2 + 2H_2O$. The NO_2 gas was freed from the water impurity by passing it through a bottle possessing a P_2O_5 dessicator. The NO_2 molecules were adsorbed on the free *por*-Si layers from vacuum. The experiments involving the adsorption, as well as the measurements of both the IR and ESR spectra, were performed in situ at room temperature.

3. RESULTS AND DISCUSSION

In Fig. 1a, we show the absorption-coefficient spectra of a type-I sample in vacuum. The following absorption bands are observed in the spectrum of the as-prepared *por*-Si: a absorption band related to the stretching vibrations of Si–H_x (x = 1, 2, 3) at wave numbers of 2070–2170 cm^{-1}, an absorption band related to the scissor vibrations of Si–H_2 at a wave number of ~910 cm^{-1}, and an absorption band related to the bending vibrations of Si–H_x at a wave number of ~660 cm^{-1} [9]. The above bands are observed against the background component related to the absorption by free charge carriers. The concentration of the latter can be calculated from the absorption spectra using the classical Drude model but including a correction for an additional scattering that manifests itself mainly in the region of low frequencies [10]. At the same time, we can analyze the high-frequency portion of the spectrum (2500–6000 cm^{-1}), where the mechanisms of scattering in nanocrystalline Si are not much different from those in *c*-Si [4, 6], to determine the charge-carrier (hole) concentration N_p within a Si nanocrystal. This analysis is achieved using the following simple relation [8]:

$$N_p = N_{\rm Si}\frac{\alpha n}{\alpha_{\rm Si} n_{\rm Si}(1-p)}. \quad (1)$$

Here, α, n, and p are, respectively, the absorption coefficient, refractive index, and porosity of *por*-Si, all of which are taken from the experimental data, and $N_{\rm Si}$, $n_{\rm Si}$, and $\alpha_{\rm Si}$ are the substrate's hole concentration, refractive index, and absorption coefficient (the values of these quantities are well known and taken from various available publications (see, for example, [9, 11])).

For the samples used in this study, the values of N_p calculated using formula (1) are listed in the table and are shown in Fig. 2. The values of N_p for the as-prepared *por*-Si samples of types I and II were equal to 4 ×

10^{18} and 2×10^{17} cm^{-3}, respectively; these values were smaller than the 10^{16} cm^{-3} value (the detectivity limit for the method used) calculated for the samples of type III. The values of N_p for the samples of types I and II are more than an order of magnitude smaller than those in the *c*-Si:B substrates used to form these samples. Indeed, the concentrations of boron atoms and free holes at a temperature of $T = 300$ K were equal to ~10^{20} cm^{-3} (a sample of type I) and 5×10^{18} cm^{-3} (a sample of type II) in the substrate. This decrease in N_p can be attributed to the capture of holes by the states of defects at the surface of Si nanocrystals [6–8, 10]. In addition, one can expect the concentration N_p to be reduced in the small-sized Si nanocrystals (the samples of types II and III) owing to an increase in the activation energy for the boron impurity [6]. It is worth noting that this smaller value of N_p, compared to that in the substrate, cannot be caused by a decrease in the boron concentration in *por*-Si. As was established by Polisski *et al.* [12], the boron concentration, on the contrary, increases as a result of the formation of porous silicon and exceeds the concentration of residual silicon atoms.

Adsorption of NO_2 at the pressures $P_{NO_2} = 0.01$–0.1 Torr led to an increase in the free-hole concentration in the samples of types I and II (see Figs. 1b, 2). We did not detect the appearance of free charge carriers in samples of type III. The largest values of N_p caused by the NO_2 adsorption were detected at $P_{NO_2} = 0.1$ Torr and were equal to 2.2×10^{19} and 4×10^{18} cm^{-3} for the samples of types I and II, respectively (see table). Thus, the higher the initial level of boron doping, the larger the value of N_p after the adsorption of NO_2.

As can be seen from Figs. 1b and 2, the value of N_p in the samples of types I and II depends nonmonotonically on P_{NO_2}. A decrease in the value of N_p at $P_{NO_2} > 0.1$ Torr can be attributed to an increase in the number of hole-trapping centers resulting from the defect production in *por*-Si during the NO_2 adsorption. Indeed, at high pressures of NO_2 (Fig. 1b), the following lines and bands are observed in the IR absorption spectra: lines located at the wave numbers 1290 and 1620–1680 cm^{-1} and related to the chemisorbed NO_2 molecules, and bands related to the absorption by Si–O–Si bonds (at 1050–1100 cm^{-1}) and O–H bonds (at 3100–3800 cm^{-1}) and caused by the adsorption-induced oxidation of the surface of the Si nanocrystals [10].

Typical ESR spectra of the samples under study are shown in Fig. 3. The shape of the ESR signal and the value of its g factor indicate that the observed defects are in fact the P_b centers that involve a silicon dangling bond at the Si/SiO_2 interface [13, 14]. It is well known that these defects are amphoteric centers for the capture of charge carriers; i.e., these centers can trap both electrons and holes [15]. We used the ESR spectra to calculate the number of detected P_b centers N_s, taking into account the porosity of the samples (as in the case of calculating the value of N_p). In the case of the as-prepared *por*-S in vacuum, we found that the value of N_s was largest for the samples of type III and smallest for the samples of type I (see table). This behavior becomes understandable if we take into account that the ESR signal can only be caused by neutral P_b centers, since the P_b centers that capture holes are not paramagnetic. The smallest ESR signal detected in the as-prepared samples with the highest concentration of doping impurity is quite satisfactorily accounted for by the transition of the defects to the state P_b^+:

$$P_b^0 + h^+ \longrightarrow P_b^+. \quad (2)$$

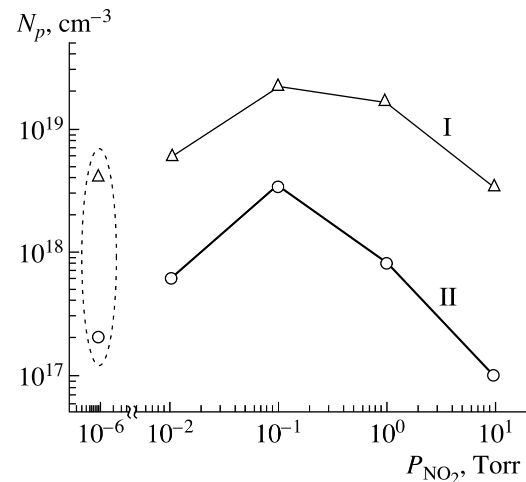

Fig. 2. Dependences of the free-hole concentration in porous silicon on the NO_2 pressure for the samples of types I and II. The dashed line encloses the values of N_p obtained for the samples as-prepared in vacuum.

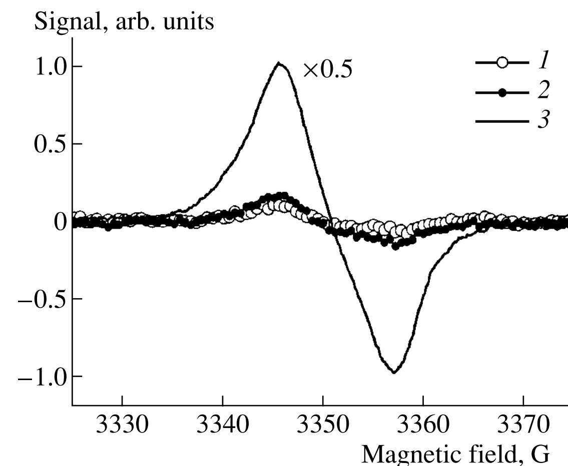

Fig. 3. The ESR spectra for a sample of type III measured (*1*) in vacuum and (*2*, *3*) in an atmosphere of NO_2 at P_{NO_2} = (*2*) 0.1 and (*3*) 10 Torr.

Thus, a variation in the concentration of P_b centers resulting from the NO_2 adsorption can be analyzed most effectively by using the ESR data for the samples of type III, as the recharging processes related to the capture of holes are unimportant for these samples. Our experiments show that the amplitude of the ESR signal is not significantly affected by the NO_2 adsorption at $P_{NO_2} \leq 0.1$ Torr (see Fig. 3); at the same time, the ESR signal increases markedly as a result of the NO_2 adsorption at $P_{NO_2} = 1$–10 Torr. The largest values of N_s are detected at $P_{NO_2} = 10$ Torr and are listed in the table for various samples. The obtained values, $N_s \sim 10^{18}$–10^{19} cm^{-3}, indicate that the defects are actively produced when the surface of the Si nanocrystals is oxidized as a result of the NO_2 adsorption at high pressures.

The experimental data on the variations in N_p and N_s resulting from the NO_2 adsorption in the *por*-Si layers can be satisfactorily accounted for in the context of a model describing the formation of the donor–acceptor pairs as anionic radicals NO_2^- combining with positively charged defects (P_b^+ centers) [8]. According to this model, anionic NO_2^- complexes can be formed at the surface of Si nanocrystals in the course of NO_2 adsorption. This circumstance means that corresponding acceptor levels appear in the band gap of the Si nanocrystals. Apparently, these levels are fairly deep; therefore, they cannot ensure the appearance of free holes in nanocrystalline Si at room temperature by themselves. However, since the sizes of the nanocrystals are small, the Coulomb interaction between the adsorbed NO_2 molecules and the P_b centers can be significant. This interaction gives rise to the P_b^+–NO_2^- donor–acceptor pairs. The formation of these pairs leads to an increase in N_p as a result of a certain passivation of P_b centers, which, if charged positively, cease to capture the free holes. Therefore, the appearance of free charge carriers can be described by the following reaction equation:

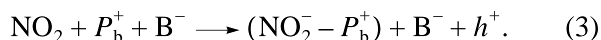

$$NO_2 + P_b^+ + B^- \longrightarrow (NO_2^- - P_b^+) + B^- + h^+. \qquad (3)$$

Thus, in the absence of the adsorption-induced defect formation, i.e., at low NO_2 pressures, the free-hole concentration is controlled by the level of boron doping and by the degree to which the initial P_b centers are passivated by the adsorbed molecules. New P_b centers are formed due to the oxidation of the surface of the Si nanocrystals at high NO_2 pressures. This circumstance leads to a decrease in the hole concentration resulting from the capture of holes by newly formed defects (see Fig. 2).

4. CONCLUSION

Adsorption of NO_2 molecules is the most effective mechanism for giving rise to free charge carriers in porous Si (*por*-Si) at pressures of $P_{NO_2} \sim 0.1$ Torr. In such a process, the defect formation related to this adsorption is nearly absent, and, therefore, the hole concentration is controlled by the level of boron doping for the substrates used in the formation of *por*-Si. The data obtained are accounted for by the appearance of the P_b^+–NO_2^- donor–acceptor pairs at the surface of the Si nanocrystals that form *por*-Si; as a result, the defects cease to act as the capture centers for holes caused by the thermal ionization of boron impurity atoms.

ACKNOWLEDGMENTS

This study was supported by grants from the Ministry of Science and Education of the Russian Federation and was carried out using equipment from the Collective Instrumentation-Usage Center of Moscow State University.

E.A. Konstantinova acknowledges the financial support provided to this study by a grant from the President of the Russian Federation (grant no. MK-2036.2003.02).

REFERENCES

1. R. Herino, G. Bomchil, K. Barla, *et al.*, J. Electrochem. Soc. **134**, 1994 (1987).
2. P. K. Kashkarov, E. A. Konstantinova, and V. Yu. Timoshenko, Fiz. Tekh. Poluprovodn. (St. Petersburg) **30**, 1479 (1996) [Semiconductors **30**, 778 (1996)].
3. L. Boarino, C. Baratto, F. Geobaldo, *et al.*, Mater. Sci. Eng. B **69–70**, 210 (2000).
4. V. Yu. Timoshenko, Th. Dittrich, and F. Koch, Phys. Status Solidi B **222**, R1 (2000).
5. A. G. Cullis, L. T. Canham, and P. D. J. Calcott, J. Appl. Phys. **82**, 909 (1997).
6. V. Yu. Timoshenko, Th. Dittrich, V. Lysenko, *et al.*, Phys. Rev. B **64**, 085314 (2001).
7. L. Boarino, F. Geobaldo, S. Borini, *et al.*, Phys. Rev. B **64**, 205308 (2001).
8. E. A. Konstantinova, L. A. Osminkina, and K. S. Sharov, Zh. Éksp. Teor. Fiz. **126**, 857 (2004) [JETP **99**, 741 (2004)].
9. W. Theiß, Surf. Sci. Rep. **29**, 91 (1997).
10. L. A. Osminkina, E. V. Kurepina, A. V. Pavlikov, *et al.*, Fiz. Tekh. Poluprovodn. (St. Petersburg) **38**, 603 (2004) [Semiconductors **38**, 581 (2004)].
11. H. Hara and Y. Nishi, J. Phys. Soc. Jpn. **21**, 1222 (1966).
12. G. Polisski, D. Kovalev, G. G. Dollinger, *et al.*, Physica B (Amsterdam) **273–274**, 951 (1999).
13. E. H. Poindexter, P. J. Caplan, B. E. Deal, and R. Razouk, J. Appl. Phys. **52**, 879 (1981).
14. J. L. Cantin, M. Schoisswohl, H. J. Bardeleben, *et al.*, Phys. Rev. B **52**, R11599 (1995).
15. V. S. Vavilov, V. F. Kiselev, and B. N. Mukashev, *Defects in Silicon and on Its Surface* (Nauka, Moscow, 1990) [in Russian].

Translated by A. Spitsyn

Semiconductors, Vol. 39, No. 3, 2005, pp. 351–353. Translated from Fizika i Tekhnika Poluprovodnikov, Vol. 39, No. 3, 2005, pp. 369–371.
Original Russian Text Copyright © 2005 by Biryukov, Kazanskiĭ, Terukov, Khabarova.

The Density of States in the Mobility Gap of Amorphous Hydrogenated Silicon Doped with Erbium

A. V. Biryukov*, A. G. Kazanskiĭ*^, E. I. Terukov, and K. Yu. Khabarova***

**Moscow State University, Vorob'evy gory, Moscow, 119899 Russia*

^e-mail: Kazanski@phys.msu.ru

***Ioffe Physicotechnical Institute, Russian Academy of Sciences, Politekhnicheskaya ul. 26, St. Petersburg, 194021 Russia*

Submitted July 15, 2004; accepted for publication August 9, 2004

Abstract—The effect of doping films of amorphous hydrogenated silicon (*a*-Si:H) with erbium on the density of the states in the mobility gap is studied. The data obtained are compared with those for *a*-Si:H films doped with arsenic. The data on the density of the states in the lower and upper halves of the mobility gap are determined from measurements of the spectral dependences of the absorption coefficient and the temperature dependences of the constant and modulated components of the photoconductivity in films exposed to modulated light, respectively. It is shown that doping the *a*-Si:H films with erbium leads to an increase in the density of states both in the lower and upper halves of the mobility gap. © *2005 Pleiades Publishing, Inc.*

Films of amorphous hydrogenated silicon doped with erbium *a*-Si:H(Er) attract the attention of researchers in connection with the fact that an intense photoluminescence and electroluminescence with an emission peak at a wavelength of 1.54 μm, which corresponds to a minimum of losses in a quartz optical fiber, is observed in them. The luminescence of Er^{3+} erbium ions in *a*-Si:H is much more intense and its thermal quenching is much less pronounced than in the case of Er^{3+} luminescence in crystalline Si [1, 2].

In the majority of the earlier publications concerned with studying the *a*-Si:H(Er) films, the photoluminescence of this material was analyzed (see, for example, [2]). It was shown that the luminescence intensity depended on the concentrations of the oxygen and erbium atoms introduced into *a*-Si:H and attained a maximum at an erbium concentration of $N_{Er} \approx 10^{20}$ cm^{-3} [3]. However, there is hardly any data concerning the effect of doping *a*-Si:H with erbium on the density of the localized electronic states in this material in the available publications. At the same time, the optical and photoelectric properties of *a*-Si:H(Er) would seem to depend, to a great extent, on the distribution of the density of the electronic states in the mobility gap. Therefore, we performed optical and photoelectric studies of the *a*-Si:H(Er) films and obtained information about the effect of doping *a*-Si:H with Er on the density of its localized electronic states; in addition, we compared the results obtained with the data on films doped with a traditional impurity (As).

In this study, we investigated *a*-Si:H(Er) films obtained by a decomposition of monosilane (SiH_4) in a high-frequency glow discharge. Films with a thickness of ~0.8 μm were deposited onto a quartz substrate at a temperature of 250°C. The films were then doped with erbium using a sublimation of the metal–organic compound $Er(C_5H_7O_2)_3$ at various temperatures T_f (90, 95, and 105°C). The compound was installed in a vacuum channel connected to the reaction chamber. According to the results of measurements of the Rutherford backscattering, the concentration of introduced erbium increased from 2×10^{19} to 3.3×10^{19} cm^{-3} as T_f was increased. Photoluminescence at a wavelength of 1.54 μm was observed in the obtained films. The films exhibited an *n*-type conductivity, and the Fermi level was located below the conduction-band bottom at a depth of $E_C - E_F = 0.34$–0.36 eV at room temperature. The value of $E_C - E_F$ was determined from the expression $E_C - E_F = kT\ln(\sigma_0/\sigma_d)$, where σ_d is the dark electrical conductivity and $\sigma_0 = 150\ \Omega^{-1}$ cm^{-1} is the lowest metallic conductivity [4].

The *a*-Si:H(As) films with the Fermi level position $E_C - E_F = 0.34$ eV were obtained as a result of introducing arsine (AsH_3) into the reaction chamber. The volume ratio of the gases was $[AsH_3]/[SiH_4] = 10^{-5}$. All the measurements were performed in vacuum with a residual pressure of 10^{-3} Pa after annealing the samples for 30 min at $T = 180$°C.

In order to gain insight into the effect of doping *a*-Si:H with Er on the density of the states in the lower half of the mobility gap, we measured the spectral dependences of the absorption coefficient α using the constant-photocurrent method [5]. The distribution of the density of the states, $N_t(E)$, in the upper half of the mobility gap was determined from measurements of the temperature dependences of the conductivity in the case where the films were exposed to light with the fre-

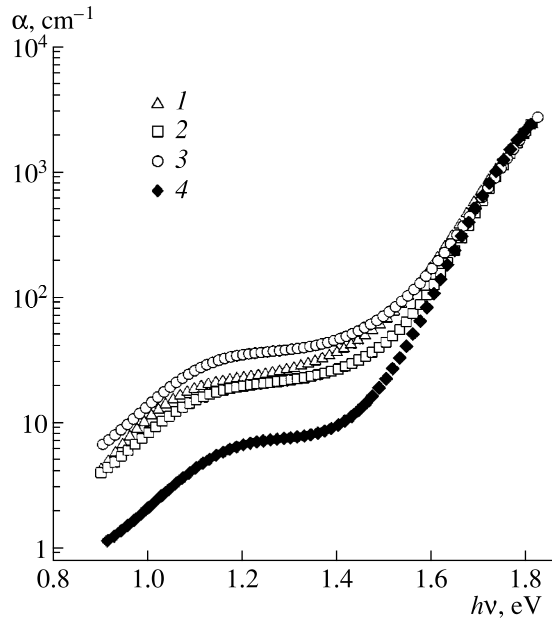

Fig. 1. Spectral dependences of the absorption coefficient α for the (*1–3*) *a*-Si:H(Er) films and (*4*) *a*-Si:H(As) films. The sublimation temperature during the process of doping with erbium was T_f = (*1*) 90, (*2*) 95, and (*3*) 105°C.

quency ω. According to [6], the distribution $N_t(E)$ can be determined from measurements of the constant and alternating components of the photocurrent. In this case,

$$N_t(E_F^n) = \frac{G}{\omega kT}\frac{\Delta\bar{\sigma}}{\Delta\tilde{\sigma}},$$

where $\Delta\bar{\sigma}$ and $\Delta\tilde{\sigma}$ are the photocurrent's constant component and the amplitude of the alternating component, respectively; E_F^n is the position of the quasi-Fermi level for electrons; and G is the amplitude of the generation rate for nonequilibrium charge carriers under modulated excitation. By varying the temperature or the excitation intensity, we can vary the position E_F^n and, correspondingly, determine the distribution $N_t(E)$ from the measurements of $\Delta\bar{\sigma}$ and $\Delta\tilde{\sigma}$. The above expression for $N_t(E_F^n)$ is valid for the range of modulation frequencies that satisfy the condition

$$\frac{1}{\tau_n} < \omega < N_C^* vS \exp[-(E_C - E_F^n)/kT],$$

where τ_n, N_C^*, v, and S are the characteristic photoresponse time; the effective density of the states in the conduction band; the thermal velocity of the charge carriers; and the cross section of the charge-carrier capture by localized states, respectively. The upper restriction imposed on the value of ω is necessary to ensure thermodynamic equilibrium between the free charge carriers and the charge carriers captured by the states in the vicinity of E_F^n in the case of modulated excitation. At the same time, under a condition in which the value of ω is limited from below, the value of $\Delta\tilde{\sigma}$ should not depend on the lifetime of the charge carriers and should vary in inverse proportion to ω.

The quantities $\Delta\bar{\sigma}$ and $\Delta\tilde{\sigma}$ were measured under the exposure of the films to modulated light from a light-emitting diode with the photon energy 1.85 eV and the amplitude of the modulated incident-photon flux $I = 9.6 \times 10^{13}$ cm^{-2} s^{-1}. The modulation frequency was $f = \omega/2\pi = 2$ kHz. Measurements of the frequency dependences of $\Delta\tilde{\sigma}$ for the films under study showed that this modulation frequency satisfied the above condition for the determination of $N_t(E)$ from the measurements of $\Delta\bar{\sigma}$ and $\Delta\tilde{\sigma}$.

In Fig. 1, we show the spectral dependences of the absorption coefficient α for the studied *a*-Si:H(Er) films. In order to aid comparison, the spectral dependence of α for *a*-Si:H(As) is also shown in Fig. 1. As can be seen, the value of α for the films doped with erbium exceeds that for the films doped with arsenic by nearly an order of magnitude in the region where radiation is absorbed by the structure defects in *a*-Si:H ($h\nu < 1.5$ eV). It is noteworthy that a certain increase in the absorption by defects is observed as the value of T_f (and, correspondingly, the concentration of erbium atoms introduced into *a*-Si:H) increases.

It is well known that the concentration of the defects (of a dangling-bond type) in the *a*-Si:H films depends on the position of the Fermi level in the mobility gap [7]. In the *a*-Si:H(Er) and *a*-Si:H(As) films studied by us, the positions of the Fermi levels were close to each other. Therefore, the larger absorption in the region corresponding to the defect states for *a*-Si:H(Er) indicates that the introduction of Er into *a*-Si:H gives rise to a higher concentration of defects than in the case of doping *a*-Si:H films with arsenic. This behavior can be related to the fact that, according to the available data [8], the Er atoms are incorporated into the *a*-Si:H structure as the ErO_x becomes more complex. Correspondingly, the introduction of Er into *a*-Si:H can lead to a larger increase in the density of the defect states located in the middle of the mobility gap than in the case of traditional impurities.

In Fig. 2, we show the temperature dependences of the constant photoconductivity component and the amplitude of the alternating component of the conductivity as obtained for the studied *a*-Si:H films. It can be seen that the amplitude of the alternating component of the photoconductivity is smaller than the constant component by two orders of magnitude. This behavior is related to the long characteristic photoresponse time of these films.

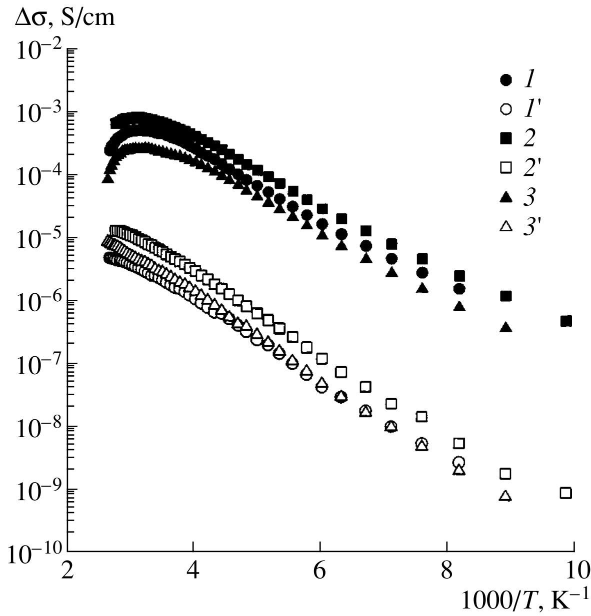

Fig. 2. Temperature dependences of the photoconductivity's constant component $\Delta\bar{\sigma}$ (curves *1–3*) and the amplitudes of the alternating component of the conductivity $\Delta\tilde{\sigma}$ (curves *1'–3'*) for the *a*-Si:H(Er) films obtained at T_f = (*1*, *1'*) 95 or (*2*, *2'*) 105°C, and (*3*, *3'*) for the *a*-Si:H(As) film.

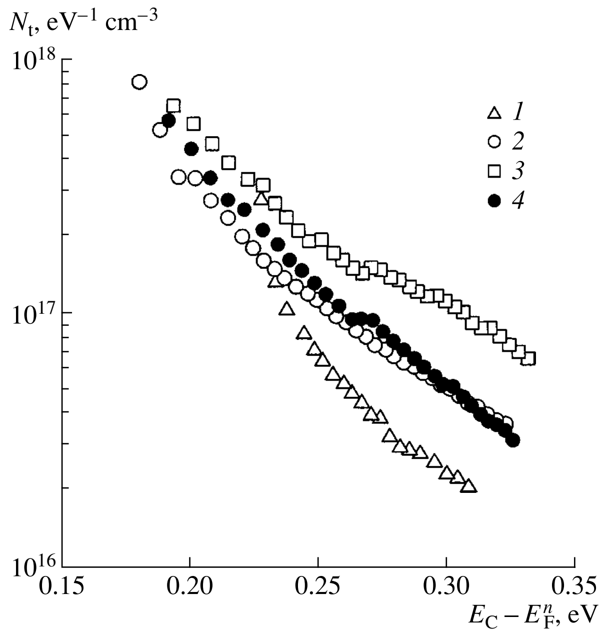

Fig. 3. Distribution of the density of the states N_t in the vicinity of the conduction-band bottom for the (*1–3*) *a*-Si:H(Er) films and (*4*) *a*-Si:H(As) films. The numbers at curves *1–3* correspond to those in Fig. 1.

The distribution of the density of the electronic states in the upper half of the mobility gap for the studied *a*-Si:H films doped with Er or As was determined from processing the temperature dependences of $\Delta\bar{\sigma}$ and $\Delta\tilde{\sigma}$ (see Fig. 3). The values of $E_C - E_F^n$ were determined from the expression

$$E_C - E_F^n = kT\ln(\sigma_0/\Delta\bar{\sigma}).$$

It can be seen in Fig. 3, by comparing the data obtained for the *a*-Si:H(Er) and *a*-Si:H(As) films, that the density of the states in the upper half of the mobility gap for the *a*-Si:H film doped with As is close to $N_t(E)$ for the *a*-Si:H film doped with Er at T_f = 95°C. It can also be seen from Fig. 3 that the density of the electronic states near the conduction-band bottom increases as T_f (and, correspondingly, the concentration of Er atoms introduced into *a*-Si) increases. We can note that the obtained result makes it possible to account for the different dynamics of the variation in the electrical conductivity under a prolonged illumination of *a*-Si:H films that have experienced various levels of doping with erbium [9]. A decrease in the relative variation in the electrical conductivity of *a*-Si:H(Er) films as the Er concentration increases under their exposure to prolonged illumination can be related to an increase in the density of the states in the region in which the shift of the Fermi level occurs.

Thus, the studies performed by us showed that the doping of *a*-Si:H films with Er led to a large increase in the density of the states in the mobility gap of this material as compared to *a*-Si:H doped with traditional donor impurities.

ACKNOWLEDGMENTS

We thank Doctor H. Mell for making films of microcrystalline Si:H doped with erbium or arsenic available.

This study was supported in part by the Russian Foundation for Basic Research, project no. 02-02-39020-GFEN-a.

REFERENCES

1. W. Fuhs, I. Ulber, G. Weiser, *et al.*, Phys. Rev. B **56**, 9545 (1997).
2. H. Kühne, G. Weiser, E. I. Terukov, *et al.*, J. Appl. Phys. **86**, 896 (1999).
3. V. Kh. Kudoyarova, A. N. Kuznetsov, E. I. Terukov, *et al.*, Fiz. Tekh. Poluprovodn. (St. Petersburg) **32** (11), 1384 (1998) [Semiconductors **32**, 1234 (1998)].
4. J. Stuke, J. Non-Cryst. Solids **97–98**, 1 (1987).
5. M. Vanecek, J. Kocka, J. Stuchlik, and A. Triska, Solid State Commun. **39**, 1199 (1981).
6. K. W. Boer and E. A. Niekisch, Phys. Status Solidi **1**, 275 (1961).
7. K. Pierz, W. Fuhs, and H. Mell, J. Non-Cryst. Solids **114**, 651 (1989).
8. C. Piamonteze, A. C. Iniguez, L. R. Tessler, *et al.*, Phys. Rev. Lett. **81**, 4652 (1998).
9. A. V. Birukov, A. V. Fenuchin, A. G. Kazanskii, and E. I. Terukov, Mater. Sci. Eng. B **105**, 153 (2003).

Translated by A. Spitsyn

Semiconductors, Vol. 39, No. 3, 2005, pp. 354–359. Translated from Fizika i Tekhnika Poluprovodnikov, Vol. 39, No. 3, 2005, pp. 372–377.
Original Russian Text Copyright © 2005 by Mnatsakanov, Yurkov, Tandoev.

PHYSICS OF SEMICONDUCTOR DEVICES

A New Physical Mechanism for the Formation of Critical Turn-On Charge in Thyristor Structures

T. T. Mnatsakanov^, S. N. Yurkov, and A. G. Tandoev

All-Russia Electrotechnical Institute, Moscow, 111250 Russia

^e-mail: mnatt@vei.ru

Submitted June 21, 2004; accepted for publication July 12, 2004

Abstract—A new mechanism for the formation of critical turn-on charge is shown to exist in thyristor structures. A new analytical model that makes it possible to derive the relations that define the critical charge in modern thyristor structures based on either Si or a new SiC material is suggested. The validity of the suggested analytical model of critical charge is verified using a numerical simulation. © *2005 Pleiades Publishing, Inc.*

1. INTRODUCTION

The critical-charge concept makes it possible to describe the main characteristics of a thyristor structure, including the critical buildup rate of anode voltage $\left(\frac{dU}{dt}\right)_{\text{crit}}$, the lowest turn-on control current, the propagation rate of the turn-on state, the turn-off time of a thyristor, etc., from a unified standpoint. The concept of critical charge Q_{cr} was first suggested by Uvarov [1] and was then developed in a number of publications [2–5].

The model of critical charge suggested by Uvarov [1] has been widely used to describe the characteristics of silicon structures. We should note that the existence of a leakage current in at least one of the emitter junctions of a thyristor is fundamentally important for a realization of the critical state in the context of the Uvarov concept. Uvarov suggested that recombination in the space-charge region (SCR) and artificial shunting of an emitter junction [1] were the leakage-current mechanisms, although the main role in actual silicon structures was attributed to artificial shunting.

However, recently reported experimental data that was obtained in studies of thyristor structures based on a promising new material (SiC) for high-power electronics [6, 7] deviated appreciably from the predictions of the critical-charge model [1]. A special feature of thyristors based on SiC is the absence of artificial shunting. In these conditions, according to the Uvarov model, the recombination in the SCR of an emitter junction is the sole feasible mechanism of leakage current. At the same time, the use of the relations suggested in [1] to calculate the critical charge yields, in this case, a theoretical value of Q_{cr} that is smaller, by two orders of magnitude, than the experimentally measured value in [6, 7]. This fact stimulated an analysis of the existing concept of critical charge, for example, the analysis performed in [8]. The analysis in [8] showed that a new mechanism of critical-charge formation existed in thyristor structures based on SiC.

The critical state of a thyristor structure was studied by Mnatsakanov *et al.* [8] in the context of a general approach, which makes it possible to hope that the new mechanism of critical-charge formation is universal and can be realized in more than just SiC-based structures. At the same time, it is worth noting that a number of simplifying assumptions were used when performing the calculations in [8].

The objective of this study is to derive the relations that make it possible to determine the value of the critical charge in modern thyristor structures based on either Si or SiC. These thyristors differ radically from the thyristors of the 1960s, for which the critical-charge model was originally developed [1].

2. THE PHYSICAL MECHANISMS OF CRITICAL-CHARGE FORMATION

The classical concept of critical charge [1] is based on the consideration of a dynamic balance of nonequilibrium charge carriers in the base layers of a thyristor structure. This balance depends, on one hand, on the regeneration processes that are caused by positive feedback and lead to an increase in the number of particles and, on the other hand, on the losses caused by the recombination and leakage currents in the emitter junctions. It is important that the inherent injection factors in both emitter junctions are assumed to be equal to unity.

The existence of positive feedback in thyristor structures gives rise to the *S*-type shape of the current–voltage (*I*–*V*) characteristic. This shape is indicative of the existence of the static nonsteady states that are defined by the expression

$$\gamma_1\alpha_{T1} + \gamma_2\alpha_{T2} = 1 - \frac{j_{k0}}{j}, \tag{1}$$

1063-7826/05/3903-0354$26.00 © 2005 Pleiades Publishing, Inc.

where j_{k0} is the generation current of the collector junction, γ_1 and γ_2 are the injection factors for the emitter junctions, and α_{T1} and α_{T2} are the coefficients of the charge-carrier transport through the base layers of the composite transistors. We will abide by the following rule, generally accepted in most publications: the designations γ_1 and α_{T1} are used for a composite transistor with a narrow and heavily doped base, whereas the designations γ_2 and α_{T2} are used for a composite transistor with a wide and lightly doped base.

A study of the balance of the nonequilibrium charge carriers in states close to those described by expression (1) made it possible [1] to determine the value of the critical charge Q_{cr}. However, we should note that it was assumed [1] that γ_2, α_{T1}, and α_{T2} are independent of the current and only γ_1, the effective injection factor of junction 1 (which lies between the emitter and the narrow heavily doped base), depends on the current density j. This assumption is often found to be justified in the silicon thyristors for which the critical-charge model was developed [1]. This circumstance is caused by the fact that, even in silicon thyristors operating at the highest voltages, the turn-on occurs, as a rule, under conditions where the coefficients of the transport through the base layers α_{T1} and α_{T2} can, to a high degree of accuracy, be considered constant. In addition, the emitter junction adjoining the heavily doped narrow base is artificially shunted by the resistance R_{sh}. The presence of shunting makes the dependence $\gamma_1(j)$ especially strong in the vicinity of the switching point, which makes it possible to disregard the dependence $\gamma_2(j)$.

A different situation is realized in thyristors based on SiC. First of all, it should be noted that there is no artificial shunting in any of the thyristors based on SiC described in previous publications. However, for the p^+–n emitter junction in the composite transistor with a narrow base, the value of the inherent injection factor γ_1 is small due to an incomplete ionization of the Al doping atoms in the p^+-type emitter. Furthermore, as was shown by Levinshtein *et al.* [7], the lowest turn-on control current $j_{g\min}$ is found to be so large that it corresponds to the average injection level in the lightly doped wide base of a thyristor. In this case, as the current increases, the condition

$$(\gamma_1\alpha_{T1} + \gamma_2\alpha_{T2}) > 1 \quad (2)$$

can be satisfied by an increase in the transport coefficient α_{T2} rather than an increase in γ_1.

Indeed, when we pass from a low injection level to a high injection level in the lightly doped p^0-type thyrister base (it is noteworthy that the SiC-based thyristors include a p-type blocking base, which is related to special features of the technology of SiC structures), the transport coefficient α_{T2} changes from $(\alpha_{T2})_L$ [9],

$$(\alpha_{T2})_L = \frac{1}{\cosh(W'_p/L_n)}, \quad (3a)$$

to $(\alpha_{T2})_H$,

$$(\alpha_{T2})_H = \frac{b}{b+1} + \frac{1}{b+1}\left(\frac{1}{\cosh(W'_p/L_a)}\right), \quad (3b)$$

where W'_p is the thickness of the electroneutral part of the wide p^0-type base; $L_n = \sqrt{D_n(\tau_n)_L}$; $L_a = \sqrt{D_a(\tau_n)_H}$; $D_a = \frac{2b}{b+1}D_p$ is the ambipolar diffusion coefficient; D_p is the diffusion coefficient for holes; and $(\tau_n)_L$ and $(\tau_n)_H$ are the lifetimes of the electrons in the wide p^0-type base at the low and high injection levels, respectively. Numerical estimations for the high-voltage structures based on SiC [10] yield the following values: $(\alpha_{T2})_L \approx 0.4$–$0.5$ and $(\alpha_{T2})_H \approx 0.90$–$0.95$. The obtained estimates indicate that, as the current increases, the dependence $\alpha_{T2}(j)$ can appreciably affect the left-hand side of formula (1).

In addition, the shunting of the second emitter junction in a number of modern silicon-based thyristor structures means that it is also important to take into account the dependence $\gamma_2(j)$.

In what follows, we present an analytical theory of the critical turn-on charge in a thyristor. In this theory, we take into account the physically justified current dependences $\gamma_1(j)$, $\gamma_2(j)$, and $\alpha_{T2}(j)$. The results of the analytical calculation are compared with data obtained from a numerical simulation using the software package "Investigation" [11].

3. AN ANALYTICAL STUDY OF THE PROBLEM

We use the charge method described in [12, 13] in order to study the problem analytically. This method has attained good results for the calculation of the key parameters in the turn-on process of thyristors based on either Si [5, 12, 13] or SiC [10, 14]. When deriving the relations of the model, we will follow the aforementioned rule: the designations γ_1 and α_{T1} are used for a composite transistor with a heavily doped narrow base, whereas the designations γ_2 and α_{T2} are applied to a composite transistor with a lightly doped wide base.

In the context of the charge method [12, 13], the equations describing variations in the charge of the minority carriers in the narrow base $Q_1 = q\int_0^{W_1} n_1(x)dx$ of the structure, as well as in the charge of the minority carriers in the wide base $Q_2 = q\int_0^{W_2} n_2(x)dx$, are written as

$$\frac{dQ_1}{dt} = -\left[(1-\gamma_1)k_1 + \frac{1}{\tau_1}\right]Q_1 + \gamma_1 k_2 Q_2 + \gamma_1(j_{k0} - j_{R1}),$$
$$\frac{dQ_2}{dt} = \gamma_2 k_1 Q_1 - \left[(1-\gamma_2)k_2 + \frac{1}{\tau_2}\right]Q_2 + \gamma_2(j_{k0} - j_{R2}), \quad (4)$$

where $k_1 = \dfrac{\alpha_{T1}}{(1-\alpha_{T1})\tau_1}$; $k_2 = \dfrac{\alpha_{T2}}{(1-\alpha_{T2})\tau_2}$; τ_1 and τ_2 are the lifetimes of the minority charge carriers in the narrow and wide bases, respectively; and j_{k0} is the density of the generation current in the collector junction. The current densities j_{R1} and j_{R2} are introduced, by making an analogy with publication [1], in the following way. It is assumed that the currents flowing through the p^+–n and n^+–p emitter junctions are given by the sum of the diffusion current and the excess currents j_{R1} and j_{R2}, which can be considered as either recombination currents or currents leaking into the shunt.

The initial conditions for Eqs. (4) are given by

$$Q_1\big|_{t=0} = Q_{10},\qquad Q_2\big|_{t=0} = Q_{20}, \tag{5}$$

where Q_{10} and Q_{20} are the initial charges in the narrow and wide bases, respectively.

In this case, the total current flowing through the structure is expressed in terms of the quantities Q_1 and Q_2 as

$$j = k_1Q_1 + k_2Q_2 + j_{k0}. \tag{6}$$

Equations (4) can be transformed by taking into account the following specific features of thyristor structures. First, the fairly large band gap makes it possible to disregard the generation current j_{k0} on the right-hand side of Eqs. (4). Second, it is noteworthy that, in the course of the change from a low injection level to a high injection level in the wide base of the structure, the electron lifetime τ_2 and the transport coefficient α_{T2} vary, which leads to a monotonic increase in the parameter k_2. By analogy with [8], we also use the following monotonically increasing approximate expressions in order to describe the variation in k_2:

$$\begin{aligned} k_2 &= (k_2)_\mathrm{L} \equiv \frac{(\alpha_{T2})_\mathrm{L}}{(1-(\alpha_{T2})_\mathrm{L})(\tau_2)_\mathrm{L}} \quad \text{at} \quad Q_2 \le Q_{2\mathrm{L}},\\ k_2 &= k_{2\mathrm{eff}} - \frac{j_{Rk}}{Q_2} \quad \text{at} \quad Q_{2\mathrm{L}} \le Q_2 \le Q_{2\mathrm{H}},\\ k_2 &= (k_2)_\mathrm{H} \equiv \frac{(\alpha_{T2})_\mathrm{H}}{(1-(\alpha_{T2})_\mathrm{H})(\tau_2)_\mathrm{H}} \quad \text{at} \quad Q_2 > Q_{2\mathrm{H}}. \end{aligned} \tag{7}$$

Here, $k_{2\mathrm{eff}} = \dfrac{(k_2)_\mathrm{H}Q_{2\mathrm{H}} - (k_2)_\mathrm{L}Q_{2\mathrm{L}}}{Q_{2\mathrm{H}} - Q_{2\mathrm{L}}}$, $j_{Rk} = \dfrac{((k_2)_\mathrm{H} - (k_2)_\mathrm{L})Q_{2\mathrm{L}}Q_{2\mathrm{H}}}{Q_{2\mathrm{H}} - Q_{2\mathrm{L}}}$, $Q_{2\mathrm{L}} = \zeta qN_2W_p$, $Q_{2\mathrm{H}} = (1/\zeta)qN_2W_p$, and ζ is a small parameter that controls the injection level in the wide base ($\zeta \approx 0.1$). It is worth noting that the value of the parameter $k_{2\mathrm{eff}}$ almost coincides with $(k_2)_\mathrm{H}$. Indeed,

$$k_{2\mathrm{eff}} = \frac{(k_2)_\mathrm{H} - (k_2)_\mathrm{L}\zeta^2}{1-\zeta^2} \approx (k_2)_\mathrm{H} + [(k_2)_\mathrm{H} - (k_2)_\mathrm{L}]\zeta^2 \approx (k_2)_\mathrm{H}. \tag{8}$$

We use a similar approximation to describe the variation in the quantity τ_n, i.e.,

$$\begin{aligned} \frac{1}{\tau_2} &= \frac{1}{(\tau_2)_\mathrm{L}}, \quad \text{at} \quad Q_2 \le Q_{2\mathrm{L}},\\ \frac{1}{\tau_2} &= \frac{1}{(\tau_2)_\mathrm{eff}} + \frac{j_{R\tau}}{Q_2}, \quad \text{at} \quad Q_{2\mathrm{L}} \le Q_2 \le Q_{2\mathrm{H}},\\ \frac{1}{\tau_2} &= \frac{1}{(\tau_2)_\mathrm{H}}, \quad \text{at} \quad Q_2 > Q_{2\mathrm{H}}, \end{aligned} \tag{9}$$

where $Q_{2\mathrm{L}}$, $Q_{2\mathrm{H}}$, and ζ are defined in the same way as above, while $j_{R\tau} = \dfrac{((\tau_2)_\mathrm{H} - (\tau_2)_\mathrm{L})Q_{2\mathrm{H}}Q_{2\mathrm{L}}}{(Q_{2\mathrm{H}} - Q_{2\mathrm{L}})(\tau_2)_\mathrm{H}(\tau_2)_\mathrm{L}}$ and $\dfrac{1}{(\tau_2)_\mathrm{eff}} = \dfrac{\dfrac{Q_{2\mathrm{H}}}{(\tau_2)_\mathrm{H}} - \dfrac{Q_{2\mathrm{L}}}{(\tau_2)_\mathrm{L}}}{Q_{2\mathrm{H}} - Q_{2\mathrm{L}}}$.

Taking into account the introduced approximations, we can represent Eqs. (4) in the following form for the current-density range of interest:

$$\begin{aligned} \frac{dQ_1}{dt} &= -\left[(1-\gamma_1)k_1 + \frac{1}{\tau_1}\right]Q_1 + \gamma_1k_{2\mathrm{eff}}Q_2 - \gamma_1j_{R1} - \gamma_1j_{Rk},\\ \frac{dQ_2}{dt} &= \gamma_2k_1Q_1 - \left[(1-\gamma_2)k_{2\mathrm{eff}} + \frac{1}{\tau_{2\mathrm{eff}}}\right]Q_2 + \gamma_2j_{R2} - j_{R\tau} + (1-\gamma_2)j_{Rk}. \end{aligned} \tag{10}$$

A solution to Eqs. (10) with boundary conditions (5) is given by [14]

$$\begin{aligned} Q_1 &= \frac{\lambda_1 - b_2}{a_2}C_1\exp(\lambda_1t) + \frac{\lambda_2 - b_2}{a_2}C_2\exp(\lambda_2t) - \frac{b_2d_1 - b_1d_2}{b_2a_1 - b_1a_2},\\ Q_2 &= C_1\exp(\lambda_1t) + C_2\exp(\lambda_2t) + \frac{a_2d_1 - a_1d_2}{b_2a_1 - b_1a_2}, \end{aligned} \tag{11}$$

where the integration constants C_1 and C_2 are determined from the initial conditions and written as

$$\begin{aligned} C_1 &= \frac{a_2}{\lambda_1 - \lambda_2}\left[Q_{10} + \frac{\lambda_1 - a_1}{a_2}Q_{20} + \frac{1}{\lambda_1}\left(d_1 + d_2\frac{\lambda_1 - a_1}{a_2}\right)\right],\\ C_2 &= -\frac{a_2}{\lambda_1 - \lambda_2}\left[Q_{10} - \frac{\lambda_1 - b_2}{a_2}Q_{20} + \frac{1}{\lambda_2}\left(d_1 - d_2\frac{\lambda_1 - b_2}{a_2}\right)\right]. \end{aligned} \tag{12}$$

The parameters a_1, b_1, a_2, b_2, d_1, and d_2 can be expressed as $a_1 = -\left[(1-\gamma_1)k_1 + \frac{1}{\tau_1}\right]$,

$$b_1 = \gamma_1 k_{2\text{eff}}, \quad a_2 = \gamma_2 k_1,$$

$$b_2 = -\left[(1-\gamma_2)k_{2\text{eff}} + \frac{1}{\tau_{2\text{eff}}}\right], \quad d_1 = -\gamma_1(j_{Rk} + J_{R1}),$$

$d_2 = -j_{R\tau} - \gamma_2 j_{R2} + (1 - \gamma_2)/j_{Rk}$, while the quantities λ_1 and λ_2 are the roots of the characteristic equation for system (10); this equation is written as

$$\lambda^2 - (a_1 + b_2)\lambda + a_1 b_2 - a_2 b_1 = 0. \quad (13)$$

If the condition for the thyristor turn-on, $\gamma_1\alpha_{T1} + \gamma_2\alpha_{T2} > 1$, is satisfied, the free term on the left-hand side of Eq. (13) is negative: $a_1b_2 - a_2b_1 < 0$ [15]. In this case, the roots λ_1 and λ_2 of the characteristic equation are real and have different signs. We assume, for clarity, that $\lambda_1 > 0$ and $\lambda_2 < 0$. By substituting the quantities λ_1 and λ_2 into expressions (11) followed by a substitution of the obtained quantities Q_1 and Q_2 into expression (6), we can easily show that the steady state corresponding to the classical concept of critical charge exists if

$$C_1 = 0. \quad (14)$$

Taking into account that $1/\lambda_1 \equiv \tau_r$ (here, τ_r is the current-buildup constant for the thyristor turn-on), we can use condition (14) to obtain the following condition for the appearance of the critical state in a thyristor:

$$Q_{10} + \chi Q_{20} = Q_{\text{cr}}. \quad (15)$$

Here, $\chi = \frac{\lambda_1 - a_1}{a_2}$ is the efficiency coefficient for the charge accumulated in the wide p-type base [1] and the critical charge Q_{cr} is defined by the expression

$$Q_{\text{cr}} = \tau_r[\gamma_1(j_{R1} + j_{Rk}) + \chi(j_{R\tau} + \gamma_2 j_{R2} - (1-\gamma_2)j_{Rk})]. \quad (16)$$

This expression makes it possible to determine the critical charge for all the known turn-on modes of thyristor structures. In a situation where only the emitter junction of a composite transistor with a narrow base ($j_{R1} \neq 0$ but $j_{R2} = 0$) is shunted, the inherent injection coefficients of both emitter junctions are equal to unity ($\gamma_1 = \gamma_2 = 1$); therefore, the turn-on occurs at invariable injection levels in both base layers ($j_{Rk} = 0$ and $j_{R\tau} = 0$), and expression (16) is transformed into the well-known result [1]

$$Q_{\text{cr}} = j_{R1}\tau_r. \quad (17)$$

We now consider a situation in which in neither emitter junction (neither $j_{R1} = 0$ nor $j_{R2} = 0$) experiences leakage and the injection factor of the composite-transistor emitter with the wide base is equal to unity ($\gamma_2 = 1$) while the injection factor of the transistor with the narrow base is smaller than unity, to the extent that a moderate level injection in the wide base is required in order to ensure the thyristor turn-on ($j_{Rk} \neq 0$ and $j_{R\tau} \neq 0$). In this case, the value of the critical charge almost coincides with that obtained previously [8]:

$$Q_{\text{cr}} = \tau_r[\gamma_1 j_{Rk} + \chi j_{R\tau}]. \quad (18)$$

The difference between expression (18) and the similar formula derived in [8] is caused by the fact that, here, we are considering a variation in the charge-carrier lifetime in a wide base under the circumstances of a moderate injection level.

It follows from expression (16) that the effect of the factors controlling the value of the critical charge depends heavily on in which of the base regions these factors are prevalent. For example, the factors related to the leakage current in the emitter of a transistor with a wide base and to a variation of the charge-carrier lifetime as the injection level increases are found to be χ times less efficient than those related to the leakage currents in the emitter of a transistor with a narrow base and the current j_{Rk}.

The dependence of Q_{cr} on γ_1 and γ_2 described by expression (16) seems, at first glance, to be paradoxical. Specifically, simple qualitative reasoning shows that, as γ_1 and γ_2 increase, the value of Q_{cr} should decrease; however, it formally follows from formula (16) that Q_{cr} increases along with γ_1 and γ_2. In fact, there is no contradiction in expression (16) since, in the course of the thyristor turn-on, the current-buildup constant τ_r also depends on γ_1 and γ_2. Using the previously reported expressions for τ_r [10], we can easily find that $dQ_{\text{cr}}/d\gamma_1 < 0$ and $dQ_{\text{cr}}/d\gamma_2 < 0$, which is completely consistent with the results of the simple qualitative consideration.

Finally, it is worth noting that expression (16) has a general form and describes the value of the critical charge in thyristors based on either on Si or on SiC. It should be taken into account that, in silicon thyristors, the wide base is typically found to be of an n-type conductivity whereas the narrow base is found to exhibit a p-type conductivity. It is important that all the quantities with the subscript 1 control the properties of the minority electrons in the narrow p-type base, whereas those with the subscript 2 control the properties of the minority holes in the wide n-type base.

A specific feature of thyristors based on SiC consists in the fact that these thyristors include both the wide p-type base and narrow n-type base. Therefore, when using expression (16) for SiC thyristors, one must be aware that the quantities with the subscript 1 describe the properties of the minority holes in the narrow n-type base, whereas those with the subscript 2 control the properties of the minority electrons in the wide p-type base.

4. RESULTS OF THE NUMERICAL SIMULATION

In order to verify the results of the analytical consideration, we performed a numerical simulation using the "Investigation" software package. This software package has previously achieved good results for analyses

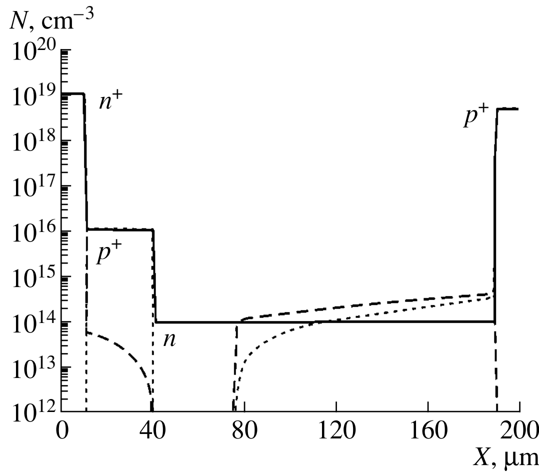

Fig. 1. The charge-carrier distribution at the stage of the exponential increase in current through the thyristor structure. The dashed lines represent the hole distribution and the dotted lines represent the electron distribution. The solid lines describe the distribution of doping impurities in the structure.

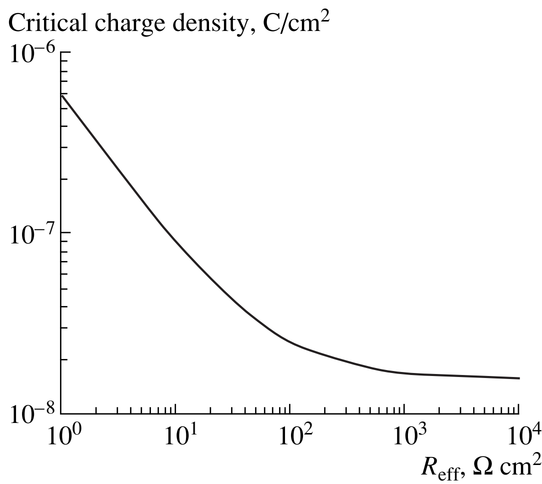

Fig. 2. The density of the critical turn-on charge in a thyristor as a function of the effective shunting of the n^+–p emitter junction.

of the static and dynamic characteristics of both Si [11, 16–19] and SiC [7, 8, 10–13, 15, 20] multilayered structures.

When studying the problem numerically, we gave most of our attention to an analysis of the special features of the model for the critical turn-on charge of thyristors for which we already had analytical predictions. Since the applicability of the new model to thyristors based on SiC has already been verified [8], we now consider a silicon n^+–p–n^0–p^+ thyristor in which the sum of the transport coefficients for the base layers does not exceed unity. We particularly chose a thyristor structure with the above combination of transport coefficients because the study of the special features of the turn-on process in this structure would make it possible to verify the efficiency of the new mechanism of critical-charge formation. Indeed, according to [1], where α_{T1} and α_{T2} are assumed to be constant, such a thyristor should remain in the turn-off state. This circumstance is due to the fact that, even in the case of $\gamma_1 = 1$ and $\gamma_2 = 1$, the sum of the transport coefficients is found to be smaller than unity (i.e., $\gamma_1\alpha_{T1} + \gamma_2\alpha_{T2} < 1$) and, therefore, the condition for turn-on (2) is not satisfied. In contrast, according to this study, the new mechanism of critical-charge formation can ensure the fulfillment of condition (2); as a result, the thyristor is converted to the turn-on state. It is worth noting that the increase in α_{T2} required for this conversion is found to be caused by an increase in the level of the injection (from a low level to a high level) of the charge carriers in the wide n^0-type base, which can be easily detected in the course of a numerical simulation of the turn-on process in the structure.

The thyristor structure is shown schematically in Fig. 1. The main parameters of the structure's layers are also shown. The characteristics of the deep level controlling the charge-carrier lifetime in the n^0-type base were chosen as follows: $\tau_{p0} = 0.1$ μs, $\tau_{n0} = 4.9$ μs, and $n_1 = p_1 = n_i$.

The calculation, taking into account the aforementioned effects, indicates that, when there is a low level of charge-carrier injection into both base layers, the sum of the coefficients of the charge-carrier transport through the layers is $\alpha_{T1} + \alpha_{T2} = 0.95 < 1$. As was already mentioned above, such a transistor cannot be converted to the turn-on state in the context of the concepts developed by Uvarov [1]. Nevertheless, the results of the numerical computation show that the thyristor structure under consideration can be turned on; however, the stage in which there is an exponential increase in the current sets in only when the transition from the low injection level to the moderate injection level occurs in the wide base layer. This inference is evidently confirmed by the distributions of electrons (dotted lines) and holes (dashed lines) shown in Fig. 1. The calculated charge-carrier distributions are completely consistent with the inferences made on the basis of the analytical model (see the previous section).

Thus, the numerical simulation confirms the existence of the new mechanism of the critical-charge formation caused by the dependence $\alpha_{T2}(j)$ when the level of the charge-carrier injection is varied in the wide and lightly doped base layer of the structure.

In Fig. 2, we show the calculated dependence of the critical-charge density for the turn-on of the thyristor on the effective shunting resistance of the n^+–p emitter junction (it was assumed, in the calculation, that there was no shunting of the p^+–n emitter junction). The dependence shown in Fig. 2 levels off at 1.7×10^{-8} C/cm² as R_{eff} increases, which is completely consistent with expression (16). It is worth noting that, for the Uvarov mech-

anism of critical-charge formation [1], the limiting critical-charge value caused by the recombination in the space-charge region of the emitter junction is found to be more than two orders of magnitude smaller and does not exceed 10^{-10} C/cm^2.

5. CONCLUSION

As a result of performed studies, we verified the existence of a new mechanism for the formation of the critical turn-on charge in thyristor structures. This mechanism is related to the transition from a low level of charge-carrier injection in the lightly doped base of the thyristor to a high injection level. The suggested mechanism complements the previously recognized mechanism of critical-charge (Q_{cr}) formation that was related to the leakage of the charge carriers in the emitter junction of a thyristor [1]. In fact, a combination of these two mechanisms for Q_{cr} formation makes it possible to extend the concept of critical charge to the region of the high current densities that trigger the turn-on process of a thyristor; as a result, this combination is conducive to the generality of this concept, which is found extremely useful for a description of the dynamic processes in both SiC and Si thyristors.

We derived the expressions that make it possible to determine the value of the critical charge in modern thyristors, taking into account all the known factors that affect Q_{cr} formation. The validity of the analytical model is verified using the numerical simulation.

ACKNOWLEDGMENTS

We thank M.E. Levinshtein for his participation in helpful discussions and his valuable comments.

REFERENCES

1. A. I. Uvarov, in *Physics of Electron–Hole Junctions and Semiconductor Devices* (Nauka, Leningrad, 1969), p. 151 [in Russian].
2. A. I. Uvarov, in *Physics of Electron–Hole Junctions and Semiconductor Devices* (Nauka, Leningrad, 1969), p. 194 [in Russian].
3. R. É. Ayazyan, A. V. Gorbatyuk, and A. I. Palamarchuk, Radiotekh. Élektron. (Moscow) **23**, 1039 (1978).
4. A. V. Gorbatyuk, Fiz. Tekh. Poluprovodn. (Leningrad) **14**, 1364 (1980) [Sov. Phys. Semicond. **14**, 806 (1980)].
5. V. A. Kuz'min, V. Ya. Pavlik, S. F. Pashukanis, and A. G. Tandoev, Élektrotekhnika **11**, 47 (1984).
6. M. E. Levinshtein, J. W. Palmour, S. L. Rumyantsev, and R. Singh, IEEE Trans. Electron Devices **45**, 307 (1998).
7. M. E. Levinshtein, P. A. Ivanov, T. T. Mnatsakanov, *et al.*, Solid-State Electron. **47**, 699 (2003).
8. T. T. Mnatsakanov, S. N. Yurkov, M. E. Levinshtein, *et al.*, Solid-State Electron. **47**, 1581 (2003).
9. A. Blicher, *Thyristor Physics* (Springer, New York, 1976; Énergoizdat, Leningrad, 1981).
10. T. T. Mnatsakanov, M. E. Levinshtein, S. N. Yurkov, *et al.*, Solid-State Electron. **46**, 525 (2002).
11. T. T. Mnatsakanov, I. L. Rostovtsev, and N. I. Philatov, Solid-State Electron. **30**, 579 (1987).
12. R. L. Davies and J. Petruzella, Proc. IEEE **55**, 1318 (1967).
13. W. Gerlach, *Thyristoren* (Springer, Heidelberg, 1981; Énergoatomizdat, Moscow, 1985).
14. E. Kamke, *Gewöhnliche Differentialgleichungen* (Akademie, Leipzig, 1959; Nauka, Moscow, 1976).
15. M. E. Levinshtein, T. T. Mnatsakanov, P. A. Ivanov, *et al.*, Solid-State Electron. **45**, 453 (2001).
16. M. E. Levinshtein, T. T. Mnatsakanov, S. N. Yurkov, *et al.*, Solid-State Electron. **46**, 1953 (2002).
17. T. T. Mnatsakanov, I. L. Rostovtsev, and N. I. Filatov, Radiotekh. Élektron. (Moscow) **37**, 296 (1992).
18. T. T. Mnatsakanov, D. Schröder, and A. Schlogl, Solid-State Electron. **42**, 153 (1998).
19. A. Schlogl, T. T. Mnatsakanov, H. Kuhn, and D. Schröder, IEEE Trans. Power Electron. **15**, 1267 (2000).
20. T. T. Mnatsakanov, M. E. Levinshtein, P. A. Ivanov, *et al.*, J. Appl. Phys. **93**, 1095 (2003).

Translated by A. Spitsyn

Semiconductors, Vol. 39, No. 3, 2005, pp. 360–363. Translated from Fizika i Tekhnika Poluprovodnikov, Vol. 39, No. 3, 2005, pp. 378–381.
Original Russian Text Copyright © 2005 by Togatov, Gnatyuk.

PHYSICS OF SEMICONDUCTOR DEVICES

A Method for Measuring the Lifetime of Charge Carriers in the Base Regions of High-Speed Diode Structures

V. V. Togatov and P. A. Gnatyuk

State University of Information Technologies, Mechanics, and Optics, St. Petersburg, 197101 Russia

Submitted July 8, 2004; accepted for publication July 29, 2004

Abstract—A method for measuring the lifetime of charge carriers in the base regions of p^+–n–n^+ structures is suggested. This method makes it possible to perform measurements in the nanosecond range of lifetimes. The developed technique implies the same shape of measuring current pulse as is used for conventional measurements of the restoring times in diode structures. The method is validated on the basis of an analysis of a solution to the continuity equation for holes in a base region. The results of the calculations are compared with experimental data. © *2005 Pleiades Publishing, Inc.*

1. INTRODUCTION

Either the duration of a stage of high reverse conductance (the restoring interval) [1–3] or the decay rate of postinjection voltage [4] is typically used as the informative parameter in measurements of charge-carrier lifetime in the base regions of p^+–n–n^+ structures. In the former case, rectangular pulses of forward and reverse currents are passed through the structure and the duration of the restoring interval is measured. It is important that the time required for the transition from the forward current to the reverse current must be an order of magnitude shorter than the measured interval itself. In the latter case, a rectangular pulse of forward current is passed through the structure and the decay of the postinjection voltage is measured immediately after the current-pulse completion. The successful use of the aforementioned methods becomes problematic if the measured times amount to several (or tens of) nanoseconds. This circumstance is related to the fact that, for the current switching in actual measuring systems, the duration of the transient processes caused by stray parameters (the barrier capacitance of a diode, inductance of the clamping device, and so on) exceeds the time intervals to be measured. At the same time, the development of new types of fast-response high-voltage structures based on Si (and, especially, on GaAs) requires the measurement of exactly these lifetime values.

2. SUBSTANTIATION OF THE MEASUREMENT METHOD

A schematic representation of the p^+–n–n^+ structure is shown in Fig. 1. We will use the duration of the stage of high reverse conductance (the restoring interval) as the informative parameter. The shape of the measurement current pulse is shown in Fig. 2. The same current-pulse shape is used in conventional measurements of the recovery time t_{rr} of diodes.

A pulse of the forward current I passes through the p^+–n–n^+ structure until the point in time t_1; this pulse gives rise to a steady-state distribution of the hole concentration in the base. Linear decay of the current sets in at t_1. The current decreases to zero by the point in time t_2, and the restoring interval begins and is complete at the moment t_3 that corresponds to the depletion of the p–p junction. It is evident that, for the specified pulse shape, first, the current switching is not instantaneous and, second, the instant of measurement and the subsequent onset of the switching are separated by the time interval $t_2 - t_1$. The duration of the restoring interval $t_{res} = t_3 - t_2$ is the hole-lifetime function under study in the base. Thus, the substantiation of the measurement method is related to an analysis of the nonsteady hole concentration in the base at the stage of linear current decay.

The hole motion in the base is described by the following time-dependent continuity equation:

$$\frac{\partial^2 p}{\partial x^2} - \frac{p}{L_p^2} = \frac{\tau_p}{L_p^2}\frac{\partial p}{\partial t}. \quad (1)$$

Here, p is the hole concentration, and τ_p and L_p are, respectively, the lifetime and diffusion length of the holes. The boundary conditions for the problem can be obtained from the condition for a one-sided injection of

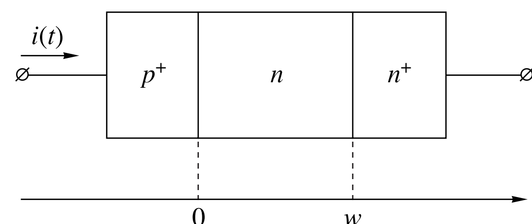

Fig. 1. Schematic representation of a p^+–n–n^+ structure.

1063-7826/05/3903-0360$26.00 © 2005 Pleiades Publishing, Inc.

charge carriers from the p^+- and n^+-type regions into the base region:

$$-\frac{\partial p}{\partial x}(0) = \frac{i(t)}{2qD_p}, \tag{2}$$

$$\frac{\partial p}{\partial x}(w) = \frac{i(t)}{2bqD_p}. \tag{3}$$

In these expressions, $i(t)$ is the time dependence of the charge density, q is the elementary charge, D_p is the diffusion coefficient for the holes, and b is the ratio between the electron and hole mobilities. In deriving boundary conditions (2) and (3), we assumed that there was a high injection level in the base. Since the onset of the measurement process is chosen to coincide with the leading edge of the measuring current pulse at $t = 0$ (Fig. 2), the initial condition of the problem is given by

$$p(x, 0) = 0. \tag{4}$$

The end of the restoring interval corresponds to a decrease in the excess concentration of the holes at the p–n junction to zero ($p(0, t_3) = 0$). Therefore, when analyzing the continuity equation, we are only interested in the nonsteady hole concentration at the junction $p(0, t)$. A solution of continuity Eq. (1), which is complemented by boundary conditions (2) and (3) and initial condition (4) and performed using the Laplace transformation, yields the following expression for the hole concentration at the junction:

$$P(0, s) = \frac{I(s)(b\cosh kw + 1)}{2bqD_p k\sinh kw}. \tag{5}$$

Here,

$$I(s) = \frac{I}{s} - \frac{a}{s^2}e^{-st_1}$$

is the transform of the current density shown in Fig. 2, $a = \frac{di}{dt}$ is the rate of the transition from the forward current to reverse current,

$$k = \frac{1}{L_p}\sqrt{1 + \tau_p s},$$

and w is the base width.

Transform (5) exhibits a multiple pole at the point $s = 0$ and simple poles at the points $s = -\frac{1}{\tau_p}$ and

$$s_n = -\frac{1}{\tau_p}\left[1 + \left(\frac{\pi n}{W}\right)^2\right],$$

where $n = 1, 2, \ldots$, and $W = w/L_p$ is the normalized base width. By determining the sum of the residues at all the critical points, we find the nonsteady hole concentration at the p–n junction:

$$p(0, t) = \frac{L_p}{2bqD_p}[F_1(t) + F_2(t)]. \tag{6}$$

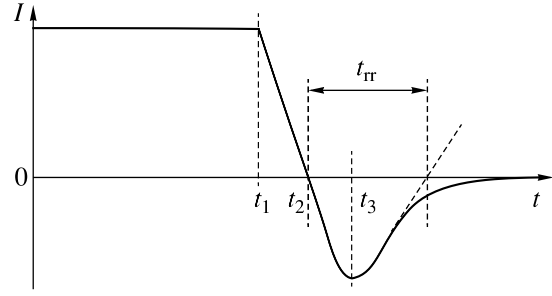

Fig. 2. The shape of the current pulse used in the measurements.

The function $F_1(t)$ determined by the residue at the multiple pole is given by

$$F_1(t) = \frac{b\cosh W + 1}{\sinh W}\left[I - a(t - t_1) + \frac{a\tau_p}{2}(1 + W\coth W) - \frac{ab\tau_p}{2}\frac{W\sinh W}{b\cosh W + 1}\right]. \tag{7}$$

The function $F_2(t)$ is given by the sum of the residues at all the simple poles and can be represented in the form

$$F_2(t) = -\frac{b+1}{W}\left(Ie^{-\frac{t}{\tau_p}} + a\tau_p e^{-\frac{t-t_1}{\tau_p}}\right) - 2\sum_{n=1}^{\infty}[b(-1)^n + 1]\left[-\frac{(-1)^n I}{s_n\tau_p W}e^{s_n t} + \frac{(-1)^n a}{s_n^2\tau_p W}e^{s_n(t-t_1)}\right]. \tag{8}$$

In expressions (7) and (8), $t > t_1$.

Let us analyze the functions $F_1(t)$ and $F_2(t)$ according to the following assumptions. First, we assume that $t_1 \gg \tau_p$. This condition is always satisfied when performing the measurements. As a result, we can disregard the first term in parentheses in expression (8) and the first term in the square brackets under the summation sign. Second, we assume that the inequality $W > 3$ is valid. This condition is known to be satisfied for high-voltage diodes with short switching times. In this case, we have $\coth W \approx 1$ and $\mathrm{cosech}\, W \approx 0$ in the functions $F_1(t)$ and $F_2(t)$. As a result, the expression for $p(0, t)$ can be written as

$$p(0, t) \approx \frac{aL_p}{2qD_p}\left[\frac{I}{a} - (t - t_1) + \frac{\tau_p}{2} - \frac{(b+1)\tau_p}{bW}e^{-\frac{t-t_1}{\tau_p}} - \frac{2}{b\tau_p W}\sum_{n=1}^{\infty}\frac{b + (-1)^n}{s_n^2}e^{s_n(t-t_1)}\right]. \tag{9}$$

Assuming that $p(0, t_3) = 0$ in expression (9), we obtain a transcendental equation that defines the point of time t_3

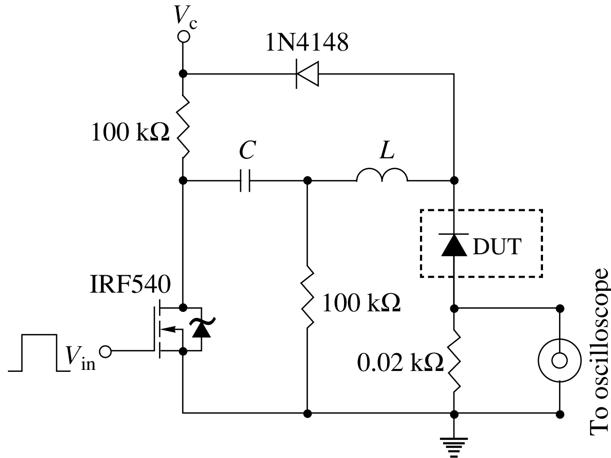

Fig. 3. A schematic diagram of the measurement setup based on a resonance *LC* circuit. DUT stands for a device under test.

that corresponds to the depletion of the *p–n* junction. In this case, t_3 appears in the obtained equation in the combination $t_3 - t_1$, which is designated as Δt. It follows from Fig. 2 that the interval $\Delta t = t_3 - t_1$ includes the time of the current decay to zero $t_d = t_2 - t_1 = I/a$ and the restoring interval $t_{res} = t_3 - t_2$; i.e.,

$$\Delta t = t_3 - t_1 = \frac{I}{a} + t_{res}. \quad (10)$$

Taking into account formula (10), we can write the equation defining t_{res} as

$$t_{res} = \frac{\tau_p}{2}\left[1 - \frac{b+1}{b}\frac{2}{W}e^{-\frac{\Delta t}{\tau_p}} - \frac{4}{bW}\sum_{n=1}^{\infty}\frac{b+(-1)^n}{(s_n\tau_p)^2}e^{s_n\Delta t}\right]. \quad (11)$$

The rapid convergence of the series in (11) is evident. We now determine the condition under which we can discard all the terms in the series in (11) (including the first term) apart from the second term. The ratio of the second term to the first term is found to be equal to $[2(b+1)/(b-1)]\exp(\Delta t/\tau_p)$ under the condition $W = \pi$. If $\Delta t/\tau_p \geq 3$, the ratio between the first term of the series and the second term is no larger than 0.025 for the devices based on GaAs where $b \gg 1$. This ratio is even smaller (0.0125) for the devices based on Si at $\Delta t/\tau_p = 3$. Thus, all the terms of the series can be discarded with confidence if the following condition is satisfied:

$$\Delta t/\tau_p \geq 3. \quad (12)$$

We now estimate the value of the second term in (11) in comparison with the first term under the condition that $\Delta t/\tau_p = 3$. Assuming (as in the previous case) that $W = \pi$, we find that the value of the second term is equal to 0.03 for the devices based on GaAs and 0.043 for the devices based on Si. Thus, if condition (12) is satisfied, we can use the following expression to determine the hole lifetime in the base to within 5%:

$$\tau_p = 2t_{res}. \quad (13)$$

When performing measurements, condition (12) can easily be satisfied by choosing the corresponding value of $a = di/dt$. For example, if $\tau_p = 0.2$ μs and the measurement is performed at a forward current of 10 A, $\Delta t = 3\tau_p = 0.6$ μs can be obtained for $di/dt = 20$ A/μs. If the forward current is reduced to 5 A, the value of di/dt should be reduced to 10 A/μs. It should be borne in mind that, in both cases, the value of the restoring interval is the same and equals $\tau_p/2 = 0.1$ μs.

The above example does not mean that the value of di/dt should be changed each time the current or the value of τ_p are varied. In studies of a certain type of device, the smallest value of di/dt that ensures the fulfillment of condition (12) in the specified ranges of currents and lifetimes is established.

We performed a similar analysis for the case of a sinusoidal measurement pulse $i = I_m \sin\omega t$. In this situation, the transform of the nonsteady hole concentration at the junction is described by expression (5), where only the current transform $I(s) = I_m/(s^2 + \omega^2)$ is varied. This expression yields residues in the complex conjugate poles $p = \pm j\omega$ when the transition to the origin is performed.

An analysis including the same procedures as in the case of a linearly decreasing current yields expression (13) if the following condition, which is similar to (12), is satisfied:

$$\omega\tau_p \leq 0.3. \quad (14)$$

This result should be expected, since a sinusoidal function is close to a linear function in the vicinity of the point $\omega t = \pi$.

3. EXPERIMENT

In order to test the validity of the suggested method, we studied various high-speed diodes experimentally: HFA08TB60, UF4004, HER108, US1J, BYG70J, 1N4148, KD212A, and a high-power diode based on GaAs (CLIFTON, Estonia).

According to (13), if conditions (12) or (14) are satisfied, the duration of the restoring interval is nearly independent of both the amplitude of the forward-current pulse and the value of di/dt. In order to verify this statement, we used a resonance *LC* circuit (Fig. 3) to form the semisinusoidal probing-current pulses.

In the first case to be considered, the circuit parameters were chosen so that condition (14) was satisfied. In Fig. 4, we show an oscilloscope pattern that illustrates the shape of the probing-current pulse. In Fig. 5, we show similar oscilloscope patterns that were recorded for four current pulses with severalfold differences in their amplitudes; the portions in the vicinity of the restoring interval can be seen in Fig. 4. It follows from the shown oscilloscope patterns that the value of the restoring interval hardly changes as the current amplitude is varied in the specified range. This result, predicted by the theory, was obtained for all the studied diodes, irrespective of the diode type or the hole lifetime in the base.

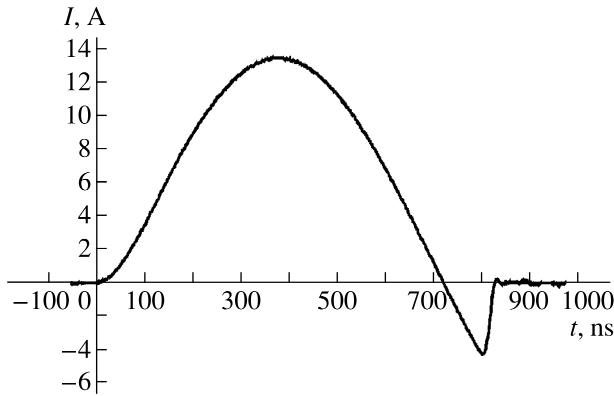

Fig. 4. An oscilloscope pattern of the current pulse used in the measurements.

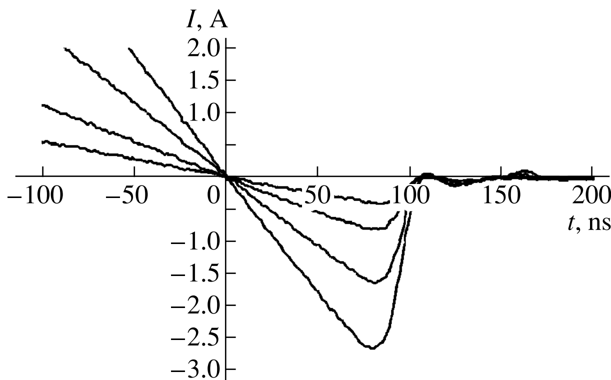

Fig. 5. Oscilloscope patterns of the current pulses with different amplitudes.

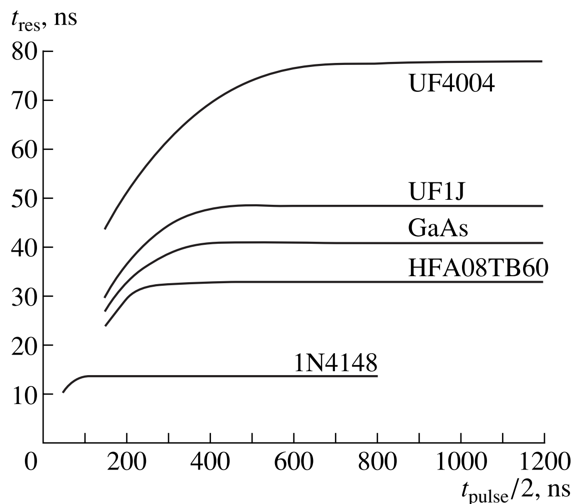

Fig. 6. Dependences of the restoring time on the half-period of the forward-current pulse $t_{pulse}/2$ for various diodes.

In the second case, the circuit parameters and the value of the initial voltage applied to the capacitor were chosen so that the pulse duration (half-period) and, consequently, *di*/*dt* varied but the amplitude remained unchanged. In Fig. 6, we show the dependences of the restoring time on the duration of the forward-current pulse t_{pulse}. The curves feature two characteristic portions for all the diodes studied. The restoring times are nearly independent of the duration of the forward-current pulse if this duration is long. A rapid decrease in the restoring interval is observed as the pulse duration decreases at small pulse durations. This dependence of the restoring time on the pulse duration is quite consistent with the results of the theoretical analysis.

The value of $\omega\tau_p$, which is measured experimentally and corresponds to an abrupt decrease in the duration of the restoring interval, is equal to about 0.4–0.5. Consequently, the theoretically derived condition $\omega\tau_p \leq 0.3$ is more rigid than that obtained experimentally. However, this contradiction is only an apparent one. Indeed, when analyzing the experimental data, we were dealing with an abrupt decrease in the duration of the restoring interval, whereas, in the theoretical analysis, we considered a general decrease in this duration within a given error. Thus, the experimental data are quite consistent with the results of the theoretical analysis.

4. CONCLUSION

In conclusion, we would like once again to emphasize the simplicity of both the method itself and its implementation. In addition, another advantage of the method is related to a decrease in the efficiency of emitters at high current densities. The charge-carrier lifetime measured using the Lax method [1] at high current densities can decrease by a factor of 1.5–2 owing to a decrease in the injection factor. In our method, we suggested the decrease in the excess charge in the base due to a decrease in the emitter efficiency is equivalent to the corresponding decrease in the forward-current amplitude. However, as follows from both the theory of the method and the experimental results, the measured value of the lifetime remains unchanged in this case. The fact that the results of measurements are independent of both the measurement-pulse amplitude and the value of *di*/*dt* in a fairly wide range makes it possible to use the suggested method for measuring the charge-carrier lifetime in any high-speed diodes based on *p*–*n* junctions.

REFERENCES

1. B. Lax and S. F. Neustadtez, J. Appl. Phys. **25**, 1148 (1954).
2. V. V. Togatov, Radiotekh. Élektron. (Moscow) **24**, 2107 (1979).
3. R. H. Kingston, Proc. IRE, No. 42, 829 (1954).
4. B. R. Gossick, Phys. Rev. **91**, 1012 (1953).

Translated by A. Spitsyn

Semiconductors, Vol. 39, No. 3, 2005, pp. 364–369. Translated from Fizika i Tekhnika Poluprovodnikov, Vol. 39, No. 3, 2005, pp. 382–387.
Original Russian Text Copyright © 2005 by Strokan, Ivanov, Kalinina, Kholuyanov, Onushkin, Davydov, Violina.

Spectrometry of Short-Range Ions Using Detectors Based on 4*H*-SiC Films Grown by Chemical Vapor Deposition

N. B. Strokan*, A. M. Ivanov*^, E. V. Kalinina*, G. F. Kholuyanov*, G. A. Onushkin*, D. V. Davydov*, and G. N. Violina**

**Ioffe Physicotechnical Institute, Russian Academy of Sciences, ul. Politekhnicheskaya 26, St. Petersburg, 194021 Russia*

^e-mail: alexandr.ivanov@pop.ioffe.rssi.ru

***St. Petersburg State Electrotechnical University, ul. Prof. Popova 5, St. Petersburg, 197376 Russia*

Submitted July 14, 2004; accepted for publication August 9, 2004

Abstract—Schottky barriers, 10^{-2} cm^2 in area, have been prepared by thermal deposition of Cr in vacuum on 50-μm-thick 4*H*-SiC epitaxial layers grown by chemical vapor deposition. The uncompensated donor concentration in these films is $(4–6) \times 10^{14}$ cm^{-3}, which makes it possible to extend the depletion region of the detector to ≈30 μm by applying a reverse bias of 400 V. The spectrometric characteristics of the detectors are determined using α particles in the energy range 4.8–7.7 MeV. The energy resolution attained for the 5.0- to 5.5-MeV lines is higher than 20 keV (0.34%), which, by a factor of 2, is second only to precision silicon detectors fabricated by specialized technology. The maximum signal amplitude corresponds, in SiC, to a mean electron–hole pair creation energy of 7.70 eV. *© 2005 Pleiades Publishing, Inc.*

1. INTRODUCTION

Detection of nuclear radiation is a high-priority issue in such fields as operational safety in nuclear power plants and spacecrafts; the utilization of nuclear waste; and activities in areas contaminated by radioactivity, particularly at elevated temperatures and in the presence of chemically corrosive media. The attendant problems cannot be solved without the development of high-temperature high-resolution detectors of nuclear radiation that are capable of spectrometric operation in extreme conditions. Devices featuring such a combination of characteristics cannot, however, be fabricated out of traditional semiconductor materials (Ge, Si, CdTe, and GaAs). The most appropriate starting material for the development of such detectors is silicon carbide, a wide-gap semiconductor.

The potential of SiC as a material for the fabrication of high-temperature detectors and spectrometers of nuclear radiation has already been convincingly demonstrated in early studies of the effect of neutrons and α particles on the properties of SiC and devices based on this material [1–3]. The high defect and carrier concentrations characteristic of this material did not, however, permit the attainment of an energy resolution higher than 8–9% [4]. In recent years, considerable progress has been made in growing high-purity SiC epitaxial layers with a low content of deep levels and relatively large carrier-diffusion lengths and lifetimes [5]. Quite recently, high-purity epitaxial layers of the 4*H*-SiC polytype, with an uncompensated donor concentration $N_d - N_a = (1–2) \times 10^{15}$ cm^{-3}, have been used in studies of short-range-ion spectrometry. In these studies, diode structures with Schottky barriers formed on these epitaxial layers were irradiated with α particles at energies of 5.1–5.5 MeV emitted by ^{239}Pu, ^{240}Pu, ^{241}Am, and ^{238}Pu isotopes. At bias voltages of 225–400 V, these structures exhibited saturation in the dependence of detector signal on reverse bias, which demonstrates a complete collection of the nonequilibrium charge produced by the irradiation and, hence, the maximum possible amplitude of the detector signal. These SiC detectors were the first to demonstrate an energy resolution of ~0.5% [6].

In this paper, we report new data on the spectrometric potential of detectors based on higher-resistivity, high-purity epitaxial 4*H*-SiC layers.

2. EXPERIMENTAL

We studied the characteristics of detector structures formed of 50-μm-thick 4*H*-SiC epitaxial layers with an uncompensated donor concentration of $N_d - N_a = (4–6) \times 10^{14}$ cm^{-3}, which were grown by chemical vapor deposition (CVD) on n^+-4*H*-SiC commercial substrates with a concentration of $N_d - N_a = 10^{19}$ cm^{-3}. The Cr Schottky barriers, 1×10^{-2} cm^2 in area and 0.1 μm thick, as well as the Cr/Al base contacts, were produced by thermal deposition in vacuum. The diode structures were bombarded with α particles at energies of 4.8–7.7 MeV using ^{226}Ra, ^{241}Am, and ^{238}Pu isotopes.

The quality of the CVD-grown films was assessed using several methods. In particular, the structure of the defect centers in the specimens was deduced from photoluminescence (PL) spectra obtained at 77 K. The diffusion lengths of the minority carriers, i.e., holes (L_D), were derived from the dependence of photocurrent on

the reverse bias in the temperature range 300–450 K. The distribution of an electrically active impurity near the Schottky barriers, as well as the characteristics of the deep levels in the band gap of 4*H*-SiC, were studied from capacitance–voltage (*C*–*V*) and DLTS data obtained in the 80–700-K temperature range. The forward and reverse *I*–*V* characteristics of the Schottky diodes were obtained in dc measurements.

The detector structures were characterized by measuring the dependence of the average signal amplitude on the diode bias (charge collection efficiency (CCE)) and measuring the energy resolution, as well as by determining the character of the noise via a comparison of the dark and photocurrent noise [7]. The data on the CCE also permitted an independent estimation of the value of $N_d - N_a$ and L_D in the CVD-grown layers. The data thus obtained were compared with the measurements of the *C*–*V* curves and the photocurrent vs. bias relation.

The above detector characteristics (including noise) were determined with the use of standard spectrometric equipment. The setup was assembled from ORTEC units and included a charge-sensitive preamplifier 142, an *RC*-shaped amplifier 571, and a precision oscillator 419. The pulse-height spectrum was analyzed by a computer-interfaced unit designed for 4000 channels (RI-161/01, St. Petersburg Institute of Nuclear Physics, Russian Academy of Sciences). The energy value of each channel was calibrated with a precision silicon detector (fabricated at the Ioffe Physicotechnical Institute RAS, St. Petersburg) using the ^{226}Ra α-decay lines [8].

3. RESULTS AND DISCUSSION

3.1. Characteristics of the Starting Material

The PL spectra of the CVD-grown epitaxial layers under study exhibited an intense main band at 390 nm (Fig. 1). This band can be assigned to free exciton recombination involving the optical phonons (FE–TO) in the 4*H*-SiC polytype [9]. The presence of triplet lines at the peak, which are resolvable even at 77 K, demonstrates the high quality of the epitaxial layers. However, the spectrum also includes weak lines related to nitrogen–aluminum donor–acceptor transitions (DAP) [10], small amounts of various defects (the peak at 460 nm), and inclusions of the 15*R* polytype [9]. Due to the high quality of the epitaxial layers, the diffusion lengths of the minority carriers (holes), which were determined from the photocurrent measurements conducted under reverse bias, were found to be 8–10 μm and increased by a factor 1.4 when the sample was heated to 450 K.

The *C*–*V* characteristics of the Schottky barriers were linear when plotted using the $1/C^2 = f(U)$ coordinates for bias voltages of up to 120 V and depended on neither frequency nor temperature within the measurement ranges covered. This behavior of the *C*–*V* characteristics suggests that there is a low content of defect centers in the CVD-grown layers. Indeed, the DLTS

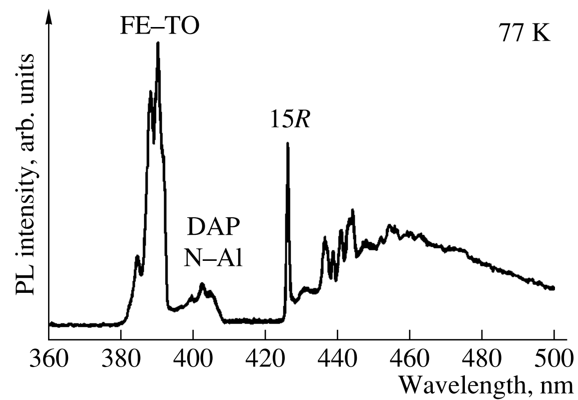

Fig. 1. The photoluminescence spectrum of CVD-grown 4*H*-SiC epitaxial layers; the spectra were measured at 77 K.

measurements revealed only one center, of a still unknown nature, with the energy 0.82 eV and with a capture cross section of 3×10^{-15} cm^2, present in the amount 1.8×10^{12} cm^{-3}.

The *I*–*V* characteristics were typical of Schottky barriers with a barrier height of 1 V and a shape coefficient of 1.1. The reverse currents did not exceed 1 nA for a reverse bias of 500 V. These characteristics of the Schottky barriers permitted us to extend the space-charge region to tens of μm and use the structures as spectrometric detectors of α particles.

3.2. Alpha Particle Spectrometry

The operation of a detector in spectrometric mode implies a high energy resolution. In order to attain this resolution, the nonequilibrium charge produced by the ions must be transported to the detector electrodes with as little loss as possible. Figure 2 (left-hand axis) plots the signal vs. the applied reverse bias U for two specimens used in the detection of α particles with the energy $E_\alpha = 5390$ keV. The energies E specified on the vertical axis were obtained using the mean electron–hole-pair creation energy $\varepsilon_{SiC} = 7.70$ eV [6]. One can clearly see that the curve levels off at voltages in excess of 150 V. This observation indicates that the charge transport for $U > 150$ V is complete.

At low biases, the particle range R exceeds the width W of the depletion region. In addition to a "fast" drift, the comparatively slow hole diffusion in the detector base also contributes to the charge transport. Recombination of the nonequilibrium carriers in the course of the diffusion brings about charge losses and accounts for the deviation of the value of CCE = E/E_α from 100%. The $E(U)$ relation can be approximated in its initial portion by the linear function

$$E = \frac{dE_\alpha}{dx}(L_D + W). \quad (1)$$

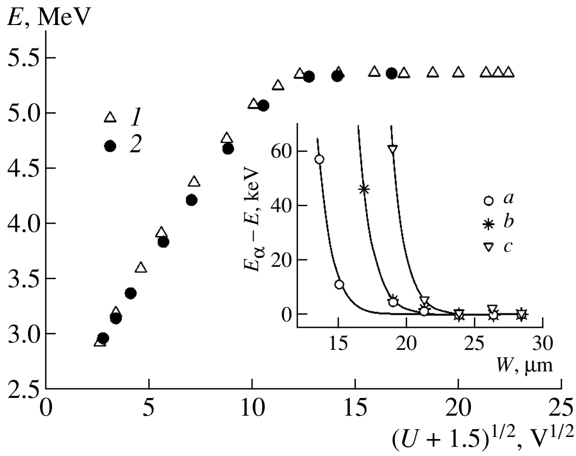

Fig. 2. The detector signal (in energy units) vs. the applied bias for two specimens (*1*, *2*). The α-particle energy was 5390 keV. The value taken for the mean energy of the electron–hole pair formation in SiC is 7.70 eV [6]. The detector-signal amplitude deficit vs. the space-charge region width is shown in the inset. The α-particle energy is equal to (*a*) 4787, (*b*) 5489, and (*c*) 6002 keV.

Here, dE_α/dx are the specific energy losses of an α particle in the initial part of its range (~200 keV/µm), L_D is the hole diffusion length, and W is the width of the space-charge region. Equation (1) permits us to estimate L_D, as well as the concentration of uncompensated impurities in the film, $N_d - N_a$, directly from the amplitude of the detector signal. The values obtained for the above specimens are $L_D = 11.2$ and 10.7 µm for $N_d - N_a = 5.85 \times 10^{14}$ and 4.40×10^{14} cm^{-3}, respectively. These values are found to be in good agreement with the data derived from the *C*–*V* characteristics and the dependence of the photocurrent on the reverse bias.

Knowing the value of $N_d - N_a$ allows us to readily determine the $W(U)$ relation and, hence, the dependence of the amplitude deficit, $E_\alpha - E$, directly on the width of the depletion region W. The inset in Fig. 2 makes it possible to compare the plots of $(E_\alpha - E)$ vs. W for three energy levels of the ^{226}Ra α particles. The sharp drop of the amplitude deficit down to zero is seen to occur in a similar way for all the energy levels in question. Significantly, the values of $E_\alpha - E \approx 0$ are observed at the widths $W = W_0 \approx R$, i.e., where the part played by diffusion in the carrier transport is reduced to a minimum. This is illustrated by the data in the table

The α-particle energies E_α and ranges R in SiC, and the extent of the depletion region W_0 accounting for the charge loss $E_\alpha - E = 6$ keV

E_α, keV	R, µm	W_0, µm
4787	15.5	15.8
5489	18.8	18.9
6002	21.6	21.2

for the chosen amplitude-deficit level $E_\alpha - E = 6$ keV (≈0.1%). As regards the fourth line of ^{226}Ra, with an energy 7687 keV, the largest value, $W = 28.4$ µm, attained is smaller than the range ($R = 31$ µm), which results in a noticeable deficit (82 keV).

Figure 3 displays a spectrum of the ^{226}Ra α decay obtained at $U = 400$ V. The incomplete charge collection in the case of 7687-keV α particles is also seen to affect the width of the spectral line. This width characterizes the energy resolution and is defined as the full linewidth at half-maximum (FWHM). As can be seen from Fig. 3, the value of FWHM for the above-mentioned line substantially exceeds that for the other three lower energy lines.

Note that the spectra of Fig. 3 yield only an estimate of the resolution of a SiC detector. As has been shown in experiments with a precision Si detector, the ^{226}Ra lines have an intrinsic width that is quite noticeable in our case; thus, in spite of the charge transport being complete, determination of the FWHM of a SiC detector from the "thin" lines in the 4.7–6.0-MeV range would be quite inappropriate. Therefore, the resolution of the SiC detector was determined using another spectrometric source emitting four closely lying lines in the 5.4–5.5-MeV range. The spectra obtained from this source were compared with those measured using a precision Si detector.

As follows from Fig. 4, the Si detector resolves the two right-hand peaks, whereas the shoulder at the left-hand peak indicates that there is a weaker (and lower energy) line. While the spectrum measured with the SiC detector is slightly blurred, the value FWHM = 18.8 keV (0.34%) is only a factor of 2 larger than that in Si detectors, which are substantially more advanced technologically. It should also be emphasied that the Si detector was fabricated with the application of a fractal boron diffusion, which provides a thin (about 300 Å in the Si equivalent) entrance window. The entrance window of the SiC detector was a 1000-Å-thick Cr layer, which gave rise to additional signal pulse-height fluctuations.

As regards the bulk properties of the material, it should be emphasized that the condition of approximate equality of the α-particle range with the width of the detector depletion region was sufficient to ensure a complete charge transport and a high detector resolution. It is instructive that it was not necessary to develop the widths $W \gg R$. Indeed, in our "range–depletion region" geometry at $W \approx R$, the top of the Bragg ionization curve fell in the region of the "weak" field that decayed linearly away from the surface. Even in such unfavorable conditions, no indication of the capture of nonequilibrium carriers was revealed.

This capture can occur by a localization of one of the electron–hole pair components or via a recombination of the pair as a whole. In both cases, the charge loss is proportional to the trapping-center concentration. As follows from our measurements, the level of the trap-

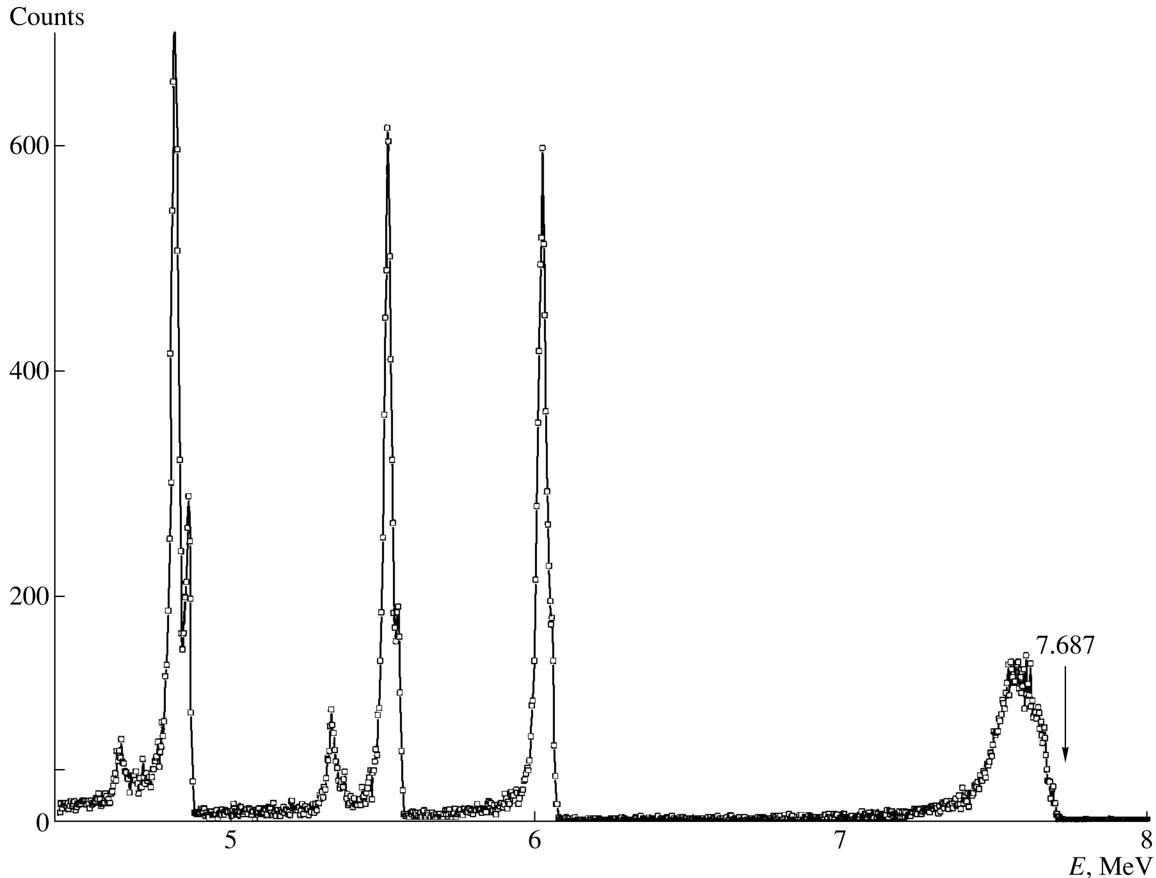

Fig. 3. The ^{226}Ra α-decay spectrum measured with a SiC detector at a bias voltage of 400 V. The position of the right-hand spectral line does not fit its energy of 7687 keV because of an incomplete transport of the nonequilibrium charge.

ping-center concentration needed to provide high detector characteristics, even for tracks located partially in the weak-field region, is attained in the films under study.

It appears safe to conclude that, in order to further improve the resolution of detectors based on silicon carbide films, one should improve the entrance-window technology of the structure. Previously, in the case of silicon detectors, a similar situation was encountered as the theoretical limit of the ultimate resolution was approached.

3.3. The I–V Characteristics and Origin of the Noise

The electric field at the detector surface in the conditions chosen for the CCE and resolution measurements was quite substantial ($\sim 3 \times 10^5$ V/cm). It appears important, therefore, to study the shape of the reverse *I–V* characteristic of the Schottky barriers, which is plotted in the log–log scale in the inset in Fig. 5. Two portions where the current increases according to a power law (with an exponent a) that is a function of the reverse bias, $(U + 1.5)^{1/2}$, are immediately seen. In the first portion ($U \leq 150$ V), the exponent a is close to unity (a = 1.22), and, in the second portion, it approaches a cubic function (a = 2.84). As is typical of Cr/SiC, the current density in the first portion corresponds to the electron emission from a metal with a barrier height of 1 eV. In the second portion, however, both the currents themselves and the increasing rate of their growth are indicative of a current flowing over the local "weak" parts of the Schottky barrier. Such currents can be accompanied by excess noise, which, in turn, contributes to the linewidth. To study the character of the noise, we used a method that involved a comparison of dark and photocurrent noise figures [7]. The photocurrent was produced by uniformly illuminating the detector with a GaN:In-based LED over the surface area. The photocarriers were generated primarily owing to extrinsic absorption. As a result, the photocurrent was determined by carriers that were generated in the bulk of the detector and flowed through the entire barrier area. In these conditions, shot noise should be generated.

The measurements were conducted at two bias voltages, U = 150 and 500 V, each corresponding to the right-hand edge of the above-mentioned regions of the *I–V* curves. The detector, together with output pulses of the precision generator, was connected to the input of the spectrometric setup. The magnitude of the noise was derived from the broadening of the generator

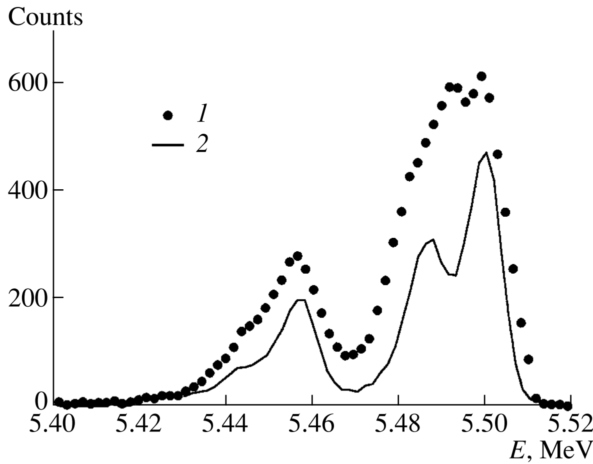

Fig. 4. The spectrum of α particles with energies in the range 5.4–5.5 MeV. For comparision, curve *1* shows the spectrum obtained with a SiC detector and curve *2* shows the results from a precision silicon detector. The bias applied to the SiC detector is 365 V and resolution is 18.8 keV (0.34%).

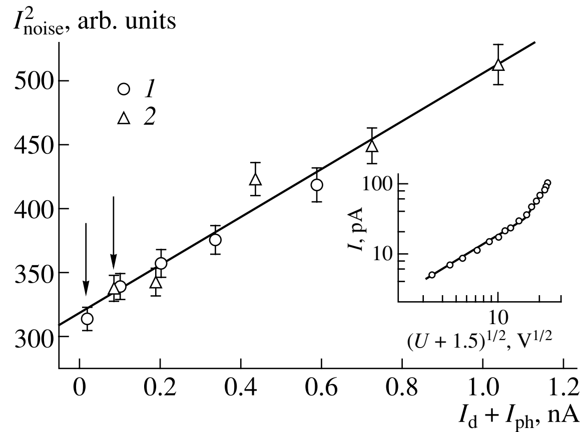

Fig. 5. Detector noise as a function of current. The dependence was obtained under specimen illumination to provide an equal probability of carrier generation over the volume. The detector bias was equal to (*1*) 150 and (*2*) 500 V. The first points indicated by the arrows correspond to the dark current. A GaN:In light-emitting diode was used to produce the photocurrent. Inset: the *I–V* characteristic of the SiC detector.

pulse-height spectrum. We may add that, in accordance with [7], to increase the noise associated with current, the amplifier transmission band was shifted toward lower frequencies.

Figure 5 shows the plot of squared noise vs. current I^2_{noise}, with the first two points corresponding to the dark current (I_d). The other points were obtained by summing I_d and the photocurrent I_{ph}. As is evident from Fig. 5, the magnitude of the noise I^2_{noise} grows linearly with the current, which is characteristic of shot noise. The increase in the bias from $U = 150$ to 500 V did not noticeably affect the photocurrent noise. As the noise at the second and third points in the plot is the same, it follows that the noise is insensitive to the origin of the current. Indeed, the current I_d at the second point in the plot was obtained by increasing U, and the total current $I_d + I_{ph}$ of the third point was obtained by illumination at a lower bias. As a consequence, the values of the dark current noise fell on the common curve. It may be conjectured that when the current flows over the "weak" regions of the barrier, the nonlinear effects at the chosen bias voltages, $U \lesssim 500$ V, are still poorly pronounced.

A further increase in the bias to ~550 V brought about a sharp rise in the current. After the breakdown, the *I–V* characteristics did not recover their original shape, and the noise rose superlinearly with the dark current (Fig. 6, curve *1*). If, however, we fix the bias U and increase the current via the illumination, the noise takes on its original shot pattern. Dark-current noise is only a background for the total noise (curves *2* and *3* in Fig. 6 are for $U = 50$ and 80 V, respectively). The difference in the noise pattern that sets in after the breakdown is additional evidence for the absence of any connection

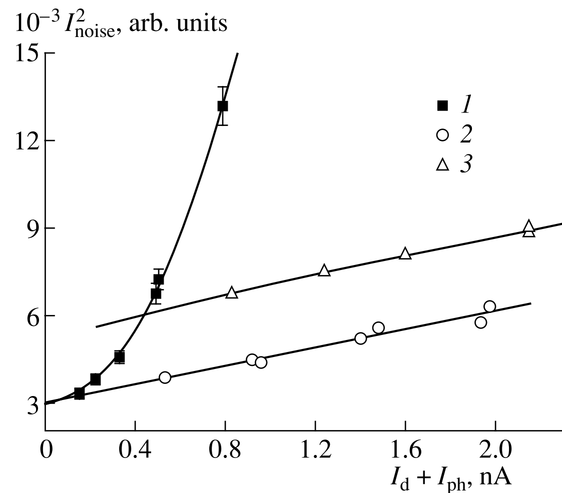

Fig. 6. The SiC detector noise vs. the current measured after the breakdown of the Schottky barrier. Curve *1* represents the dark-current noise, and curves *2* and *3* represent the detector noise under illumination. The detector bias voltage was equal to (*2*) 50 and (*3*) 80 V.

between the Schottky barrier dark current and carrier generation in the bulk of the structure.

4. CONCLUSION

An energy resolution of 0.34% for 5.1- to 5.5-MeV α particles, which is comparable with that attained for the best Si detectors, has been obtained for detector structures grown in the form of Schottky barriers on high-purity 4*H*-SiC epitaxial layers. This achievement was made possible by the low defect-center concentration ($\lesssim 2 \times 10^{12}$ cm^{-3}) in the epitaxial layer, which pro-

vided fairly large diffusion lengths, 8–13 μm, for the minority carriers (holes). This factor, in addition to the low uncompensated donor concentration, made it possible to attain a complete collection of the nonequilibrium charge at a reverse bias as low as 150 V, although, in these conditions, part of the track with the highest ionization density was located within the weak-field region of the detector. The α particles with the highest energies in the 4.8- to 7.7-MeV range exhibited a signal-amplitude deficit of $\lesssim 1\%$.

The high quality of the Schottky barriers, in turn, accounts for the low currents ($\lesssim 1$ nA) found up to reverse biases of 500 V. As a result, no excess noise was observed, and the shot noise associated with this current did not noticeably contribute to the detector spectral linewidth.

The attained characteristics of the films suggest that, in order to further improve the detector resolution, the technology for growing the entrance window of the structure should be refined.

The above results were obtained with α-particle spectrometry. There is no doubt, however, that they are valid for any short-range ions (nuclear fission fragments, accelerated ions of light, or heavy elements). Considering, for instance, fission-fragment spectrometry, the above problem of ionization by an ion at the edge of the depletion region should be less acute, because the ionization produced by a fragment falls off at the end of its range.

ACKNOWLEDGMENTS

We thank the CREE Company for providing us with a sample containing a high-purity 4*H*-SiC epitaxial layer.

This study was supported in part by a grant from the President of the Russian Federation (project no. NSh-2223.2003.02) and a research program of the RD-50 collaboration (CERN).

REFERENCES

1. L. W. Aukerman, H. C. Gorton, R. K. Willardson, and V. E. Bryson, in *Silicon Carbide,* Ed. by J. R. O'Connor and J. Smiltens (Pergamon, Oxford, 1959), p. 388.
2. V. E. Bryson, Wright Patterson Air Force Base, Ohio Report AD-215601 (1959).
3. G. F. Kholuyanov and B. V. Gavrilovskiĭ, Fiz. Tekh. Poluprovodn. (Leningrad) **2**, 573 (1968) [Sov. Phys. Semicond. **2**, 472 (1968)].
4. V. A. Tikhomirova, O. P. Fedoseeva, and G. F. Kholuyanov, Fiz. Tekh. Poluprovodn. (Leningrad) **6**, 957 (1972) [Sov. Phys. Semicond. **6**, 831 (1972)].
5. E. Kalinina, G. Kholujanov, A. Zubrilov, *et al.*, J. Appl. Phys. **90**, 5402 (2001).
6. A. M. Ivanov, E. V. Kalinina, A. O. Konstantinov, *et al.*, Pis'ma Zh. Tekh. Fiz. **30** (14), 1 (2004) [Tech. Phys. Lett. **30**, 575 (2004)].
7. A. M. Ivanov and N. B. Strokan, Zh. Tekh. Fiz. **70** (2), 139 (2000) [Tech. Phys. **45**, 281 (2000)].
8. V. K. Eremin, E. M. Verbitskaya, N. B. Strokan, *et al.*, Zh. Tekh. Fiz. **56**, 1987 (1986) [Sov. Phys. Tech. Phys. **31**, 1186 (1986)].
9. M. Ikeda and H. Matsunami, Phys. Status Solidi A **58**, 657 (1980).
10. A. Suzuki, H. Matsunami, and T. Tanak, J. Electrochem. Soc. **124**, 241 (1977).

Translated by G. Skrebtsov

Semiconductors, Vol. 39, No. 3, 2005, pp. 370–373. Translated from Fizika i Tekhnika Poluprovodnikov, Vol. 39, No. 3, 2005, pp. 388–392.
Original Russian Text Copyright © 2005 by Vinokurov, Zorina, Kapitonov, Murashova, Nikolaev, Stankevich, Khomylev, Shamakhov, Leshko, Lyutetskiĭ, Nalyot, Pikhtin, Slipchenko, Sokolova, Fetisova, Tarasov.

High-Power Laser Diodes Based on Asymmetric Separate-Confinement Heterostructures

D. A. Vinokurov, S. A. Zorina, V. A. Kapitonov, A. V. Murashova, D. N. Nikolaev, A. L. Stankevich, M. A. Khomylev, V. V. Shamakhov, A. Yu. Leshko, A. V. Lyutetskiĭ, T. A. Nalyot, N. A. Pikhtin^, S. O. Slipchenko, Z. N. Sokolova, N. V. Fetisova, and I. S. Tarasov

Ioffe Physicotechnical Institute, Russian Academy of Sciences, St. Petersburg, 194021 Russia

^e-mail: nike@hpld.ioffe.ru

Submitted July 14, 2004; accepted for publication August 9, 2004

Abstract—Asymmetric separate-confinement laser heterostructures with ultrawide waveguides based on AlGaAs/GaAs/InGaAs solid solutions, with an emission wavelength of ~1080 nm, are grown by MOCVD. The optical and electrical properties of mesa-stripe lasers with a stripe width of ~100 μm are studied. Lasers based on asymmetric heterostructures with ultrawide (>1 μm) waveguides demonstrate lasing in the fundamental transverse mode with an internal optical loss of as low as 0.34 cm^{-1}. In laser diodes with a cavity length of more than 3 mm, the thermal resistance is reduced to 2°C/W, and the characteristic temperature T_0 = 110°C is obtained in the range 0–100°C. A record-breaking wallplug efficiency of 74% and an output optical power of 16 W are reached in CW mode. Mean-time-between-failures testing for 1000 h at 65°C with an operation power of 3–4 W results in the power decreasing by 3–7%. © *2005 Pleiades Publishing, Inc.*

1. INTRODUCTION

Recently, a record-high power for optical emission from semiconductor lasers has been attained [1–7]. The principal concept behind this achievement is a reduction of the internal optical loss in separate-confinement laser heterostructures. The problems related to this reduction were discussed in detail in one of our earlier papers [8]. The principal way to reduce the internal optical loss in separate-confinement heterostructures is to make the waveguide in the laser heterostructure wider [1, 3, 4, 9]. A natural limitation is imposed on the waveguide thickness in a symmetric laser heterostructure by a condition related to the generation of higher order waveguide modes [4]. Several strategies have been offered to suppress higher order waveguide modes in wide waveguides [4, 10, 11]. All these methods allow the selection of higher order modes and a narrowing of the far-field pattern, but they result in an enhancement of the optical loss, which reduces the power of the optical emission of a laser diode.

To suppress these high-order modes, we previously offered an asymmetric heterostructure with the active region shifted away from the waveguide center [7, 12]. In an asymmetric heterostructure with an ultrawide waveguide, the generation of higher order modes can be suppressed using the difference in their optical-confinement factors, with the internal optical loss and beam divergence in the plane normal to the epitaxial layers being simultaneously diminished [7]. In our study in [12], an asymmetric heterostructure with an ultrawide waveguide was first used to simultaneously reduce the internal optical loss and beam divergence in the plane normal to the *p–n* junction plane. Making the waveguide wider, to 4 μm, allowed us to reduce the internal optical loss to 0.7 cm^{-1} and the emission divergence to 16°–18° without any significant loss in the maximum emission power, which was 8.6 W [12].

In this paper, we present the results of an investigation of AlGaAs/GaAs/InGaAs laser diodes based on an asymmetric separate-confinement laser heterostructure with an ultrawide waveguide. The properties of these laser diodes, based on asymmetric and the similar symmetric wide-waveguide structures are compared.

2. EXPERIMENTAL LASER HETEROSTRUCTURE AND LASER DIODES

Experimental laser heterostructures based on AlGaAs/GaAs/InGaAs solid solutions were grown by MOCVD in an Emcore GS-3100 machine. The laser structures were quantum-well separate-confinement heterostructures with an asymmetric position of the active region in the ultrawide waveguide. Figure 1 shows a band diagram of the structures, which consisted of two wide-bandgap $Al_{0.3}Ga_{0.7}As$ emitters, a GaAs waveguide layer, and a strained InGaAs quantum well (QW) of 90 Å in thickness.

The shift of the active region in respect to the symmetric position was chosen based on the selection of a minimum optical-confinement factor in the active region for the higher order modes and its maximum value for the fundamental mode (Fig. 1). Under these circumstances, the generation of the fundamental mode

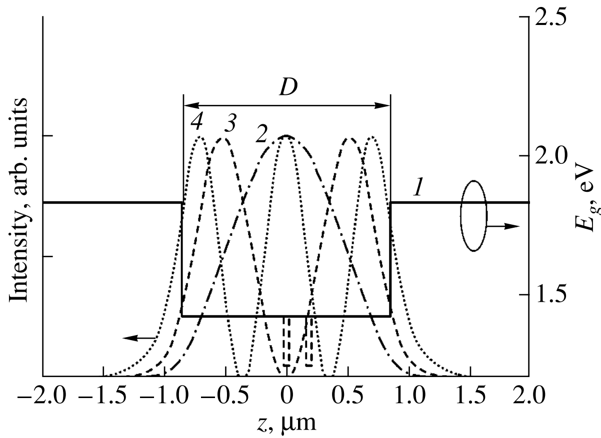

Fig. 1. (*1*) An energy diagram of the symmetric and asymmetric separate-confinement laser heterostructures with the waveguide width $D = 1.7$ µm. (*2–4*) Electric field distributions for the (*2*) zeroth, (*3*) 1st, and (*4*) 2nd modes. The z direction is normal to the structure layers.

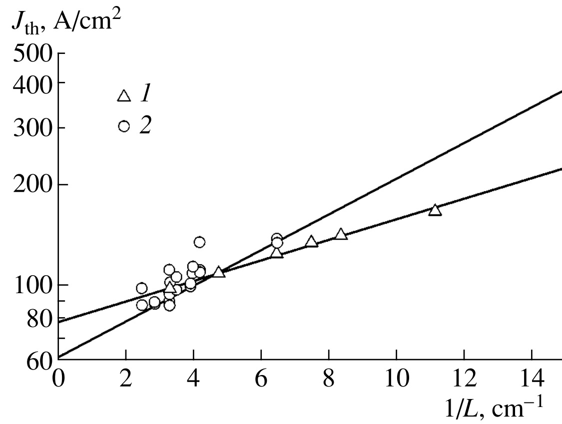

Fig. 2. The threshold current density J_{th} vs the inverse cavity length $1/L$ in lasers based on (*1*) symmetric ($D = 0.4$ µm) and (*2*) asymmetric ($D = 1.7$ µm) heterostructures.

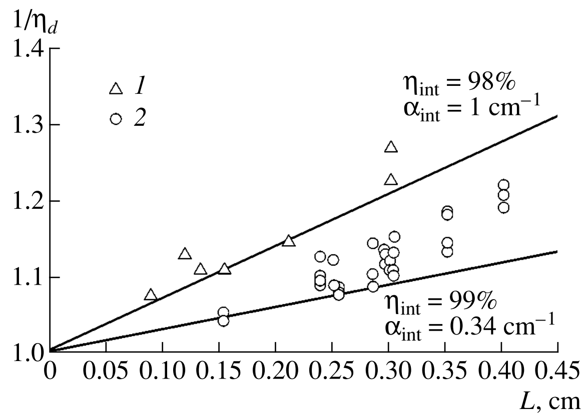

Fig. 3. Experimental dependences of the inverse differential quantum efficiency ($1/\eta_d$) on the cavity length L in lasers based on (*1*) symmetric ($D = 0.4$ µm) and (*2*) asymmetric ($D = 1.7$ µm) heterostructures.

is preferred to higher order modes, in accordance with the threshold condition for a laser diode:

$$\Gamma_{QW} g(n_{QW}, p_{QW}) = \alpha_{int} + \alpha_{ext}, \quad (1)$$

where $g(n_{QW}, p_{QW})$ is the material gain in the active medium; n_{QW} and p_{QW} are the free carrier (electron and hole) densities in the active region; α_{int} and α_{ext} are the internal and external optical loss, respectively; and Γ_{QW} is the optical-confinement factor in the active region. Our calculations [7] show that the threshold density for higher order modes can exceed that for the fundamental mode by 10–20% in asymmetric laser heterostructures with the waveguide-layer thickness $D = 1.7$ µm.

Multimode lasers with 100-µm-wide contacts and different cavity lengths were fabricated from the laser heterostructures. Laser diodes were mounted onto a copper heat sink with the stripe down. The properties of the semiconductor lasers were studied at the stable 20°C temperature of the heat sink.

The best results attained by our group for similar symmetric separate-confinement laser heterostructures were presented in [1, 3]. We now compare the properties of the laser diodes based on asymmetric heterostructures with these earlier data.

3. STUDIES OF THE PROPERTIES OF LASER DIODES BASED ON ASYMMETRIC HETEROSTRUCTURES

The study was performed on a series of lasers with various cavity lengths from 1 to 5 mm. The output mirror of the Fabry–Perot cavity was given an antireflection coating to make its reflectance equal to 5–6%; a multilayer dielectric SiO_2/Si mirror with a reflectance of over 95% was deposited onto the opposite facet. Figure 2 shows the dependences of the threshold current density J_{th} on the inverse cavity length $1/L$ for both the symmetric [1, 3] and asymmetric (EM-474) structures. The introduction of asymmetry into the design of the laser heterostructure did not enhance the threshold current density for cavities of $\gtrsim$2 mm in length, though the optical-confinement factor in the active region for the asymmetric structure was somewhat smaller than that for the symmetric structure. In lasers with a cavity length over 2 mm, the threshold current density decreased, which correlates with the decrease of the threshold density and, therefore, with the reduction of the internal optical loss as the cavity length increases [13]. Figure 3 shows the dependences of the inverse differential quantum efficiency $1/\eta_d$ on the cavity length. The analysis of these dependences allows us to determine the internal optical loss α_{int} typical of the heterolasers under study and the stimulated quantum yield η_{int}. Two factors can adversely affect the stimulated quantum yield and internal optical loss in laser heterostructures: a small depth of the QW for electrons, which results in electron emis-

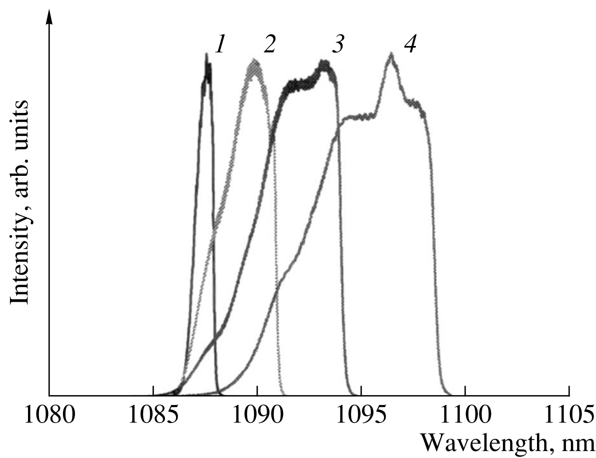

Fig. 4. The shift of the emission spectrum of a laser with an asymmetric heterostructure. The waveguide width D = 1.7 μm, and the drive currents are (*1*) 0.45, (*2*) 3, (*3*) 6, and (*4*) 9 A.

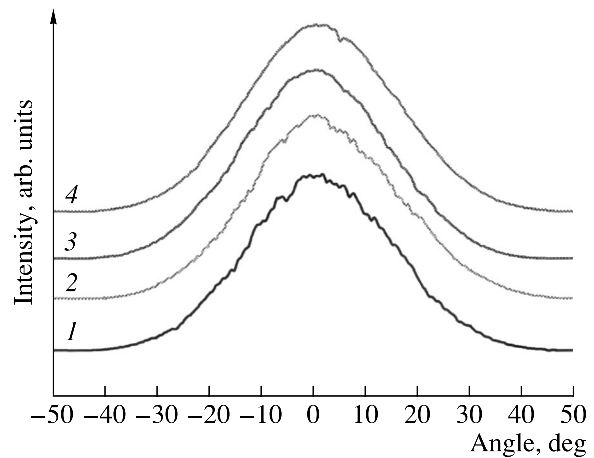

Fig. 5. The far-field emission pattern in the plane normal to the *p–n* junction plane, as function of the angle, for the drive currents (*1*) 0.5, (*2*) 5, (*3*) 10, and (*4*) 15 A. The FWHM of the pattern was (*1*) 30°, (*2*) 33°, (*3*) 31°, and (*4*) 33°.

sion [14, 15], and a large width of the waveguide layers, which stimulates the leakage of electrons into the *p*-type emitter [16]. In a symmetric structure with a waveguide of 0.4 μm in width [1, 3], the stimulated quantum yield was as high as 98%, which indicates the absence of current leakage above the generation threshold. In an asymmetric structure, the stimulated quantum yield was as high as 99%. In our opinion, this fact indicates a strong confinement of the holes in the active region, which suppresses the diffusion of the emitted electrons toward the *p*-type emitter. At the same time, an increase of the waveguide width to 1.7 μm resulted in a threefold reduction of the internal optical loss in an asymmetric structure in respect to the symmetric one (Fig. 3).

The low internal optical loss (α_{int} = 0.34 cm^{-1}) allowed us to enlarge the length of the laser diodes to 3–5 mm without decreasing the differential quantum efficiency (Fig. 3). The possibility of enlarging the cavity length is favorable for several of the parameters of laser diodes. The main advantage is a reduction in the series resistance. In our case, the series resistance was as low as 20–40 mΩ at the Fabry–Perot cavity length of 3–5 mm and the stripe contact width 100 μm.

The thermal resistance of the laser diodes strongly depended on the cavity length and was 2–2.5°C/W at a length of 5 mm. The thermal resistance was determined in the following way. The emission spectra of lasers with different lengths of the Fabry–Perot cavity were studied. In all the lasers, a red shift related to the heating of the active region was observed as the drive current increased (Fig. 4). The thermal resistance for the lasers with different cavity lengths was determined using the thermal coefficient of the band gap width, ~4 Å/deg.

Owing to the low thermal resistance, the overheating of the active region in the working drive current was only 7–10°C, which has a favorable effect on the service life of laser diodes based on asymmetric heterostructures.

Figure 5 shows the dependences of the emission intensity on the angle in the plane normal to the epitaxial layers for different drive currents. The shape, halfwidth, and position of the peak in the far-field pattern did not change, which indicates generation in the fundamental transverse mode in the entire studied range of drive currents.

The introduction of asymmetry into a laser structure allowed us to increase the waveguide width to 1.7 μm, with lasing in the fundamental transverse mode being preserved. An irregular dependence of the emission intensity on the angle was observed in the plane parallel to the epitaxial layers, which indicates an inhomogeneous irregular generation in a 100-μm-wide stripe, which is unfortunately typical of heterostructures with an active region thickness below 100 Å. However, at the working drive current, the FWHM of the far-field pattern did not exceed 12°, which is a good parameter for the application of lasers in optical and fiber systems.

A study of the temperature dependences of the threshold-current density in the temperature range 0–100°C demonstrated no distinctions when compared with the lasers based on symmetric heterostructures. The average characteristic temperature was ~110°C, which coincides with the parameter of the lasers with a symmetric waveguide structure [1, 3].

Figure 6 shows the dependences of the CW emission power and wallplug efficiency on the driving current of the laser diode. The laser diode parameters, such as the internal optical loss and the series and thermal resistance, were optimized, and the energy density on the mirrors of the Fabry–Perot cavity was reduced. As a result, the maximum emission power and the wallplug efficiency of a laser with an asymmetric structure are high; indeed, they reach the record-breaking values of

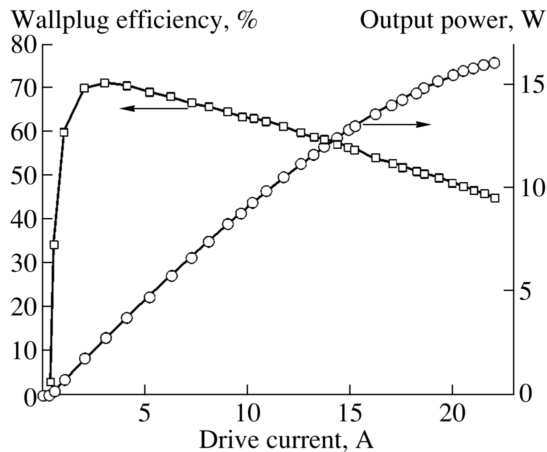

Fig. 6. The light–current characteristic and wallplug efficiency as functions of the drive current for a laser diode with the cavity length L = 3040 μm, stripe width 100 μm, and high-reflection (95%) and antireflection (5%) coatings on the cavity faces (CW mode at the temperature 20°C).

16 W at a stripe width of 100 μm and 72% at a cavity length of ~3 mm. The most important factor is the high wallplug efficiency at the working emission power of 4–6 W. In semiconductor lasers with an asymmetric heterostructure that has the cavity length 2–4 mm, the maximum wallplug efficiency exceeds 70%, reaching a value of up to 74%.

Degradation tests with the produced lasers were performed at an elevated temperature and drive current. The lasers were preliminary selected using the data obtained in electrical and optical studies. They were tested in a clean enclosed volume at the operation power 3–4 W and a heat-sink temperature of 65°C for at least 1000 h of continuous operation. In all the lasers, the power decreased by no more than 3–5%.

4. CONCLUSION

Asymmetric quantum-well separate-confinement laser heterostructures with ultra-wide waveguides based on AlGaAs/GaAs/InGaAs solid solutions were grown by MOCVD.

Mesastripe laser diodes with a 100-μm aperture were fabricated, and their light–current and current–voltage characteristics were studied. A record-breaking output optical power of 16 W and wallplug efficiency of 74% at the emission wavelength of 1080 nm were obtained. A threshold-current density of 80–100 A/cm^2, an internal optical loss of 0.34 cm^{-1}, and a 99% internal quantum yield of stimulated emission was reached.

Lasing in the fundamental transverse mode in the entire range of drive currents was obtained in lasers with an asymmetric heterostructure and a waveguide width of 1.7 μm. In the plane parallel to the p–n junction plane, the beam divergence was 8°–12° and, in the normal plane, it was 30°–32°.

ACKNOWLEDGMENTS

The study was supported in part by the Russian Foundation for Basic Research (project no. 04-02-17641) and the Program "Technology of Nanosized Objects and Systems."

REFERENCES

1. D. A. Livshits, A. Yu. Egorov, I. V. Kochnev, *et al.*, Fiz. Tekh. Poluprovodn. (St. Petersburg) **35**, 380 (2001) [Semiconductors **35**, 365 (2001)].
2. F. Bugge, G. Erbert, J. Fricke, *et al.*, Appl. Phys. Lett. **79**, 1965 (2001).
3. D. A. Livshits, I. V. Kochnev, V. M. Lantratov, *et al.*, Electron. Lett. **36**, 1848 (2000).
4. A. Al-Muhanna, L. J. Mawst, D. Botez, *et al.*, Appl. Phys. Lett. **73**, 1182 (1998).
5. A. V. Lyutetskiĭ, N. A. Pikhtin, S. O. Slipchenko, *et al.*, Fiz. Tekh. Poluprovodn. (St. Petersburg) **37**, 1394 (2003) [Semiconductors **37**, 1356 (2003)].
6. E. G. Golikova, V. A. Kureshov, A. Yu. Leshko, *et al.*, Pis'ma Zh. Tekh. Fiz. **26** (20), 40 (2000) [Tech. Phys. Lett. **26**, 913 (2000)].
7. S. O. Slipchenko, D. A. Vinokurov, N. A. Pikhtin, *et al.*, Fiz. Tekh. Poluprovodn. (St. Petersburg) **38**, 1477 (2004) [Semiconductors **38**, 1430 (2004)].
8. N. A. Pikhtin, S. O. Slipchenko, Z. N. Sokolova, and I. S. Tarasov, Fiz. Tekh. Poluprovodn. (St. Petersburg) **38**, 374 (2004) [Semiconductors **38**, 360 (2004)].
9. M. R. Gokhale, J. C. Dries, P. V. Studenkov, *et al.*, IEEE J. Quantum Electron. **33**, 2266 (1997).
10. I. A. Kostko, V. P. Evtikhiev, E. Yu. Kotel'nikov, and G. G. Zegrya, Fiz. Tekh. Poluprovodn. (St. Petersburg) **33**, 752 (1999) [Semiconductors **33**, 693 (1999)].
11. V. I. Shveĭkin and V. A. Gelovani, Kvantovaya Élektron. (Moscow) **32**, 683 (2002).
12. S. O. Slipchenko, N. A. Pikhtin, N. V. Fetisova, *et al.*, Pis'ma Zh. Tekh. Fiz. **29** (23), 26 (2003) [Tech. Phys. Lett. **29**, 980 (2003)].
13. V. P. Evtikhiev, D. Z. Garbuzov, Z. N. Sokolova, *et al.*, Fiz. Tekh. Poluprovodn. (Leningrad) **19**, 1420 (1985) [Sov. Phys. Semicond. **19**, 873 (1985)].
14. L. V. Asryan, N. A. Gunko, A. S. Polkovnikov, *et al.*, Semicond. Sci. Technol. **15**, 1131 (2000).
15. N. A. Pikhtin, S. O. Slipchenko, Z. N. Sokolova, and I. S. Tarasov, Fiz. Tekh. Poluprovodn. (St. Petersburg) **36**, 364 (2002) [Semiconductors **36**, 344 (2002)].
16. D. Z. Garbuzov, A. V. Ovchinnikov, N. A. Pikhtin, *et al.*, Fiz. Tekh. Poluprovodn. (Leningrad) **25**, 928 (1991) [Sov. Phys. Semicond. **25**, 560 (1991)].

Translated by D. Mashovets

Semiconductors, Vol. 39, No. 3, 2005, pp. 374–375. Translated from Fizika i Tekhnika Poluprovodnikov, Vol. 39, No. 3, 2005, pp. 393–394.
Original Russian Text Copyright © 2005 by Mil'vidskiĭ, Ufimtsev.

BOOK REVIEW

A Review of the Book *Atomy legiruyushchikh primeseĭ v poluprovodnikakh* (Atoms of Doping Impurities in Semiconductors) by V.I. Fistul' (Moscow: Fizmatlit, 2004)

In recent years, monographs concerning semiconductors have not been published in Russia. Understandably, we were pleased when, in 2004, the Fizmatlit publishing house released the book that is reviewed here, which is concerned with a generalization of the data on the state and behavior of impurities in semiconductors. A special feature of this book is the fact that it was written by a man who has been deeply involved with this subject for a long time. The author, Professor V.I. Fistul', himself has made an appreciable contribution to the development of the current concepts concerning the nature and properties of various classes of impurities in elemental semiconductors and in III–V semiconductor compounds and their solid solutions. The reviewed book encompasses a great variety of impurities. The data on the solubility and migration of the most important impurities in various semiconductors are critically analyzed. In addition, the role of the interaction of these impurities with the accompanying impurities and inherent point defects of a crystal lattice is established in a conclusive way.

Although there is little to differentiate the general structure of the book from previously published works, the author's concept and understanding of the phenomena under consideration, as well as the allowance made for new data, is clearly communicated in each chapter of the book. In this review, we would like to draw attention to the book's notable features and a number of new treatments of the subject offered by Fistul'.

It is particularly important to note that the author considers three approaches to calculating the equilibrium concentrations of point defects in a crystal, including the atoms of doping impurities. One of these approaches, based on the method of quasi-chemical reactions (the Kröger–Brauer method), is well known; the second approach involves a method of minimization for the free energy in a system that consists of a crystal and an external phase; and the third approach, based on the quantum-mechanical method, is comparatively new and has not been described so far in any monographs.

The main limitations of the first method are related to the facts that the partial thermodynamic characteristics of the components involved in the reactions are unknown and possible interactions between existing defects are disregarded. The second method is free from these disadvantages but requires well-defined thermodynamic concepts in the context of a specific model of solid solutions. This limitation is removed to a great extent for semiconductor–impurity solid solutions if various regular-solution approximations are used. It is understandable, therefore, that Fistul' gives preference to the second method.

The third method was suggested by V.I. Fistul' himself in collaboration with D.A. Volkov. In spite of the fact that this method requires time-consuming calculations and is debatable from the standpoint of the theoretical concepts used, it undoubtedly offers the prospect of further development.

A major portion of the book is devoted to a description of the state and behavior of various classes of impurities in semiconductors. These classes include hydrogen-like impurities; impurities with partially filled electronic shells (the d and f impurities); and amphoteric, isovalent, and gas-forming impurities. This is practically the first time that such a comprehensive consideration of impurities, accompanied by a profound analysis of their behavior, has been carried out.

Chapter 4 is of particular interest as it is devoted to the theory of the solubility of impurities developed by Weiser. Fistul' attributes the main flaw of this theory to the so-called radius approach used in the Weiser theory; i.e., the radii of vacancies, self-interstitials, and impurity atoms are assumed to be constant. In order to remove this limitation, it is suggested that a rearrangement of the energy spectrum of the doping-impurity atoms when the atoms are transferred from a lattice site to an interstice is taken into account. This approach is realized by V.I. Fistul' and V.A. Shmugurov and represents undoubted progress in the development of ideas about the nature of impurity solubility.

Chapters 7 and 8 of the book illustrate the extent to which our ideas about the diffusion-related phenomena in semiconductors have been extended and expanded in recent times. Nowadays, one cannot disregard the special features of the interaction between existing point defects, and this circumstance is clearly outlined by Fistul' when considering the migration processes involving impurities. The main results of this treatment are analytical expressions that quite adequately describe the phenomena under analysis and specific illustrations of the impurity distributions that are most often encountered in practice. An analysis of special features of these distributions makes it possible to gain insight into the mechanisms of impurity diffusion and

1063-7826/05/3903-0374$26.00 © 2005 Pleiades Publishing, Inc.

assess the role of the impurity–impurity and impurity–vacancy interactions in these diffusion processes.

With respect to the shortcomings of the book, we should note that, along with adsorption processes, the very important phenomena involving the interaction of impurity atoms with dislocations and other extended crystal-lattice defects are ignored in this book. Furthermore, when considering the behavior of gas-forming impurities (in particular, oxygen and hydrogen), Fistul' did not use the new data reported in original recent publications. Nor can we agree with all the concepts used by Fistul'. For example, Fistul' considers the subsystems of the lattice sites and interstices in a crystal as separate phases between which an exchange of particles (and energy) occurs. Each of the subsystems is understood in the form of an infinite cluster with a fractal (rather than planar) interphase boundary. From the standpoint of the concepts of classical physical chemistry, the above-described approach makes a treatment of the phase rule and the use of the mass action law when describing various quasi-chemical reactions rather problematic.

Finally, we feel that, in the next editions of the book, particular attention should be given to the special features of the behavior of impurities in low-dimensional nanocompositions.

Assessing the monograph as a whole, we can state that the semiconductor-concerned scientific community now has extremely valuable generalizing printed material at its disposal, whose active use will undoubtedly be conducive to further progress in the physics and technology of semiconductors. We should be grateful to Fistul' for taking so much trouble to prepare the book and to the Fizmatlit publishing house for printing such an excellent edition.

Professor M.G. Mil'vidskiĭ,
Doctor of Technical Sciences
(State Research Institute for the Rare-Metal Industry)
Professor V.B. Ufimtsev,
Doctor of Chemistry
(Institute of Chemical Problems in Microelectronics)

Translated by A. Spitsyn